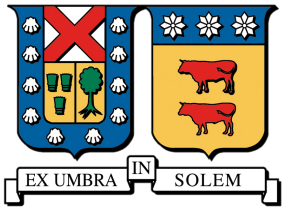
UNIVERSIDAD TÉCNICA FEDERICO SANTA MARÍA
DEPARTAMENTO DE INGENIERÍA MECÁNICA
VALPARAÍSO - CHILE



"DESIGN AND DEVELOPMENT OF A PLANAR CABLE-DRIVEN VSA BASED ROBOT FOR UPPER-LIMB REHABILITATION"

FRANCISCO ALBERTO RAMÍREZ REYES

MEMORIA PARA OPTAR AL TÍTULO DE
INGENIERO CIVIL MECÁNICO

PROFESOR GUÍA : Dr. Ing. DANILO ESTAY BARRIENTOS

PROFESOR CORREFERENTE : Dr. Ing. CHRISTOPHER NIKULIN CHANDIA

NOVIEMBRE 2016

A mi familia

Resumen

Los accidentes cerebrovascular son una de las principales causas de discapacidad en el mundo, y los daños al cerebro pueden resultar en parálisis y contracción involuntaria de los músculos. La rehabilitación se desarrolla a través de un proceso de recuperación de la movilidad del miembro afectado, con sesiones de ejercicios que simulan los movimientos cotidianos. Los robots son particularmente adecuados para este fin, ya que son capaces de realizar sesiones intensivas, introducir elementos interactivos y reducir la carga física para el terapeuta. Los dispositivos de rehabilitación actualmente en comercio son grandes, pesados y costosos, lo cual los hace exclusivos para centros dedicados a la rehabilitación.

El objetivo de esta memoria es concebir, diseñar y realizar la parte mecánica de un dispositivo mecatrónico para la rehabilitación del miembro superior, con el objetivo de ser un dispositivo de bajo costo y fácilmente transportable para que su uso sea aplicable también en el ambiente doméstico. El dispositivo es también concebido para ser del tipo *end-effector*, con un área de trabajo plana donde es prevista la utilización de actuadores con rigidez variable.

Para satisfacer las especificaciones, se desarrolla una arquitectura cinemática ortogonal, compuesta de dos actuadores a rigidez variable dispuestos perpendicularmente, que utilizan un innovador sistema leva-resorte para implementar la rigidez no linear. Este sistema permite controlar independientemente posición y rigidez en dos direcciones. Contrario a lo previsto, a través de un análisis cineto-estático, se ha encontrado una dependencia entre la rigidez de las dos direcciones ortogonales.

Se realiza el completo diseño mecánico del dispositivo, que incluye la definición de los requerimientos, y el diseño en detalle de cada componente. La etapas de manufactura y ensamble son descritas y realizadas, resultando en el primer prototipo mecánico del robot. El costo total del mecanismo se encuentra en torno a los €2400, muy por debajo al precio de robots de rehabilitación que se encuentra en circulación actualmente. Sin embargo, este costo no considera las partes mecanizadas, *hardware* y *software* para el sistema de control, ni las horas-hombre utilizadas en el diseño y construcción del prototipo.

Se realizan finalmente pruebas estáticas para analizar la curva de la fuerza en función del desplazamiento. Las pruebas evidencian un comportamiento cualitativo coherente con las predicciones, sin embargo, muestran también una discrepancia numérica, por lo que para implementar un sistema de control, es necesario el estudio y definición de la curva fuerza-desplazamiento experimental del robot.

Abstract

Stroke is one of the worldwide major causes of disability, and the brain injury can end up in paralyzation of muscles and their involuntary contraction. Post-stroke rehabilitation consists of a restorative learning process that, through sessions of task-specific exercises, allows the patient to recover the physical capacity of the limb. Robotic devices are highly suitable for this purpose, as they are capable of introducing high-intensity sessions, with interactive interfaces for the patient and the possibility of reducing the physical workload of the therapist. By now, rehabilitation robots are bulky and expensive, restricting their use to clinical environments.

The purpose of this dissertation is to conceive, design and assemble the mechanical components of a mechatronic device for upper limb rehabilitation, with the aim of being low-cost and easily transportable, in order to allow its use at patient's home. The device is also aimed to be end-effector based, have a planar workspace and include variable stiffness actuators.

In order to to achieve the specifics, an orthogonally-arranged kinematic architecture is conceived, consisting on two antagonistic variable stiffness actuators positioned orthogonally to each other, which exploit a novel cam-based series elastic actuator that introduces the necessary non-linear stiffness. This system was conceived to independently control position and stiffness on two orthogonal directions. Contrary to the expectations, a kinetostatic analysis shows a coupling effect between the stiffness in the two directions.

The entire mechanical design of the device is done afterwards, which includes the definition of the requirements and the detailed dimensioning of every component. The manufacturing operations and assembly phases are described and actually realized, resulting in a prototype of the robot. The overall cost of the mechanism is about €2400.00, which represents a very low cost considering the upper-limb rehabilitation robots in circulation today. Although, this cost does not consider mechanized parts, the control hardware and software, neither man-hours employed for the development of the prototype.

A few static tests were conducted on the prototype to observe the force vs displacement behavior that have highlighted a qualitative coherence with the model, but showed a discrepancy in terms of numerical values, which is to be studied and solved in order to properly implement a control strategy.

Glossary

CDPR Cable-Driven Parallel Robot.

DoF Degrees of Freedom.

FDM Fused Deposition Modeling.

LinWWC-VSA Linear Wire-Wrapped Cam VSA.

LinWWC-SEA Linear Wire-Wrapped Cam SEA.

SEA Series Elastic Actuator.

VIA Variable Impedance Actuator.

VSA Variable Stiffness Actuator.

Nomenclature

$(\mathbf{e}_{x,f}, \mathbf{e}_{y,f})$ Unit vectors of the reference frame $\{f\}$. If no $\{f\}$ is denoted, $\{w\}$ is assumed.

$\dot{x}$ $\ddot{x}$ First and second time derivate of x.

$\overline{PQ}$ Line passing through point P and Q.

$\mathbf{P}$ Vector with the cartesian components $[P_x, P_y]$.

$\mathbf{u}(P, Q)$ Unit vector from point P to Q.

$\mathbf{v}(P, Q)$ Vector from point P to Q.

$\{f\}$ Reference frame f, with $\{w\}$ denoting the global reference frame.

$d(P, Q)$ Distance between points P and Q.

O_f Origin of $\{f\}$.

P Geometric point with cartesian coordinates $[P_x, P_y]$.

w.r.t. With respect to

Contents

1 Introduction **1**
- 1.1 Upper Limb Rehabilitation Devices . . . 4
  - 1.1.1 State of the Art . . . 4
  - 1.1.2 Critical Analysis . . . 8
- 1.2 Variable Stiffness Actuators . . . 9
  - 1.2.1 VSAs State of the Art . . . 10
- 1.3 Aim of the Work . . . 13

2 Conceptual Design **15**
- 2.1 Three-directionally Arranged Actuator . . . 17
  - 2.1.1 Stiffness Ellipsoid Resolution . . . 17
  - 2.1.2 Negative Stiffness Based Device . . . 18
  - 2.1.3 Force and Stiffness Mapping . . . 22
- 2.2 Orthogonally-Arranged Actuator . . . 26
  - 2.2.1 Stiffness Analysis . . . 26

3 Kinetostatic Analysis **31**
- 3.1 Kinematic Architecture . . . 33
- 3.2 Force and Stiffness Analysis . . . 38
- 3.3 The Linear Wire-Wrapped Cam *SEA* . . . 43
  - 3.3.1 Logarithmic Spiral . . . 46
- 3.4 The Linear Wire-Wrapped Cam VSA . . . 48

4 Mechanical Design **51**
- 4.1 Performance Targets . . . 52
  - 4.1.1 Workspace . . . 52
  - 4.1.2 Target Force . . . 52
  - 4.1.3 Impedance Range . . . 53
- 4.2 Designing Calculations . . . 54
  - 4.2.1 Cable Tension and Force Distribution . . . 54
  - 4.2.2 Spring and Cam Definition . . . 55
  - 4.2.3 Motor Requirements . . . 56
  - 4.2.4 Load on Carriages and Bars . . . 56
  - 4.2.5 Drum Height . . . 58
  - 4.2.6 Numeric Results . . . 61
- 4.3 Detailed Design . . . 62
  - 4.3.1 Structure . . . 64
  - 4.3.2 End-effector . . . 66

4.3.3 Transmission System . . . 67
4.3.4 Belt-tensioning System . . . 68
4.3.5 Actuation . . . 72
4.3.6 Non-linear Elastic Elements . . . 72
4.3.7 Hardware . . . 72

5 Prototype Development **77**
5.1 Purchased Elements . . . 77
5.2 Manufacturing . . . 78
5.2.1 3D Printed Elements . . . 78
5.3 Mounting . . . 82
5.4 Electronic Connections . . . 85
5.5 Control Architecture . . . 87
5.5.1 Feedback Information . . . 87
5.5.2 Control Strategies . . . 88
5.5.3 Open-loop Control . . . 88
5.5.4 Closed-loop Control . . . 88
5.6 Experimental Testing . . . 91
5.6.1 Test Bench . . . 91
5.6.2 Results . . . 93
5.6.3 Discussion . . . 97

6 Conclusions **99**
6.1 Future Work . . . 100

A Technical Drawings **105**

B Resumen en Español **143**

List of Figures

1.1 Examples of robots . . . 2
1.2 Visual representation of a stroke . . . 3
1.3 MIT-Manus robot. . . . 4
1.4 Sophia robots. . . . 5
1.5 CBM-Motus robot. . . . 6
1.6 NeReBot robot. . . . 7
1.7 MACARM robot. . . . 8
1.8 Spring preload VSAs. . . . 10
1.9 NEUROexos Robot . . . 11
1.10 Compact linear-motion device. . . . 11
1.11 *LINarm*. . . . 12
1.12 Planar cable-driven robot for stiffness modulation studies. . . . 12

2.1 Stiffness ellipse. . . . 16
2.2 Three-directionally arranged actuator scheme. . . . 17
2.3 Highest obtainable stiffness ratio. . . . 19
2.4 Unstable behavior device scheme. . . . 20
2.5 Free body diagrams of the negative stiffness based device. . . . 21
2.6 Force and stiffness as function of the displacement. . . . 22
2.7 Concept design for a three-directionally arranged actuator. . . . 23
2.8 Force field along the workspace. . . . 24
2.9 Stiffness on x and y along the workspace. . . . 24
2.10 Contour plot of the stable zones. . . . 25
2.11 Orthogonally-arranged actuator scheme. . . . 26
2.12 Orthogonally-arranged actuators model. . . . 27
2.13 Stiffness along both directions x and y. . . . 29
2.14 Stiffness ratio as function of the spring lengths ratio. . . . 29

3.1 3D representation of a single antagonistic VSA. . . . 32
3.2 Top view of the orthogonally-arranged actuator's kinematic architecture. 33
3.3 Top view of the components included in a generic module . . . 34
3.4 Effects of synchronous movement of the rotational actuators. . . . 36
3.5 Forces applied to the end-effector. . . . 38
3.6 States of force when an external force is applied. . . . 39
3.7 Effects of a non-symmetric stiffness in the VSA to the force fields. . . . 41
3.8 Maps of force components and stiffness . . . 42
3.9 Radial cam of the LinWWC-SEA. . . . 43
3.10 Scheme of the LinWWC-SEA. . . . 44

3.11 Top view of the device after including the LinWWC-VSAs. 48
3.12 Schematic representation of the VSA 50

4.1 CAD drawing of the *PLANarm*. 51
4.2 Scheme of arm's weight distribution. 52
4.3 Distribution of cable tension. 54
4.4 Logarithmic spiral cam profile. 56
4.5 Force and stiffness of the obtained LinWWC-SEA 57
4.6 Effect of cable forces on carriages. 58
4.7 Effect of cable forces on the structural tubes. 58
4.8 Schematic representation of the wire inclination. 59
4.9 End-effector position for unwrapped and wrapped pulley. 60
4.10 Main elements of the *PLANarm*. 63
4.11 Tubes connection through L-shaped plates. 64
4.12 Exploded view of the corner box. 65
4.13 Assembled corner box. 66
4.14 End-effector's elements. 66
4.15 Disposition of the five pulleys for each cable circuit. 68
4.16 Tensioning system. 69
4.17 Mounted carriage. 70
4.18 Carriage's layouts 71
4.19 Actuated and free-spinning shafts. 71
4.20 Assembled cam. 73
4.21 Exploded view of the potentiometer's connection. 74
4.22 Hardware box. 74
4.23 Cable circuit. 75

5.1 Overview of parts obtained through mechanical processing. 78
5.2 Overview of pieces obtained through 3D printing. 79
5.3 Phases of the 3D printing process. 80
5.4 Component with overhang features and respective supports. 81
5.5 Assembly phases. 84
5.6 Electronic boards included in the *PLANarm* 85
5.7 Electronic scheme of the *PLANarm*. 86
5.8 External force mapping. 88
5.9 Scheme of the open-loop control. 89
5.10 Scheme of the closed-loop control. 90
5.11 Test bench. 92
5.12 Actuators blocking system. 93
5.13 Displacement vs force on the center of the workspace. 94
5.14 Hysteretic effect. 95
5.15 Displacement vs force on a corner of the workspace. 95
5.16 Planar displacement with a diagonal external force. 96

List of Tables

4.1 Results for the design calculations. 61

5.1 List of purchased elements. 77
5.2 List of elements manufactured with FDM. 81

List of Technical Drawings

A.1 Final assembly. . . . 106
A.2 Assembled corner box. . . . 107
A.3 Assembled unactuated shaft. . . . 108
A.4 Assembled actuated shaft. . . . 109
A.5 Assembled cam. . . . 110
A.6 Assembled end-effector. . . . 111
A.7 Assembled carriage 0. . . . 112
A.8 Assembled carriage 1. . . . 113
A.9 Ground element of the corner box. . . . 114
A.10 Middle element of the corner box. . . . 115
A.11 Top of the corner box. . . . 116
A.12 Cam cover. . . . 117
A.13 Carriage 0. . . . 118
A.14 Carriage 1. . . . 119
A.15 End-effector bottom. . . . 120
A.16 End-effector cover. . . . 121
A.17 Unactuated shaft. . . . 122
A.18 Actuated shaft. . . . 123
A.19 Cam shaft. . . . 124
A.20 End-effector shaft. . . . 125
A.21 Rectangular tube. . . . 126
A.22 Plane. . . . 127
A.23 Hardware box. . . . 128
A.24 Top L-plate. . . . 129
A.25 Bottom L-plate. . . . 130
A.26 Cam. . . . 131
A.27 Drum. . . . 132
A.28 Belt pulley A. . . . 133
A.29 Belt pulley B. . . . 134
A.30 Handgrip. . . . 135
A.31 Potentiometer support. . . . 136
A.32 Spacers A. . . . 137
A.33 Spacer B. . . . 138
A.34 Spacer C. . . . 139
A.35 Cover of the hardware box. . . . 140
A.36 Doubled-sided tensioning element. . . . 141
A.37 Single-sided tensioning element. . . . 142

Chapter 1

Introduction

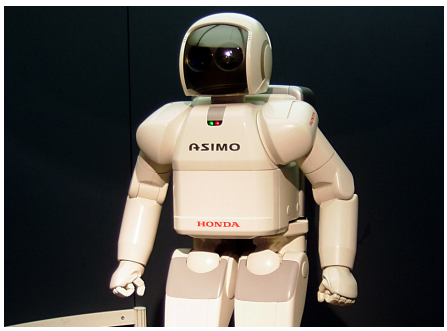
The use of robotic devices in human activities has greatly increased in different fields of production and service sectors, mainly in automatic production systems, but also in medical assistance and rehabilitation, space and underwater research, etc. Everyone has an idea of what they should be capable to do thanks to press, science-fiction books and films (Fig. 1.1), but a more precisely definition is provided by the Robotics Institute of America, a robot is;

"*a reprogrammable, multifunctional manipulator designed to move material, parts, tools, or specialized devices through various programmed motions for the performance of a variety of tasks*"

The motivation of introducing robotic devices in an activity is to exploit the vantages of replacing a human worker. Some of those vantages are: better performance in terms of physical characteristics; difficulty, or even impossibility, of a job to be executed by a person due to high risky environments; the lower-cost of employing robots in repetitive and tiring activities; etc. In medical area, robotic devices have been introduced for surgery, medical training, rehabilitation therapy, prosthetics and assisting people with disabilities, being the rehabilitation field the most extensive use of this technology [1].

Stroke is one of the worldwide major cause of disability [2], affecting about 17 million people worldwide every year, 5 million of them resulting in severe post-stroke handicaps and disabilities [3]. In Italy, from 200000 cases, about 30 result in permanent disability [4]. Stroke occurs when blood flow to the brain is interrupted, either for a vessel blocked by a clot or for a burst vessel, causing the deprivation of oxygen to brain cells, resulting in their decease. Depending on the area of the brain where the stroke happens, the subject suffers a lost of capacities, as memory, muscle control, sight, etc. There is another type of stroke that is caused by bleeding inside the brain, that covers around 20% of cases (both kinds of stroke are depicted in Fig. 1.2). The brain injury from stroke can cause the paralyzation of muscles, and their involuntarily contraction after trying to move a limb. A deeper explanation of the causes, preventions and afterward disorders can be found in [5].

The goal of post-stroke rehabilitation is to hasten and maximize recovery of the disabilities caused by the stroke through a restorative learning process [6]. Since stroke affects directly the brain, every aspect of the body is compromised, and the listed disabilities are not restricted to the impossibility of basic movements. It also includes



(a) Honda's Asimo, a two-legged humanoid robot designed and built by Honda.



(b) A Kuka's industrial robot working on a mechanical piece.



(c) NASA's Curiosity Mars, an exploring robotic rover investigating the Martian climate and geology.



(d) R2D2, a fictional robot from Star Wars's films.

Figure 1.1: Some examples of robots.

vegetative state, cognitive and communicative abilities, physical pain, emotional distress, loss of sensations, among others.

The recovery of the limb's mobility considers the restoration of lost neural tissue, restoration of the ability to perform the movement as it was before the injury, and successful task completion as done by healthy not-disabled persons. Diverse modes of intervention to accomplish the rehabilitation process are reviewed in [7]. Most of them exploit the use-dependent plasticity of the human neuromuscular system. That means the use of a limb modifies the properties of neurons and muscles, including the pattern of their connectivity [8]. The practice of task-specific exercises lets the patient re-learn how to perform the desired movements, repairing the neural connections associated with that movement and recovering the physical capacity of the limb. One of the approaches considers frequent sessions of different exercises training, where the affected limb is treated with an active motor sequence performed repetitively, aimed towards the recovery of a functional task. In this path, robotic devices are highly suitable, capable of introduce high-intensity repetitive session, including interactive features and the possibility of incrementing the independence from the therapist's constant presence.

At the current stage, there is no totally consensus about the effectiveness of using

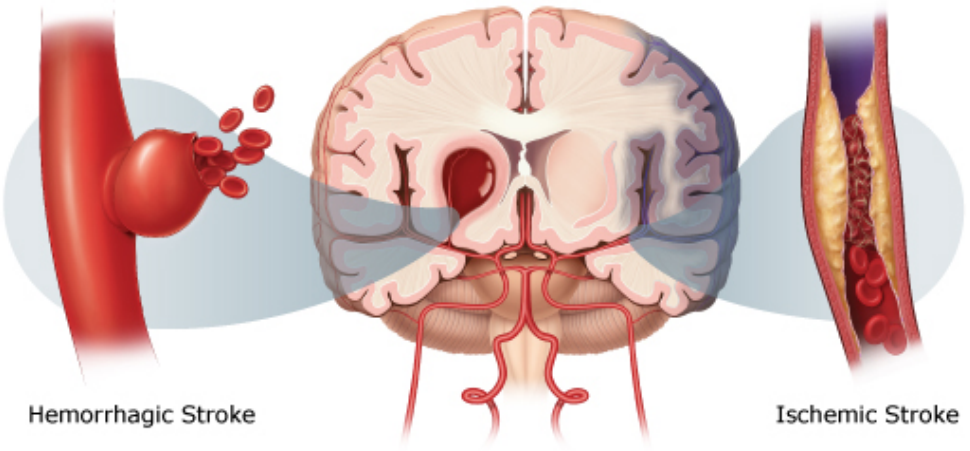


Figure 1.2: Visual representation of both types of stroke. On the left, an Hemorrhagic stroke, where the vessel bursts filling the brain tissues with blood. On the right, an Ischemic stroke, where a vessel is blocked and the brain cells are deprived of oxygen.

robotic devices for rehabilitation in confront with conventional rehabilitation therapies. Some researches have presented results in favor ([9, 10, 11, 12]), others against ([13, 14]) and some others finding no significant differences when using robotic-assisted therapies ([15, 16]). Nevertheless, it seems that bad results in clinical proves are restricted to low limb robot-aided rehabilitation, where gait training robots are still considered "in development" [17]. Previous research concludes that upper limb robotic rehabilitation is, at least, as effective as conventional rehabilitation, while it can still enjoy the advantages of robotic devices.

There are several advantages of using a robotic device to help therapists performance in rehabilitation. Some of them are [1, 17]:

- They can provide more accurate, intensive and consistent performance than conventional therapy, specially in long sessions involving repetitive movement training.
- They can continuously measure the performance of the patient by collecting data, that can be used to quantitatively measure the patient's improvement through the rehabilitation process, allowing to obtain a force feedback and optimize the treatment techniques.
- They can allow patients to perform extended periods of therapy without the continual presence of a specialized therapist. Although, the presence of a care-giver is required for safety reasons.
- The capability of introducing virtual reality as an add-on to the process allows patients to improve the compliance of a session. Virtual environments and videogames encourage the patients throughout the sessions, providing instant feedback and improving the attitude to the process, that directly helps to the effectiveness of the recovery.

1.1 Upper Limb Rehabilitation Devices

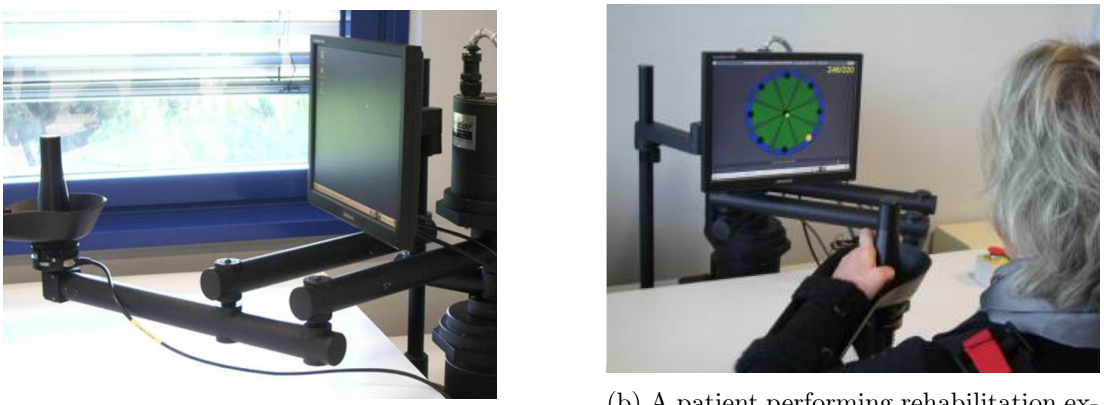
Robotic rehabilitation devices are usually classified between upper- or lower-limb rehabilitation, due to the functional disparities between the two structures, and the necessity of different mechanisms. In addition, despite the limb involved, two different typologies of robots can be identified and are commonly used to classify the devices, the exoskeletons and end-effectors. The main difference is the kinematical structure adopted. Exoskeletons are wearable mechatronic systems that replicate the kinematical structure of the human limb. As it follows the whole patient's limbs movement, the exercise is directly defined in patient joint space. In the end-effector devices, the contact between the patient and the device takes place only at the end-effector, and there is no replication of the limb's kinematical structure. Exoskeletons are also used as assistance devices conceived for day-to-day use in common situations, whilst end-effector are mainly considered for the rehabilitation process.

From now on, and in accordance with the aim of this work, this dissertation will focus on upper-limb end-effector robots. An historical perspective from 1960 to 2003 of rehabilitation robots has been carried out in [18]. Moreover, a state of the art's review can be found in [19] for lower-limb robotic rehabilitation, and in [20] for exoskeleton robots for upper-limb rehabilitation.

1.1.1 State of the Art

There are several devices used for rehabilitation of the upper limb. A state of the art about upper limb rehabilitation devices has been largely treated [21, 22, 23]. Therefore, just the most relevant ones regarding the aim of this work are presented in this section. Those are the planar end-effector robots that present a cable-driven parallel kinematic architecture.

MIT-Manus



(a) Side view.

(b) A patient performing rehabilitation exercises.

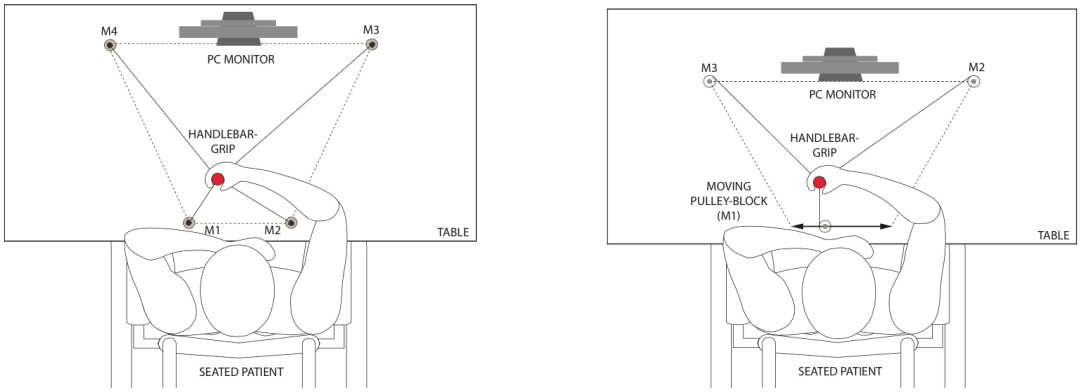
Figure 1.3: MIT-Manus robot.

The most famous upper-limb rehabilitation device is the MIT-Manus [24]. Despite not having all the characteristics mentioned before, it is worth mentioning due to his

commercial diffusion and being the pioneer in this field. It is a pentalateral planar device developed at the. It consists of a direct-drive five bar-linkage robot driven by 2 coaxial brushless motors (stall torque 9.65 or 7.86 [Nm]), with absolute encoders for position and velocity measurements. A six Degrees of Freedom (DoF) force sensor, mounted on the end effector, combined with the encoders, makes various control strategies available. A display monitor gives a visual feedback to the patient during the rehabilitation exercises (Fig. 1.3).

The behavior of the device is anisotropic and depends heavily on the position of the end effector. The workspace is about 38x45 [cm], in which the robot can supply 17.86 [N] of maximum isotropic force [23]. Peak force reaches 45 [N] and impedance achievable is in a range between 0 and 8 $[\frac{\text{N}}{\text{mm}}]$. Hand and wrist modules have been designed to be implemented on this device.

Sophia-4 and Sophia-3



(a) Sophia-4. (b) Sophia-3.

Figure 1.4: Sophia robots.

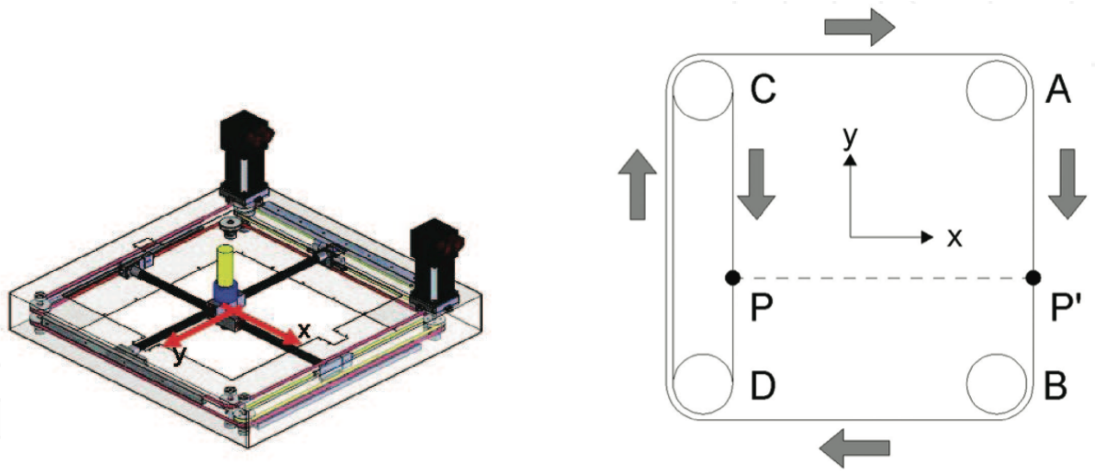
The Sophia robots (string-operated planar haptic interface for arm rehabilitation) [25, 26] is based on a handlebar-grip mounted on the end-effector, that is commanded by 3 or 4 stiff cables for a 2 DoF movement. The patient, while sitting in front of the device, holds the handlebar-grip that can be moved within the table (Fig. 1.4). A real time feedback for the patient is shown on a PC monitor, in front of the table, like the status of the exercise and a visual feedback.

There are two control levels, the low level control calculates the effective tension of each cable to compute a desired assistive planar force, while the high level control can be employed in any kind of logic control, for example, to compute a tunnel-like impedance control. The system creates a tunnel-like force field along the desired trajectory, where assistive virtual elastic force are effectuated by the device on the patient as soon as the end-effector comes out of the tunnel.

The main difference between the two versions is the substitution of the two lower pulleys in the 4 cables version for a single mobile pulley, that follows the position of the end effector in the Sophia-3. Also, in its 3 cable version, the device is capable of changing the slope of the table, from totally horizontal to a maximum tilting angle of 60°, allowing the robot to assist in exercises performed against gravity.

The maximum cable force is 87 [N], and the minimum 5 [N] (because the cables must be in constant tension). Defining the workspace as the area of the device where it is capable of exerting an isotropic force greater than 40 [N], these ranges of tension allow the robots to work in an workspace of 30x45 [cm] for the Sophia-4 and 30x35 [cm] for Sophia-3.

CBM-Motus



(a) Isometric view. (b) Kinematical architecture.

Figure 1.5: CBM-Motus robot.

The CBM-Motus is a planar device with kinematical isotropy due to its orthogonal architecture [23]. The robot has a cartesian kinematic structure based on two modules, that control the two translational DoF. Each module has 6 pulleys, 2 belts, a DC servomotor and a rigid bar (Fig. 1.5a). The layout of each module (Fig. 1.5b) allows a pure translational independent movement of the two bars, the end-effector is connected to them through two prismatic joints.

This robot has a very large workspace (50x50 [cm]) considering the overall dimensions of the device (83x82x11 [cm]). The executable force in each direction is 80 [N] with a peak force of 200 [N] (using 2 to 5 [N m] servomotors). Due to its geometry, the CBM-Motus has an isotropic dynamic behavior, that enables highly repeatable upper-limb training all over the workspace, without additional difficulty caused by the robot anisotropic dynamic features. The presence of moving parts with non negligible weight results in a considerable amount of mass perceived at the end effector. An impedance control has been developed where feedback is given by encoders, to record position, and by a measure of servo-amplifier electric current, to give an indirect measure of the interaction force at the end effector.

NeReBot

The NeReBot (Neuro-rehabilitation robot) [27] is a three DoF wire-driven robot for post stroke upper-limb rehabilitation. The patient's forearm is fastened onto a splint as end-effector while the patient is sitting on a wheelchair or lying on bed (Fig. 1.6).



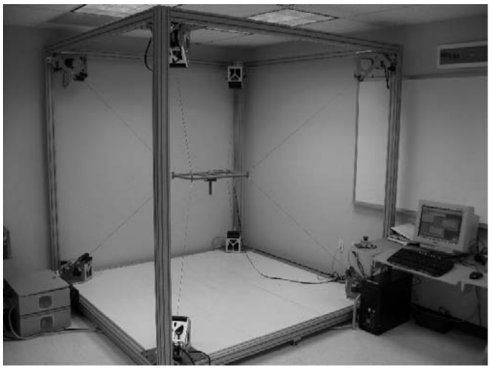
Figure 1.6: NeReBot robot.

The mechanical structure that holds the end-effector with cables consists of 3 horizontal rotating arms made up of aluminum tubes positioned above the patient. The motors only command the cable's length, hence the angular position of the upper bars and their cable entry point have to be set previously to the therapy session, that have been calculated and optimized with respect to the arm (left or right), the size of the patient and the kind of exercise to be performed. As known, for a three DoF movement at least seven wires are needed to produce the forces and torques. In this case, the device takes advance of the arm's weight itself, that acts as the fourth force. Therefore, with the three cables set, the device provides only three unidirectional constraints, hence the patient's forearm can still swing over an approximately horizontal surface. This under-constrained kinematics allow the patients to feel less restricted, that is an advantage in this kind of devices.

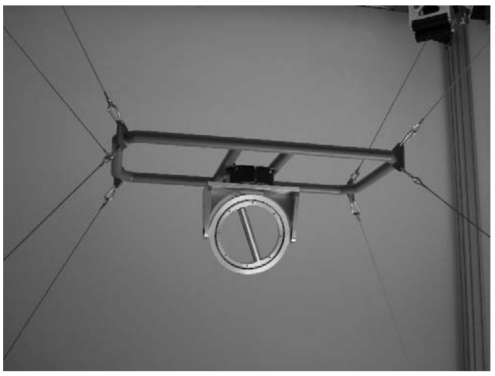
The exercises are recorded by manually moving the end-effector. The therapist prepare the exercise storing each required position by pressing a button, and the robot stores the angular positions in the control system. The device interpolates the path with cubic-spline trajectories, while in the learning phase, the motors produce a constant torque to keep all the wires stretched. Then, during the actual therapy, the wire length is controlled by each motor, and the speed can be changed by the therapist.

MACARM

The MACARM robot (Multi-axis cartesian-based arm rehabilitation machine) is a cable robot for upper limb rehabilitation [28, 29], that consists of an aluminum cube frame of 234 [cm], with an approximately workspace of 140 x 160 x 200 [cm] (X, Y and Z). The end-effector is a suspended tube stock rectangular prism of 51x33x5 [cm], commanded by 8 nylon-coated stainless-steel cables with a diameter of 1.6 [mm] (Fig. 1.7). Each cable



(a) Full view.



(b) Manipulandum.

Figure 1.7: MACARM robot.

is coupled with an active module, consisting of a brushless DC motor, an encoder, an harmonic gearbox, a cable spool and a cable fairlead. Each module is able to produce approximately 310 [N] of tension at up to 0.5 $[\frac{\mathrm{m}}{\mathrm{s}}]$. Depending on the application, different configurations of the end-effector or different number of cables can be used.

This device can be operated in diverse ways due its versatile architecture. One way is operating the MACARM through a specific path defined by the operator. It can be a geometric path, such a line or an arc defined in the software, or a recorded trained segment, where the inputs are previously registered by the operator moving the end-effector by hand. It can be also operated to interact with a virtual environment, capable of produce dynamic simulation, such as collisions, virtual boundaries defined by different surfaces or moveable objects.

1.1.2 Critical Analysis

All of these devices achieve the needed requirements with different approaches and different results. All of them have a workspace of at least 30×35 [mm], which is enough for typical rehabilitation exercises. Particularly, MACARM and NeReBot largely cover the maximum reach of the human arm, that is around 50×90 [mm] in the transverse plane [30], but are unsuitable for daily use at patients home, due to their size and weight. As shown in (Fig. 1.6 and 1.7) both devices require a lot of space and instrumentation which make them suitable only for clinical environments.

The wires-based devices have the advantage of low moving mass, that allow them to achieve good dynamic performances. MIT-Manus and CBM-Motus, due to the weight of the moving parts, have considerably high inertia which results in high force and power requirements from the actuators and inferior acceleration capacity. The parallel kinematical architecture allow the motors to be grounded, decreasing the load on the single joints

In terms of interaction with the patient, all the machines guarantee a certain degree of mobility of the patient's arm, which is achieved in different ways depending on the attachment of the arm to the end-effector. MACARM and NeReBot are based of the hypostatic configuration of the wires, hence they are not able to regulate the compliance. Sophia 3-4, MIT-Manus and CBM-Motus implement virtual stiffness through feedback

control on the actuators. The two main control logic approaches to set the degree of assistance are impedance and admittance control [31]. An alternative solution is to use Variable Stiffness Actuators (VSAs). The motivation of using VSAs is explained further and as a consistent part of this work, deserves a deepened description which is given in the next section.

1.2 Variable Stiffness Actuators

VSAs belong to the group of the Variable Impedance Actuators (VIAs). VIAs are different from traditional actuators because they allow displacement from the set position. Therefore, the position of the actuator is defined by the equilibrium point, where the actuator generates zero force or torque, and the displacement. When an external force moves the joint from the equilibrium point, the actuator reacts with a force or torque function of the displacement to recover the equilibrium position. This behavior is suitable for robots that interact with environments that have unknown dynamics, such as interaction with human beings.

VSAs are a sub-group of VIAs, that achieve adaptable compliance through elastic elements capable of storing energy and modifying stiffness. Two motors are required on this kind of actuators, in order to control both the equilibrium position and stiffness. Although, these two DoF are not necessarily matched to the actuator's single coordinates.

There are different types of configurations to obtain a VSA. In [32], a consistent overview and classification has been done for these devices. The most relevant VSAs concerning this work are Spring Preload based actuators, that exploit the preload of a non-linear spring to obtain stiffness variation. Three sub-classes can be identified in this group

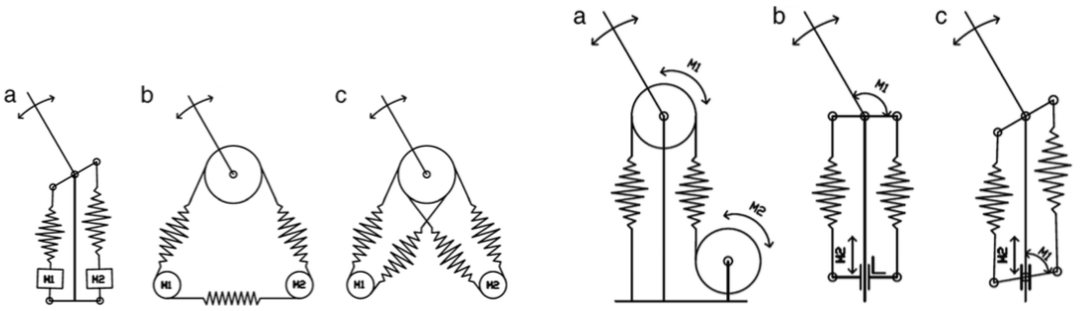
Antagonistic springs with antagonistic motors Two springs and two motors are placed in antagonist setup (Fig. 1.8a). To change stiffness, the two motors have to move in opposite directions to modify the preload of the springs. To change the equilibrium position, instead, they have to move in the same direction.

Antagonistic springs with independent motors It also requires two springs and two motors, but the setup partly decouples equilibrium position and stiffness control (Fig. 1.8b).

Preload adjustment of single spring It adopts a non-linear connection between the output link and the spring element, therefore just one linear spring is required.

The adoption of VSA in alternative to software control of rigid structures results in the following main advantages:

- A safer approach of the human-robot interaction [33]. Because of higher back-drivability on the transmission and mechanical compliance, it allows the movement of the robot regardless of eventual malfunctioning of the motors or the control software. This results in the capacity of absorbing shocks and unexpected quick movements from the user, as much as accidental behavior of the robot that could get the user under physical risk. The mechanical compliance behaves with a more-friendly interaction, closer to a human-human synergy.



(a) Antagonistic springs with antagonistic motors.

(b) Antagonistic springs with independent motors.

Figure 1.8: Spring preload VSAs.

- A simpler and cheaper implementation of the variable stiffness aspect, since there is no requirement of force sensors, commonly more expensive than position sensors. The impedance controller is usually complex, requires an accurate system dynamics model and presents a limited bandwidth that restrict the absorbing of impacts. Mechanical compliance has a better performance in terms of robustness to external perturbations and model mistakes, is capable of storing elastic energy, and possesses a virtually infinite bandwidth, allowing it to absorb collisions.

1.2.1 VSAs State of the Art

VSAs have already been used in upper limb rehabilitation, the most relevant devices are here presented:

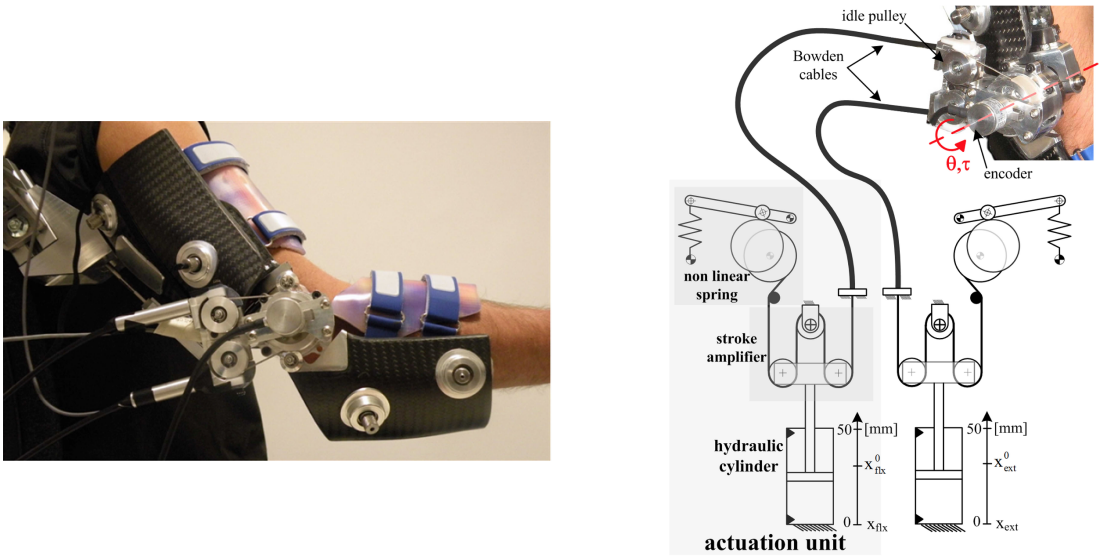
NEUROExos

The NEUROexos [34] is a robotic elbow exoskeleton for which an antagonistic VSA system has been implemented (Fig. 1.9a). This device is characterized by a 4 DoF mechanism in charge of avoiding misalignment between human and robot at the elbow joint where an antagonistic-driven compliant joint is responsible of the actuation.

The mechanism shown in (Fig. 1.9b) is made of two non linear elastic elements obtained by coupling a linear spring to a cam, two hydraulic motors, and a cable-based transmission system that transfers the forces to the elbow joint. This device exerts up to 15 [Nm] of torque and the stiffness range achieved is 20 to 60 $\left[\frac{\text{Nm}}{\text{rad}}\right]$.

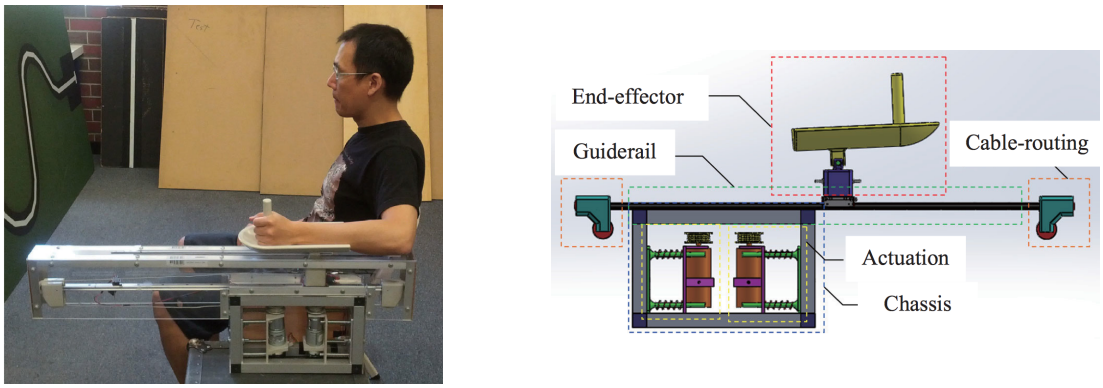
Compact Linear-motion Device

It is an upper limb reaching rehabilitation robot that exploits VSA [35]. The architecture of this device, shown in Fig. 1.10a, is based on two antagonistic motors, responsible of the movement of a manipulandum on a linear guide-rail. Four preloaded springs connect each actuator to the structure (Fig. 1.10b), the presence of which makes the overall device an antagonistic VSA based robot. The use of VSAs, coupled with a controller on the actuators, allows to set position and impedance simultaneously and to confer safety, as it prevents the transmission of excessive forces from the robot to the user.



(a) Full view. (b) Actuation scheme.

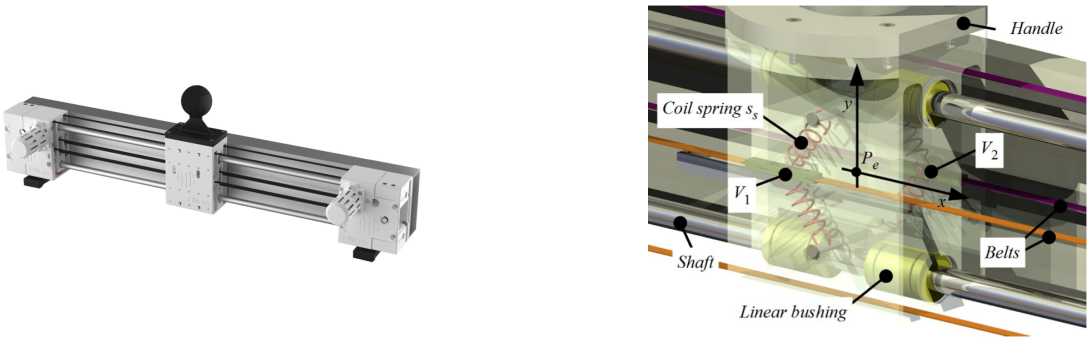
Figure 1.9: NEUROexos robot.



(a) Full view. (b) CAD design.

Figure 1.10: Compact linear-motion device.

LINarm



(a) CAD design. (b) VSA system.

Figure 1.11: *LINarm*.

The *LINarm* [36] is a linear device for upper-limb rehabilitation. This device has a VSA based architecture that confers safety and gives adjustable compliance to the interaction between user and robot. It consists of a couple of antagonistic actuators located at the two extremities of a linear guide, on which a manipulandum translates. The end-effector is equipped with a couple of triangularly arranged springs, which composes the non linear elastic component of the VSA (Fig. 1.11).

Stiffness Modulating Planar Cable-driven Robot

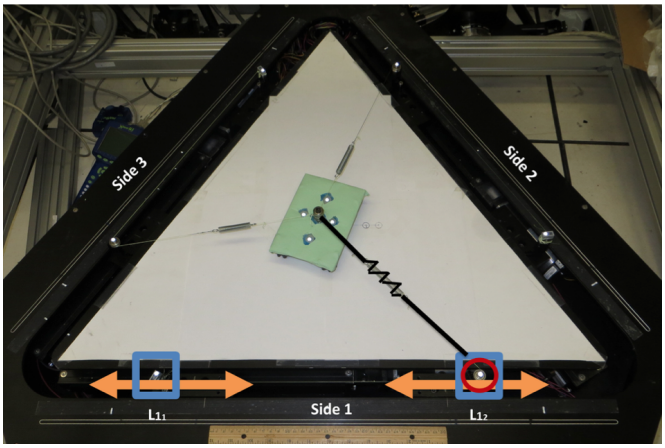


Figure 1.12: Planar cable-driven robot for stiffness modulation studies.

Even if it is not thought for rehabilitation purposes, this device is worth mentioning as it explores stiffness modulation through non-linear springs in a planar workspace [37]. The architecture is very simple: a slide, free to move in a planar workspace is attached to three non linear springs, each of which actuated in terms of both attachment point and preload (Fig. 1.12). Different combinations of position and preload for the three springs allow to impose a certain stiffness to the slide. Different stiffness values can be achieved in terms of both intensity and direction.

1.3 Aim of the Work

The purpose of this dissertation is the design and construction of an innovative robotic device for upper limb neuro-rehabilitation, under the support and supervision of the Institute of Industrial Technologies and Automation (*ITIA*), from the National Research Council of Italy (*CNR*). From this point it will be denominated *PLANarm*, as the natural development of the concept employed by *LINarm* [36], an upper-limb neuro-rehabilitation device designed and constructed in the institute.

The mechatronic device is aimed to contain the following characteristics:

Planar Workspace This devices is intended to be the natural evolution of the *LINarm*, where a one DoF VSA is used for a linear robotic device. The planar workspace (2 DoF) answers the ambition of bringing the limb exercises closer to the actual traditional therapy, capable of spacial movements (3 DoF). The extension of the area, where the exercises are performed, is 50x50 [cm] (Ref. 4.1.1). In this area, the end-effector must be capable of moving, exerting a target force of 40[N] (Ref. 4.1.2) in all directions and adjust the stiffness desired levels.

Cable-Driven Parallel Kinematic Architecture This kind of robots, named Cable-Driven Parallel Robots (CDPRs) have particular properties that can be exploited in different fields [38, 39]. Some of them are the huge size of their workspace, high payload, high speed and good dynamic capacities since the cables boast low weight and inertia. The parallel kinematic also allows to ground the motors, reducing the inertia with respect to a serial manipulator, where the mass of a motor is moved by the motor of the previous link. As a trade-off, CDPR presents moderate accuracy, and the cables impose an unidirectional constrain (since a cable can only pull) instead of a bidirectional constrain provided by a rigid link.

Variable Stiffness Actuators One of the main challenges of this project is to bring the concept of the linear VSA to a two DoF actuator, to control both movement and impedance on a planar workspace. The adoption of mechanical impedance rather than control methods is due to the safety that the human-robot interaction is supposed to have (i.e. against malfunction of motors that may inflict undesired movement or even collisions with the arm). It also requires position sensors, that are more economic than force sensors needed for admittance or impedance control.

Low-Cost By 2009, robot therapy devices were used in less than 2% of clinics, and very rarely at home [17]. The designed robot is intended to be used also outside the clinical environment, and its use at patient's home with no presence of a specialist is encouraged. On this purpose, the device is intended to be manufacturable with cheap and easy-to-obtain components, following an 'Open Source' philosophy in every aspect. The components drawings, materials, assembly and software code involved shall be of public domain, to be reproducible by any person who needs the device. The *InMotion Arm* has a commercial price of €92,000 around. In order to keep the constructive cost of the device low, the components to be used are acquired in domestic stores. Specifically, we intended to maintain the materials cost under €5,000.

Chapter 2

Conceptual Design

The *PLANarm* consists of a two DoF cable-driven parallel robot for neuro-rehabilitation. The robot consists of an end-effector as the only link between the robot and the patient, and a parallel kinematic architecture in charge of allowing planar movement to the grip and regulating the compliance of the robot. In rehabilitation exercises based on this configuration, the patient, while seated in front of the device, grabs the grip with his hand, and the robot performs the required force to produce the movement pre-defined by the therapist.

The compliance of the robot is essentially the resistance that the robot opposes to an external force. A variable to measure this resistance is the stiffness, computed as the force exerted by the robot per unit of displacement. Since the robot covers a two DoF planar workspace, it is expected that the stiffness is viable to be different depending on the directions of the displacement, and settable by the therapist.

Prior to the presentation of the conceptual approaches that led to the actual prototype, it is important that a definition of stiffness in a planar workspace is given. Hence, the stiffness ellipse is now introduced.

Stiffness Ellipse

To define the compliance on the end-effector, a single numerical value is not enough, since it is also needed the information in terms of orientation in the plane. The stiffness in different directions on a robot's end-effector is often represented by the stiffness ellipsoid [37, 40, 41, 42]. It is the graphical representation of the distribution of stiffness in the cartesian space. For a robot aimed to move on a planar 2 DoF space, the ellipsoid becomes an ellipse centered in the end-effector position. The ellipse is defined by three parameters, as shown in Fig. 2.1, its semi-axes σ_1 and σ_2, and its orientation φ. In a robot, these values depend on the kinematic structure, the stiffness on joints and actuators, and the device configuration. The kinematics and the configuration are evidenced trough the jacobean matrix.

The jacobean matrix describes the transmission ratio between the joint space and the cartesian space. Let $Q = [q_1\ q_2\ \dots]^\intercal$ be the the position coordinates of the actuators and $S = [s_1\ s_2\ \dots]^\intercal$ the coordinates of the end-effector position. The velocity of the end-effector can be computed from the velocity of the joints as:

$$\dot{Q} = J\dot{S} \tag{2.1}$$

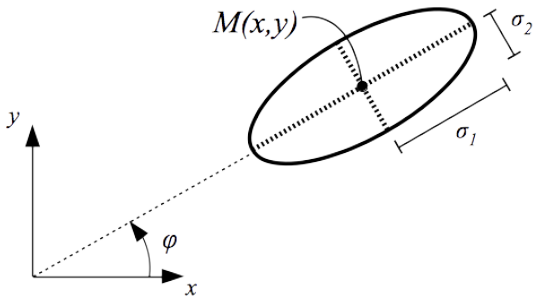


Figure 2.1: Stiffness ellipse, centered in the end-effector M with position coordinates (x, y), orientation φ and semi-axes σ_1 and σ_2 representing the extreme values of stiffness. In the figure, the direction of σ_2 is softer than σ_1, since its semi-axis is smaller. That means the robot reacts stronger to a displacement along σ_1 direction.

where the jacobean matrix is defined as

$$J = \begin{bmatrix} \frac{ds_1}{dq_1} & \frac{ds_1}{dq_2} & \cdots & \frac{ds_1}{dq_n} \\ \frac{ds_2}{dq_1} & \frac{ds_2}{dq_2} & \cdots & \frac{ds_2}{dq_n} \\ \vdots & \vdots & & \vdots \\ \frac{ds_m}{dq_1} & \frac{ds_m}{dq_2} & \cdots & \frac{ds_m}{dq_n} \end{bmatrix} \tag{2.2}$$

being n the number of actuators, and m the number of DoF that defines the position of the end-effector.

In a robot, the stiffness of the end-effector depends on multiple factors: materials of the structure, length of the links, transmission mechanisms, etc. For the cable-driven parallel robot, an approximation is to be made, in order to simplify the computation without a great loss of accuracy. Since the actuators are intended to be VSA, it is assumed that the resulting stiffness is only affected by their stiffness, whilst all the structure, links, and the cables are assumed as rigid elements. Lets now define the stiffness on the joint space as $K_q = diag(k1, k2, \ldots, k_n)$. The stiffness on the end-effector is computed as [43]:

$$K_s = JK_qJ^\intercal \tag{2.3}$$

the eigenvalues of K_s represent the values of σ_1 and σ_2, and the direction of the eigenvector defines the orientation φ.

In order to take advantage of the planar property of the device, the two semi-axes of the end effector's ellipse need to be independently adjustable. Design configurations to achieve a stiffness ellipse fully tunable, also in terms of orientation, have been evaluated. Therefore, it is also studied the possibility of adding a new degree of freedom, corresponding to the direction of the stiffness ellipsoid.

Different approaches to achieve the design specifications are now presented.

2.1 Three-directionally Arranged Actuator

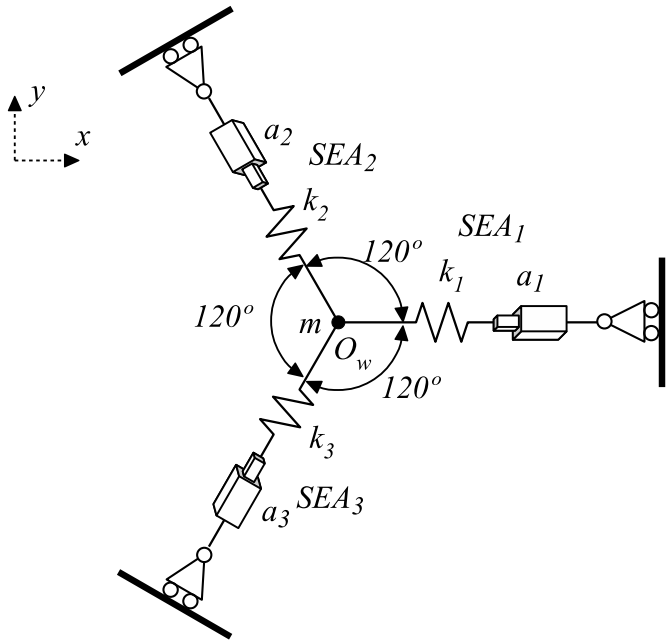


Figure 2.2: Scheme of the three-directionally arranged actuator configuration, with three Series Elastic Actuator (SEA) to control position and local stiffness of the end-effector M.

The first conceived kinematic architecture is based on a planar parallel cable driven manipulator with three cables attached to the end-effector, oriented at 0°, 120° and 240° with respect to (w.r.t.) the global reference frame $\{w\}$, as shown in Fig. 2.2. It is the most simple architecture to put in motion the end-effector since at least three cables in tension are needed to achieve a 2 DoF planar movement [44]. The stiffness characteristics on the end-effector are here studied, depicted by the stiffness ellipse in the neighborhood of the center of the workspace.

Each cable is connected to the ground through a Series Elastic Actuator (SEA). A single SEA is made up of a spring with stiffness k_i and a rigid actuator a_i, making it capable of execute a tension force $\mathbf{f}_i$, $\forall i \in 1, 2, 3$.

2.1.1 Stiffness Ellipsoid Resolution

Lets define q_i the position coordinate of the linear actuator a_i, and (x, y) the position of the end-effector w.r.t. $\{w\}$. The stiffness on the end-effector for a single configuration is described by the jacobean matrix [43]:

$$J = \begin{bmatrix} \frac{dx}{dq_1} & \frac{dx}{dq_2} & \frac{dx}{dq_3} \\ \\ \frac{dy}{dq_1} & \frac{dy}{dq_2} & \frac{dy}{dq_3} \end{bmatrix} = \begin{bmatrix} \cos(0) & \cos(\frac{2\pi}{3}) & \cos(\frac{4\pi}{3}) \\ \\ \sin(0) & \sin(\frac{2\pi}{3}) & \cos(\frac{4\pi}{3}) \end{bmatrix} \tag{2.4}$$

and the stiffness matrix in the workspace:

$$K_s = JK_qJ^T \tag{2.5}$$

with:

$$K_q = \begin{bmatrix} k_1 & 0 & 0 \\ 0 & k_2 & 0 \\ 0 & 0 & k_3 \end{bmatrix} \tag{2.6}$$

The eigenvalues and eigenvectors of K_s represent the semi-axes and the direction of the stiffness ellipse. Let φ be the angle between x and σ_1. The diagonalized stiffness matrix in the principal directions is

$$K_\sigma = \begin{bmatrix} \sigma_1 & 0 \\ 0 & \sigma_2 \end{bmatrix} \tag{2.7}$$

thus, K_s can be also expressed as

$$K_s = RK_\sigma R^T \tag{2.8}$$

where R is the rotation matrix:

$$R = \begin{bmatrix} \cos(\varphi) & -\sin(\varphi) \\ \sin(\varphi) & \cos(\varphi) \end{bmatrix} \tag{2.9}$$

that takes the diagonalized matrix to be expressed in the cartesian directions. Combining (2.5) and (2.8), it is possible to obtain the values of k_1, k_2 and k_3 that return a stiffness ellipsoid with semi-axes σ_1 and σ_2 in the direction φ:

$$\begin{aligned} k_1 &= (\sigma_1 - \frac{\sigma_2}{3})\cos^2(\varphi) + (\sigma_2 - \frac{\sigma_1}{3})\sin^2(\varphi) \\ k_2 &= \frac{2\sigma_2}{3}\cos^2(\varphi) + \frac{2\sigma_1}{3}\sin^2(\varphi) + \frac{2\sqrt{3}}{3}(\sigma_2 - \sigma_1)\cos(\varphi)\sin(\varphi) \\ k_3 &= \frac{2\sigma_2}{3}\cos^2(\varphi) + \frac{2\sigma_1}{3}\sin^2(\varphi) + \frac{2\sqrt{3}}{3}(\sigma_1 - \sigma_2)\cos(\varphi)\sin(\varphi) \end{aligned} \tag{2.10}$$

for $0 \leq \varphi \leq 2\pi$.

The absolute values of the ellipse can be easily escalated incrementing or decreasing the values of the stiffness in each SEA. The limitation of the architecture is found in the stiffness ratio $\Gamma_\sigma = \frac{\sigma_1}{\sigma_2}$ between the two semi-axes if it is assumed that the stiffness of the SEAs are positive. In Fig. 2.3 the highest ratio obtainable as function of the angle φ is presented.

The most restricted directions are the ones perpendicular to any of the SEAs. To achieve higher stiffness ratios, it is necessary to give up the constrain on the SEA stiffness, and to allow it to be negative. It is therefore indispensable to implement an actuator capable of producing negative stiffness ($k < 0$), that is with an unstable behavior, with the disfavor of bringing complicated dynamics that need to be studied.

2.1.2 Negative Stiffness Based Device

In Fig. 2.4 it is shown the conceptual design of a VSA capable of accomplishing negative stiffness. The device consists of a mobile end-effector that moves horizontally w.r.t. the

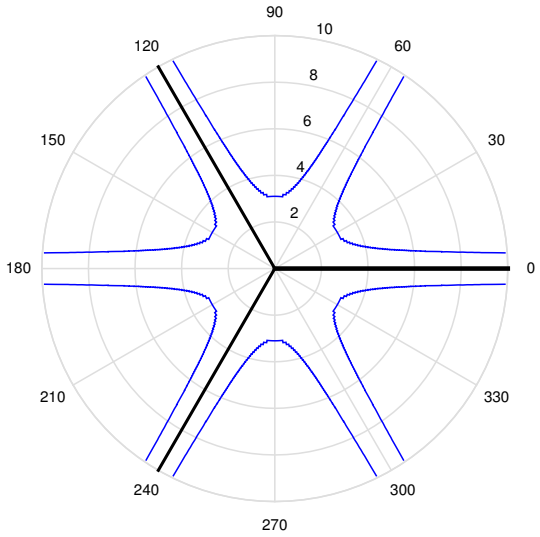


Figure 2.3: Polar graphic of the highest obtainable stiffness ratio Γ_σ as function of the ellipse inclination φ. The most restricted directions are those perpendicular to any of the SEA, where the maximum ratio is $\Gamma_\sigma = 3$. In the directions parallel to the SEA the ratio is not limited.

big platform, that in turn moves in the same direction w.r.t. the ground. The end-effector is also constrained to a traction spring k through a rod, in such a way that the spring follows the movement of the point P, making it leave its equilibrium position. The height of P is regulated by a linear actuator a_p, that is able to position P above or below the hinge B through the rod. The equilibrium position of the VSA is controlled by another external linear actuator (not presented in the scheme for clarity) that works on the coordinate q, and Δq is the displacement of the end-effector from the equilibrium position due an external force.

This device can be configured as a planar three-directional arrangement (Fig. 2.2) to let it achieve negative stiffness in the required directions (Fig. 2.7). To study the stability of the configuration, it is necessary to define the force produced by a single device as function of a displacement Δq. As shown in Fig. 2.4, let α be the inclination angle of the rod, β the inclination angle of the spring, and l the length of the spring. The geometric variables can be expressed as:

$$\begin{aligned} \theta &= \arctan\left(\frac{\Delta q}{c}\right) \\ \alpha &= \frac{\pi}{2} - \theta \\ l &= \sqrt{\left(b + p\sin(\alpha)\right)^2 + \left(p\cos(\alpha)\right)^2} \\ \beta &= \arccos\left(\frac{p\cos(\alpha)}{l}\right) \end{aligned} \tag{2.11}$$

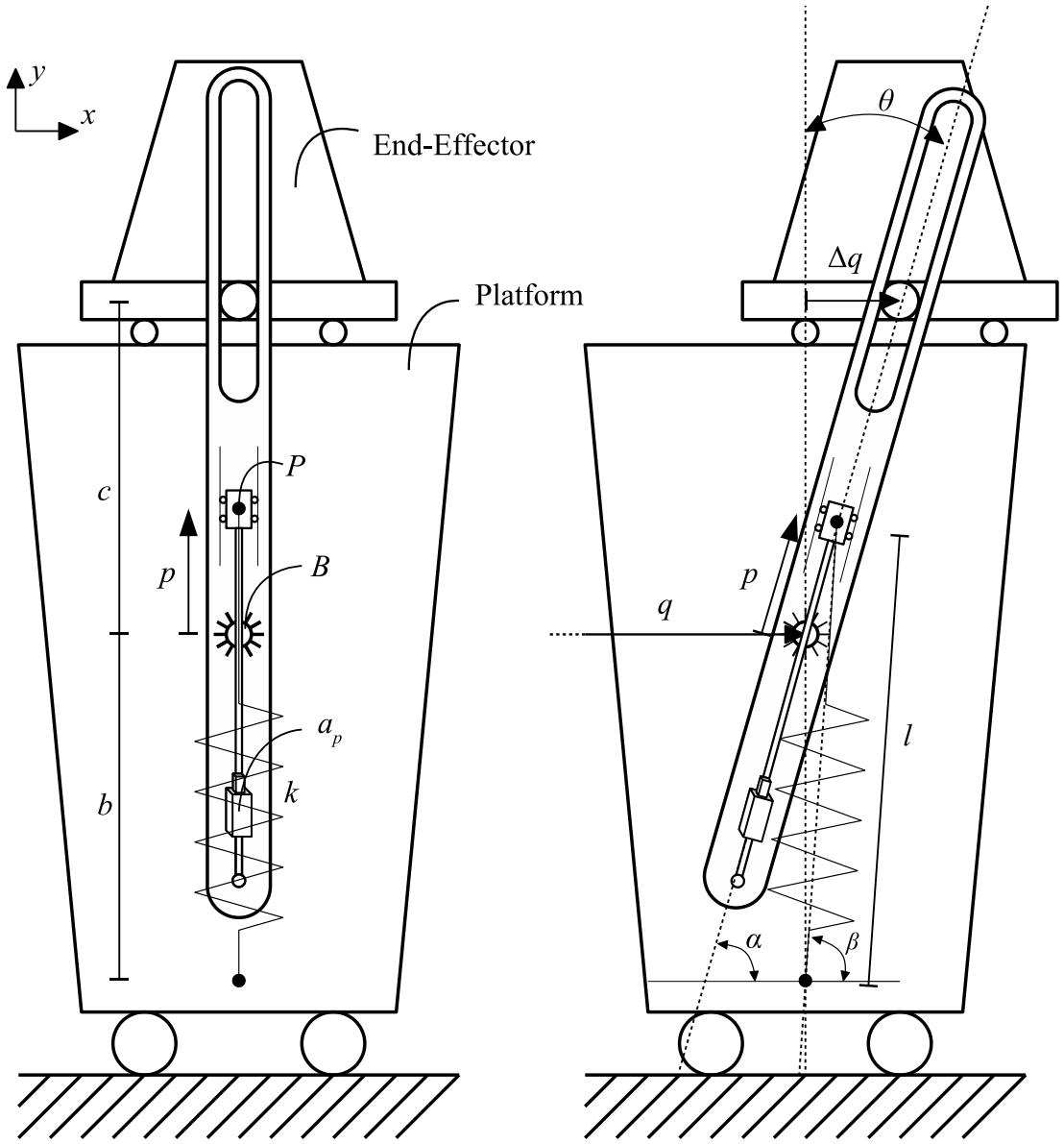


Figure 2.4: Scheme of the unstable behavior device. The equilibrium position of the VSA, working in the direction x, is defined as the coordinated q, and Δq is the displacement due to an external force. The coordinate p, positioned by the actuator a_p, is defined from the position of the hinge B, hence the sign of p determines the stability aspect of the device ($p > 0$ implies an unstable behavior, and $p < 0$ a stable one).

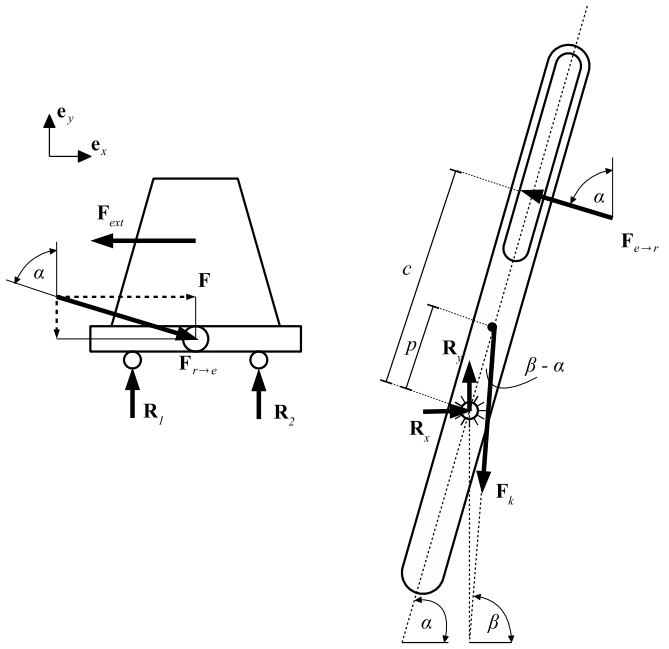


Figure 2.5: Free body diagrams of the negative stiffness based device. For a displacement Δq, $\mathbf{F}_{ext}$ is the required force to maintain equilibrium, and $\mathbf{F}$ is the projection in x (the operational direction of the VSA) of the force transmitted from the rod $\mathbf{F}_{r\to e}$.

In reference to Fig. 2.5, the force produced by the actuator $\mathbf{F}$ as function of the displacement is defined as the projection in x of the force performed by the rod to the end-effector $\mathbf{F}_{r\to e}$. Let also $\mathbf{F}_{e\to r}$ be the action-reaction couple of $\mathbf{F}_{r\to e}$. The above mentioned force is:

$$\mathbf{F} = F_{r\to e,x}\cdot\mathbf{e}_x = -F_{e\to r,x}\cdot\mathbf{e}_x = -F_{e\to r}\cos\left(\frac{\pi}{2}+\alpha\right)\mathbf{e}_x = F_{e\to r}\sin(\alpha)\mathbf{e}_x \tag{2.12}$$

Considering the static model shown in Fig. 2.5, $F_{e\to r}$ can be expressed as a function of the displacement Δp solving the equilibrium torque equation for the rod around the hinge B:

$$\begin{aligned} \sum \mathbf{M}_{i(B)} &= 0 \\ \frac{c}{\sin\alpha}F_{e\to r} - pF_k\sin(\beta-\alpha) &= 0 \\ F_{e\to r} &= \frac{p}{c}F_k\sin(\alpha)\sin(\beta-\alpha) \end{aligned} \tag{2.13}$$

F_k is the force produced by the spring:

$$F_k = k(l-l_n) \tag{2.14}$$

with l_n the natural length of the spring, and where α, β and l are function of the displacement Δq. Combining (2.12) and (2.13):

$$\mathbf{F} = \frac{p}{a}F_k\sin^2(\alpha)\sin(\beta-\alpha)\mathbf{e}_x = F\mathbf{e}_x \tag{2.15}$$

the local stiffness on the end-effector is computed by derivation w.r.t. the displacement Δq:

$$K = -\frac{dF}{d\Delta q} \tag{2.16}$$

and the dimension are arbitrary defined as:

$$\begin{aligned} a = &\quad 100[mm] \\ b = &\quad 100[mm] \\ k = &\quad 1\left[\frac{N}{mm}\right] \\ l_n = &\quad 0[mm] \end{aligned}$$

Same behavior is found when the device is set in stable configuration ($p < 0$). Force and stiffness curves can be found in a same way, presented in Fig. 2.6.

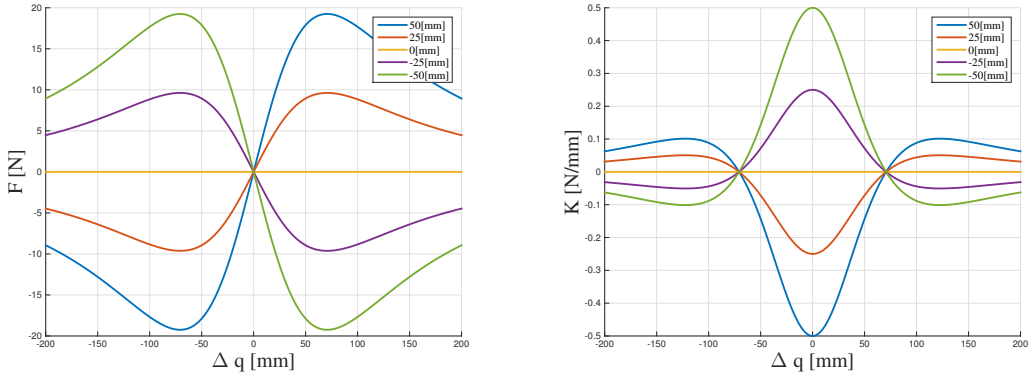


Figure 2.6: Force and stiffness curves as function of displacement for different values of p. The device decreases its stiffness as the displacement increases. It's worth underlining that the device actually changes its stability behavior for $|\Delta q| > 70$[mm].

The stiffness of both configurations decreases in absolute terms when a displacement is presented. Furthermore, stiffness shifts its sign with a displacement of $|\Delta q| > 70$[mm]. Therefore, its work range has to be small enough to avoid considerable discrepancies between the device's instant stiffness and the fixed stiffness on the equilibrium point.

2.1.3 Force and Stiffness Mapping

Having defined the behavior of a single device in terms of force and stiffness, it is studied the effect on the overall stiffness and the stability on the end-effector for a fixed equilibrium position as three devices are arranged in a planar configuration, as depicted in Fig. 2.2. A concept design is presented in Fig. 2.7, where the end-effector is capable of a planar displacement and the adjustment of its stiffness for all three directions.

It is important to verify if an unstable single device, setting its direction with negative stiffness, affects the stability of the overall configuration. For that, it is computed

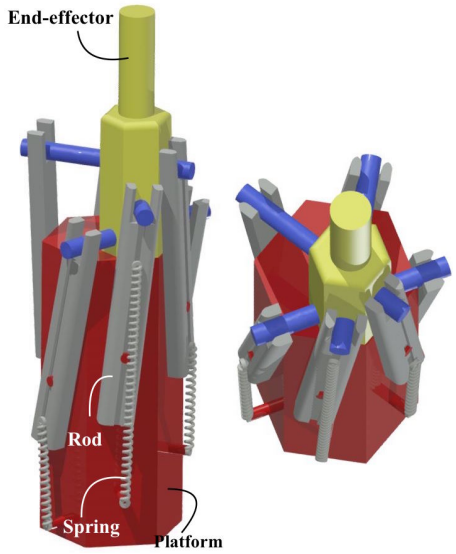


Figure 2.7: Concept design for a three-directionally arranged actuator. For a fixed position of the platform, the end-effector is capable of planar displacement. As described in Fig. 2.4, the rods contain an actuator that drives the attach point of the spring, allowing them to adjust the stiffness on its direction.

the directional stiffness in x and y as:

$$\begin{aligned} K_x &= -\frac{dF_x}{dx} \\ K_y &= -\frac{dF_y}{dx} \end{aligned} \tag{2.17}$$

where F_x and F_y are the projected forces in x and y of the resultant force F computed by the three VSA for a specific position.

The graphics in Fig. 2.8 and Fig. 2.9 show the generated force field and stiffness for a displacement along the workspace, when the VSAs are set to compute an ellipsoid with $\sigma_1 = 0.1\left[\frac{N}{mm}\right]$, $\sigma_2 = 0\left[\frac{N}{mm}\right]$ and $\varphi = 90°$ as arbitrary values (stiff on y and soft on x), which is one of the most extreme situations in terms of semi-axes ratio of the ellipse as shown in Fig. 2.3. To achieve this ellipse, according to (2.10), the VSAs have to adjust a value of p to perform stiffness of:

$$\begin{aligned} k_1 = \quad -0.0333\left[\frac{N}{mm}\right] \quad &\rightarrow \quad p_1 = \quad 3.33[mm] \\ k_2 = \quad 0.0667\left[\frac{N}{mm}\right] \quad &\rightarrow \quad p_2 = -6.67[mm] \\ k_3 = \quad 0.0667\left[\frac{N}{mm}\right] \quad &\rightarrow \quad p_3 = -6.67[mm] \end{aligned}$$

Stability Discussion

In Fig. 2.8 it is shown the force generated by the three devices when it moves along the workspace. The devices fail to maintain a null force in direction x, hence generating a

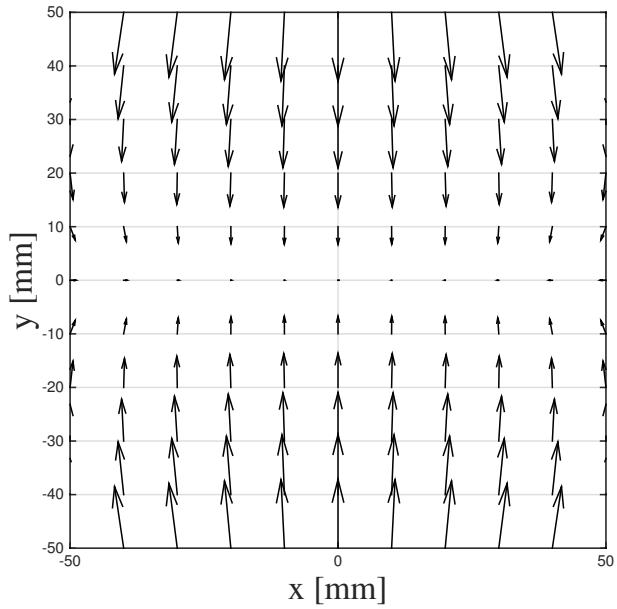


Figure 2.8: Force field generated by the three-directional actuator caused by a displacement of the end-effector. The characteristics of the stiffness ellipse were set to generate a stiff response in y, and a soft one in x. Therefore, most of the force vectors are highly oriented in y, although low components in x are noticeable, due to the non-linear aspect of the devices and the asymmetry of the arrangement in most of the workspace.

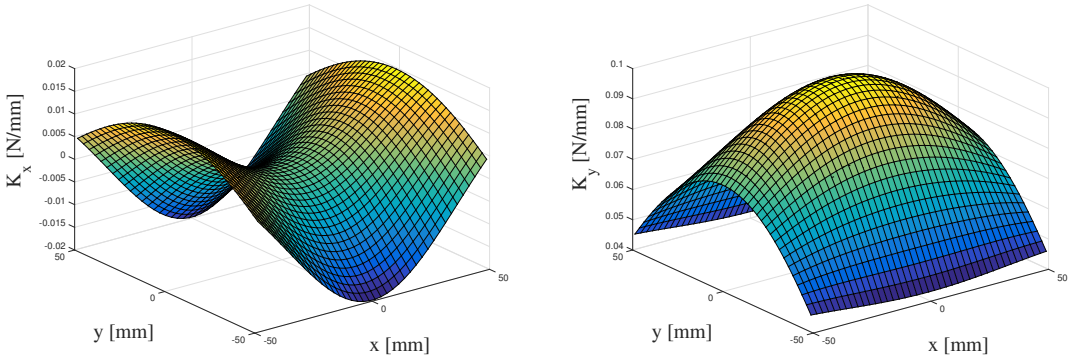
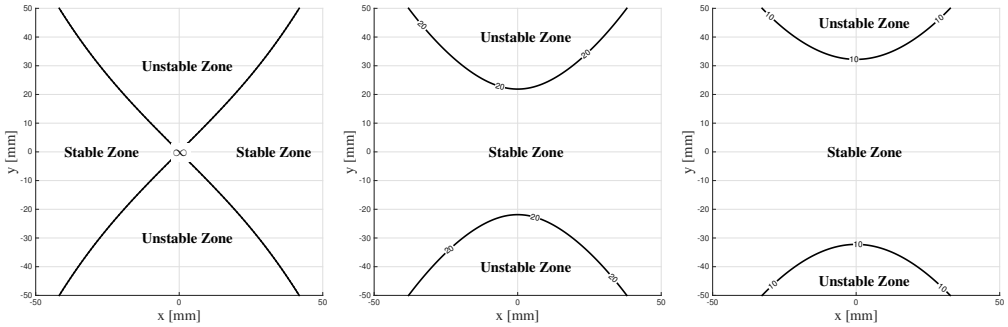


Figure 2.9: Directional stiffness along x and y on the end-effector, when it's displaced from its equilibrium position. While in the equilibrium position $(0, 0)$, the stiffness presents same values as the ones described in the stiffness ellipse, they change when the end-effector leaves that position, due to the change of stiffness on each single device.

low stiffness as the end-effector leaves the equilibrium position.

In Fig. 2.9, it is appreciated how the directional stiffness in both directions changes as the end-effector gets farther from the equilibrium point, even reaching some points where the stiffness in x becomes negative, and the end-effector is in an unstable position. This agrees with [45], where based on a study of the force-stiffness characteristics of muscles, Shadmehr claims that "in order to maintain stability in a pair of antagonistic spring-like elements attached to a single joint, the stiffness must grow at least linearly with force at isometric conditions". Fig. 2.6 evidences that in our device, the stiffness actually decreases with the force, thus the stability is not guaranteed even if the devices are all imposed to perform a positive stiffness.



(a) $\Gamma_\sigma \to \infty$. (b) $\Gamma_\sigma = 20$. (c) $\Gamma_\sigma = 10$.

Figure 2.10: Contour plots of the stable zones for different stiffness ratios Γ_σ. The unstable zone corresponds to the area above and below the curves, as indicated. For $\Gamma_\sigma \to \infty$, the center of the workspace is the converge point of the curves, so it is considered an unstable position. To increment the stable zone, it is necessary to decrease the stiffness ratio imposed to the ellipse.

In Fig. 2.10 are presented the zones where K_x acquires a positive or negative value, defined as stable and unstable zone respectively, for difference values of Γ_σ (ratio between the major and minor axes of the stiffness ellipse). For the extreme case where $\Gamma_\sigma \to \infty$, the central equilibrium position presents an indifferent stability condition ($K_x = 0$), but it turns in an unstable position immediately when it moves inside the unstable area. The instability zone becomes smaller as the ratio decreases, and moves further from the equilibrium position.

The adoption of negative stiffness elements, unstable by themselves,has been already studied for new composite materials to achieve better overall performances[46, 47]. In terms of overall stability, the general conclusion is that a state of stability can be reached under certain constrains. In this case, this constrain is related to the stiffness ellipse's ratio and the displacement of the end-effector from the equilibrium point.

Unstable systems are not suitable for mechatronic devices, since they give back undetermined dynamics, to be stabilized through feedback control. A position feedback control would introduce a stiffness in the system, that goes against the aim of the work, since it is pursued to introduce the stiffness with mechanical elements through the VSAs. A force feedback control requires force sensors, more expensive than position sensors, that would rise the cost of the device. Therefore, it is considered a diverse kinematical architecture, giving up one the capability of orienting the ellipse.

2.2 Orthogonally-Arranged Actuator

Another possible configuration is an orthogonally arranged actuator. Compared to the previous solution, this one doesn't allow to regulate the orientation of the stiffness ellipse but it is still able to vary independently the values of the two semi-axes σ_1 and σ_2, and more importantly, it has no areas in which the device is unstable. In this architecture, the end effector is connected to two couples of SEAs. Each SEA is composed by a linear actuator in series with a non-linear spring. The two couples are orthogonally arranged as shown in Fig. 2.11 and operate on two fixed directions, x and y respectively.

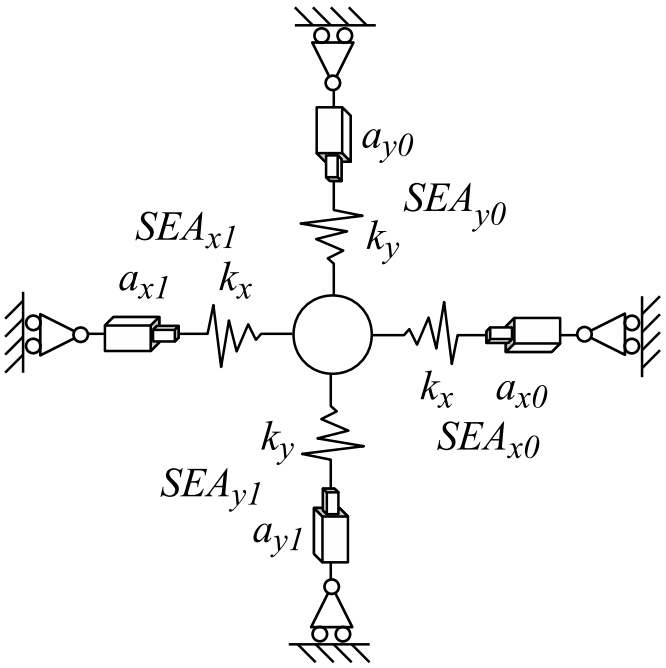


Figure 2.11: Scheme of the 2 DoF orthogonal arranged actuators, with two antagonist VSAs.

Each couple of actuators sets the equilibrium position of the end effector M for the direction they are related to and regulates the load on the corresponding non-linear springs. Each SEA is grounded through a carriage, allowing movement on its perpendicular direction, and synchronized in such a way that carriages and M remain aligned. Hence, a variation of the position of one couple of actuators does not affect position or load on its perpendicular direction. Moreover, since the springs have non-linear behavior, a synchronized and opposite movement of a couple of SEAs is capable of changing the stiffness accomplished on that direction.

2.2.1 Stiffness Analysis

To understand how the stiffness of each SEA affects the directional stiffness of the configuration in a static mode, the model in Fig. 2.12 is presented. Each SEA is replaced by a non-linear spring, assumed to be a quadratic spring with constant ζ and natural length l_n. Denoting M as the element attached to the four springs, h_{ij} the distance from M to the attach points P_{ij}, and l_{ij} the length of the spring, each spring

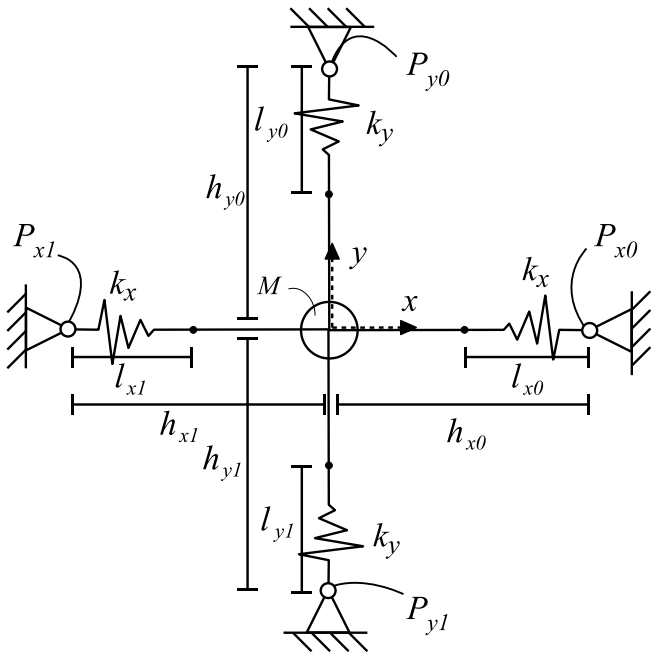


Figure 2.12: Orthogonally-arranged actuators model, where on each SEA the actuator has been removed for clearness to study the directional stiffness of the end-effector in function of the force and stiffness performed by each spring.

performs a force to M of:

$$f_{ij} = \zeta(l_{ij} - l_n)^2 \tag{2.18}$$

for $i \in \{x, y\}$ and $j \in \{0, 1\}$. It is also defined the stiffness performed by the non-linear spring as:

$$k_{ij} = \frac{\partial f_{ij}}{\partial l_{ij}} = 2\zeta(l_{ij} - l_n) \tag{2.19}$$

The actuator of a SEA has been removed to focus the following studies on the stiffness characteristics of the configuration. Since ζ and l_n are values considered constants, equal for every spring, and part of their proprieties, the force and stiffness performed for a single springs is function of its length.

The choice of a quadratic non-linear spring is due to the fact that a quadratic force-length function in an antagonist VSA assure the independence between stiffness of the mobile body and external load in a 1 DoF configuration [48].

In the equilibrium point $(M_x, M_y) = (0, 0)$ the force equilibrium for each direction is fulfilled:

$$\sum_{j=0,1} \mathbf{f}_{ij} = 0 \rightarrow \mathbf{f}_{i0} = -\mathbf{f}_{i1} \rightarrow |\mathbf{f}_{i0}| = |\mathbf{f}_{i1}| = f_i \tag{2.20}$$

Hence, the following relation is also satisfied:

$$k_{i0} = k_{i1} = k_i \tag{2.21}$$

The total force computed by the four springs in function of the position of $M = (x, y)$

when the end-effector is displaced:

$$\begin{aligned} F_x =& \zeta \left((h_{x0} - x) \frac{(l_{x0} - h_{x0} - l_n + \Phi_{x0})^2}{\Phi_{x0}} - (h_{x1} + x) \frac{(l_{x1} - h_{x1} - l_n + \Phi_{x1})^2}{\Phi_{x1}} \right) \\ & -\zeta x \left(\frac{(l_{y0} - h_{y0} - l_n + \Phi_{y0})^2}{\Phi_{y0}} + \frac{(l_{y1} - h_{y1} - l_n + \Phi_{y1})^2}{\Phi_{y1}} \right) \\ F_y =& \zeta \left((h_{y0} - y) \frac{(l_{y0} - h_{y0} - l_n + \Phi_{y0})^2}{\Phi_{y0}} - (h_{y1} + y) \frac{(l_{y1} - h_{y1} - l_n + \Phi_{y1})^2}{\Phi_{y1}} \right) \\ & -\zeta y \left(\frac{(l_{x0} - h_{x0} - l_n + \Phi_{x0})^2}{\Phi_{x0}} + \frac{(l_{x1} - h_{x1} - l_n + \Phi_{x1})^2}{\Phi_{x1}} \right) \end{aligned} \tag{2.22}$$

with

$$\begin{aligned} \Phi_{x0} &= \sqrt{(h_{x0} - x)^2 + y^2} \\ \Phi_{x1} &= \sqrt{(h_{x1} + x)^2 + y^2} \\ \Phi_{y0} &= \sqrt{(h_{y0} - y)^2 + x^2} \\ \Phi_{y1} &= \sqrt{(h_{y1} + y)^2 + x^2} \end{aligned} \tag{2.23}$$

The directional stiffness on the equilibrium position is computed differentiating (2.22), evaluating in the equilibrium point and combining (2.18) and (2.19). The directional stiffness can be expressed as:

$$\begin{aligned} K_x &= 2k_x + f_y \left(\frac{1}{h_{y0}} + \frac{1}{h_{y1}} \right) \\ K_y &= 2k_y + f_x \left(\frac{1}{h_{x0}} + \frac{1}{h_{x1}} \right) \end{aligned} \tag{2.24}$$

An interesting effect is revealed in (2.24) with the orthogonal arrangement of the springs. The arrangement does not assure the decoupling of the stiffness on the 2 DoF. The stiffness of one VSA influences the other VSA's stiffness and this contribution depends on the distance of the springs attachment point h_{ij}. This contribution becomes null if $h_{ij} \to \infty$ and is neglegible in the neighborhood of the equilibirium position.

The effect can also be mitigated minimizing the pre-load of the springs on the equilibrium position. On the other hand, since it is considered a configuration with wires, the springs are only able to produce traction force, therefore, a minimization of the pre-load affect also the maximum displacement capable of maintaining the wires in traction.

The force and the stiffness of one SEA on M is function of the length of the spring h_{ij}, thus can be changed with a convenient movement of the actuators. In Fig. 2.13 it is shown how the stiffness, and therefore change of force, affects also the stiffness in the perpendicular direction. In Fig. 2.14 it is shown how high preloads decrease the maximum stiffness ratio on M. The dimensions values are arbitrary defined:

$$\begin{aligned} \zeta &= 1 \left[\frac{\mathrm{N}}{\mathrm{mm}^2} \right] \\ l_n &= 10[\mathrm{mm}] \\ h_{x0} = h_{x1} = h_{y0} &= h_{y1} = 1000[\mathrm{mm}] \end{aligned}$$

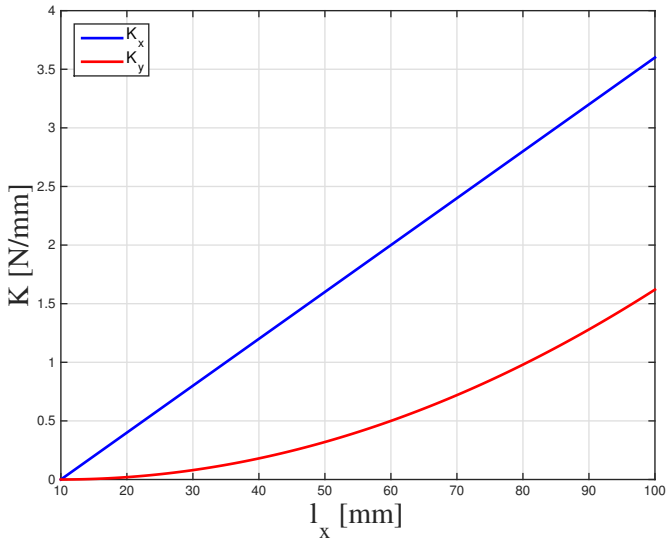


Figure 2.13: Stiffness along both directions x and y as function of the spring's length l_x, assuming $l_y = l_n = 10[mm]$. The orthogonal arrangement does not assure the decoupling of the stiffness along x and y. Stiffness varies in y with different preload lengths in SEA_x.

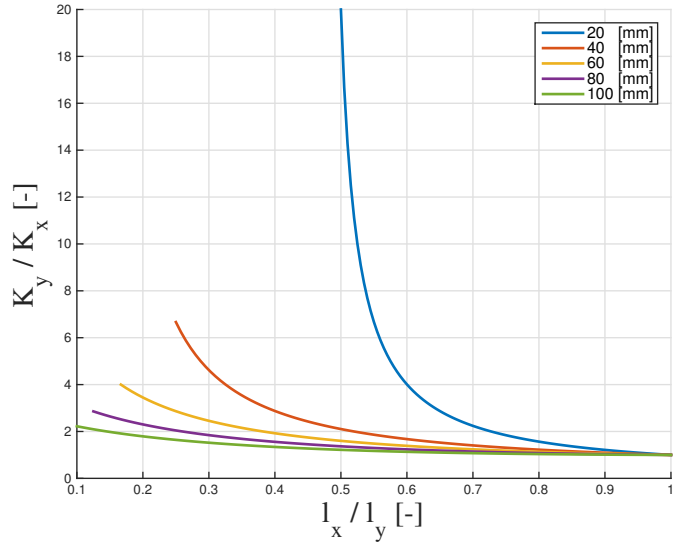


Figure 2.14: Stiffness ratio as function of the spring lengths ratio for different values of l_y. The curves initiate in different points of l_x/l_y since for a certain value of l_y, it is computed the stiffness ratio for $l_x \in [l_n, l_y]$. High ratios can be reached working with low spring lengths since the force also maintain low values, decreasing the effect on the perpendicular direction.

Chapter 3

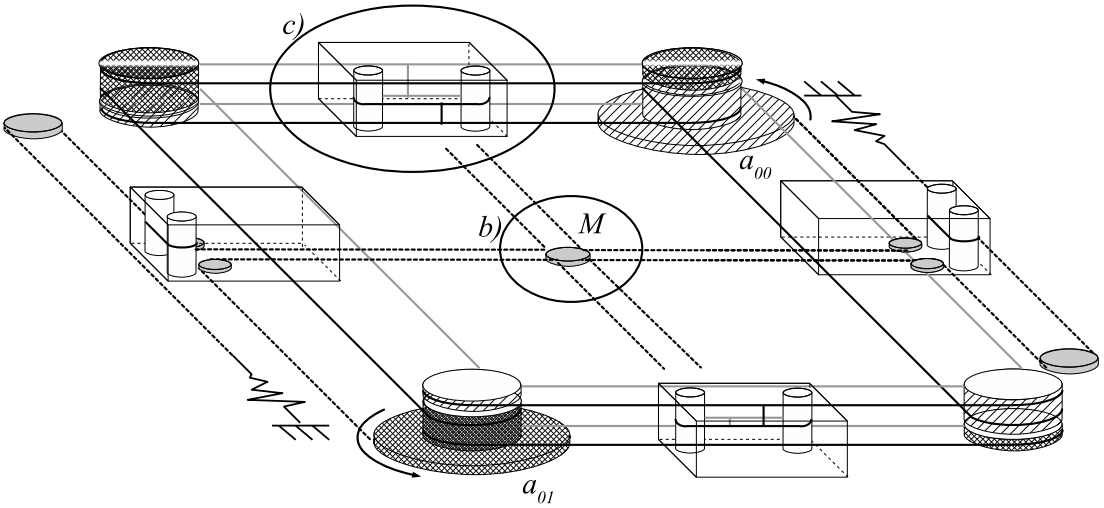
Kinetostatic Analysis

Having selected the concept to accomplish the specifics, it is now presented a kinematic architecture for the orthogonally-arranged actuator. The kinematic of the device has the aim of fulfilling the main characteristics of the actuator, which are: a couple of SEAs should keep an aligned position, to perform as a VSA and both of them need to keep the orthogonal configuration w.r.t. each other.

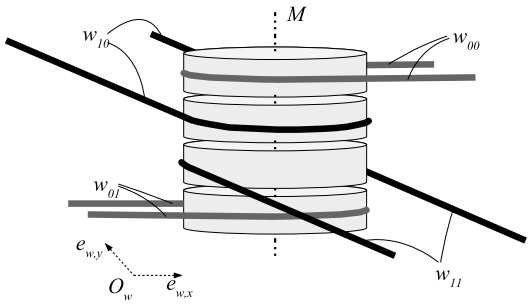
In Fig. 3.1a a single VSA of the two DoF actuator is presented. It is fundamentally in charge of two important characteristics: performing the force in its corresponding direction through two wires stretched by springs and guaranteeing the orthogonality of the force performed by the other VSA by moving the opposite carriages through a belt transmission system.

By exerting a linear force on the wire, the actuator changes the wire tension and stiffness through the extension of a non-linear spring grounded at the free end of the wire. Whilst, due to the pulley in the end-effector, the wires exert the forces that produce the movement of the manipulandum. Different combinations of the actuators movement generates different effects on the end-effector. It is possible, for example, by equally pulling both wires, to keep null the resultant force on the end-effector, but to change the stiffness as a consequence of extending the non-linear spring. It is worth underlining that, as shown in Fig. 3.1b, the four wires pass through the manipulandum by four coaxial pulleys in vertical configuration. Hereafter, the vertical displacement between the pulleys will be neglected, and the forces from the wires are considered coplanar.

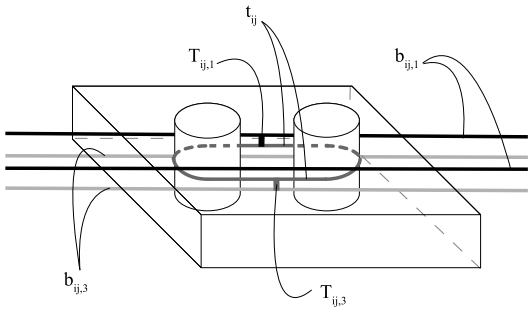
The rotational actuator is also attached to a belt transmission system, that moves the carriages of the other VSA by conveniently constraining the belt transmission of both actuators and an internal belt in each carriage. As shown in Fig. 3.1c, the internal belt in the carriage is attached to two other belts, each one actuated by a different actuator. Different combinations of linear velocity on the actuated belts generate the required movement of the carriage to follow the end-effector and keep the orthogonality of the forces. A synchronous movement of the belt, producing an equal velocity of the attachment points in the same direction, generates the same velocity on the carriage. On the other hand, an equal but opposite velocity of the attachment point generates the scrolling of the belt, keeping the carriage still. This last behavior is required when a change of stiffness is to be set on the end-effector.



(a) 3D view of a single VSA, that commands the wire exerting the forces in the corresponding directions, and the movement of the carriage that contains the wires of the other VSA. The wires are depicted in dashed lines, and the belts in continuous lines. The actuator a_{00} commands pulleys with inclined lines pattern and a_{01} commands pulleys with crossed lines pattern.



(b) 3D view of the end-effector.



(c) 3D view of a carriage.

Figure 3.1: 3D representation of a single antagonistic VSA.

3.1 Kinematic Architecture

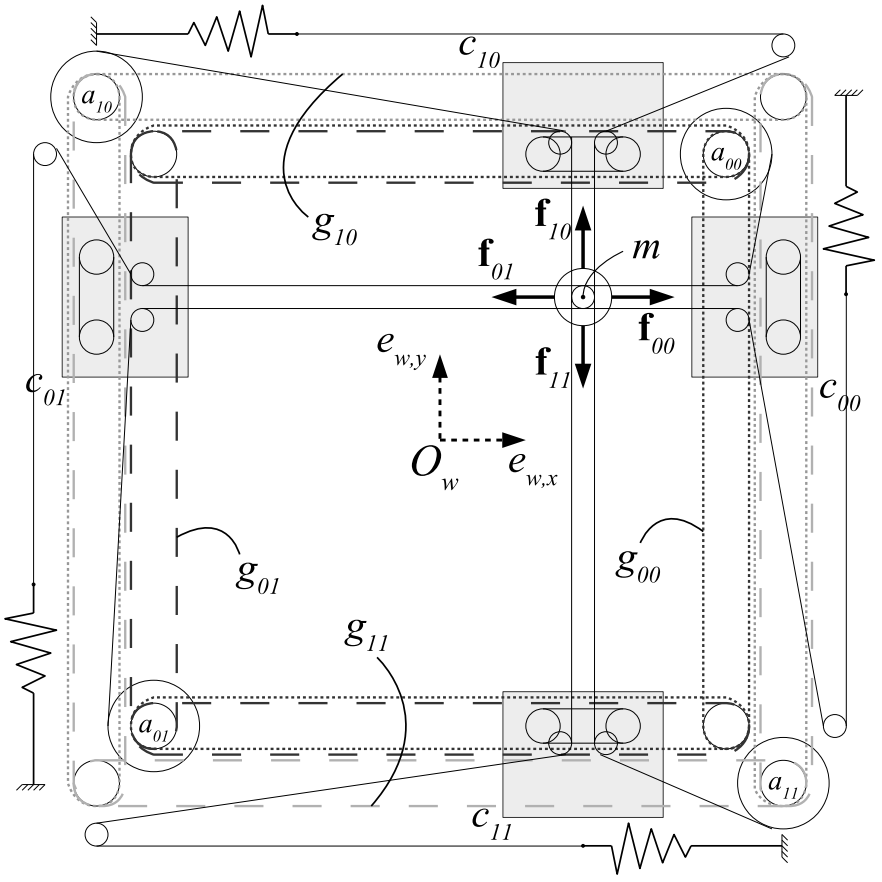


Figure 3.2: Top view of the orthogonally-arranged actuator's kinematic architecture. Each actuator a_{ij} commands the wire exerting the force $\mathbf{f}_{ij}$ to the end-effector. The belt transmission are configured as follows: a_{00} actuates dark dotted belts,a_{01} actuates dark dashed belts, a_{10} actuates light dotted belts and a_{11} actuates light dashed belts.

In Fig. 3.2 the kinematic architecture of the planar device is presented . It is made up of four essentially identical modules denoted by g_{ij}, each one producing a force $\mathbf{f}_{ij}$ to the end-effector M, with $i \in \{0, 1\}$ and $j \in \{0, 1\}$. The i index denotes the direction of the actuation, where $i = 0$ and $i = 1$ correspond to the $\mathbf{e}_{w,x}$ and $\mathbf{e}_{w,y}$ direction respectively, and j denotes the orientation of the force produced by the actuator in the equilibrium point[1] $\mathbf{f}_{ij}$, where $j = 0$ and $j = 1$ denotes the $+\mathbf{e}_{w,i}$ and $-\mathbf{e}_{w,i}$ directions respectively. Moreover, let us define $\bar{\imath}$ and $\bar{\jmath}$ the complement to 1 of i and j respectively (e.g. if g_{ij} refers to an arbitrary module, $g_{i\bar{\jmath}}$ denotes the one perpendicular and with the same orientation to g_{ij}, and $g_{\bar{\imath}j}$ denotes the one in the same direction but opposite orientation to g_{ij}).

In Fig. 3.3 it is presented the scheme of a single generic module g_{ij} and all of its components. Each module consists of:

[1]Since the wires are able to perform only traction force, the orientation of the force remains always invariable when no external forces are applied to M.

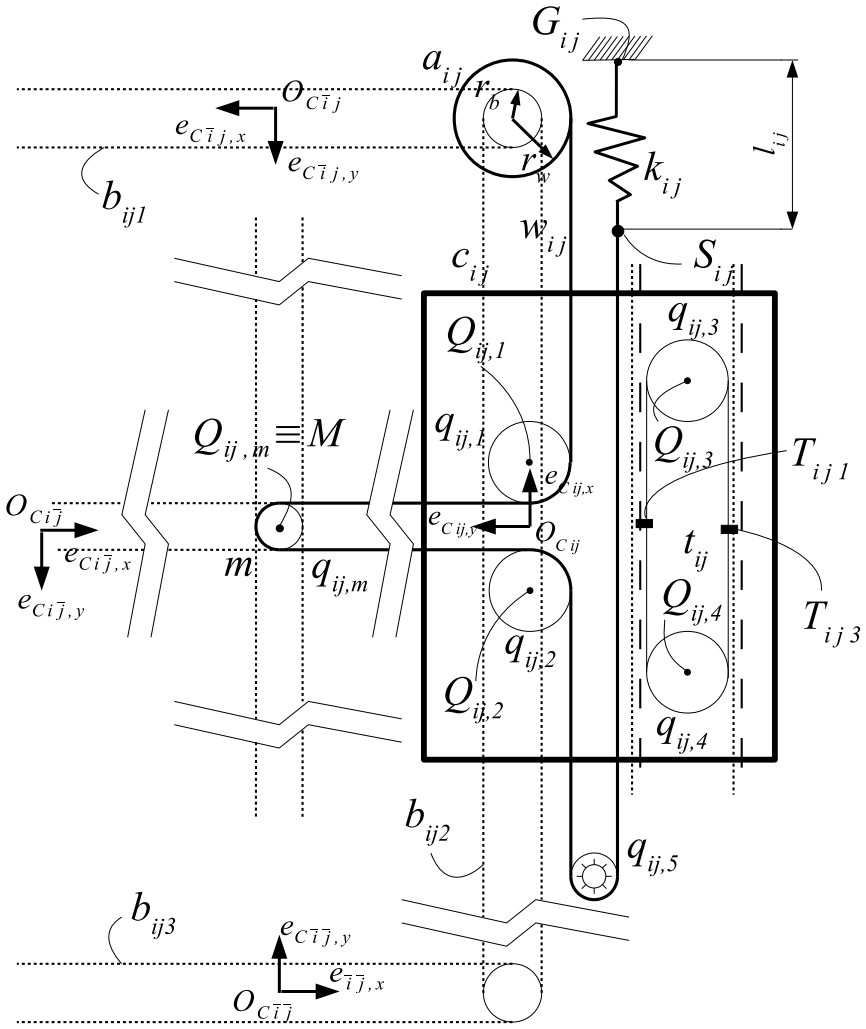


Figure 3.3: Top view of the components including in a generic module g_{ij}.

- a rotational actuator a_{ij}, characterized by the rotational coordinate θ_{ij} and the torque τ_{ij}.
- a non-linear spring $k_{w,ij}$ (assumed identical $\forall i, j$) with a length $l_{ij} = l_{ij,eq} + \Delta l_{ij}$, with $l_{ij,eq}$ the length of the spring at the equilibrium point and Δl_{ij} the length variation of the spring due an external force.
- a carriage c_{ij}, thats guarantees the correct direction of $\mathbf{f}_{ij}$ as a result of the belts transmission system.
- a wire w_{ij} with tension $f_{w,ij}$ pulled by the actuator a_{ij} through a pulley with radius r_w, and performing a pulling force $\mathbf{f}_{ij}$ to M due the elongation of $k_{w,ij}$. The wire connects a_{ij}, M and $k_{w,ij}$ through the pulleys $q_{ij,1}$, $q_{ij,2}$, (constrained to c_{ij}), $q_{ij,m}$ (constrained to M) and $q_{ij,5}$ (constrained to the ground).
- a set of synchronous belts[2] b_{ijl}, $l \in \{1, 2, 3\}$, actuated by a_{ij} through a pulley with

[2]The third index l denotes the belt's height-level, being 1 the highest one and 3 the lowest one.

radius r_b, that, together with $b_{i\bar{j}l}$, conducts the synchronization of the movements of $c_{\bar{i}j}$ and $c_{\bar{i}\bar{j}}$ w.r.t. M to guarantee the orthogonality of $\mathbf{f}_{\bar{i}j}$ and $\mathbf{f}_{\bar{i}\bar{j}}$ to $\mathbf{f}_{ij}$ and $\mathbf{f}_{i\bar{j}}$.

- an internal belt t_{ij} with its two corresponding pulleys $q_{ij,3}$ and $q_{ij,4}$, connecting the synchronous belts of $g_{\bar{i}j}$ and $g_{\bar{i}\bar{j}}$ to c_{ij} through the attachment points[3] $T_{ij,1}$ and $T_{ij,3}$.

Let us also denote as VSA_i the couple g_{i0} and g_{i1} constituting an antagonistic variable stiffness actuator, $\mathbf{f}_m$ the external force applied to M, and, as shown in Fig. 3.6, let us call $\mathbf{M}_{eq}$ the equilibrium position[4] of the end-effector when no external force is applied ($\mathbf{f}_m = \mathbf{0}$), and $\mathbf{M}_f$ the position when an external force is presented ($\mathbf{f}_m \neq \mathbf{0}$).

It is also important to underline

- The two set of synchronous belts b_{ijl} and $b_{\bar{i}jl}$ $\forall j, l$ differ only in the length of the belts for assembly reasons, as can be deductible from Fig. 3.2.
- The end-effector M contains four pulleys $q_{ij,m}$ $\forall i, j$ (one for each g_{ij}), centered in M, coaxial and placed side by side along their principal axis. Despite the displacement between the pulleys, it is approximated $\mathbf{f}_{ij}$ as coplanar $\forall i, j$.

The aim of the transmission system is to keep the orthogonal arrangement of the forces produced by the actuators:

$$(\mathbf{f}_{ij} \perp \mathbf{f}_{\bar{i}j}) \quad \wedge \quad (\mathbf{f}_{ij} = -\mathbf{f}_{i\bar{j}}) \quad \forall i, j \tag{3.1}$$

In a single carriage c_{ij} a local frame $\{c_{ij}\}$ it is defined (as shown in Fig. 3.3), positioned in $O_{c_{ij}}$ in such a way that $\mathbf{v}(Q_{ij,1}, O_{c_{ij}}) = -\mathbf{v}(Q_{ij,2}, O_{c_{ij}})$, and with $\mathbf{e}_{c_{ij},x} = \mathbf{u}(O_{c_{ij}}, Q_{ij,1})$. The wire w_{ij} performs a force $\mathbf{f}_{ij}$ to M through the pulley $q_{ij,m}$ in the point $Q_{ij,m} \equiv M$ due to the spring attached to one of its extremes. Hence, the force fulfills $\mathbf{f}_{ij} \parallel \mathbf{u}(M, O_{c_{ij}})$. Therefore, to satisfy (3.1), the following relation must be verified:

$$M \in \mathbf{e}_{c_{ij},y} \quad \forall i, j \tag{3.2}$$

Let us now focus on a single VSA_i, as shown in Fig. 3.4, that with two actuators is able to control 2 variables: the movement and the stiffness along i direction. The velocity $\dot{M}_i$ is defined by the kinematic relation of the actuators a_{i0} and a_{i1} through the wires w_{i0} and w_{i1}, expressed as:

$$\dot{M}_i = \frac{1}{2}\left(\dot{\theta}_{i0} r_w - \dot{l}_{i0}\right) = -\frac{1}{2}\left(\dot{\theta}_{i1} r_w - \dot{l}_{i1}\right) \tag{3.3}$$

To satisfy (3.1), since all the springs are identical, in the equilibrium position:

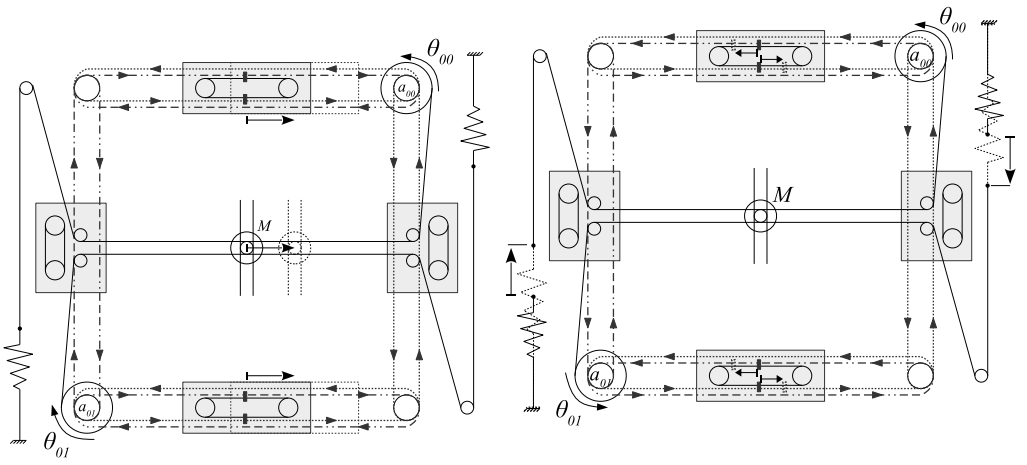
$$\begin{aligned} l_{i0} &= l_{i1} = l_i \\ \dot{l}_{i0} &= \dot{l}_{i1} = \dot{l}_i \end{aligned} \tag{3.4}$$

Therefore, (3.3) can be written in the following form:

$$\dot{l}_i = \frac{r_w}{2}\left(\dot{\theta}_{i0} + \dot{\theta}_{i1}\right) \tag{3.5}$$

[3] The third index l denotes at which height level correspond the attachment point.

[4] As said in Ref. 1.2, the equilibrium position of a VSA is the position where zero force or torque is generated by the actuators. In this case, the equilibrium position of VSA_i fulfills $\sum_j \mathbf{f}_{ij} = 0$



(a) $\theta_{00} = -\theta_{01}$: M translates with no change of stiffness. The carriages follow the movement of the end-effector.

(b) $\theta_{00} = \theta_{01}$: M keeps steady and the stiffness changes due to the elongation of the springs. The carriages remain still.

Figure 3.4: Effects of synchronous movement of the rotational actuators a_{00} and a_{01}, in case of opposite or same direction.

which substituted in (3.3), leads to:

$$\dot{M}_i = \frac{r_w}{4}\left(\dot{\theta}_{i0} - \dot{\theta}_{i1}\right) \tag{3.6}$$

On the other hand, let us now focus on the carriages $c_{\bar{i}0}$ and $c_{\bar{i}1}$. Their velocities are commanded by the synchronous belt transmission b_{ijl}, through the attachment points $T_{\bar{i}j1}$ and $T_{\bar{i}j3}$, that drive the velocity of the internal belt $t_{\bar{i}j}$ $\forall j, l$. Let us denote as B_{ijl} a generic point of the belt b_{ijl}, the velocity of this point is:

$$|\dot{\mathbf{B}}_{ijl}| = r_b\dot{\theta}_{ij} \qquad \forall i, j, l \tag{3.7}$$

The velocity of the attachment points w.r.t. the velocity of the carriage, expressed as the velocity of its local frame $\dot{\mathbf{O}}_{c_{\bar{i}j}}$, results as:

$$\dot{\mathbf{O}}_{c_{\bar{i}j}} = \frac{1}{2}\left(\dot{\mathbf{T}}_{\bar{i}j1} + \dot{\mathbf{T}}_{\bar{i}j3}\right) \tag{3.8}$$

To satisfy (3.1), it has to be fulfilled that $\dot{\mathbf{M}}_i = \dot{\mathbf{O}}_{c_{\bar{i}j}} \quad \forall i, j$. Therefore, conveniently constraining [5] B_{ijl} with T_{ijl}, and combining (3.6), (3.7) and (3.8) the following geometrical condition is identified:

$$r_w = 2r_b \tag{3.9}$$

to be used as a design parameter to guarantee (3.1).

[5] The constrains that assure the correct operation of the device are
$B_{0j1} \leftrightarrow T_{1j1}$
$B_{0j3} \leftrightarrow T_{1\bar{j}3}$
$B_{1j1} \leftrightarrow T_{0\bar{j}1}$
$B_{1j3} \leftrightarrow T_{0j3} \quad \forall j$

As shown in Fig. 3.4, and expressed in equations (3.5) and (3.6), depending on the synchronized movement of both actuators, it is possible to modify the position of the end-effector M without changing the directional stiffness, or vice versa. Since a requirement for a antagonistic VSA is to incorporate non-linear springs, the instantaneous stiffness of each spring k_{ij} is function of its length l_{ij}. Consequently, a synchronized in-phase movement of the actuators generates a change of the springs lengths l_{ij} that varies the generated stiffness $k_{w,ij}$ with no movement of M. Otherwise, a synchronized opposite movement generates a movement of M with no change of the generated stiffness $k_{w,ij}$.

3.2 Force and Stiffness Analysis

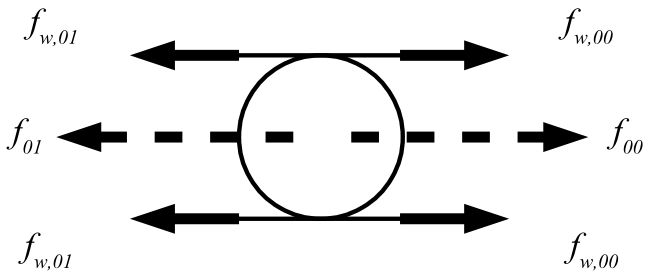


Figure 3.5: Forces applied to the end-effector.

Let us consider the forces performed in direction x when no external forces are applied, as shown in Fig. 3.5. Due to the pulley transmission, the resultant force performed by a single wire is:

$$f_{0j} = 2f_{w,0j} \tag{3.10}$$

The stiffness provided by the single module is computed as the spacial derivate of the force:

$$k_{0j} = \frac{\partial f_{0j}}{\partial M_x} = 2\frac{\partial f_{w,0j}}{\partial l_{0j}}\frac{\partial l_{0j}}{\partial Mx} = 4k_{w,0j} \tag{3.11}$$

The same procedure can be applied to direction y obtaining the same results. In the equilibrium position, the wire's tension and stiffness are equal for both modules, leading to exclude the subindex j in the notation:

$$\begin{aligned} f_{w,ij} &= f_{w,i\bar{j}} = f_{w,i} \\ k_{w,ij} &= k_{w,i\bar{j}} = k_{w,i} \end{aligned} \tag{3.12}$$

Combining (2.24), (3.10) and (3.11) the stiffness on the end-effector can be computed as:

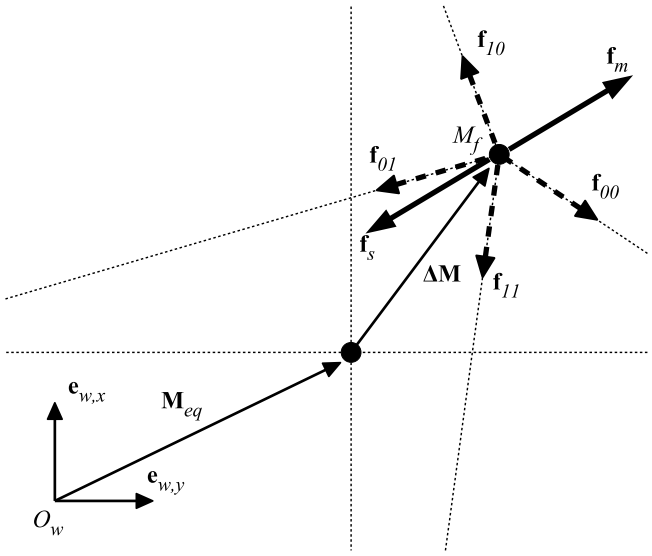
$$\begin{aligned} k_x &= 8k_{w,0} + 2f_{w,1}\left(\frac{1}{h_{10}} + \frac{1}{h_{11}}\right) \\ k_y &= 8k_{w,1} + 2f_{w,0}\left(\frac{1}{h_{00}} + \frac{1}{h_{01}}\right) \end{aligned} \tag{3.13}$$

with h_{ij} being the distance from the end-effector to the carriage c_{ij}, obtained with:

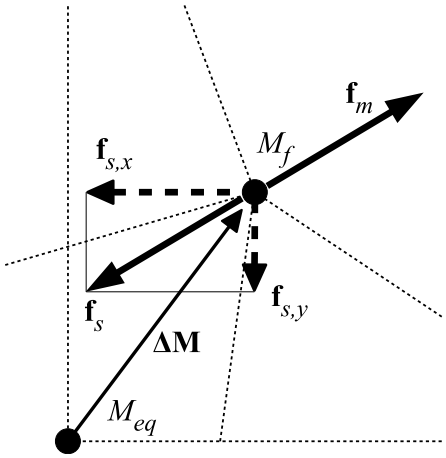
$$h_{ij} = d(M_{eq}, O_{c_{ij}}) \tag{3.14}$$

.

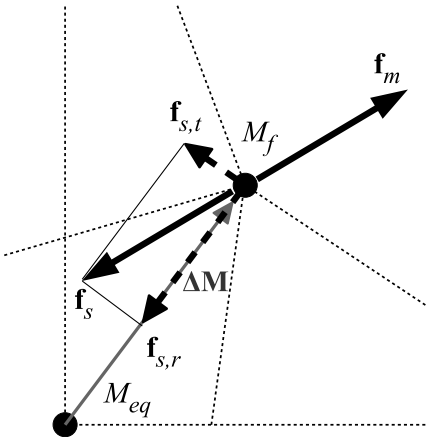
It is considered that in the actual operation of the device, generally $\mathbf{f}_m \neq 0$, and M deviates from its equilibrium position, leading not to satisfy (3.1), and losing the orthogonality between VSA_0 and VSA_1. Therefore, it is important to evaluate the behavior of the device, in terms of force and directional stiffness, when a considerable displacement of M is presented. An analytical equation is complicate to obtain, hence, a numerical procedure is now presented.



(a) The external force $\mathbf{f}_m$ causes a displacement ΔM, and the actuator reacts with a force $\mathbf{f}_s$, resulting from the single ones generated by the four modules.



(b) Cartesian projection of $\mathbf{f}_s$.



(c) Polar projection of $\mathbf{f}_s$.

Figure 3.6: States of force when an external force $\mathbf{f}_m$ is applied.

In figure 3.6a are presented the forces performed by the actuators when an external force $\mathbf{f}_m$ execute a displacement $\mathbf{\Delta M} = \mathbf{M}_f - \mathbf{M}_{eq}$. Lets define $\mathbf{f}_s$ the resultant force performed by the device. The position of M can be computed solving the equilibrium equation:

$$\sum_{i=0}^{1}\sum_{j=0}^{1}\mathbf{f}_{ij} + \mathbf{f}_m = \mathbf{f}_s + \mathbf{f}_m = \mathbf{0} \tag{3.15}$$

Let us moreover define the projected forces of $\mathbf{f}_s$ as shown in Fig. 3.6b and 3.6c:

$$f_{s,x} = \mathbf{f}_s \cdot \mathbf{e}_{w,x} \quad f_{s,y} = \mathbf{f}_s \cdot \mathbf{e}_{w,y} \quad f_{s,r} = \mathbf{f}_s \cdot \mathbf{e}_{w,r} \quad f_{s,t} = \mathbf{f}_s \cdot \mathbf{e}_{w,t} \tag{3.16}$$

where $\mathbf{e}_{w,r} = \mathbf{u}(\mathbf{\Delta M})$, and $\mathbf{e}_{w,t}$ fulfills

$$\mathbf{e}_{w,r} \times \mathbf{e}_{w,t} = \mathbf{e}_{w,x} \times \mathbf{e}_{w,y} \tag{3.17}$$

$f_{s,x}$ and $f_{s,y}$ are the cartesian components in x and y directions w.r.t. $\{w\}$, and $f_{s,r}$ and $f_{s,t}$ are the parallel and normal components to $\mathbf{\Delta M}$ respectively. More clearly, $f_{s,r}$ denotes the amount of force oriented towards the equilibrium point M_{eq}, and $f_{s,t}$ the amount of force perpendicular to the displacement, due to non-orthogonality, misalignment and asymmetry reasons.

It is also defined the local stiffness of M along different directions, computed as the partial derivates of $\mathbf{f}_s$:

$$k_x = \frac{\partial f_{s,x}}{\partial x} \quad k_y = \frac{\partial f_{s,y}}{\partial y} \quad k_r = \frac{\partial f_{s,r}}{\partial r} \quad k_t = \frac{\partial f_{s,t}}{r\partial \theta} \tag{3.18}$$

with $x = M_{f,x}$, $y = M_{f,y}$, $r = |\mathbf{\Delta M}|$ and $\theta = arctan2(\Delta M_y, \Delta M_x)$[6]. Known the force-displacement curve of the springs, the force and stiffness in each direction can be numerically computed.

The non-linear springs are considered to be quadratic, as explained in Ref. 2.2.1, performing to the wire a force and a stiffness:

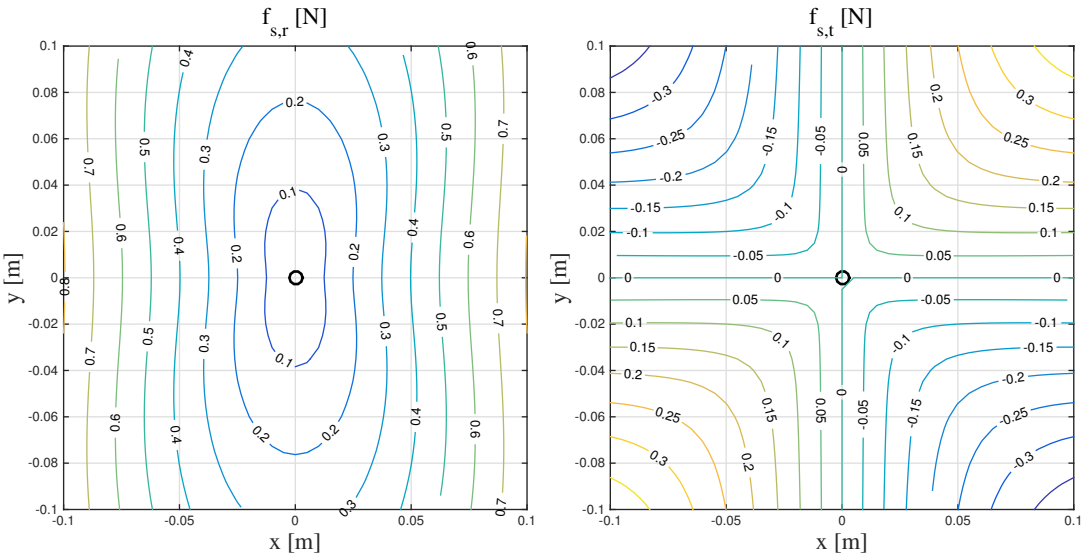
$$\begin{aligned} f_{ij} &= \zeta(l_{ij} - l_n)^2 = \zeta(l_{ij,eq} + \Delta l_{ij} - l_n)^2 \\ k_{ij} &= \frac{df_{ij}}{dl_{ij}} = 2\zeta(l_{ij,eq} + \Delta l_{ij} - l_n) \end{aligned} \tag{3.19}$$

leading to numerically compute the force and stiffness for every point of the workspace.

The radial and tangential force field is presented in Fig. 3.7 arbitrary defining $l_0 = 0.5$[m] and $l_1 = 0.1$[m], considering a workspace of 2×2[m], $\zeta = 1\left[\frac{\mathrm{N}}{\mathrm{m}^2}\right]$ and $l_n = 0$. From eq. (2.19), these values lead to a stiffness of $k_x = 8.04\left[\frac{\mathrm{N}}{\mathrm{m}}\right]$ and $k_y = 2.60\left[\frac{\mathrm{N}}{\mathrm{m}}\right]$. Even as the stiffness ratio on the wires is $\Gamma_{k_w} = 5$, it decreases on the end-effector to $\Gamma_k = \frac{8.04}{2.60} = 3$ due to the coupling effect (Ref. 2.2.1).

The mapping of force and stiffness performed by the device is presented in Fig. 3.8, as the end-effector is displaced from different equilibrium positions M_{eq}, in a 2×2[m] workspace and arbitrary setting $\zeta = 1\left[\frac{\mathrm{N}}{\mathrm{m}^2}\right]$, $l_n = 0$ and $l_0 = l_1 = 1$[m]. Radial forces keep a symmetric behavior, according to the symmetric configuration on the VSA's stiffness. As M_{eq} is moved farther from the center of the workspace, an evident increment of tangential forces is noted. Because of these forces, the return trajectory of the end-effector to its equilibrium position does not follow a straight line, instead it leads to curvilinear path. This effect can be neglected since the device is intended to work in the neighborhood of the equilibrium position, where tangential forces are low w.r.t. radial forces.

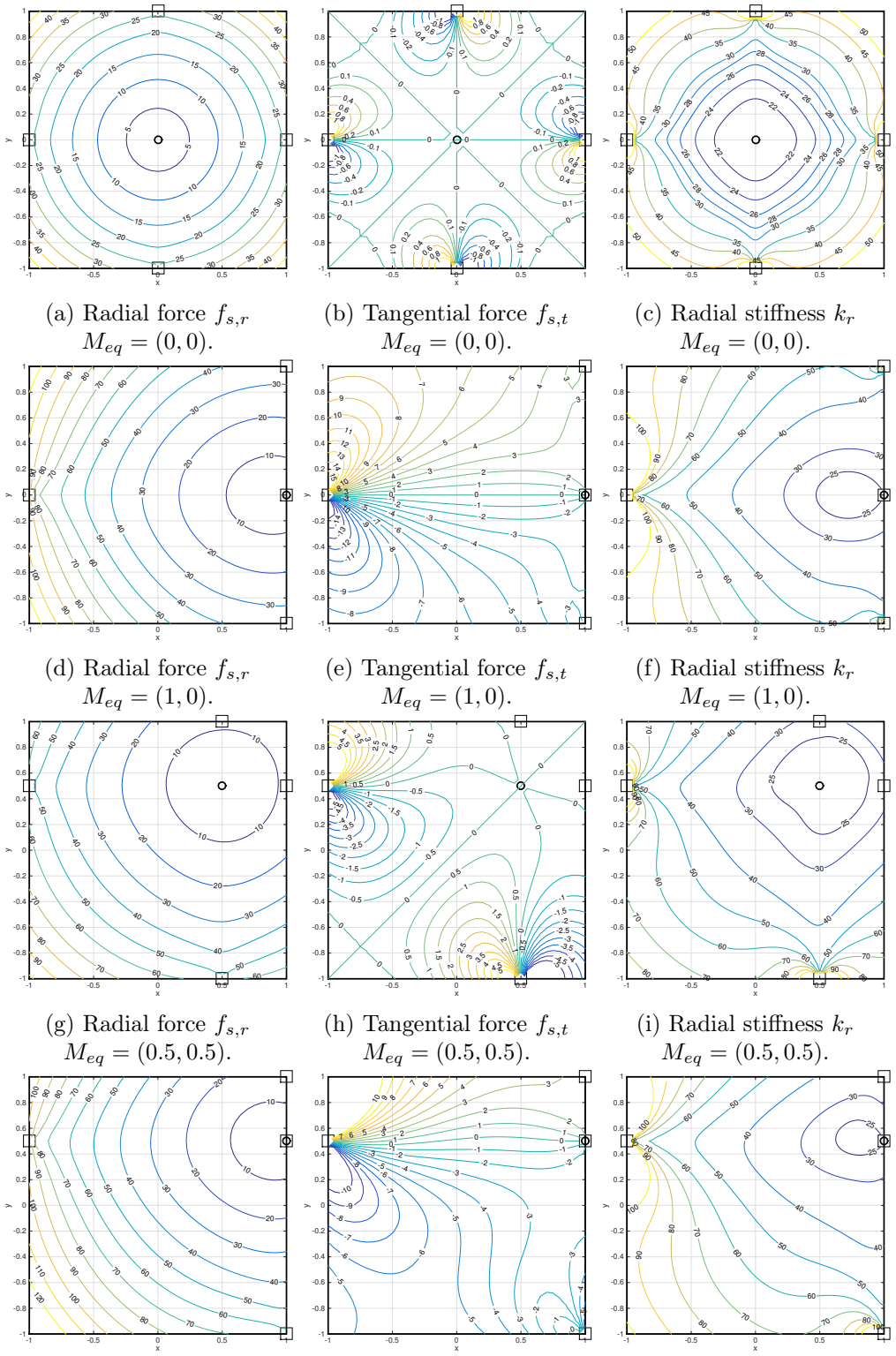
[6] $arctan2$ is the four-quadrant inverse tangent



(a) Radial force.

(b) Tangential force.

Figure 3.7: Effects of a non-symmetric stiffness in the VSAs to the force fields in the neighborhood of the equilibrium position. The radial force shows a non symmetric behavior, according to the difference of the stiffness in both VSAs (set to achieve $k_x > k_y$). As expected, the force increases in a major ratio whilst displaced in x direction than in y. Tangential forces evidence the effects of the device's asymmetries in most zones of the workspace, although their numerical value is low w.r.t. radial forces.



(a) Radial force $f_{s,r}$ $M_{eq} = (0, 0)$.
(b) Tangential force $f_{s,t}$ $M_{eq} = (0, 0)$.
(c) Radial stiffness k_r $M_{eq} = (0, 0)$.
(d) Radial force $f_{s,r}$ $M_{eq} = (1, 0)$.
(e) Tangential force $f_{s,t}$ $M_{eq} = (1, 0)$.
(f) Radial stiffness k_r $M_{eq} = (1, 0)$.
(g) Radial force $f_{s,r}$ $M_{eq} = (0.5, 0.5)$.
(h) Tangential force $f_{s,t}$ $M_{eq} = (0.5, 0.5)$.
(i) Radial stiffness k_r $M_{eq} = (0.5, 0.5)$.
(j) Radial force $f_{s,r}$ $M_{eq} = (1, 0.5)$.
(k) Tangential force $f_{s,t}$ $M_{eq} = (1, 0.5)$.
(l) Radial stiffness k_r $M_{eq} = (1, 0.5)$.

Figure 3.8: Maps of force components and stiffness with M_{eq} in some notable points of the workspace.

3.3 The Linear Wire-Wrapped Cam *SEA*

The architecture presented for the *PLANarm* requires the inclusion of non-linear springs attached to the wires in order to obtain the adaptable stiffness. Different ways to achieve a non linear-spring behavior in the output of a mechanism are listed in [32], and considering the many alternatives of mechanical realizations, two main branches of development can be identified: preload variable design and transmission variable design [49]. In the *PLANarm*'s kinematic configuration, including antagonistic motors to control the end-effector position and stiffness, the preload variable design is the most suitable design path. On this purpose, the Linear Wire-Wrapped Cam SEA (LinWWC-SEA) is preferred because of its versatility when modeling force-displacement curves, and manufacturing simplicity, since it is considered to be manufactured with Fused Deposition Modeling (FDM). In [50] a full development of the concept is done, whilst for this work, the fundamental concepts for the definition of the correct cam profile are presented.

The LinWWC-SEA is made up of a torsion spring, a cam, a wire and a pulley, as depicted in Fig. 3.10. The cam is hinged to ground in O_c, and its rotation is constrained to a torsion spring, that reacts with a torque in relation to the cam's rotation. The profile of the cam, as depicted in Fig. 3.9, models the transmission between the displacement of the wire and the rotation of the torsion spring. Thus, adjusting the cam's profile with an appropriated function, it's possible to obtain an arbitrary transmission between the displacement of the wire and the tension force that it performs, capable of simulating a virtual non-linear spring at the free end of the wire.

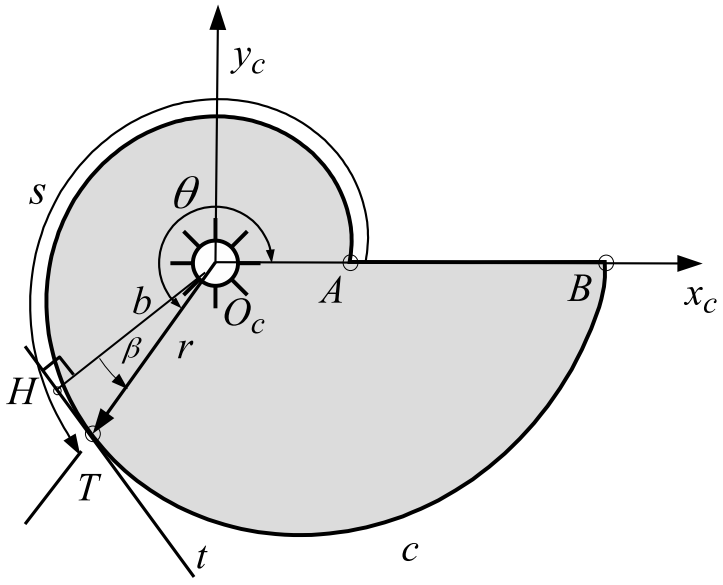


Figure 3.9: Radial cam used in the LinWWC-SEA, defined in the polar coordinates (r, θ) w.r.t. the local frame $\{c\}$ constrained to the came rotation.

Referring to Fig. 3.9, let us define the curve of the cam c with the polar coordinates (r, θ), w.r.t the local frame $\{c\}$. The cam radius r is conveniently considered monotonically increasing w.r.t. θ. Let $A(r_A, \theta_A)$ and $B(r_B, \theta_B)$ be the points on the cam's profile

with the minimum and maximum value of r respectively[7]. Let us moreover consider the point $T(r_T, \theta_T)$ along the cam profile, with $\theta_A \leq \theta_T \leq \theta_B$. It's also denoted $t = \overline{HT}$ the line passing through T and tangent to c, b is the minimum distance between t and O_c, and H is the point on t where that minimal distance is found.

Using the well known equations for curves defined in polar coordinates, it's computed the curvilinear coordinate of T along the cam profile:

$$s = \int_{\theta_A}^{\theta_T} ds = \int_{\theta_A}^{\theta_T} \sqrt{r^2 + \left(\frac{dr}{d\theta}\right)^2}\, d\theta \tag{3.20}$$

the pitch angle β, between r and $\overline{O_c H}$:

$$\beta = \arctan\left(\frac{1}{r}\frac{dr}{d\theta}\right) \tag{3.21}$$

and the minimum distance b between t and O_c:

$$b = r\cos\beta \tag{3.22}$$

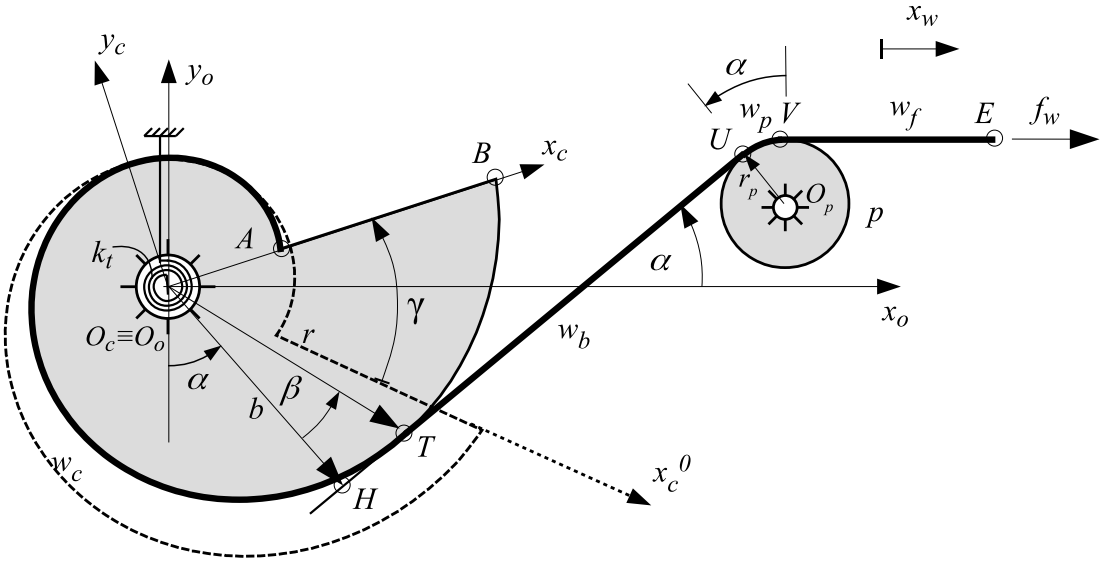


Figure 3.10: Scheme of the LinWWC-SEA. The tight line represents the wire w, and the dashed line represents the initial position of the *SEA*, defined by $T \equiv B$.

Now referring to Fig. 3.10, let us now define T as the point where the wire detaches from the cam and θ the wrapped angle of the cam. A pulley is added into the configuration to guarantee the proper direction of the wire at its free point E. Let us also define the tension force of the wire f_w, constant in the whole wire as consequence of neglecting friction, and k_w as the stiffness perceived in the wire at E. It is intended to completely define the position of the cam, the tension force and the local stiffness on

[7]In Ref. 4.2.2, these point will be considered as the work range of the cam, since a torsional spring has a limited rotation range

the wire for each value of θ, with $\theta_A \leq \theta \leq \theta_B$, assuming that the cam profile is known in its polar coordinates.

Let w be the constant total length of the wire, that is composed by:

- the part wrapped around the cam w_c (between points A and T);
- the free wire between the cam and the pulley w_b (between points T and U);
- the part wrapped around the pulley w_p (between U and V);
- the free wire at the end w_f (between V and E).

The angle α denotes the inclination of the line $\overline{HT}$ w.r.t. x_o, coincident with the wire w_b.

To completely know the position of the cam as function of the wrapped angle θ, α needs to be determined. Given $r(\theta)$ and $b(\theta)$, it can be obtained through (3.21) and (3.22). Therefore, the cartesian coordinates of $H = (H_x, H_y)$ are $(b\sin\alpha, -b\cos\alpha)$, and it is possible to describe the line t w.r.t. $\{o\}$ with the line equation:

$$m(x - H_x) - (y - H_y) = \tan(\alpha)\, x - y - \frac{b}{\cos\alpha} = 0 \tag{3.23}$$

with $m = \tan\alpha$ the slope of the line. The condition on the line t is to be tangent to the pulley, hence the minimum distance between t and the center of the pulley O_p is given by the pulley radius r_p:

$$d(O_p, t) = r_p \tag{3.24}$$

For the line t in the form of the eq. (3.23), the distance r_p between the line and the point is computed as:

$$r_p = \frac{c_a O_{p,x} + c_b O_{p,y} + c_c}{\sqrt{c_a^2 + c_b^2}} \tag{3.25}$$

where $c_a = \tan\alpha$, $c_b = -1$ and $c_c = \frac{-b}{\cos\alpha}$. Consequently, from eq. (3.25), α is obtained for a given value of θ.

Once $\alpha(\theta)$ is known, the length of the wire can be computed by the following equations:

$$\begin{aligned} w_c(\theta) &= \int_{\theta_A}^{\theta} \sqrt{r^2 + \left(\frac{dr}{d\theta}\right)^2}\, d\theta \\ w_b(\theta) &= d(T, U) = \sqrt{(U_x - T_x)^2 + (U_y - T_y)^2} \\ w_p(\theta) &= \alpha\, r_p \end{aligned} \tag{3.26}$$

whilst $w_f(\theta)$ can be determined by knowing the total length of the wire w as:

$$w_f(\theta) = w - w_c(\theta) - w_b(\theta) - w_p(\theta) \tag{3.27}$$

The absolute angular position of the cam is determined as $\angle(x_c, x_o)$. Let us now define the initial angular position of the cam, as the position where T coincides with B, and the cam is totally wrapped by the wire. The angle between x_o and x_c^0 is:

$$\angle(x_c^0, x_o) = -\frac{\pi}{2} + \alpha(\theta_B) + \beta(\theta_B) \tag{3.28}$$

where x_c^0 is $x_c|_{\theta=\theta_B}$. Let γ be the rotation of the cam from the initial position, defined as:

$$\gamma = \angle(x_c, x_c^0) \tag{3.29}$$

and let x_w be the displacement of E w.r.t. the initial position. It is obtained with the equation:

$$x_w = w_f - w_f|_{\theta=\theta_B} \tag{3.30}$$

The torque produced by the spring as function of the rotation of the cam can be computed through numerical integration:

$$\tau_c = \int_0^{\gamma} k_t d\gamma + \tau_{c,0} \tag{3.31}$$

where k_t is the constant torsional stiffness of the spring, and $\tau_{t,0}$ is the preload torque when $\gamma = 0$. Given a force f_w applied in E, in a quasi-static equilibrium, the torque applied by the torsion spring is:

$$\tau_c = f_w b \tag{3.32}$$

the mechanism turns the torsion stiffness k_t in a linear stiffness k_w at the free end of the wire E:

$$k_w = \frac{k_t}{b^2} \tag{3.33}$$

At this point, with a proper knowledge of the cam profile, the displacement, the tension force and the linear stiffness at the free point of the wire can be numerically computed. The aim now is to properly define the cam profile that suits the stiffness requirements of the device.

3.3.1 Logarithmic Spiral

To completely define the cam, a curve profile has to be chosen to achieve the required stiffness performance in the wire. The logarithmic spiral has a special characteristic that simplifies the computation of the cam's profile: the pitch angle β is constant for any value of θ. In polar coordinates, the logarithmic spiral is defined as

$$r = c_1 \mathrm{e}^{c_2 \theta} \tag{3.34}$$

with e the natural logarithms base, c_1 and c_2 arbitrary real positive constants.

Let us define the stiffness ratio between the maximum and minimum linear stiffness on the point E as a design parameter:

$$\Gamma_{k_w} = \frac{k_{w(A)}}{k_{w(B)}} \tag{3.35}$$

where $k_{w(A)}$ and $k_{w(B)}$ denote k_w when T coincides with A and B, respectively. Considering a constant torsional stiffness k_t, and combining (3.22), (3.33) and (3.35):

$$\Gamma_{k_w} = \left(\frac{r_{(B)}}{r_{(A)}}\right)^2 \tag{3.36}$$

using the polar definition of r in (3.34):

$$\Gamma_{k_w} = \left(\frac{c_1 \mathrm{e}^{c_2 \theta_B}}{c_1 \mathrm{e}^{c_2 \theta_A}}\right)^2 \rightarrow c_2 = \frac{\ln(\Gamma_{k_w})}{2\Delta\theta} \tag{3.37}$$

where $\Delta\theta = \theta_B - \theta_A$. Given arbitrary values of the maximum cam radius $r_{(B)}$ and a total wrapping angle $\Delta\theta$, c_1 is calculated as:

$$c_1 = \frac{r_{(B)}}{\mathrm{e}^{c_2 \Delta\theta}} \tag{3.38}$$

Consequently, given the design parameters Γ_{k_w}, $r_{(B)}$ and $\Delta\theta$, the cam profile is entirely defined, and all the required curves of force, stiffness and wire displacement can be numerically computed.

3.4 The Linear Wire-Wrapped Cam VSA

The kinematic architecture requires the adoption of four SEAs antagonists in couples, in order to generate two perpendicular VSAs. In Fig. 3.11, the introduction of the LinWWC-SEA into the architecture is depicted, where each non-linear spring is replaced by a cam and a torsion spring (with identical stiffness k_t for each cam). Let SEA_{ij} be the set of elements including the actuator a_{ij} and its respective LinWWC-SEA, that generates a stiffness k_{ij} on the wire.

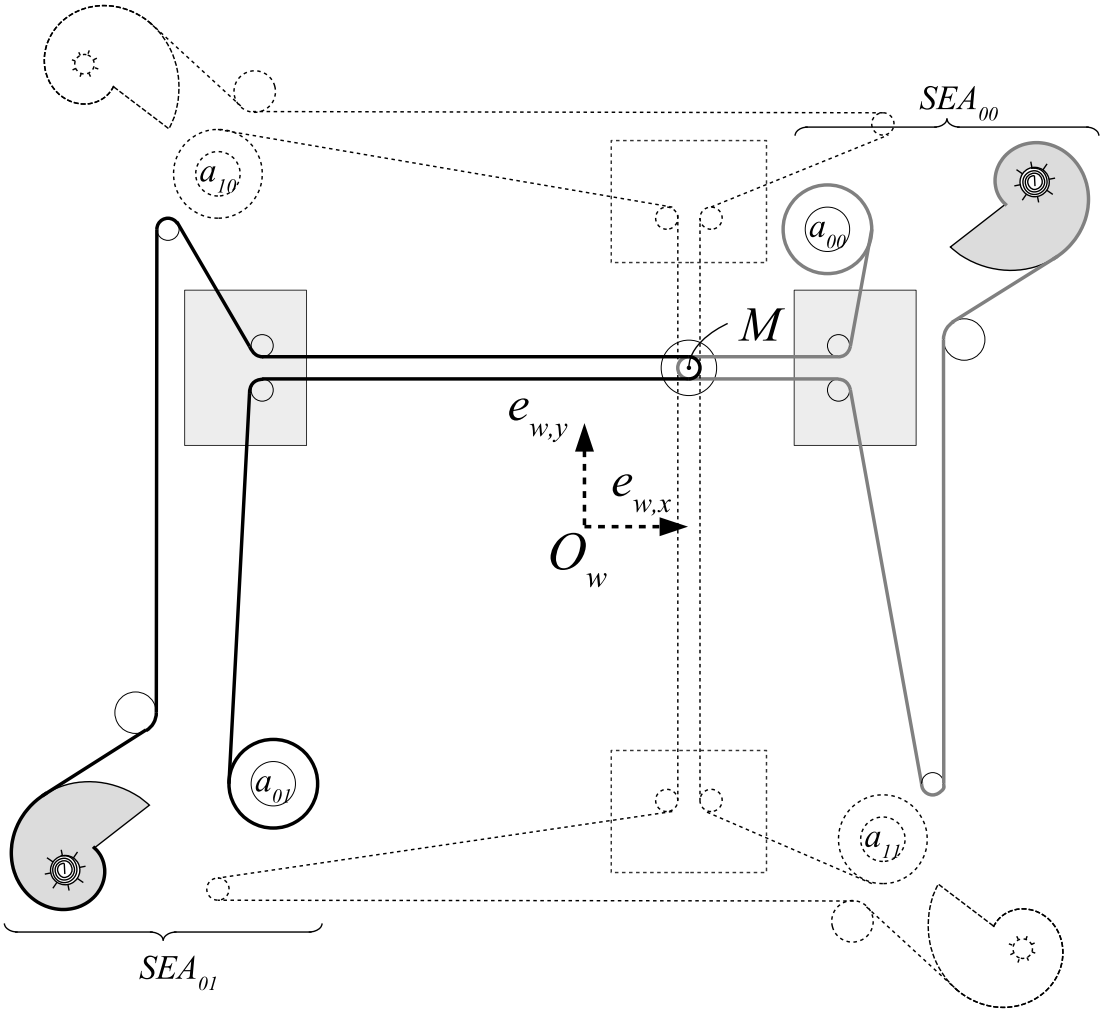


Figure 3.11: Top view of the device after including the LinWWC-VSAs.

The Linear Wire-Wrapped Cam VSA (LinWWC-VSA) is made up of two antagonistic LinWWC-SEA. To define the behavior in terms of force and stiffness of a single antagonistic actuator, let's now focus on a single module in the generic direction i. A reduced configuration of the LinWWC-VSA is presented in Fig. 3.12, where some pulleys have been neglected since their only function is to deviate wires between the actuator and the SEA. Under the hypothesis of no friction, the model presents the same characteristics in terms of kinematical architecture and dynamic behavior.

Let us define SEA_j, with $j = \{0, 1\}$, the two antagonistic SEAs that conform the

VSA_i. j denotes the orientation of the force performed by the SEA, where $j = 0$ and $j = 1$ correspond to the orientations $+\mathbf{e}_{w,i}$ and $-\mathbf{e}_{w,i}$ respectively. Let's also define θ_j the joint coordinate of the rotational actuator a_j, and γ_j the angular rotation of the cam. Each actuator generates a stiffness $k_{w,j}$ and a tension force $f_{w,j}$ on the wire, that, due to the pulleys in M, become a force of $f_j = 2f_{w,j}$ and a stiffness $k_j = 4k_{w,j}$ on the end-effector (Ref. 3.2). Let $x_{w,j}$ be the displacement of the wire due to a rotation of the cam. It is worth underlining that having totally defined the cam profile, f_w, k_w and x_w are known functions of γ, and $x_{w,l}$ can be obtained form the displacement ΔM (Ref. 3.1).

When no external force f_m is applied to the end-effector, the VSA is on its equilibrium position, an no displacement ΔM is generated. Otherwise, an external force introduces a displacement on the end-effector, that in turn produces a rotation of the cam. In both cases, in quasi-static terms, the force equilibrium equation is fulfilled:

$$\mathbf{f_m} = \mathbf{f_0} + \mathbf{f_1} = \mathbf{f_s} \tag{3.39}$$

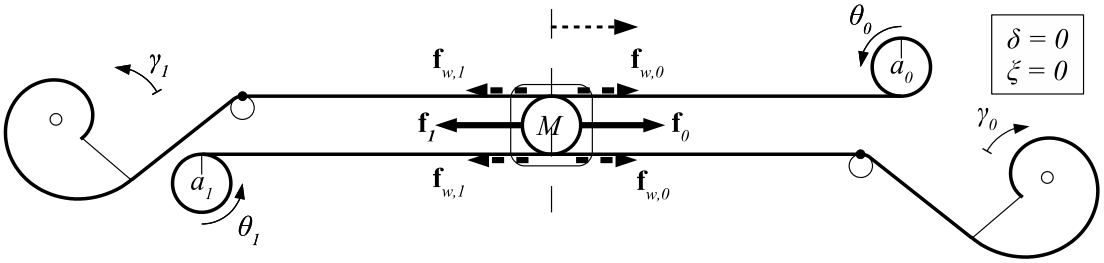
Let's define two conveniently independent parameters to define the state of the VSA:

$$\begin{aligned} \delta &= \frac{x_{w,0} + x_{w,1}}{2} \\ \xi &= \Delta M \end{aligned} \tag{3.40}$$

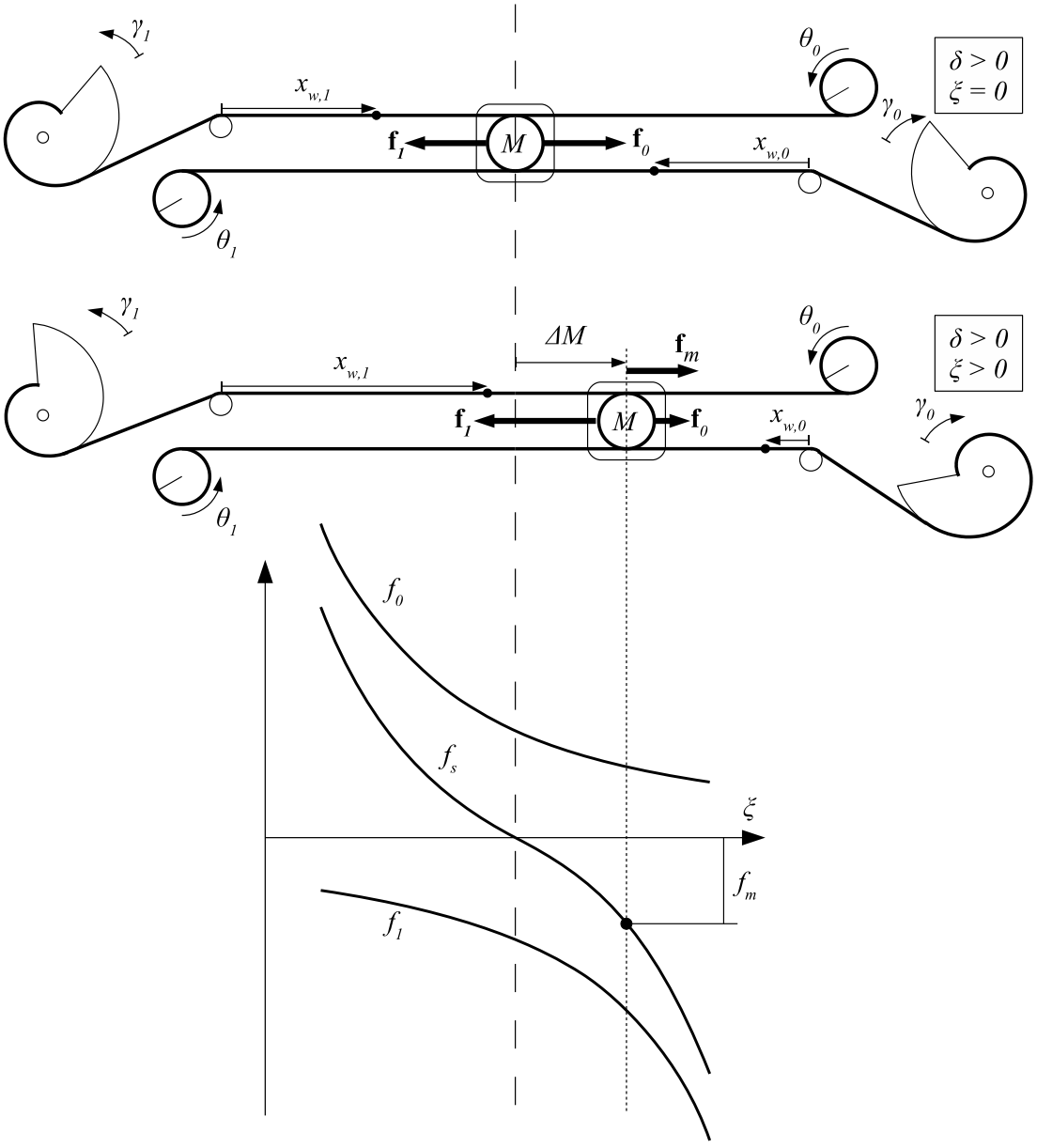
The external force f_m is consequently obtained by knowing δ, ξ and the cam profile with all of its parameters. The resultant stiffness on the end effector is obtained through:

$$k = k_0 + k_1 \tag{3.41}$$

In Fig. 3.12 three different configurations for the VSA are presented . With $\delta = 0$ is defined the configuration with minimal stiffness, and the wire is totally wrapped around the cam. The forces behavior for $\delta > 0$ are depicted in the graph below. The external force f_m moves along the curve of f_s as function of ξ.



(a) Configuration with minimal stiffness ($\delta = 0$) on the equilibrium position.



(b) Configuration with ($\delta > 0$) for both equilibrium position ($\xi = 0$) and displaced position ($\xi \neq 0$), with the curve of the forces as function of ξ.

Figure 3.12: Schematic representation of the VSA.

Chapter 4

Mechanical Design

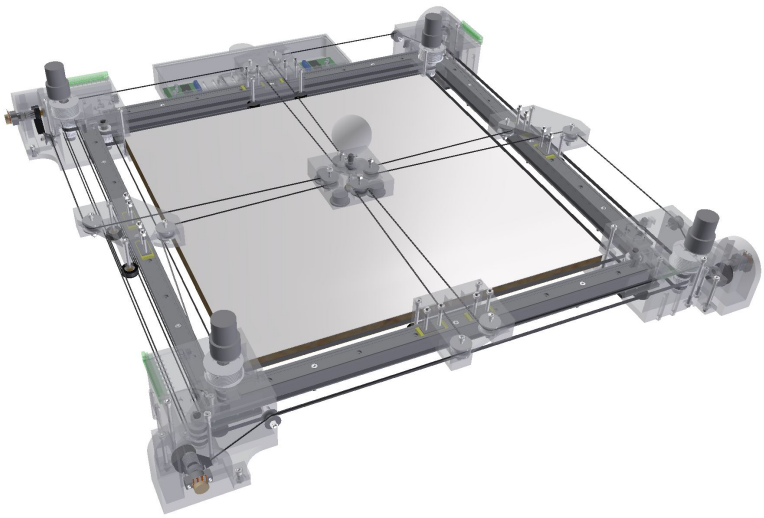


Figure 4.1: CAD drawing of the *PLANarm*.

The design of the *PLANarm* is now presented. During the design process the following main aspects have been kept in consideration as guidelines for the decisions that led to the prototype presented in this work:

- Keep the overall cost and size of the device low. The device is meant to be an affordable alternative to expensive and bulky machines, to be kept and used at home by patients.
- Use, where possible, standard or at least easily manufacturable components. In a forward-looking prospective, the reproduction of the device would be much easier if the components were easily reachable.
- Arrange the assembling to be simple and to allow easy substitution of parts. As the work presented is the first prototype of the concept, it is reasonable to think that, in order to explore further potentialities, or to optimize some aspects, the prototype needs to be easily modifiable.
- Fulfill the numeric specifications presented below.

4.1 Performance Targets

In the definition of the requirements for the device, a compromise between optimization of the performances and limitation of weight, size and cost of the overall machine is reached.

4.1.1 Workspace

The workspace of the device is expressed in terms of planar extension of the area in which the end effector has to move and work correctly. The choice of the workspace is made taking into consideration the anthropometry of the upper limb of an adult man and the typical workspace of the existing rehabilitation devices. As the robot is conceived to work with the patient sitting in front of it, the anthropometric values considered for the choice of the workspace are the frontal and lateral reach of the arm. This area consists of an horizontal plane placed 30 [cm] above the seat reference point. Referring to [30], the grasp reach of the hand is around 60x80 [cm]. As post-ictus patients have reduced mobility, current rehabilitation devices do not cover such distances and their typical workspaces do not exceed 50x50 [cm]. Based on this considerations, the target workspace set for the presented device is a square surface 50x50 [cm], in which the end effector has to move, exert the target force in every directions, and adjust the impedance level through the target range.

4.1.2 Target Force

The target force is expressed in terms of force that the device is expected to impress to the manipulandum, in the whole workspace, in every direction. The numeric value of this force is set according to the performances needed for rehabilitation exercises. From a static point of view, the device is asked to sustain the arm's weight. Depending on the angle between the planar workspace and the horizontal plane w.r.t. $\{w\}$, the opposing force varies. The most severe condition is when the plane is positioned vertically. In Fig. 4.2,a simple approximation of the arm's weight W distribution is shown, that overestimates the resultant load f_m on the manipulandum.

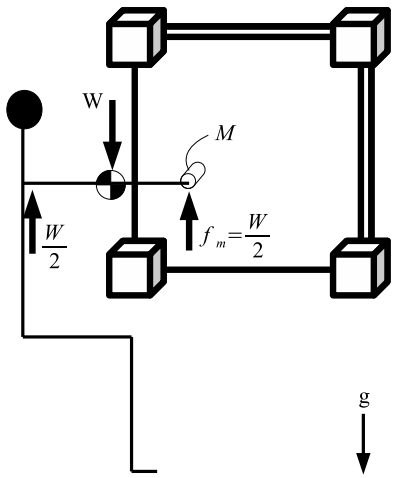


Figure 4.2: Scheme of arm's weight distribution. It is shown that, in first approximation, weight W is equally distributed between the shoulder and the manipulandum

The arm of an adult man does not exceed 40 [N], which, at the manipulandum, produces a force of at most 20 [N]. Inertia is not considered in the definiton of the target force, as rehabilitation exercises require low acceleration on the end-effector.

Therefore the target force on the manipulandum is set to $f_m^{max} = 40[N]$, 100% higher then the value obtained before, in order to take into account friction and eventual forces from the patient, such as spasms. The choice of 40 [N] is reasonable value, if compared to typical target forces for existing devices (Ref. 1.1.1), that span from 25 [N] to 50 [N].

4.1.3 Impedance Range

The presence of VSAs requires the definition of a maximum and minimum value for stiffness at the equilibrium. When an external force, coming from the arm, distances the manipulandum from the equilibrium position, the perceived stiffness at the handgrip has to be adjustable. In fact, the resistance encountered by the patient while using the device has to span between strong and barely noticeable, depending on the type of exercise and degree of recovery. The maximum stiffness has to allow the end effector to be felt as it was constrained by a virtual wall. The set value for the required maximum stiffness is $k^{max} = 4.2[\frac{N}{mm}]$, above human perception for a virtual wall [30]. The ideal value for the minimum stiffness is zero, a condition in which the displacement from the equilibrium position does not encounter any resistance. This condition isn't achievable in practice , because in order to have no stiffness the cable tension would need to be null. A null cable tension would cause the fall of the wires, that would compromise the functionality of the entire device.

4.2 Designing Calculations

Given the kinematic structure and the requirements, the design of the device is planned. The most significant calculations that led to the dimensioning of the components are here presented.

4.2.1 Cable Tension and Force Distribution

Based on the kinematic configuration, the distribution of tension on the cables is shown in Fig. 4.3.

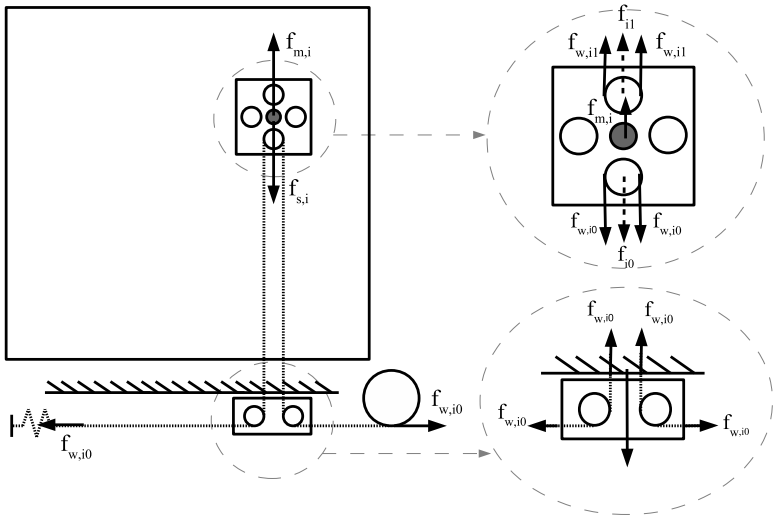


Figure 4.3: Distribution of cable tension.

For a generic equilibrium condition, where $f_{m,i} = 0$, the stiffness on the end-effector is set; therefore a preload $f^0_{w,i}$ is exerted by both springs of each module i and the tensions $f_{w,i0}$ and $f_{w,i1}$ on the two cable circuits are:

$$f_{w,i0} = f_{w,i1} = f^0_{w,i} \tag{4.1}$$

The corresponding forces on the end-effector at the equilibrium are $f^0_{i0} = 2f^0_{w,i0}$ and $f^0_{i1} = 2f^0_{w,i1}$.

When a force $f_{m,i}$ parallel to main direction i is applied on the end effector, a new equilibrium position is reached, in which the force redistributes between the two couples of wires:

$$f_{i0} - f_{i1} = f_{m,i} \tag{4.2}$$

It is assumed that force equally distributes on the two components:

$$\begin{aligned} f_{i0} &= f^0_{i0} - \frac{f_{m,i}}{2} \\ f_{i1} &= f^0_{i1} + \frac{f_{m,i}}{2} \end{aligned} \tag{4.3}$$

This is an approximation, as the non linearity of the springs causes a force distribution

dependent on the value of $f_{m,i}$. The resulting forces on the single wires are:

$$\begin{aligned} f_{w,i0} &= \frac{f_{i0}}{2} \\ f_{w,i1} &= \frac{f_{i1}}{2} \end{aligned} \tag{4.4}$$

The worst case scenario, from a resistance point of view, is when both the preload on the wires and external forces are at maximum target values: $f_{w,i}^{0\,max}$ and $f_{m,i}^{max}$ for which the resulting maximum tension at the wires is:

$$f_w^{max} = f_{w,i}^{0\,max} + \frac{f_{m,i}^{max}}{4} \tag{4.5}$$

The dimensioning of the single parts is done considering f_w^{max} as cable tension.

4.2.2 Spring and Cam Definition

To completely define a cam profile suitable for the device's specifics, four design parameters are to be determined: the maximum and minimum stiffness on the wire $k_{w(A)}$ and $k_{w(B)}$, the maximum cam radius $r_{c(B)}$ and the cam rotation range $\Delta\theta$.

The rotation angle is chosen considering that a common torsion spring works within a range of 270° to 360°. Further, as a spring preload needs to be considered for the initial position, $\Delta\theta_c = 270°$ is defined as a design parameter. Moreover, to minimize the size of the mechanical piece, it is specifically defined $\theta_{c(A)} = 90°$ and $\theta_{c(B)} = 360°$, to assure that the portion of the cam aside the work range develops with a minimal radius $r_c(\theta_c) \sim r_{c(A)}$.

The maximum radius $r_{c(B)}$ is constrained by the geometry in the physical position of the cam within the device, described in Ref. 4.3.1. It is defined as a maximum possible radius $r_{c(B)} = 35$[mm].

Referring to eq. (3.13) in section 3.2, and neglecting the coupling effect produced by the forces, the relation between the stiffness on the wire and the resultant directional stiffness is:

$$k_i = 8k_{w,i} \tag{4.6}$$

The maximum desired stiffness on the end-effector is $k^{max} = 4.2\left[\frac{\mathrm{N}}{\mathrm{mm}}\right]$, therefore:

$$k_w^{max} = \frac{k^{max}}{8} \tag{4.7}$$

The ideal minimum stiffness is zero, a value impossible to reach in real conditions. An acceptable ratio between the maximum and minimum stiffness is 10. Since it is not considered, for simplicity reasons, the coupling effect of the stiffness in two orthogonal directions, a ratio of 16 is chosen for the stiffness on the wire.

Having established the design parameters of the cam, the logarithmic spiral's constants c_1 and c_2 presented in (3.34) can be calculated with (3.38) and (3.37). In Fig. 4.4 the obtained cam profile is depicted.

The selection of the torsion spring is obtained using (3.33) evaluated in the maximum stiffness configuration, that is $T \equiv A$, resulting in:

$$k_t = k_{w(A)} b_{(A)}^2 \tag{4.8}$$

In Fig. 4.5 the curves of tension force and linear stiffness on the wire are presented, and four different configurations of the cam position are graphically depicted.

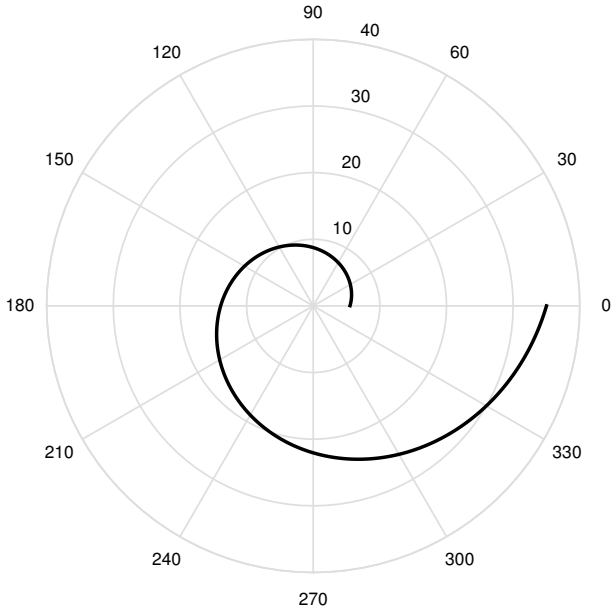


Figure 4.4: Logarithmic spiral cam profile obtained from the design parameters. The minimum radius at $\theta = 0°$ is 5.52[mm]. Within the range work, the radius monotonically increase from $r(\theta_A) = 13.90$[mm] to $r(\theta_B) = 35.00$[mm].

4.2.3 Motor Requirements

The choice of motors is made considering stall torque and speed. Based on the limit condition described in the previous paragraph, the maximum tension at cables is f_w^{max}, which leads to a definition of the stall torque τ required to the actuators:

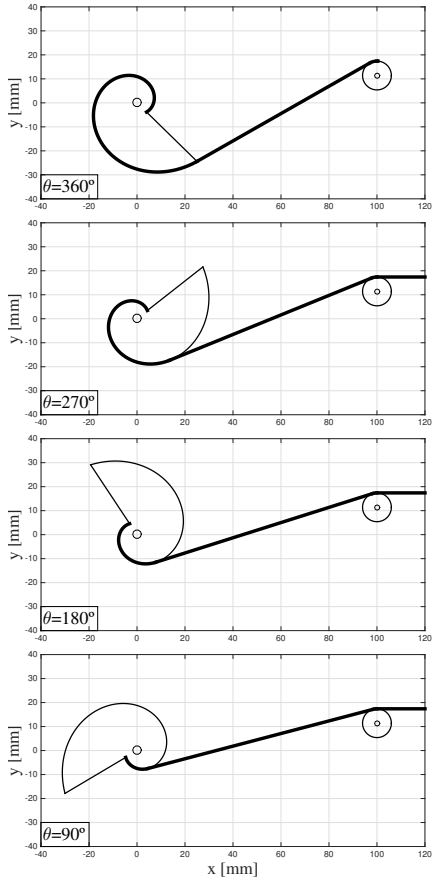
$$\tau = f_w^{max} r_w \tag{4.9}$$

The maximum speed for the motors is evaluated from considerations on the moving speed of the patient's arm. If the manipulandum was faster than the response of motors, the corresponding spring would lose tension, causing the fall of the cable. The maximum speed ω at the manipulandum is set at $v_m^{max} = 40[mm/s]$; the required maximum speed for motors is the following:

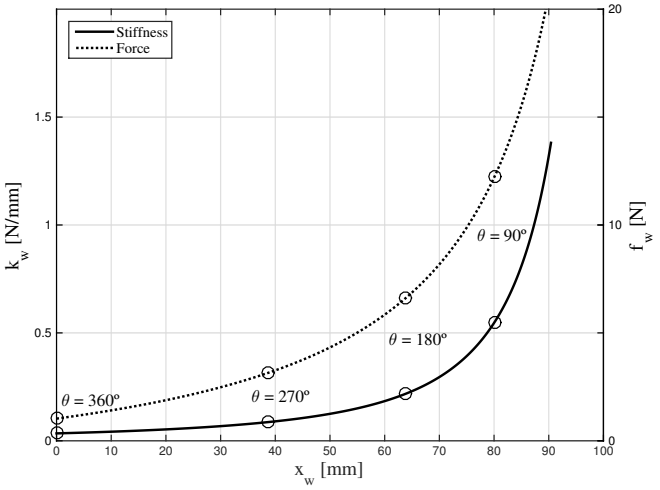
$$\begin{aligned} v_w^{max} &= 2v_m^{max} \\ \omega &= \frac{v_w^{max}}{r_w} \end{aligned} \tag{4.10}$$

4.2.4 Load on Carriages and Bars

The carriages are a delicate component from a structural point of view. They are supposed to sustain the load caused by cable tension while being free to move in the direction of the slides. In Fig. 4.6 a representation of the distribution of forces on the carriages is given. The maximum inward force F_{in} and momentum M_{in} on the slides



(a) Graphic representation of the cam for the four indicated points.



(b) Force and stiffness. The maximum displacement within the work range is $x_w = 80$ [mm], leading to a force range of $1.0 \leq f_w \leq 12.2$[N] and a stiffness range of $0.034 \leq k_w \leq 0.550 \left[\frac{\text{N}}{\text{mm}}\right]$.

Figure 4.5: Force and stiffness of the obtained LinWWC-SEA, pointing out four configurations within the work range

are respectively:

$$\begin{aligned} F_{in} &= 2f_w^{max} \\ M_{in} &= 2f_w^{max} h_w \end{aligned} \tag{4.11}$$

where h_w is the vertical distance between cables and slide.

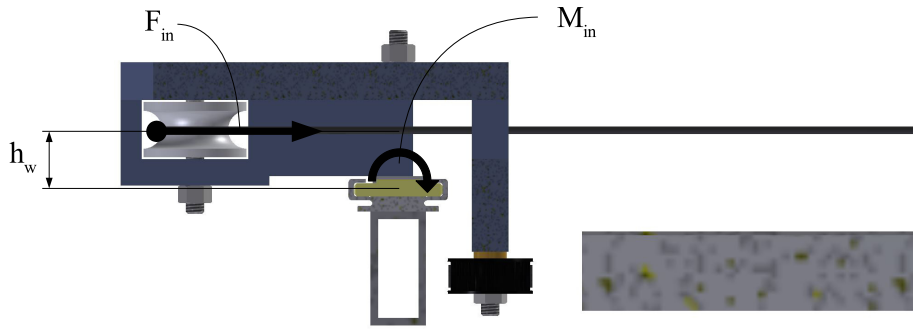


Figure 4.6: Effect of cable forces on carriages.

The structure itself is expected to bear the cable loads. A momentum is transferred from the carriages to the respective structural tubes, on which the linear guides are linked. The most critical condition (Fig. 4.7) is when the carriage is at the center of the guide, for which:

$$M_z = 2f_w^{max} \frac{l_{tube}}{2} \tag{4.12}$$

where M_z is the bending momentum and l_{tube} is the total length of the tube.

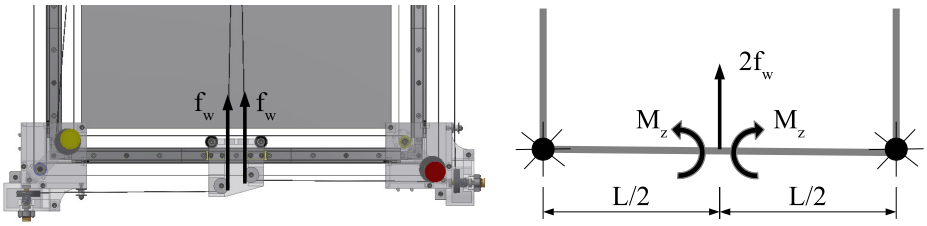


Figure 4.7: Effect of cable forces on the structural tubes.

4.2.5 Drum Height

The drums on which the wires wind up are a critical component of the design of the *PLANarm*. As a matter of fact, in order to guarantee a correct wrapping of the cable,

the fleet angle β at the detachment point from the groove has to be included in the range $-10° : 10°$. This angle depends on the vertical misalignment between the points A and B referring to Fig. 4.8. Depending on the amount of cable wrapped on the drum

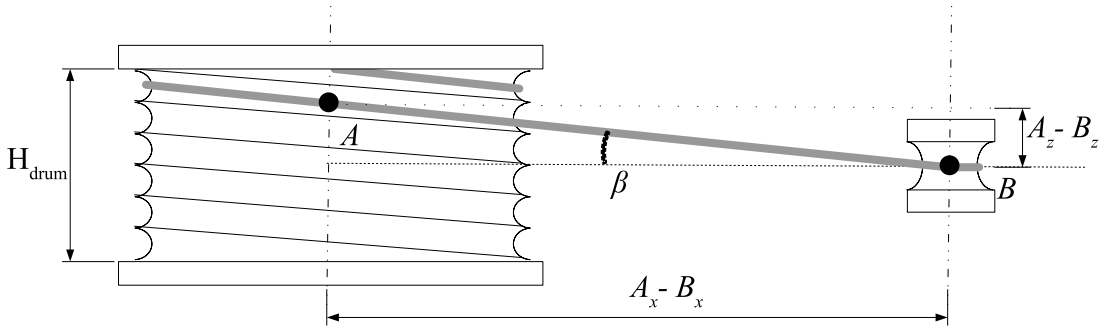


Figure 4.8: Schematic representation of the wire inclination.

and the distance between drum and carriage, β varies as follows:

$$\beta = \tan \frac{A_z - B_z}{A_x - B_x} \tag{4.13}$$

The highest value is achieved when the carriage is in the closest position w.r.t. to the drum and the cable is either fully wrapped or fully unwrapped, for which:

$$\beta = \tan \frac{(A_z - B_z)^{max}}{(A_x - B_x)^{min}} = \tan \frac{H_{drum}/2}{(A_x - B_x)^{min}} \tag{4.14}$$

where H_{drum} is the height of the drum. Therefore, in order to have $\beta < \beta^{max} = 10°$:

$$H_{drum}^{max} = 2(A_x - B_x)^{min} \arctan \beta^{max} \tag{4.15}$$

On the other hand, each drum is asked to guarantee enough windings to the wires. As shown in Fig. 4.9 each drum has to store about $2L$ of wire, where L is the width of the workspace, which, in terms on drum height, leads to a definition of a minimum value:

$$H_{drum}^{min} = p_{drum} n = p_{drum} \left(\frac{2L}{2\pi r_w} \right) \tag{4.16}$$

where p_{drum} is the pitch of the windings and n is the number of windings needed.

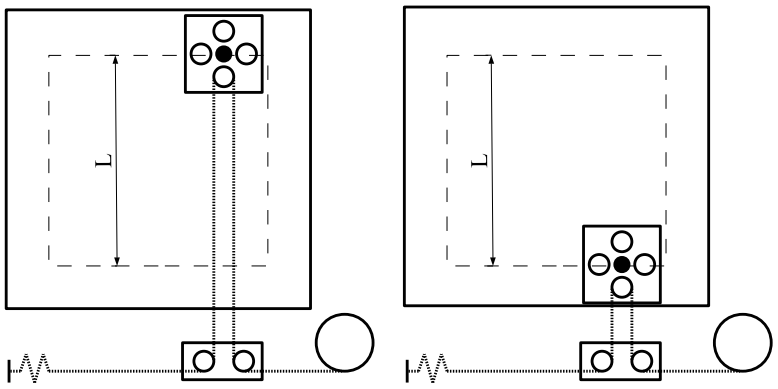


Figure 4.9: Position of the end-effector for totally unwrapped pulley and totally wrapped pulley.

4.2.6 Numeric Results

The summary of numeric values resulting from the calculations mentioned before are presented in Table 4.1

Table 4.1: Results for the design calculations.

$f_{m,i}^{max}$	$40[N]$	Ref. 4.1.2
$f_{w,i}^{0\,max}$	$12.2[N]$	Fig. 4.5
f_{w}^{max}	$22.2[N]$	Eq. (4.5)
k^{max}	$4.2[\frac{N}{mm}]$	Ref. 4.1.3
k_{w}^{max}	$0.525[\frac{N}{mm}]$	Eq. (4.7)
c_1	$8.75[mm]$	Eq. (3.38)
c_2	$0.2942[-]$	Eq. (3.37)
k_t	$38.755[\frac{N}{mm}]$	Eq. (4.8)
r_w	$22[mm]$	Ref. 4.3.3
τ	$488.4[Nmm]$	Eq. (4.9)
v_{m}^{max}	$40[mm/s]$	Ref. 4.2.3
ω	$3.63[rad/s]$	Eq. (4.10)
h_w	$15[mm]$	Fig. 4.6
F_{in}	$44.4[N]$	Eq. (4.11)
M_{in}	$666[Nmm]$	Eq. (4.11)
l_{tube}	$625[mm]$	Fig. 4.7
M_z	$13875[Nmm]$	Eq. (4.12)
β^{max}	$10°$	Ref. 4.2.5
$(A_x - B_x)^{min}$	$60[mm]$	Fig. 4.8
H_{drum}^{max}	$21[mm]$	Eq. (4.15)
p_{drum}	$2,3[mm]$	Ref. 4.3.3
L	$500[mm]$	Ref. 4.1.1
H_{drum}^{min}	$17[mm]$	Eq. (4.16)

4.3 Detailed Design

The whole architecture can be divided into the following six main elements:

Structure It is the framework on which everything is connected. It guarantees firmness, covers the moving parts from being in contact with the user and allows the stable placement of the device on a planar surface.

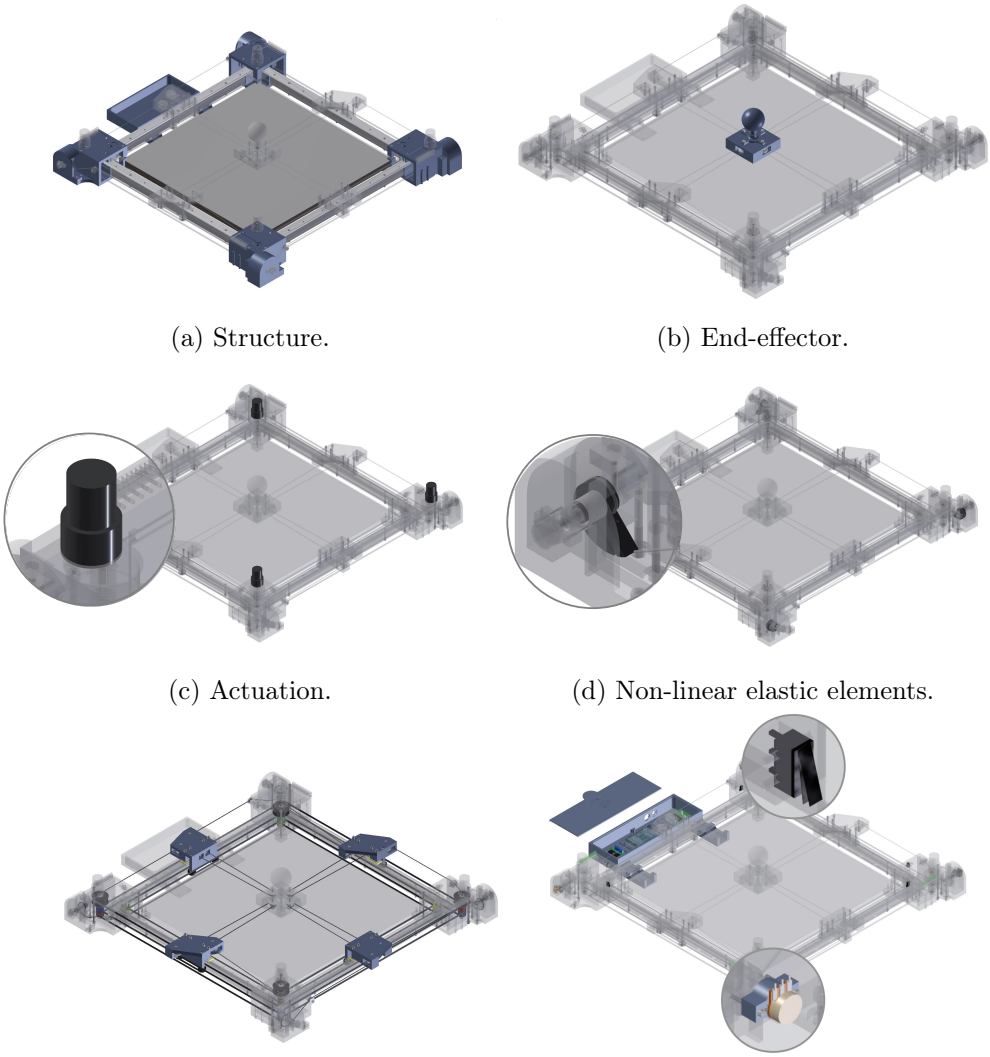
End-effector It is the terminal joint between the machine and the user. It moves in the two dimensional planar workspace and is connected to motors and cams through wires, as shown in Ref. 3.1.

Actuation It is composed by four motors. In combination with the cams, the actuators manage the behavior of the end-effector, in terms of position, movement and stiffness ellipse.

Non-linear elastic elements They are the only compliant part of the device, and are in charge of the adjustability of the device's stiffness. This elements interact with the end-effector and the motors through wires (Ref. 3.4).

Transmission system It is a system composed by belts, pulleys, shafts, wires and carriages. It allows to connect the end effector to the non-linear elements and the motors, in order to control position and stiffness of the end-effector, and to maintain the orthogonal arrangement of the architecture.

Hardware It is composed by sensors, drivers, controller board and cables. It is functional to give a feedback to the motors, in order to allow the execution of the rehabilitation exercises for which the device is designed.



(a) Structure.

(b) End-effector.

(c) Actuation.

(d) Non-linear elastic elements.

(e) Transmission system.

(f) Hardware.

Figure 4.10: Main elements of the *PLANarm*.

4.3.1 Structure

Tubes

Four tubes create the square main framework of the device. They are rectangular aluminum tubes, whose size, 30x15 [mm], is chosen in order to sustain the loads calculated previously in Ref. 4.2.4. Couples of L-shaped steel plates, make the connection between tubes and are also in charge of linking them to the corner boxes (Fig. 4.11). Four screws fasten the two plates. Each bottom plate has a threaded hole on which a leveling leg is installed. The overall device ends up being supported by four legs on the corners of the square framework.

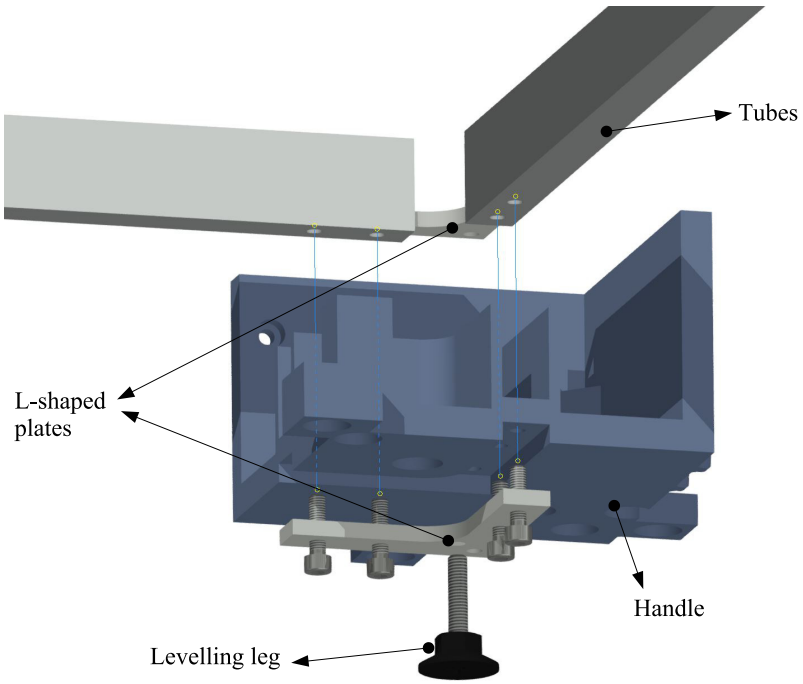


Figure 4.11: Tubes connection through L-shaped plates.

Corner Boxes

The corner boxes are 3D printed elements on which all the mechanical and electronic components are installed. Each corner box is designed to have two vertical shafts, one horizontal shaft, one actuator, two switches, one potentiometer, one connector and one corner of the plane. In order to allow easy mounting to installed parts, each corner box is made of 4 separated components (Fig. 4.12):

Ground element Directly connected to the tubes, the ground element is the main component of the corner box. The tubes, surrounded by a couple of thin walls, divide the inside into two areas, where two shafts with the related pulleys and belts are allocated. On the outside, the inner corner has a support for the main plane, the external sides are provided with a guide for the electric cable, a hole for the 5^{th} pulley of the wire circuit, a hole for a ball-bearing sustaining the cam

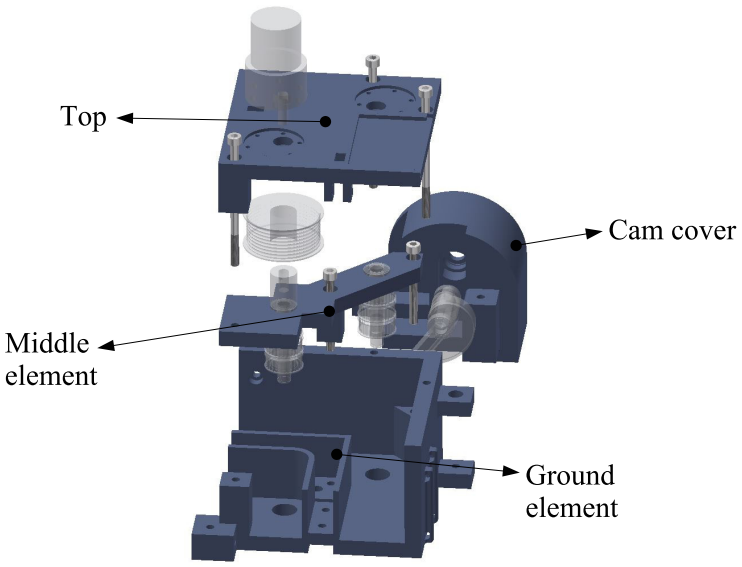


Figure 4.12: Exploded view of the corner box.

shaft and three flanges in charge of the connection with the cam cover. The middle element, the top and the cam-cover are linked to this first element, through bolted connections.

Middle element This second element is a diagonal platform in charge of giving an upper support to the two pulley-shafts. There are two holes, in charge of sustaining two ball bearings.

Top The top covers the previous two elements. It holds the actuator, two switches and a connector. It is designed to be assembled separately from the rest of the device in order to be easily plugged and unplugged. The position of the actuator is on the external corner, for two of the four boxes, and on the internal corner, for the remaining two. Although the design of the top elements is identical, with holes for both the external and internal configuration. The switches, whose function is to detect the contact of the carriages on the corner boxes, are installed on the sides. The connector, linked to the top through self-tapping screws, gather the wires belonging to motor and switches.

Cam-cover The cam-cover houses a ball bearing for the cam-shaft, a potentiometer and is in charge of grounding one extremity of the torsion spring to the structure.

Plane

The plane is a flat surface where the end-effector is supposed to slide. The plane is made of a single piece square plywood plate, on top of which a thin steel foil is glued. The foil is needed in order to have a ferromagnetic material on the plate, as the connection

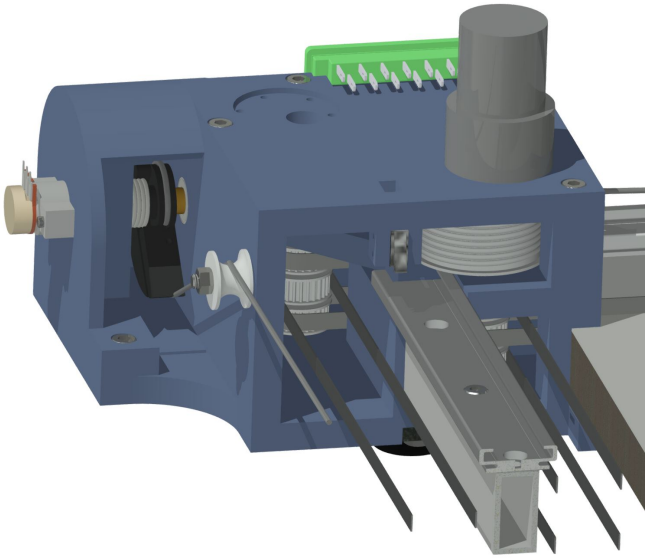


Figure 4.13: Assembled corner box.

between manipulandum and planar workspace is obtained through a magnet installed on the end-effector.

4.3.2 End-effector

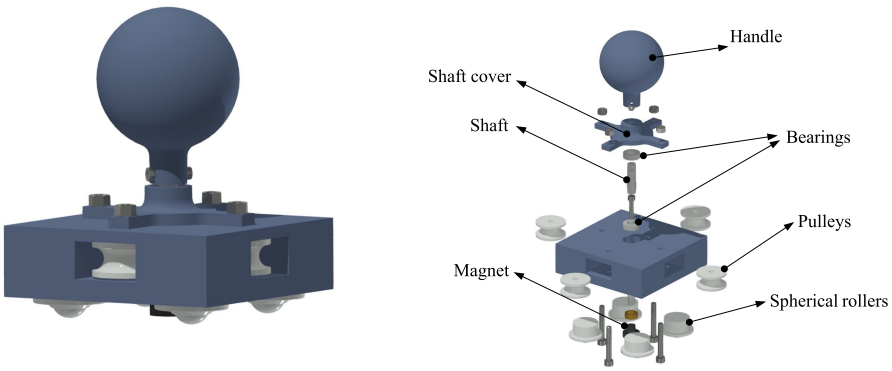


Figure 4.14: End-effector's elements.

It's two main functions are: to remain linked to the planar surface and to transfer forces coming from the wires to the hand of the user.

Platform

It is a 3D printed element, on which, on the surface facing the plane, four spherical rollers are installed, in order to allow movement on a planar surface. An important difference from the original arrangement (Fig. 3.1b). To assure the coplanarity of the pulling forces, the pulleys are not coaxial and are placed as depicted in Fig. 4.14.

A magnet is placed at the center of the inferior face. It's role is to guarantee an attractive force between the end-effector and the ferromagnetic surface on which it moves. It is important that the magnet stays as close as possible to the plane beneath, without touching it, as contact would introduce strong undesired disturbance due to friction. A simple regulating system, composed by a screw and a compression spring, allows to adjust the offset between magnet and surface. On the sides of the platform there are four rectangular holes in which wire pulleys are placed. The walls that surround the pulleys are intentionally very close to the borders. This guarantees that the wires remain on track, even if there was a loss of cable tension.

Handle

A revolute joint between platform and handle was introduced to avoid the transmission of torque, normal to the surface, from the patient's hand to the platform. The joint is obtained through a shaft linked to a couple of ball bearings. The first bearing is placed into a hole on the top surface of the platform, whilst the second is contained in a cover, that closes onto the platform. The shaft protrudes over the cover and has a through hole for the connection to the actual hand-grip. The hand-grip is spherical, a versatile shape in terms for variety of rehabilitation exercises.

4.3.3 Transmission System

The transmission system is the most complex part of the device. Its main functions are to connect the end-effector to the actuation and to allow the kinematic congruence presented in Ref. 3.1.

Wires

The wires transfer the force generated by the motors to the end effector and the cams. The chosen wire is a *dyneema*-sk78 rope with a diameter of 2[mm]. The *dyneema* is a fiber extremely resistant to traction. The combination of high resistance, great flexibility and low elongation makes this material perfect for this application. The high resistance allows to use a thin rope, which reduces the dimensions of pulleys. The breaking load is around 450[daN] way above the required resistance to traction (Ref. 4.2.1). The reason why this apparently excessive choice makes sense is that, cables are considered as infinitely rigid, and all the compliance is concentrated at the cams. Considering the extremely low elongation of this fiber (3.5% at break), on the operating conditions of the device, its behavior is essentially rigid. Steel cables would have been a valid alternative, but, a path that has steep curves and windings makes a *dyneema* rope a better solution, as it offers zero resistance to torque.

Pulleys

Pulleys guide each of the four ropes through their path depicted in Fig. 4.15.

Drums The drums, in order to maintain the kinematic congruence between the end effector and the carriages, have twice the diameter of the toothed pulleys that move the belts ($\oslash 22[mm]$). The geometry of the ellipsoid on which the wire winds up, has been defined w.r.t. standard values, to avoid the wire winding up on itself, which would result in a variation of the radius and consequently in the loss of

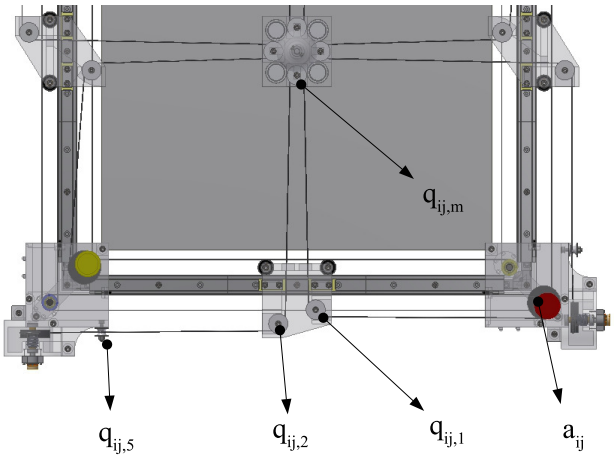


Figure 4.15: Disposition of the five pulleys for each cable circuit. The nomenclature refers to Fig. 3.3.

the kinematic congruency. The chosen value for the pitch is $p_{drum} = 2.3[mm]$, and drum height H_{drum} was determined considering the calculations previously presented (Ref. 4.2.5).

Pulleys The pulleys that guide the rope are produced by *Viadana* and are *delrin* pulleys designed for nautical use, with a preinstalled ball bearing. The fact that they come with their own bearing makes them a compact low friction element that is easy to assemble through a simple bolted connection.

Synchronous Belts

The synchronous belts are in charge of the movement of the carriages. They are T2.5x6[mm] polyurethane belts with a breaking load of 234[N]. It is a standard belt commonly used in transmission systems for 3D printers. The pulleys on which the belts are wrapped on are T2.5x28 flanged aluminum pulleys, with a $\oslash 11[mm]$. The size of the belts is chosen taking into consideration the traction force that the belts have to overcame while pulling the carriages. The main contribution to the forces that oppose the movement of the slides is friction. It is generated by the scrolling of slides on their guides and the rotation of bearings that sustain the shafts. A quantification of friction is hardly evaluable, as it depends not only on the components but also on the configuration. Therefore, maximum tension that the belts might receive is evaluated from another point of view. In the worst case scenario, in which friction between slides and guides tends to infinite, the carriages are stuck, and the motors apply their maximum torque trying to move them. The breaking load of the chosen belts is way above the maximum force that the motors are able to exert.

4.3.4 Belt-tensioning System

Once belts and pulleys are defined, a tensioning system is developed. The tensioning devices are responsible of three tasks:

1. Closing each belt once installed;

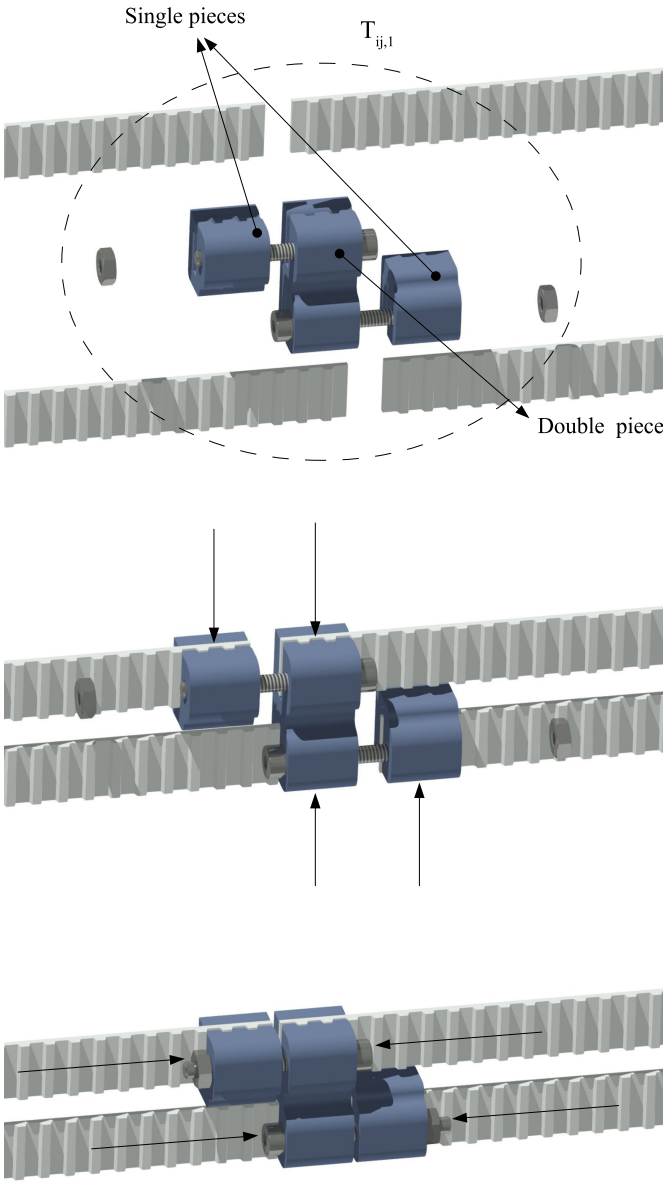


Figure 4.16: Tensioning system, for a generic $T_{ij,l}$.

2. Giving the needed tension to each belt;

3. Creating the connections $T_{ij,l}$ between belts, responsible of transferring motion to the carriages (Ref. 3.1)

An extremely compact 3D printed component is designed for this task (Fig: 4.16). It is made of two single sided pieces and a double sided piece. Each belt has one extremity clipped to a single piece and the other to the double piece. The piece-belt connection is obtained by simply inserting the belt in the cavity. The side facing the teeth of the pulleys has teeth itself, this prevents the belt to slip out when tensioned. Two screw allow to close and tighten the two belts separately.

Carriages

The carriages are the sliding elements that allow to the wires that connect motor, end-effector and elastic elements to remain orthogonally arranged. The carriages are four, and move onto linear guides on the four borders of the workspace. The translational joint is obtained through linear slides and guides produced by *Igus* (*drylin* N - Low profile linear guide system NK-02-27). The slides are linked to the carriages, and have to sustain the loads coming from the wires as previously presented in Ref. 4.2.4. As this slides are not designed to sustain normal torque w.r.t. the workspace, a configuration with two in-series slides for each carriage is adopted, in order to prevent the system to jam (Fig. 4.17).

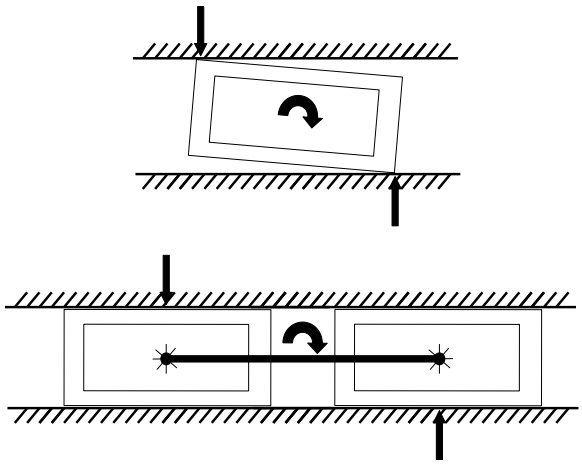


Figure 4.17: Carriage mounted on a single slide and on two in series slides.

Each carriage houses an internal synchronous belt. The two toothed belt pulleys and the wire-guiding pulleys are connected to the carriage through bolted connections. There are two different layouts for the carriages, in order to take in consideration the different geometry of the two belt circuits (Fig. 4.18).

For both of the layouts, the vertical distance h_w between wire pulleys and the contact surface of the slides is minimized, in order to reduce the inbound torque M_{in} caused by the tension of the wires.

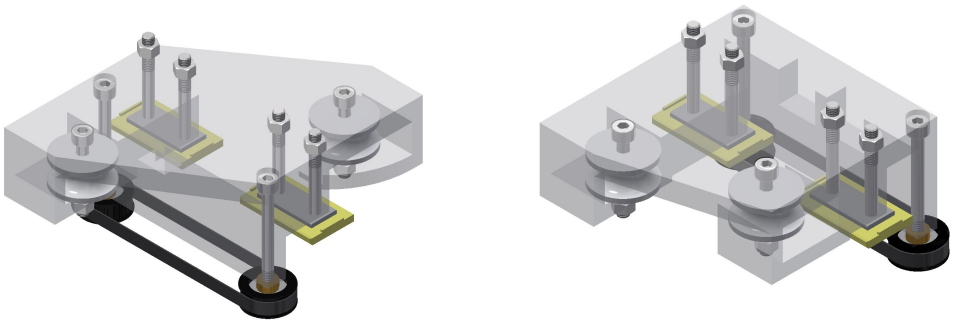


Figure 4.18: Two different carriage's layouts.

Shafts

There are two shafts for each of the four circuits of the device, one driven by a motor, and the other free-spinning. The actuated shafts are in charge of transferring torque from motors to wires and belts, whilst the free-spinning ones synchronize the movement of the belts. The complex mechanism of the device develops on four vertical layers, the first regarded to the wires, and the other three dedicated to belts. Therefore each actuated shaft has a top part, on which the drum is placed, and an inferior part in which three belt pulleys are housed. Similarly, the free-spinning shafts have only the inferior part, with the three belt pulleys. The actuated shafts are attached to the structure through a couple of ball bearings, as shown in Fig. 4.19. A seeger ring is in charge of sealing the shaft at the bottom. The top two belt pulleys are constrained through a set screw, the bottom one is free-spinning, through an inner ball bearing. This in-series bearings and pulleys are kept separated trough spacers. The top part, where the grooved pulley is housed, has a hole for the connection to the motor's shaft. A couple of set screws constrain the grooved pulley to the shaft and the shaft to the motor. The free-spinning shafts are almost identical to the actuated ones, the only differences are the absence of the drum in the top part, and the fact that the constrained pulleys are at the two bottom levels.

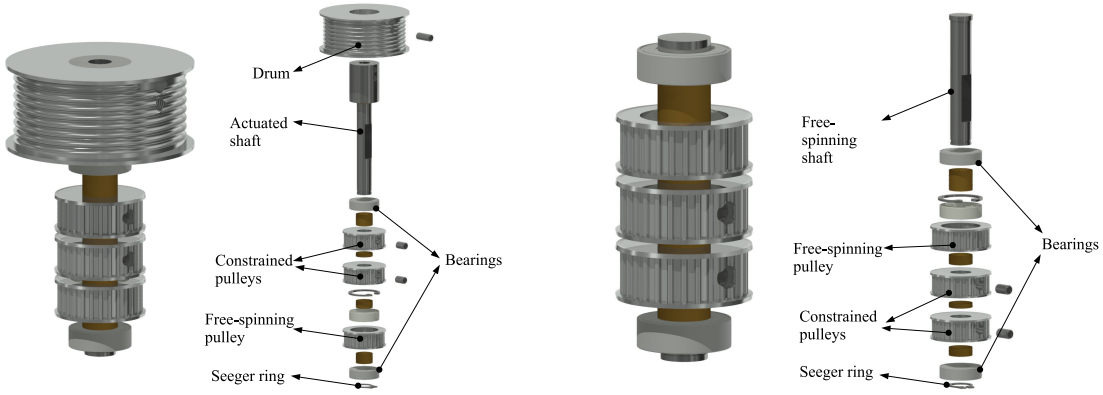


Figure 4.19: Actuated and free-spinning shafts.

4.3.5 Actuation

The actuation is composed by four DC motors *Pololu* 30:1 Metal Gearmotor 37Dx68L mm with 64 CPR Encoder. The chosen product has gearbox and encoder included. Model and gear are selected considering torque and speed requirements defined previously in Ref. 4.2.3, and lead to the choice of a 12V motor with 30:1 gear ratio. The connection to the framework is obtained through a dedicated flange on the top piece of the corner box.

4.3.6 Non-linear Elastic Elements

The elastic elements are composed by a torsion spring paired to a cam. Cam profile and spring characteristics have been defined in Ref. 4.2.2. Here the design of the cam system is presented:

Cam The cam's profile is obtained through 3D printing. On the external perimeter, a U shaped support prevents the wire to fall off the cam's profile. At the end of the profile there is a hole for inserting and blocking the extremity of the wire. An hexagonal cavity is in charge of connecting the cam to its shaft. The side facing the cover has an incision for one of the two legs of the spring (the second leg is grounded on the cam-cover).

Spring The spring is supplied by *Vanel*. The choice of the model is made considering both the requirements and the dimensional constraints of the spring's placing.

Shaft The shaft has an hexagonal profile at the center and cylindrical extremities. The hexagonal profile couples with the cam and the cylinders are connected to the bearings. A hole on the face oriented towards the extern is in charge of the connection to the potentiometer.

4.3.7 Hardware

The controlling system of the *PLANarm* requires potentiometers for the four cams, limit switches for the carriages, encoders for the motors and a controlling hardware composed by two motor-drivers and an *Arduino Due* board. A cable system is in charge of conducting information from the four corners to a box, linked to one of the bars. The single hardware components and their collocation in the device are here defined:

Potentiometers The potentiometers are in charge of measuring the rotation of the four cams. An *Alpha* 10kOhm linear rotary potentiometer is chosen. Its connection, shown in Fig. 4.21, is obtained through a plastic support, that links the stator to the cam-cover. When the support is installed, the rotor of the potentiometer is integral to the cam-shaft.

Encoders The encoders read the rotation of the motors. The *Pololu* motors chosen for the *PLANarm* are already provided with encoders, therefore no additional elements are required.

Limit switches As the motor encoders are incremental, a calibration of the position is required. Four pairs of limit switches are installed on the sides of the corner boxes

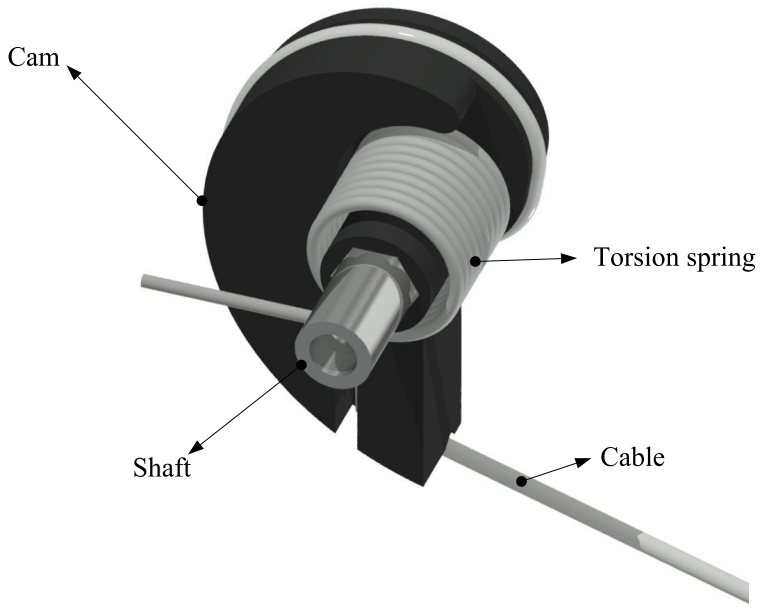


Figure 4.20: Assembled cam.

facing the carriages. The switches are triggered when the side surfaces of the carriages hit the corner boxes. The switches used are *Panasonic* AH1462619-A.

Box The box contains the *Arduino* and the two motor-drivers. It is a 3D printed component (Fig. 4.22), installed on one of the lateral tubes and the wooden plate. In order to avoid overheating, the inferior surface of the box is open-work and the two motor-drivers and the *Arduino* are installed on dedicated raised supports. The cables coming from the inferior surface of the plane are conveyed into the box through two holes. The front face of the box houses a *USB 2.0* plug and an electric socket. A thin panel covers the box, to protect the electric contacts.

Motor-drivers The motor-drivers are *Pololu* Dual VNH2SP30. They are in charge of feeding the correct tension to the motors, based on the information elaborated by the *Arduino*. Each board can manage up to two motors, therefore two drivers are needed for the *PLANarm*.

Arduino Due The *Arduino Due* is an open source micro-controller board. It has 54 I/O digital ports and 12 analog inputs. There is an *USB* port to connect the board to a computer.

Cables route There are 13 cables for each of the four corners of the device: 6 regarding the motor, 3 for the potentiometer, 2 for each of the two limit switches. From the four corners, the cables are conveyed to the box passing beneath the plane (Fig. 4.23). There is a connector on each of the four tops, in charge of separating each route into two parts. The first, integral to the main structure, conveys the 13 cables from the corner ground elements to the box. The second, in-built on the top element, distributes the 13 wires to motor and sensors. This configuration allows to easily remove the top by simply unplugging the connector, without

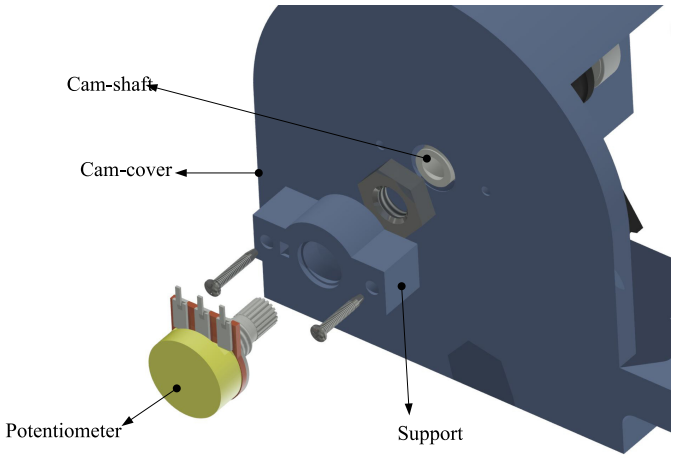


Figure 4.21: Exploded view of the potentiometer's connection.

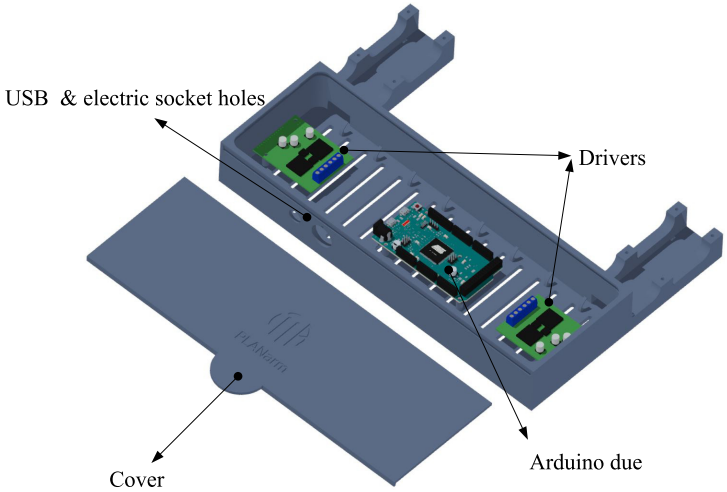


Figure 4.22: Hardware box.

being forced to disconnect the single contacts. The connectors used are *Phoenix* Contact DFK-MC 1,5/16-GF-3,81.

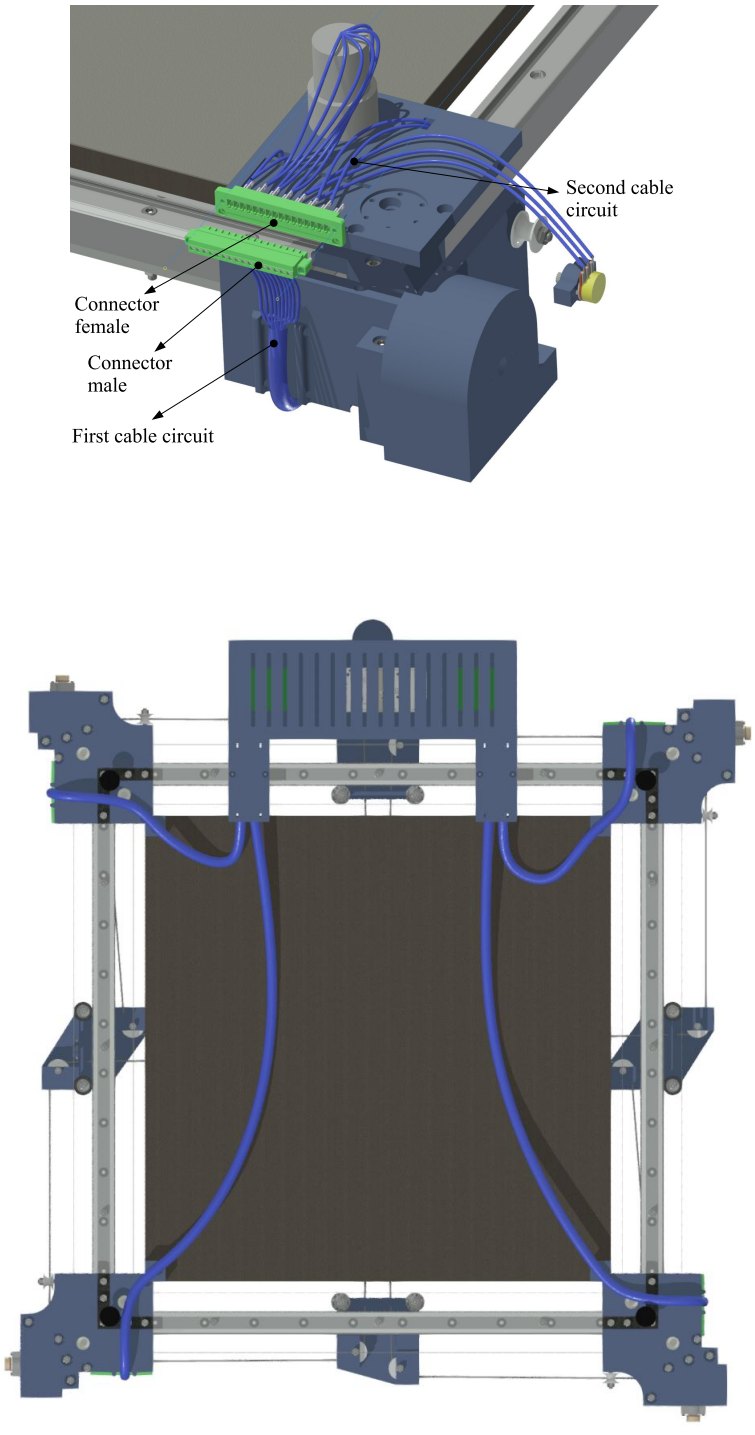


Figure 4.23: Cable circuit.

Chapter 5

Prototype Development

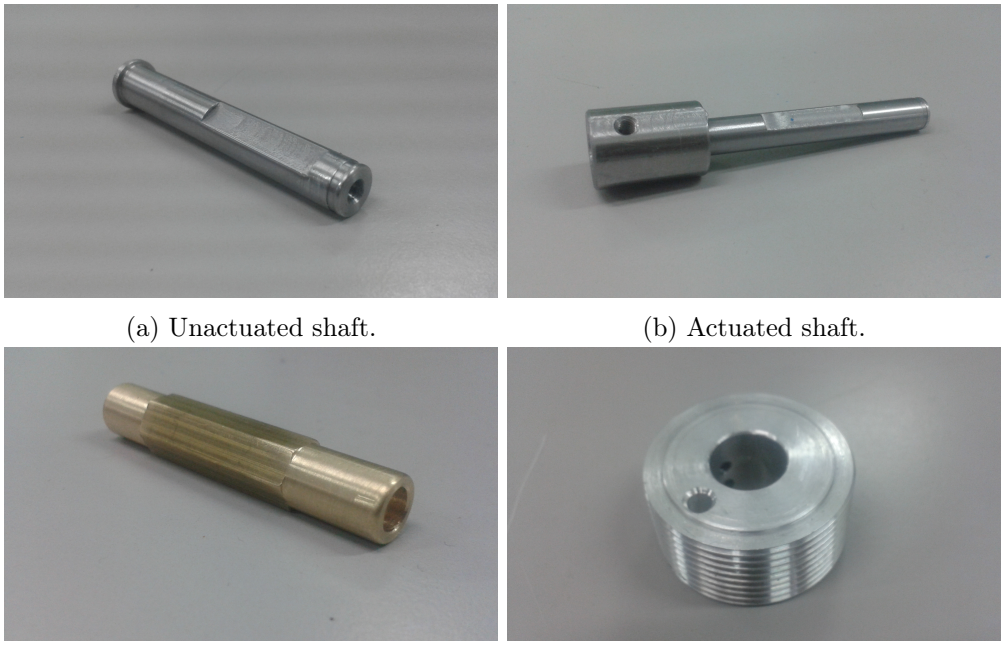
5.1 Purchased Elements

Most of the components used in the *PLANarm* are purchased in locals stores located in Lombardy, Italy. A list of this elements and their costs is presented in Table 5.1.

Table 5.1: List of purchased elements.

Element	**Brand**	**Quantity**	**Unit Price**	**Total Price**
Mechanical Elements				
Bearings	Misumi	40	€1.98	€79.20
Torsion Springs	Vanel	4	€3.00	€12.00
Synchronic Pulley	RS	32	€7.14	€228.48
Belt	GTC	18 [m]	€3.20	€57.60
Wire Pulley 1	Viadana	16	€5.33	€85.28
Wire Pulley 2	Viadana	4	€4.40	€17.60
Wire	Dyneema	10 [m]	€1.24	€12.42
Linear Guide	Igus	4	€13.74	€54.96
Linear Carriage	Igus	8	€3.31	€26.48
Foot	Nu-Tech	4	€2.84	€11.37
Magnets	Eclipse	2	€3.80	€7.60
Rotational Motor DC	Pololu	4	€37.82	€151.28
			Sub-Total	**€744.27**
Electronic Elements				
Arduino Due	Arduino	1	€42.70	€42.70
Motor Driver Shiled	Pololu	2	€49.70	€99.40
Potentiometer	Alpha	8	€1.01	€8.08
Limit Switch	Panasonic	8	€1.34	€10.72
16 Pin Male Conector	Phoenix	4	€10.04	€40.16
16 Pin Female Conector	Phoenix	4	€16.78	€67.12
3 Poles BF Male Conector	-	1	€5.83	€5.83
3 Poles BF Female Conector	-	1	€5.83	€5.83
Female USB Conector	-	1	€13.19	€13.19
			Sub-Total	**€293.03**
TOTAL €1037.30				

5.2 Manufacturing



(a) Unactuated shaft. (b) Actuated shaft.

(c) Cam's shaft. (d) Drum.

Figure 5.1: Overview of parts obtained through mechanical processing.

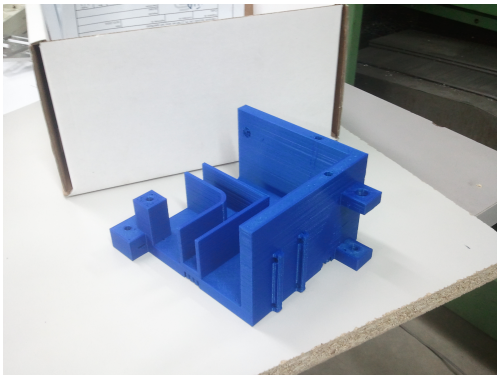
The components of the *PLANarm* which were not purchased are manufactured with the technologies available at *CNR*'s workshop. Metal elements are obtained through standard mechanical processing and plastic components are achieved through FDM. Shafts, L-shaped plates and drums are obtained through turning and milling operations (Fig. 5.1). The materials used for this elements are steel or brass, depending on the mechanical function of each component and the difficulty of the mechanical processing of its production. Some of the purchased elements also require mechanized operation to correctly couple with the other elements of the device. In particular the structural aluminum tubes are drilled to be screwed with the linear guides and the belt pulleys are mechanized to fit in the shafts.

On the other hand, complicate-shaped parts, such as corner boxes, end-effector and cams, are manufactured exploiting FDM, a 3D printing technology that is worth deeper explanation, given in the following section.

5.2.1 3D Printed Elements

The plastic elements of the device are obtained through FDM, a very commonly used technique in rapid prototyping [51]. This technology allows to design and produce parts with complicated features and shapes, which would be arduous to manufacture with traditional mechanized processes. Examples of pieces manufactured with this technology are presented in Fig. 5.2.

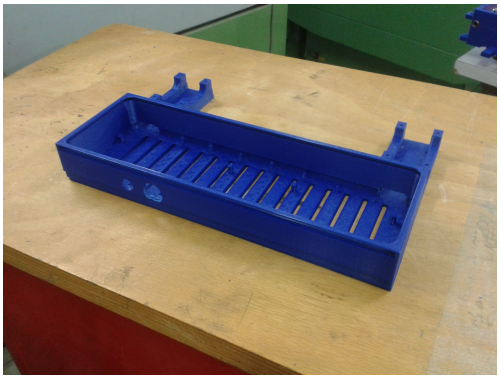
The operations needed for the production of each component, starting from the CAD drawing, are:



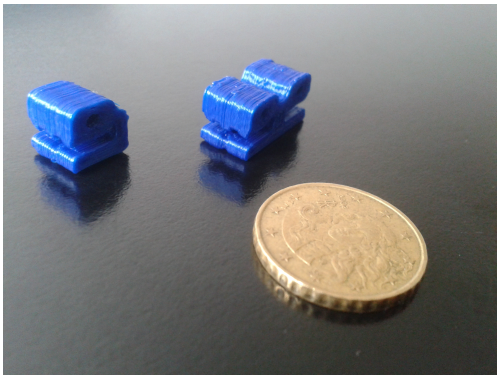
(a) Ground element of the corner box.



(b) Cam.



(c) Hardware box.



(d) Belt tensioning system.

Figure 5.2: Overview of pieces obtained through 3D printing.

1. The CAD file of the component, designed with *Inventor*, is exported to *.stl* format (Fig. 5.3b). The *.stl*, a mesh based file format, contains only the information regarding the shape of the component, and it is defined by a mesh of triangular planar surfaces. In the conversion to *.stl*, mathematical and geometric information is lost, therefore, once it is exported, the file is not editable.

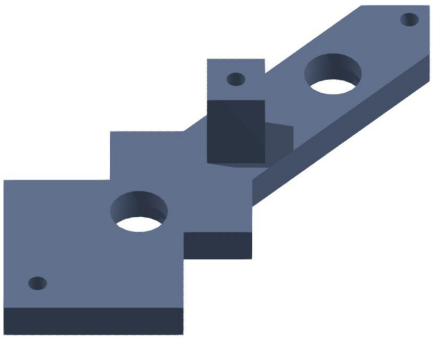
2. Through a dedicated open source software (*Slic3r*), extruder speed, outline rounds, filling density, supports, among other settings, are defined (Fig. 5.3c) . From the *.stl*, a *.gcode* file containing information regarding the extruder's path is obtained.

3. The *.gcode* is downloaded on the printer that produces the component. The printing process consists of the deposition of successive layers of fused plastic filament, that creates the shape of the component. The filament is heated and extruded, and, as soon as it reaches the surface of the previous layer, it solidifies.

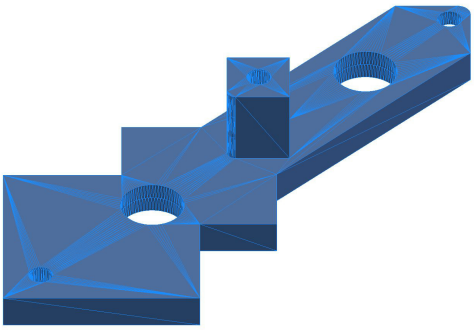
4. At the end of the printing process, eventual supports are manually removed and the component is complete.

Any shape can be easily achieved with this 3D printing process, but few important aspects that need particular attention are to be evaluated singularly for each component:

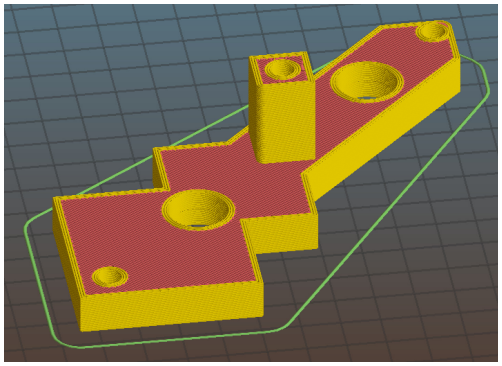
- Depending on the structural function of each component, number of layers for



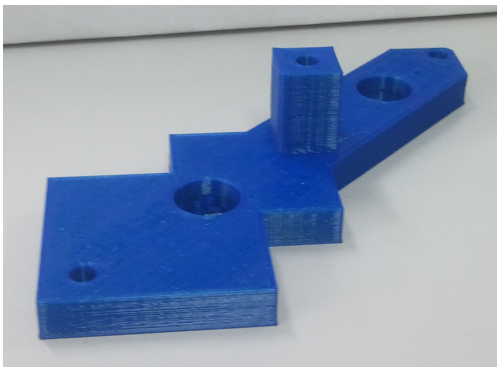
(a) CAD model in *.ipt* fomat.



(b) CAD model in *.stl* format.



(c) *Slic3r*'s interface for generating the *.gcode*.



(d) 3D printed component.

Figure 5.3: Phases of the 3D printing process.

the external surfaces, outline rounds and infill are set. High density guarantees solidity to the parts, but increases the manufacturing time.

- The orientation of the components during the printing process is defined in order to have a steady surface, from which printing the entire element, and minimizing the number of supports. In fact, considering that the printer creates the final shape through successive vertical layers, overhang features require sustaining supports to be built (Fig. 5.4). Where possible, an orientation of the component that reduces the number of supports is preferable, as extra supports result in material waste and additional working time.

- The finished components tend to have incorrect dimensions w.r.t. the CAD model. Exterior borders tend to be thicker than the nominal value, which happens to be an issue for those features that regard coupling with other elements. Therefore, to compensate this effect, corrections on the original CAD model, such as enlarging holes, are necessary.

All the elements considered for the *PLANarm* were manufactured in *ITIA's* laboratories, hence the cost of material, man-hours and machine-hours is not considered as a cost in this specific project. Nevertheless, and only for illustrative motives, the esti-

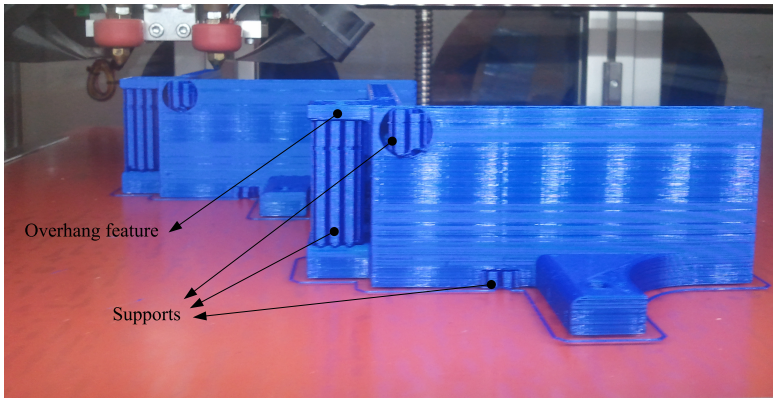


Figure 5.4: Component with overhang features and respective supports.

Table 5.2: List of elements manufactured with FDM, considering a commercial price of 0.3 €/cm^3.

Element	**Part Number**	**Quantity**	**Volume [cm^3]**	**Cost**
Corner Box - Base	00001	4	340.14	€408.17
Corner Box - Middle	00002	4	131.20	€157.44
Corner Box - Cover	00003	4	47.32	€56.78
Carriage 0	00005	2	197.21	€118.33
Carriage 1	00006	2	184.57	€110.74
Cam	00021	4	10.10	€12.12
Cam Cover	00004	4	158.51	€190.21
End Effector - Base	00007	1	204.52	€61.36
End Effector - Middle	00008	1	10.98	€3.29
End Effector - Grip	00028	1	15.32	€34.60
Electronics - Box	00018	1	479.41	€143.82
Electronics - Cover	00052	1	126.29	€37.89
TOTAL €1334.75				

mated cost of every printed element is presented in Table 5.2, considering a commercial price of 0.3 €/cm^3.

5.3 Mounting

The mounting of the *PLANarm* is a delicate part of the realization. The complex architecture of the device and the presence of multiple concatenated moving parts required a well designed assembling procedure in which single steps are to be respected.

1. In a first phase, the ball bearings are installed on the corner elements and the end effector. The holes are manually re-drilled to remove eventual imperfections on the surface and, afterwards, the bearings are placed (Fig. 5.5a and 5.5b).

2. In a second phase, the main framework is mounted. The four tubes are connected to the four top L-shaped plates, forming a square element. The four corners of this square are then inserted in the ground elements of the corner box, on the bottom of which inferior L-plates are attached. Screws are then fastened to the top L-plates from the bottom, closing the main framework.

3. Then the carriages are assembled. On each of them the two wire pulleys, the slides and the toothed pulleys are mounted. Afterwards, the carriages with the slides are inserted in the guides, and the guides are screwed to the four tubes (Fig. 5.5c).

4. The shafts are then mounted: on each of them the top ball bearing installed to the middle element, the series of pulleys and spacers are assembled. Then the shafts are mounted on the bearing already installed in the ground corner element. A seeger ring closes the shafts on the structure. The bolted connection between middle and ground element of the corner box is then fastened and afterwards, the drums are coupled with the actuated shafts (Fig. 5.5d and 5.5e).

5. At this point the belt system is assembled. The open belts are singularly closed, tensioned and connected as explained in Ref. 3.1, through the tensioning and connecting system presented in Ref. 4.3.4. Particular attention is needed in this phase, since the connection between the different levels has to be perfectly centered to guarantee the proper excursion to the inner belts (Fig. 5.5f and 5.5g).

6. The wooden plane is glued to the steel foil, and then fastened to the four corners. The end effector is then assembled: the magnet, the rollers, and the free spinning shaft are installed (Fig. 5.5h). The wire pulleys are initially kept apart, as, when closing the wire system, they are the last element to be connected.

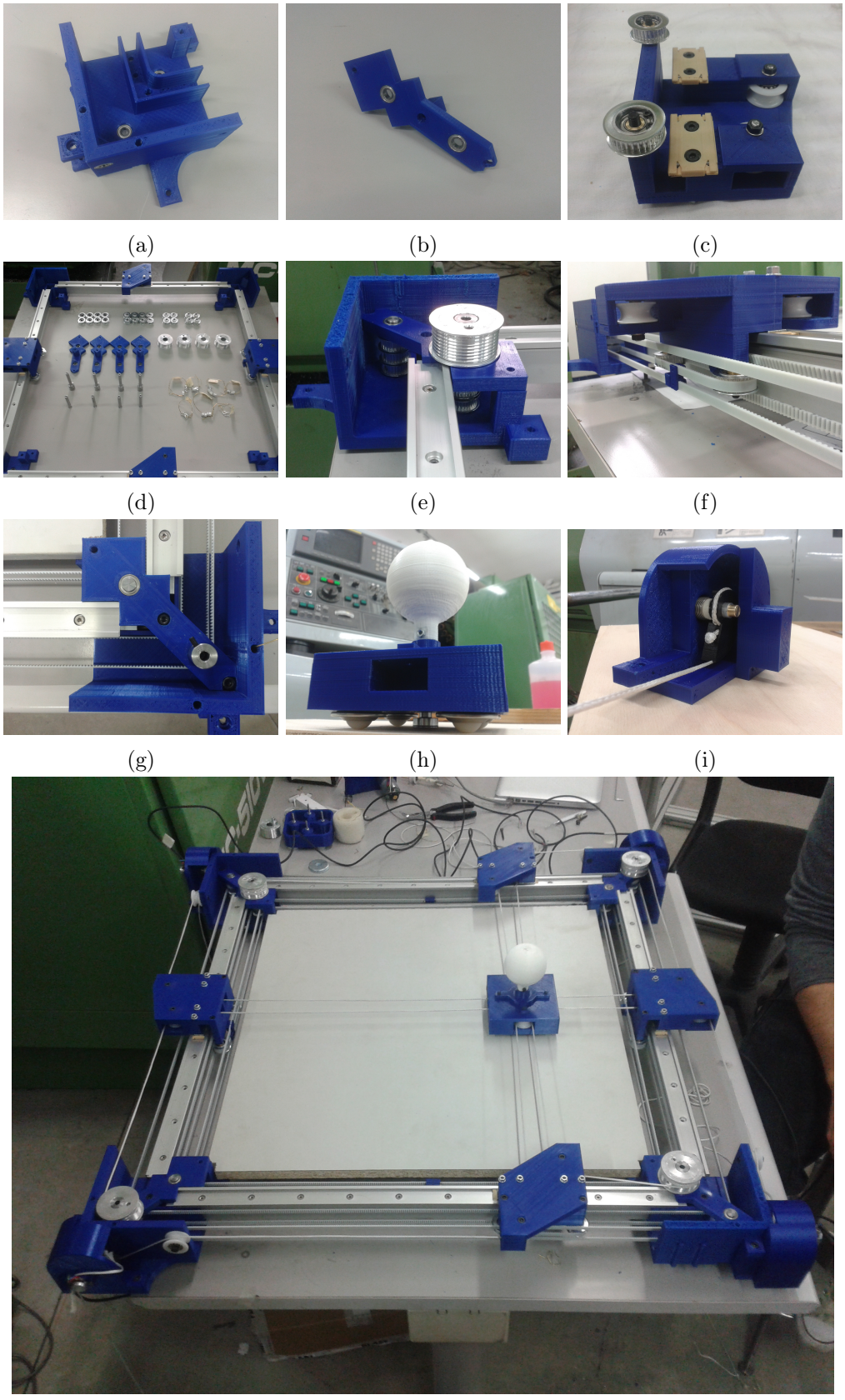
7. The wire system is then mounted. For each circuit, one extremity is first wrapped on the drum, conducted around the pulleys and finally rolled and fixed to the cam (Fig. 5.5i). Afterwards the cam with the shaft, the springs and the wire are installed on the corner element. This operation is done by first inserting the shaft in the cam-cover, with the spring positioned in its respective placing, then the cover is closed on the corner box. At last, the four wire pulleys of the end effector are installed (Fig. 5.5j).

8. At this point, the top elements and the electric components are assembled. Motors, sensors and connectors are installed with their respective electric cables. The box containing the boards and the sockets is assembled and properly cabled.

9. The hardware box is then attached to the framework and the cables, coming out of it, are sent to the four corners where they are linked to the plug of the connector. The four tops are installed on the corner boxes and finally a set screw for the motor-to shaft connection is placed.

10. Finally, the connectors, the usb interface and the alimentation cable are plugged in.

At the current state, the mountain phases have reached the 7th step, as it is shown in Fig. 5.5j.



(a) (b) (c)

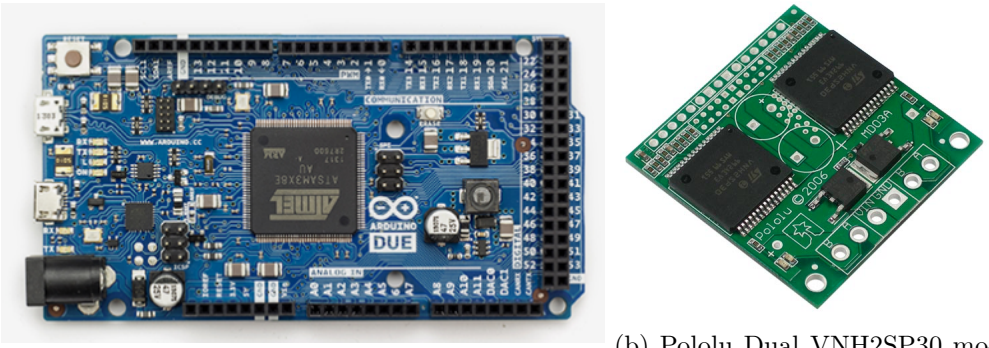
(d) (e) (f)

(g) (h) (i)

(j)

Figure 5.5: Assembly phases.

5.4 Electronic Connections



(a) *Arduino Due* micro-controller

(b) Pololu Dual VNH2SP30 motor driver

Figure 5.6: Electronic boards included in the *PLANarm*

The electronic hardware includes an *Arduino Due* micro-controller in charge of the low-lever control, and two motor-drivers that drive the four actuators (Fig. 5.6). The *Arduino Due* is a micro-controller based on the *Atmel* SAM3X8E ARM Cortex-M3 CPU [52]. It has 54 digital input/output pins, of which 12 a be used as PWM outputs, and 12 analog inputs. Like other devices created at *CNR*, the real-time software is planned to be programmed in C++, which gives a software abstraction oh the *PLANarm* physical elements, as motors, encoders, cams, among others. The motor-drivers are two *Pololu* Dual VNH2SP30 Motor Driver Carrier MD03A [53].

Depicted in Fig. 5.7, the electronic scheme shows all the electronics components and the connections required to properly command the robot. The *Arduino* is connected to a computer with a micro-USB cable, to obtain the information from the high-level control.

The *Arduino* and both motor-drivers are connected to a 12[V] power supply, that is also necessary to power the actuators. A single motor-driver is in charge of commanding two motors, and receives the information from the *Arduino* through six digital inputs (three for each motor). The velocity information is sent through a pulse-width modulation signal (PWM), and two additional digital inputs command the rotation direction.

The *Arduino* reads the necessary information from different sensors. Each motor bears an encoder that reads the angular position, with a resolution of 1920 counts for revolution. The signal is sent to a digital input in the *Arduino*. Eight switches are positioned at the dead-end of the carriage's guides. They send the signal when the carriage reaches the maximum movement range, and are used to implement the zeroing procedure. The digital signal is sent to a digital input in the *Arduino*. To read the rotation of the cam, four potentiometers are included, each of which reads the rotation of a single cam, and sends an analog signal to the *Arduino*.

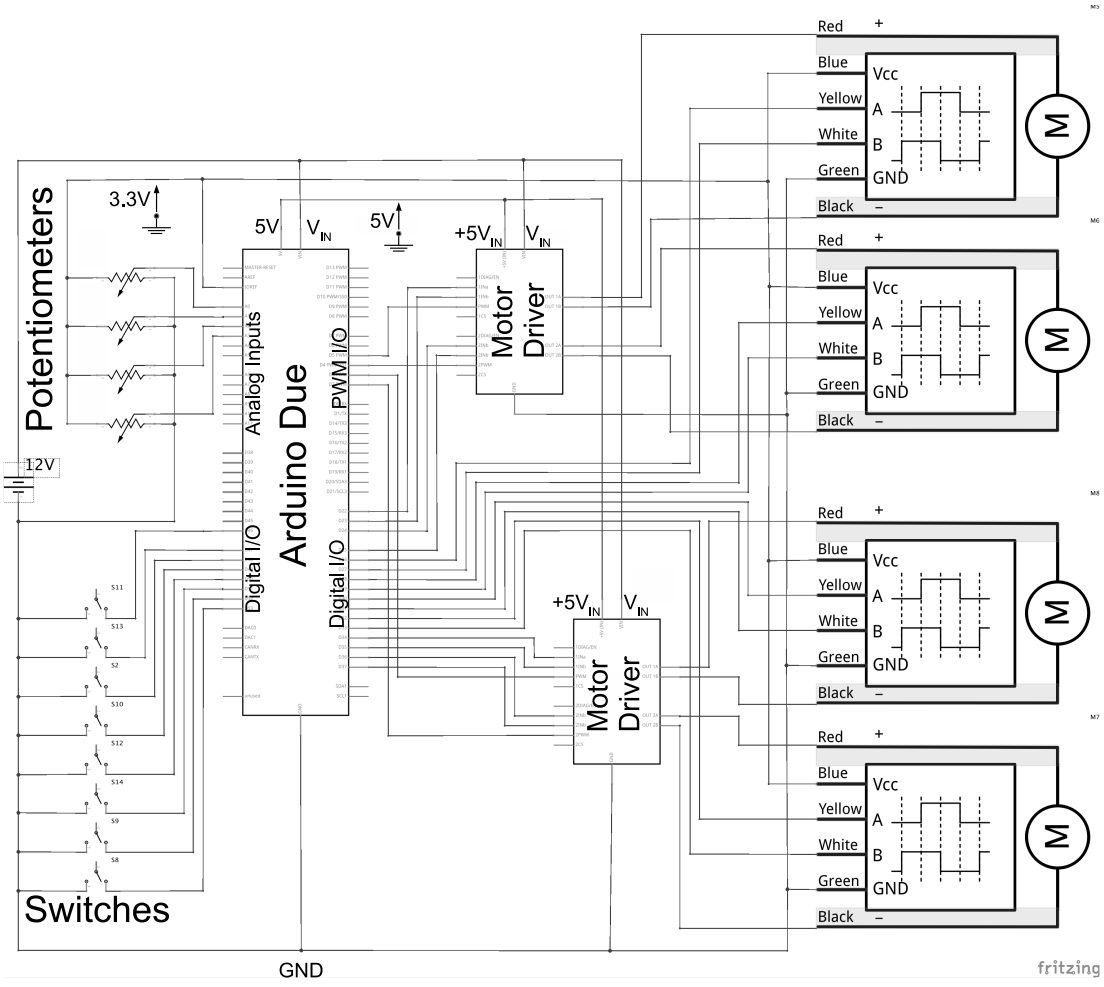


Figure 5.7: Electronic scheme of the *PLANarm*.

5.5 Control Architecture

The control of rehabilitation robots is usually defined in two levels. The high level is in charge of the interface between the patient, the therapist and the device. It includes an user interface for the therapist and for the patient, with graphical or numerical feedback, and fundamentally provides the low level control with the information to correctly command the actuators of the device, regarding the type of exercise set by the therapist.

The low level control directly commands the actuators to achieve the required performance provided by the high level control. In this section, a description of the low level control system is presented. The definition of a high level control is left to further studies and was not a topic of this work.

The device is asked to: set equilibrium position M_{eq}, set stiffness at the equilibrium (k_x^0, k_y^0), and read the external force $\mathbf{f}_m$. These three parameters are determined by the joints position θ_{ij} and two independent variables δ_i and ξ_i that define the force and stiffness condition for a single VSA_i (Ref. 3.4). Let us define the reference initial position in which $M_{eq} = (0, 0)$, and both VSAs are at minimal stiffness configuration, for which $(\delta_0, \delta_1) = (0, 0)$. In this configuration the joint coordinates θ_{ij} are arbitrary set to 0. The relation between θ_{ij} and M_{eq} is shown in the following equation:

$$\mathbf{M_{eq}} = \left[\frac{r_w}{4}(\theta_{00} - \theta_{01}), \frac{r_w}{4}(\theta_{10} - \theta_{11})\right]^T \tag{5.1}$$

The stiffness and force produced by a single VSA are obtained from δ and ξ as explained in Ref. 3.4. In the orthogonal configuration with two VSAs working together, the coupling effect presented in eq. (3.13) causes the resulting force and stiffness to be conditioned by a larger amount of parameters:

$$\begin{aligned} \mathbf{f} &= \mathbf{f}(\delta_0, \delta_1, \xi_0, \xi_1, M_{eq}) \\ k &= k(\delta_0, \delta_1, \xi_0, \xi_1, M_{eq}) \end{aligned} \tag{5.2}$$

Based on eq. (3.40) and considering the reference values introduced through the zeroing procedure, for a single VSA_i:

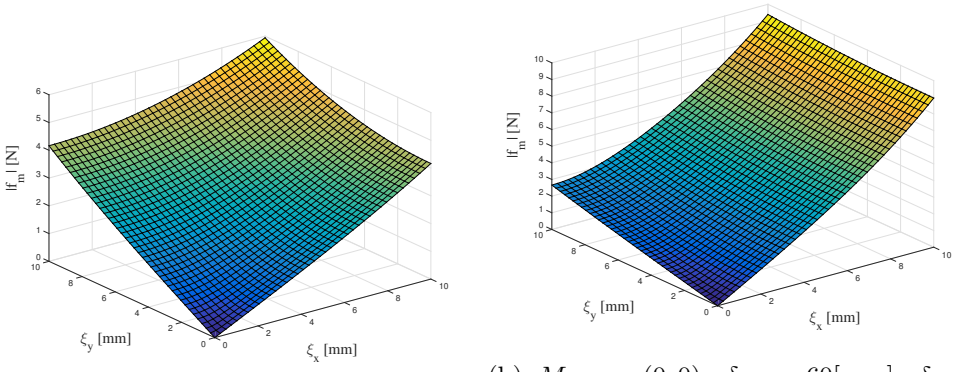
$$\begin{aligned} \delta_i &= \frac{r_w(\theta_{i0} + \theta_{i1})}{2} \\ \xi_i &= \Delta M_i \end{aligned} \tag{5.3}$$

Hence, by knowing all the dimensions and stiffness characteristics of the device, the force and stiffness can be calculated for every value of δ_i, ξ_i and M_{eq} for $i \in \{0, 1\}$. The mapping of the values is done offline to be stored and used during real-time feedback control. The graphs in Fig. 5.8 shown the external force as function of ξ_0 and ξ_1 for two arbitrary conditions. It can be also mapped for any combination of δ_0, δ_1 and M_{eq}.

5.5.1 Feedback Information

As just presented, in order to obtain δ, ξ and M_{eq}, information regarding, ΔM and θ_{ij} is needed.

- The rotation θ is read through the encoders installed on the motors. Although, as the encoders are incremental, a zeroing system which exploits the switches on the four corners of the device is introduced.



(a) $M_{eq} = (0, 0)$, $\delta_0 = \delta_1 = 40[mm]$.

(b) $M_{eq} = (0, 0)$, $\delta_0 = 60[mm]$, $\delta_1 = 20[mm]$.

Figure 5.8: External force mapping.

- ΔM is obtained through potentiometers on the cams. The potentiometers read the rotation γ_{ij} based on which it is possible to obtain ΔM. As an external force produces an unknown ΔM on the end-effector, the amount of wire $x_{w,ij}$ wrapped on the four cams varies, modifying the value of $\gamma i0$ and γ_{i1}. Known the dependency between γ and x_w (Ref. 3.3) it is possible to read ΔM from γ.

5.5.2 Control Strategies

5.5.3 Open-loop Control

A first mode, based on an open-loop control system, allows to reach a certain condition, regardless of external perturbations. It allows to perform passive rehabilitation exercises where a trajectory $M_{eq,ref}$ and a stiffness condition $(k_x^0, k_y^0)_{ref}$ are set, and the device drags the patient's arm through the workspace. When working in this mode, no information regarding the interaction between patient and machine is read by the controlling system. Although, due to the presence of physically compliant elements between actuators and end-effector, the user-robot interface is intrinsically safe. For each module, given a target equilibrium position $M_{eq,ref}$ and stiffness values $(k_x^0, k_y^0)_{ref}$, the corresponding values for the rotations of the four actuators $\theta_{ij,ref}$ are certainly determined. In Fig. 5.9 a scheme of this control architecture is shown. Reference values are set and reached controlling the four actuators in position. An inner PID loop is used for the position control of the actuators. In this inner PID controllers, information regarding θ_{i0} andθ_{i1} are given through the encoders installed on the motors.

5.5.4 Closed-loop Control

A second type of low level control is an admittance control-loop. Actively controlled rehabilitation exercises can be performed with this control strategy. Given a task to the patient, such as reaching a certain point on the workspace, the device opposes a force to the arm movement.

When working in this mode, stiffness is set at a reference value, and the admittance control imposes a velocity of:

$$\dot{M}_{eq} = c_a f_m \tag{5.4}$$

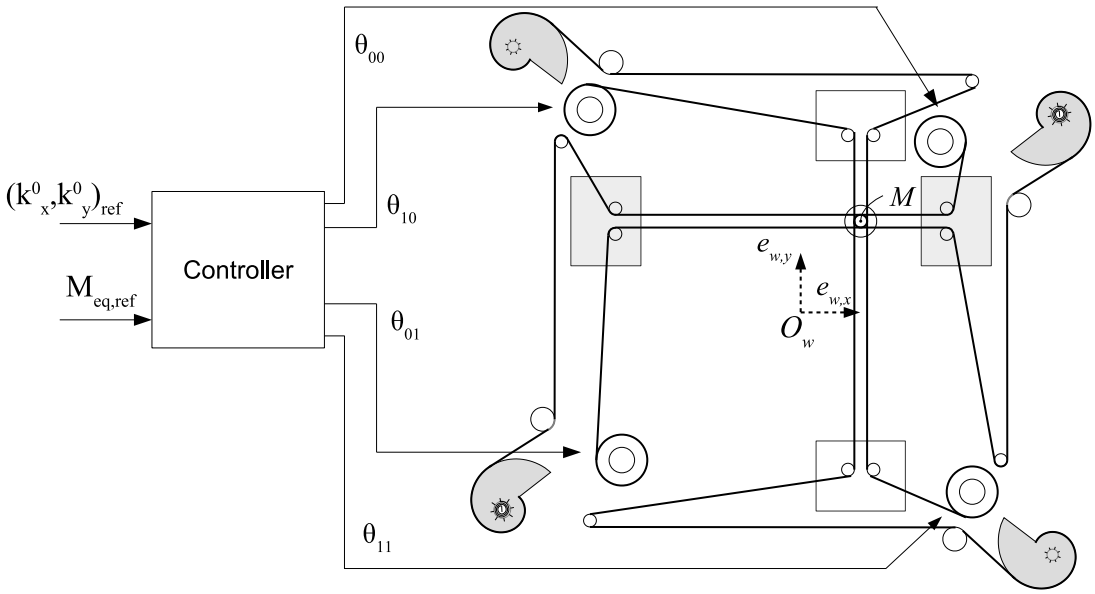


Figure 5.9: Scheme of the open-loop control.

where c_a is an arbitrary gain and f_m is the external force exerted by the patient. The stiffness value univocally defines the relation between f_m and ΔM, which is obtained by reading γ_{ij} (Ref. 5.5.1). As the actuators are controlled in position, velocity is integrated in time, as shown in Fig. 5.10. By setting the value of c_a, it possible to regulate the degree of resistance opposed by the device. For a high value of c_a, the device reacts with a high velocity which leads to a smooth perception of the movement. On the other hand, low values of c_a causes low velocity and the perception of a big force opposing the movement.

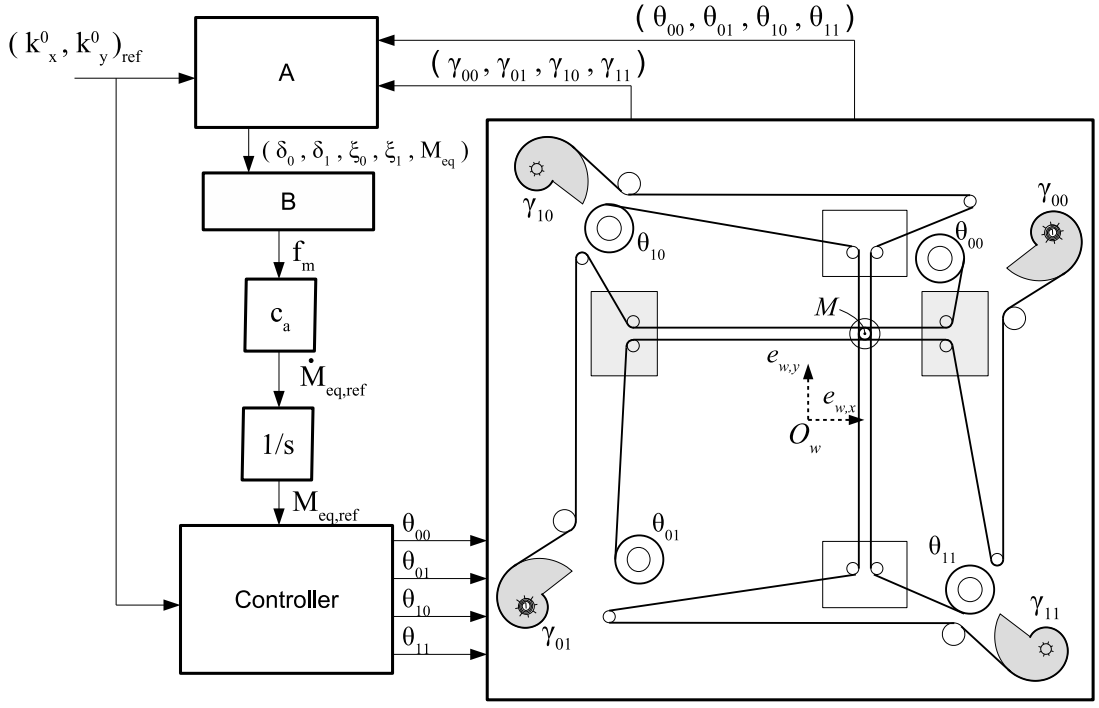


Figure 5.10: Scheme of the closed-loop control.

5.6 Experimental Testing

An experimental setup is configured in order to have a validation of the kinetostatic behavior of the device, w.r.t. the theoretical considerations described in Ref. 3.2. The aim of the tests is to enlighten eventual inconsistencies between the numeric results and the actual behavior of the robot, in order to have a solid starting point for future development and improvement of the *PLANarm*.

The experiments conducted are static tests in which the force vs displacement behavior is analyzed. This type of analysis is meant to validate the process of force measurement employed in the closed-loop control, as explained in Ref. 5.5.

5.6.1 Test Bench

The tests are conducted on the motor-less device, where the top elements of the corners, together with the hardware components, are not installed (Fig. 5.5j). The experiments consist in the application of known directional loads on the end effector. The displacement produced by the external load is obtained by reading the rotation of the four cams through the potentiometers.

The test bench is organized as follows:

- The *PLANarm* is firmly positioned on a steady desk.
- The four potentiometers, linked to the respective cams, are connected to an *Arduino Uno* board, that elaborates the signals which are read by a PC.
- An external structure, consisting of a stool with an overhang pulley, allows the exertion of a load on the end effector. At the extremity of the wire, four 250$[g]$ weights can be successively attached (Fig. 5.11).

Calibration

The analog signal of each potentiometer returns a value v, that is proportional to the amount of voltage being applied to the pin. v spans between 0 and 1023 which correspond respectively to 0°and 300°of the potentiometer rotation ϕ, therefore:

$$\phi = v\frac{300}{1024} \tag{5.5}$$

To calibrate the signal of each potentiometer w.r.t. the reference cam rotation γ, the cam is positioned in a physically known position for which $\gamma = \bar{\gamma}$. By reading the corresponding $\bar{\phi}(\bar{\gamma})$, the offset Δ° between γ and ϕ is:

$$\Delta^\circ = \bar{\gamma} - \bar{\phi} \tag{5.6}$$

Once known Δ° of each potentiometer, the relation between γ and signal v is:

$$\gamma = \phi + \Delta^\circ = v\frac{300}{1024} + \Delta^\circ \tag{5.7}$$

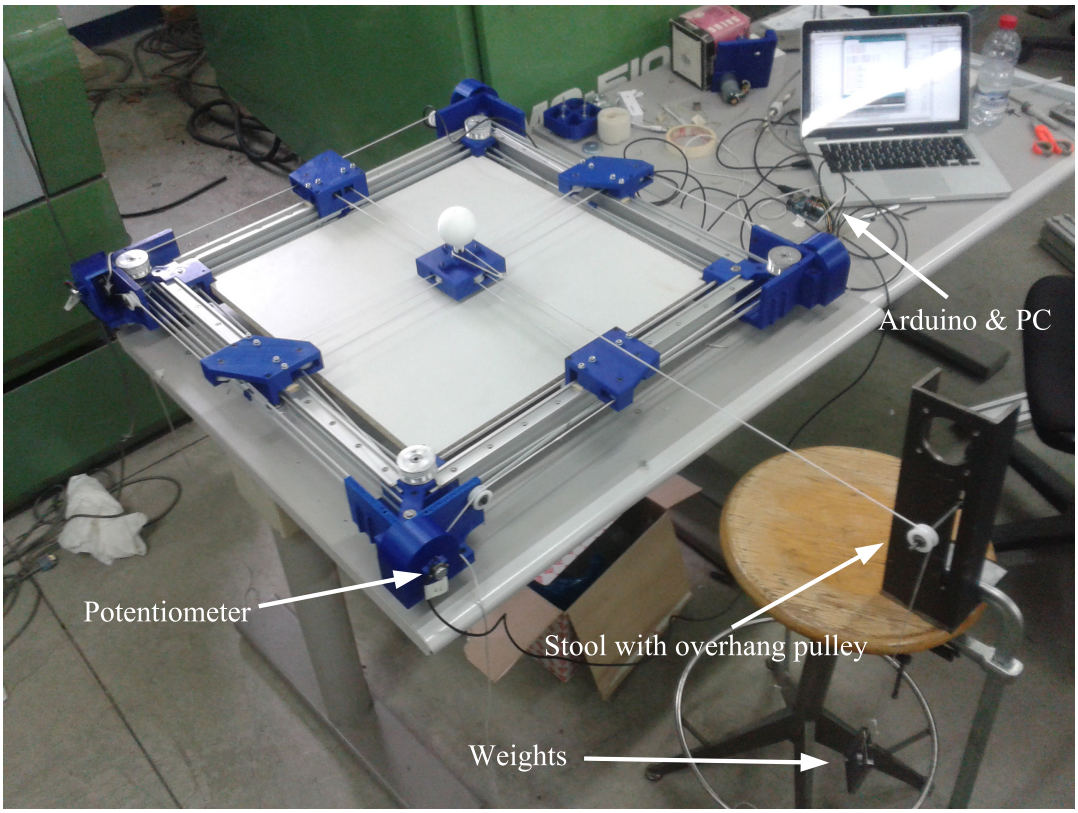


Figure 5.11: Test bench. In different tests equilibrium position of the end-effector, direction and magnitude of the pulling force and the initial rotation of the cams are arbitrary imposed. The output of the experiments is the rotation of the cams due to the external force.

Testing Procedure

Each testing session has the following steps:

1. Definition of the configuration for the testing session: equilibrium position M_{eq} and stiffness condition, defined by δ_i, are set by manual positioning the four joint rotations θ_{ij}. M_{eq} is determined by measuring the distance of the end-effector from the sides of the workspace and δ_i by imposing the corresponding γ_i^0.

2. The set position for θ_{ij} is blocked by closing the belt systems as shown in Fig. 5.12, as the test is conducted with blocked actuators.

3. A load W is applied to the end effector through the overhang pulley system. The direction of the load is set by conveniently positioning the stool w.r.t. the device. The intensity of the pulling force is defined by the number of weights attached to the wire. Load W is varied by successively adding and removing weights. For each load condition, the four rotations γ_{ij}, read by the potentiometers, are saved on the PC.

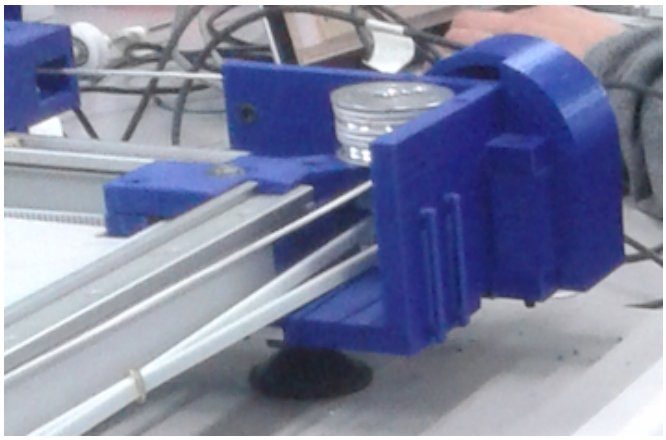


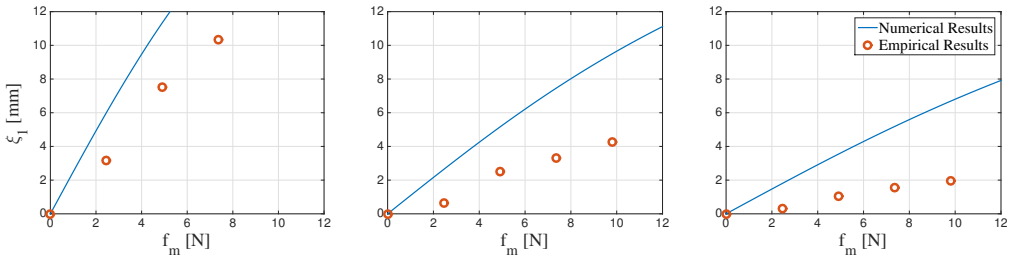
Figure 5.12: Blocking system for the joint rotations θ. The belt is closed onto itself to prevent the movement of the transmission.

5.6.2 Results

In a first testing mode the pulling force W is oriented in y and the end-effector is positioned at the center of the workspace ($M_{eq} = 0$). Loads of $250[g]$, $500[g]$, $750[g]$ and $1000[g]$ are successively attached to the pulling wire for three different configurations, in terms of stiffness imposed by the initial position of the cams.

Fig. 5.13 shows that the actual behavior of the *PLANarm* is tougher than expected. The trend is coherent with the model but the displacement values are low when compared to the numerical curve. This inconsistency is mainly caused by the presence of non-negligible friction in the cam-cover connection, not considered in the model. Friction introduces a contribution which opposes to the movement of the cam.

To further detect this effect a second test is done, where the loads are first applied, then removed, then applied in the opposite direction and finally removed again. Fig.



(a) $\delta_1 = 20.5[mm]$ $k_y = 0.44[N/mm]$.

(b) $\delta_1 = 48.7[mm]$ $k_y = 0.96[N/mm]$.

(c) $\delta_1 = 58.7[mm]$ $k_y = 1.40[N/mm]$.

Figure 5.13: Displacement vs force on the center of the workspace ($M_{eq} = (0, 0)$). $0[g]$, $250[g]$, $500[g]$, $750[g]$ and $1000[g]$ are successively applied on the end-effector in direction y, with fixed $\delta_0 = 20,5[mm]$ for direction x. The red dots represent the experimental values of displacement ξ_1 for each load, the blue curve shows the trend of the numerical model.

5.14 shows an hysteresys, direct consequence of damping introduced by friction on the cams.

Successively, a similar test is done in a different equilibrium position, close to one border of the workspace. This test shows how, both in the numerical model and the experimental setup, the behavior of the *PLANarm* is hardly affected by the end-effector position (Fig. 5.15). A slight increase of the stiffness is noted in the corner.

A last test is done with the external force directed at 45° w.r.t. $\{w\}$. This test is done with a high stiffness in direction y and a low one in x. Fig. 5.16 shows that, in both the model and the experiment, the direction of the displacement is deviated w.r.t. the applied force, due to the different rigidity of the cable circuits in the two main directions. When loading and then unloading the end-effector, the empirical curve shows an hysteretic behavior in both directions. The effect of friction is more evident in x, where stiffness is lower.

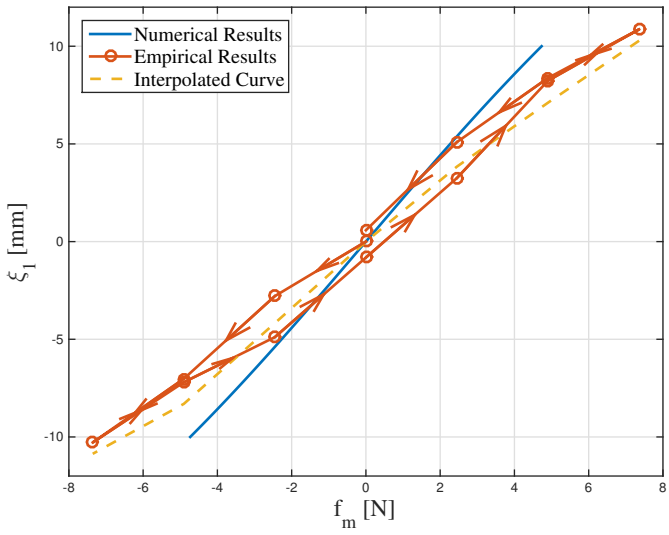


Figure 5.14: Hysetertic effect at the center of the workspace ($M_{eq} = (0, 0)$), with $\delta_0 = 20.5[mm]$ $\delta_1 = 58.7[mm]$ that correspond to a stiffness $k_x = 0.48[N/mm]$ and $k_y = 1.40[N/mm]$. The loads succession is applied and removed, first in direction $-y$ and afterwards in direction $+y$. The arrows enlighten the succession of the loads. The yellow dashed curve is the interpolation of the hysteretical curves, that can be used to measure the external force as function of the displacement.

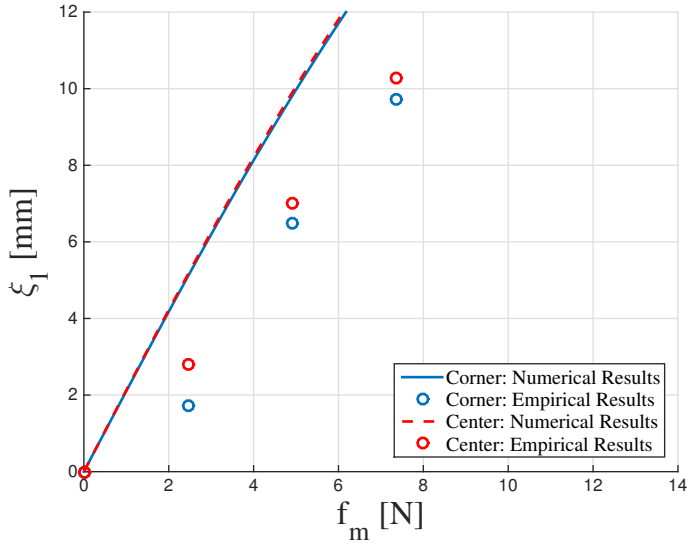


Figure 5.15: Displacement vs force on a corner of the workspace ($M_{eq} = (150, 150)[mm]$). $\delta_0 = 20.5[mm]$ $\delta_1 = 20.5[mm]$. The load succession is the same as explained in Fig. 5.13. The numerical and empirical results for this configuration (blue) are compared to the results with the end effector positioned at the center (red).

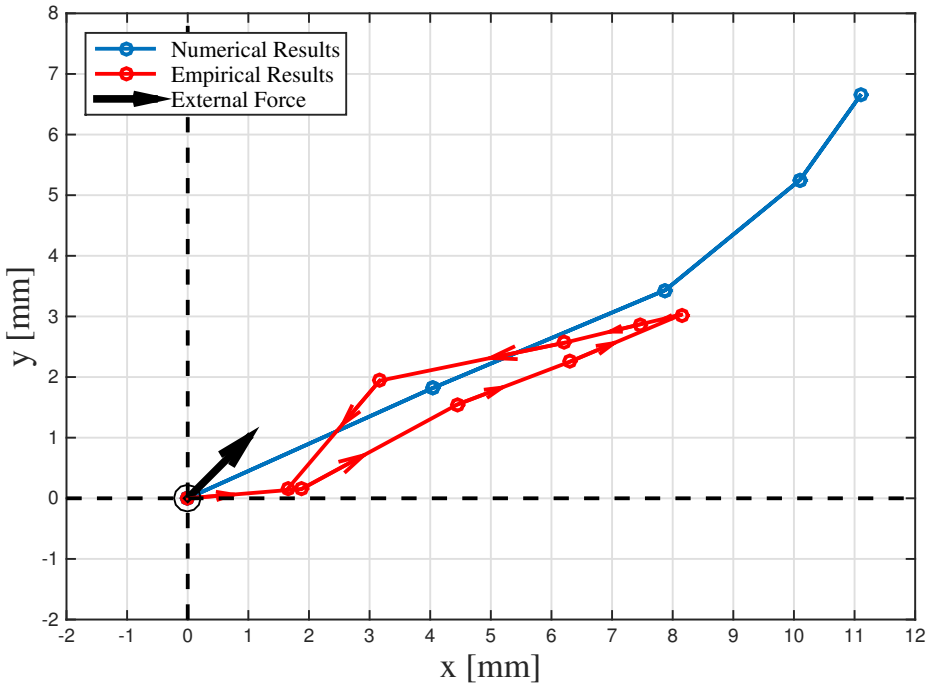


Figure 5.16: Planar displacement with a diagonal external force (45° w.r.t. $\{w\}$). The end-effector is positioned at the center of the workspace ($M_{eq} = (0, 0)$). The stiffness condition for this test is: $\delta_0 = 20.5[mm]$ and $\delta_1 = 49.6[mm]$ which result in $k_x = 0.47[N/mm]$ and $k_y = 1.00[N/mm]$. The arrows enlighten the displacement when the loads succession is applied and removed.

5.6.3 Discussion

A first qualitative aspect, highlighted when inspecting the physical device, is an overall kinematic behavior coherent with the model. As a matter of fact, when manually actuating the motor shafts, the carriages constantly maintain an orthogonal arrangement. Moreover, the coherence between belts and wires transmission is able to keep still the position of the carriages when a change of stiffness is performed on the end-effector.

The tests, aimed to enlighten the relation between force and displacement, reveal some differences between the model and the experimental results. The physical device happens to be tougher than the model, as the forces produce displacements consistently lower than expected. A probable explanation to this phenomena is that the performance of the single cam has not been tested, in terms of force and stiffness as function of the displacement, and it is probably different from the computed curves. By manually checking the transmission elements, the connection between cams, springs and structure exhibits non-negligible friction. In fact when a cam is rotated and released, its return movement is incomplete and does not oscillate. Friction seems to be one of the major causes of the discrepancy between model and physical behavior. The reaction of the device to the application and removal of loads highlights an hysteresis that typically occurs in presence of friction.

At the current stage, the measurement process is not capable of returning an accurate and precise force feedback using the numerical model. Therefore, an experimental calibration of the relation between force and displacement needs to be done on the single cam-based SEA and on the end-effector. This process is aimed to computed the real force vs displacement curves of the device. Despite the application of this process, the hysteretic behavior of the curves still affects the force lectures, since the displacement also depends on the previous position of the end-effector. Nevertheless, the effect is common in mechanical system under friction forces, and, in this particular case, it is not significant to compromise the measurement process, as the curve can be calibrated by interpolating the real curves, as shown in Fig. 5.14.

Chapter 6

Conclusions

In this work the *PLANarm*, a low cost robot for upper limb rehabilitation, has been conceived, designed, manufactured and assembled. The purpose of the work was to create a planar VSA-based cable driven device that could transfer an adjustable force to the patient's arm through a manipulandum in order to resemble traditional rehabilitation exercises performed by therapists.

At the conception of the kinematic architecture for the robot, a three-directional cable driven configuration has been studied, consisting of three antagonist SEAs. To overcome the found limitations, in terms of achievable stiffness ratio, a negative stiffness based device was design. The overall results showed the architecture presenting instability zones. Hence, the kinematic architecture was rejected. A second architecture was conceived, a more simple orthogonally-arranged configuration, with two antagonists VSAs perpendicular to each other. This kinematical architecture does not present instability zones, although it presents the impossibility of orienting the stiffness ellipsoid as a trade-off. This configuration was chosen despite this limitation.

The study on the kinetostatic behavior of this configuration highlighted a coupling between the stiffnesses in the two directions, which was priorly unexpected. The analytical evaluation showed how different parameters affect stiffness and the coupling between stiffness in the two directions. The study showed the possibility to achieve a reasonably wide range of stiffness values and ratios, conveniently defining spring characteristics. To achieve the proposed kinematic architecture, a belt and wire based transmission was conceived to maintain the orthogonal arrangement of the two VSAs using the minimal quantity of actuators, which is four.

As for the VSAs, the LinWWC-SEA was adopted. The cam based SEA has the advantage of being compact, simply manufacturable and having an easily adjustable force-displacement curve. The LinWWC-SEA was studied, developed and dimensioned for the application on the *PLANarm*. The numeric results showed a satisfactory behavior in terms of achievable stiffness range and practical feasibility.

The design of the device, oriented towards low cost, low weight and easy feasibility started from the kinematic concept and led to the realization of a prototype. The mechanism of the device is about 8 [kg] and the overall cost of the purchased elements was €1037.30. This cost does not include parts manufactured inside *ITIA*'s laboratories, as mechanized elements or structures manufactured by FDM, the controller system (PC, software), neither the man-hours spent in design, manufacture and assembly of the device. Considering the commercial price of FDM elements, the cost could raise to about €2,400. This valor is still pretty far from the commercial price of rehabilitation robots

in circulation, of above €75,000. This is an excellent start point for the development of a completely functional low-cost robot for upper-limb rehabilitation.

Finally experimental tests were carried out to observe the relation between external force and displacement and compare it to the numerical predictions. The tests highlighted an inconsistency between the model and the physical prototype which makes it unfeasible to implement the force feedback control based on the numerical curves.

6.1 Future Work

First of all, to properly continue the development of the *PLANarm*, the assembling process needs to be completed. The last steps of the mounting process are to be realized: the motors, the sensors and the cable system are yet to be installed. The overall behavior is to be improved by reducing the friction in the LinWWC-SEAs. In order to implement a accurate force feedback control, the measurement procedure needs to be calibrated by exploiting the empirical curves rather than the numerical ones, to empirically validate the accuracy and precision of the force-displacement dependance.

For what concerns control, an introductory study was made. It consisted in the definition of the relation between inputs, position of the four actuators, and outputs, position and stiffness at the end-effector. Two approaches for the low-level control have been briefly discussed, but need deeper analysis. Detailed definition of the control at both high and low level is certainly a priority in terms of future developments, as it is the main gap that separates the *PLANarm* from being an usable rehabilitation robot to all intents and purposes.

Dynamic simulations and tests would certainly allow to have a more detailed overview of the behavior of the actuated device in terms of dynamic response and performance, in order to find eventual problems that might affect the proper functioning of the robot.

Specific tests are to be done to observe the interaction between robot and patient, in terms of safety and applicability of therapeutical exercises, in order to finally validate the suitability of the *PLANarm* for rehabilitation purposes.

Bibliography

[1] J. E. Speich and J. Rosen, "Medical robotics," *Encyclopedia of biomaterials and biomedical engineering*, vol. 983, p. 993, 2004.

[2] World Health Organization, "World report on disability," 2011.

[3] World Stroke Organization, "Annual report 2014," 2015.

[4] S. Mazzoleni, "Sistemi robotici e meccatronici per la riabilitazione," *Manuale sulla disabilità*, pp. 159–179, 2012.

[5] World Stroke Campaign, "Learn about stroke." http://www.worldstrokecampaign.org/learn.html [January 26, 2016].

[6] G. E. Gresham, P. W. Duncan, and W. B. Stason, *Post-stroke rehabilitation*. DIANE Publishing, 1997.

[7] P. Langhorne, F. Coupar, and A. Pollock, "Motor recovery after stroke: a systematic review," *The Lancet Neurology*, vol. 8, no. 8, pp. 741–754, 2009.

[8] H. M. Van der Loos and D. J. Reinkensmeyer, "Rehabilitation and health care robotics," in *Springer Handbook of Robotics*, pp. 1223–1251, Springer, 2008.

[9] P. S. Lum, C. G. Burgar, P. C. Shor, M. Majmundar, and M. Van der Loos, "Robot-assisted movement training compared with conventional therapy techniques for the rehabilitation of upper-limb motor function after stroke," *Archives of physical medicine and rehabilitation*, vol. 83, no. 7, pp. 952–959, 2002.

[10] G. B. Prange, M. J. Jannink, C. G. Groothuis-Oudshoorn, H. J. Hermens, M. J. IJzerman, *et al.*, "Systematic review of the effect of robot-aided therapy on recovery of the hemiparetic arm after stroke," *Journal of rehabilitation research and development*, vol. 43, no. 2, p. 171, 2006.

[11] R. Riener, *Robot-aided rehabilitation of neural function in the upper extremities*. Springer, 2007.

[12] C. Werner, S. Von Frankenberg, T. Treig, M. Konrad, and S. Hesse, "Treadmill training with partial body weight support and an electromechanical gait trainer for restoration of gait in subacute stroke patients a randomized crossover study," *Stroke*, vol. 33, no. 12, pp. 2895–2901, 2002.

[13] J. Hidler, D. Nichols, M. Pelliccio, K. Brady, D. D. Campbell, J. H. Kahn, and T. G. Hornby, "Multicenter randomized clinical trial evaluating the effectiveness of the lokomat in subacute stroke," *Neurorehabilitation and Neural Repair*, vol. 23, no. 1, pp. 5–13, 2009.

[14] T. G. Hornby, D. D. Campbell, J. H. Kahn, T. Demott, J. L. Moore, and H. R. Roth, "Enhanced gait-related improvements after therapist-versus robotic-assisted locomotor training in subjects with chronic stroke a randomized controlled study," *Stroke*, vol. 39, no. 6, pp. 1786–1792, 2008.

[15] G. Kwakkel, B. J. Kollen, and H. I. Krebs, "Effects of robot-assisted therapy on upper limb recovery after stroke: a systematic review," *Neurorehabilitation and neural repair*, 2007.

[16] J. Mehrholz, T. Platz, J. Kugler, and M. Pohl, "Electromechanical and robot-assisted arm training for improving arm function and activities of daily living after stroke," *The Cochrane Library*, 2008.

[17] J. L. Pons and D. Torricelli, *Emerging Therapies in Neurorehabilitation*. Springer, 2014.

[18] M. Hillman, "Rehabilitation robotics from past to present-a historical perspective," in *The 8th International Conference on Rehabilitation Robotics PROCEEDINGS*, pp. 1–4, 2003.

[19] I. Díaz, J. J. Gil, and E. Sánchez, "Lower-limb robotic rehabilitation: literature review and challenges," *Journal of Robotics*, vol. 2011, 2011.

[20] H. S. Lo and S. Q. Xie, "Exoskeleton robots for upper-limb rehabilitation: state of the art and future prospects," *Medical engineering & physics*, vol. 34, no. 3, pp. 261–268, 2012.

[21] P. Maciejasz, J. Eschweiler, K. Gerlach-Hahn, A. Jansen-Troy, and S. Leonhardt, "A survey on robotic devices for upper limb rehabilitation," *J. Neuroeng. Rehabil*, vol. 11, no. 3, pp. 10–1186, 2014.

[22] A. Prochazka, "Passive devices for upper limb training," in *Neurorehabilitation Technology*, pp. 159–171, Springer, 2012.

[23] G. Rosati, R. Secoli, D. Zanotto, A. Rossi, and G. Boschetti, "Planar robotic systems for upper-limb post-stroke rehabilitation," in *ASME 2008 International Mechanical Engineering Congress and Exposition*, pp. 115–124, American Society of Mechanical Engineers, 2008.

[24] H. I. Krebs, M. Ferraro, S. P. Buerger, M. J. Newbery, A. Makiyama, M. Sandmann, D. Lynch, B. T. Volpe, and N. Hogan, "Rehabilitation robotics: pilot trial of a spatial extension for mit-manus," *Journal of NeuroEngineering and Rehabilitation*, vol. 1, no. 1, p. 5, 2004.

[25] G. Rosati, D. Zanotto, R. Secoli, and A. Rossi, "Design and control of two planar cable-driven robots for upper-limb neurorehabilitation," in *Rehabilitation Robotics, 2009. ICORR 2009. IEEE International Conference on*, pp. 560–565, June 2009.

[26] D. Zanotto, G. Rosati, S. Minto, and A. Rossi, "Sophia-3: A semiadaptive cable-driven rehabilitation device with a tilting working plane," *Robotics, IEEE Transactions on*, vol. 30, pp. 974–979, Aug 2014.

[27] G. Rosati, P. Gallina, and S. Masiero, "Design, implementation and clinical tests of a wire-based robot for neurorehabilitation," *Neural Systems and Rehabilitation Engineering, IEEE Transactions on*, vol. 15, pp. 560–569, Dec 2007.

[28] D. Mayhew, B. Bachrach, W. Rymer, and R. Beer, "Development of the macarm - a novel cable robot for upper limb neurorehabilitation," in *Rehabilitation Robotics, 2005. ICORR 2005. 9th International Conference on*, pp. 299–302, June 2005.

[29] R. Beer, D. Mayhew, C. Bredfeldt, and B. Bachrach, "Technical evaluation of the macarm: A cable robot for upper limb neurorehabilitation," in *Biomedical Robotics and Biomechatronics, 2008. BioRob 2008. 2nd IEEE RAS EMBS International Conference on*, pp. 942–947, Oct 2008.

[30] W. T. Dempster, *Space Requirements of the Seated Operator: Geometric, Kinematic, and Mechanical Aspects of the Body with Special Reference to Limbs*. NTIS, 1955.

[31] L. Marchal-Crespo and D. J. Reinkensmeyer, "Review of control strategies for robotic movement training after neurologic injury," *Journal of neuroengineering and rehabilitation*, vol. 6, no. 1, p. 20, 2009.

[32] B. Vanderborght, A. Albu-Schaeffer, A. Bicchi, E. Burdet, D. G. Caldwell, R. Carloni, M. Catalano, O. Eiberger, W. Friedl, G. Ganesh, M. Garabini, M. Grebenstein, G. Grioli, S. Haddadin, H. Hoppner, A. Jafari, M. Laffranchi, D. Lefeber, F. Petit, S. Stramigioli, N. Tsagarakis, M. Van Damme, R. Van Ham, L. C. Visser, and S. Wolf, "Variable impedance actuators: A review," *Robot. Auton. Syst.*, vol. 61, pp. 1601–1614, Dec. 2013.

[33] A. Bicchi, G. Tonietti, M. Bavaro, and M. Piccigallo, "Variable stiffness actuators for fast and safe motion control," in *Robotics research. The eleventh international symposium*, pp. 527–536, Springer, 2005.

[34] N. Vitiello, T. Lenzi, S. Roccella, S. M. De Rossi, E. Cattin, F. Giovacchini, F. Vecchi, and M. Carrozza, "Neuroexos: A powered elbow exoskeleton for physical rehabilitation," *Robotics, IEEE Transactions on*, vol. 29, no. 1, pp. 220–235, 2013.

[35] L. Cui, Z. R. Eng, J. Devene, T. Tan, and G. Allison, "A compact robotic device for upper-limb reaching rehabilitation," in *Cyber Technology in Automation, Control, and Intelligent Systems (CYBER), 2014 IEEE 4th Annual International Conference on*, pp. 502–507, IEEE, 2014.

[36] M. Malosio, M. Caimmi, G. Legnani, and L. M. Tosatti, "Linarm: a low-cost variable stiffness device for upper-limb rehabilitation," in *2014 IEEE/RSJ International Conference on Intelligent Robots and Systems*, 2014.

[37] X. Zhou, S.-k. Jun, and V. Krovi, "Stiffness modulation exploiting configuration redundancy in mobile cable robots," in *Robotics and Automation (ICRA), 2014 IEEE International Conference on*, pp. 5934–5939, IEEE, 2014.

[38] A. Pott and T. Bruckmann, *Cable-Driven Parallel Robots*. Springer, 2013.

[39] I. Ebert-Uphoff, P. Voglewede, *et al.*, "On the connections between cable-driven robots, parallel manipulators and grasping," in *Robotics and Automation, 2004. Proceedings. ICRA'04. 2004 IEEE International Conference on*, vol. 5, pp. 4521–4526, IEEE, 2004.

[40] J. K. Salisbury and J. J. Craig, "Articulated hands force control and kinematic issues," *The International journal of Robotics research*, vol. 1, no. 1, pp. 4–17, 1982.

[41] F. A. Mussa-Ivaldi, N. Hogan, and E. Bizzi, "Neural, mechanical, and geometric factors subserving arm posture in humans," *The Journal of neuroscience*, vol. 5, no. 10, pp. 2732–2743, 1985.

[42] G. Legnani, D. Tosi, I. Fassi, H. Giberti, and S. Cinquemani, "The "point of isotropy" and other properties of serial and parallel manipulators," *Mechanism and Machine Theory*, vol. 45, no. 10, pp. 1407–1423, 2010.

[43] G. Legnani, I. Fassi, and A. Visioli, *Robotica industriale*. CEA, 2003.

[44] X. Tang and R. Yao, "Dimensional optimization of completely restrained positioning cable driven parallel manipulator with large span," 2010.

[45] R. Shadmehr and M. A. Arbib, "A mathematical analysis of the force-stiffness characteristics of muscles in control of a single joint system," *Biological cybernetics*, vol. 66, no. 6, pp. 463–477, 1992.

[46] Y. Wang and R. Lakes, "Extreme stiffness systems due to negative stiffness elements," *American Journal of Physics*, vol. 72, no. 1, pp. 40–50, 2004.

[47] R. Lakes and W. Drugan, "Dramatically stiffer elastic composite materials due to a negative stiffness phase?," *Journal of the Mechanics and Physics of Solids*, vol. 50, no. 5, pp. 979–1009, 2002.

[48] A. Jafari, "Coupling between the output force and stiffness in different variable stiffness actuators," in *Actuators*, vol. 3, pp. 270–284, Multidisciplinary Digital Publishing Institute, 2014.

[49] O. Eiberger, S. Haddadin, M. Weis, A. Albu-Schäffer, and G. Hirzinger, "On joint design with intrinsic variable compliance: derivation of the dlr qa-joint.," in *ICRA*, pp. 1687–1694, 2010.

[50] M. Malosio, *Variable stiffness mechatronic devices for neurorehabilitation*. PhD thesis, Dipartimento di Ingegneria Meccanica e Industriale - Università degli Studi di Brescia, 2015.

[51] K. V. Wong and A. Hernandez, "A review of additive manufacturing," *ISRN Mechanical Engineering*, vol. 2012, 2012.

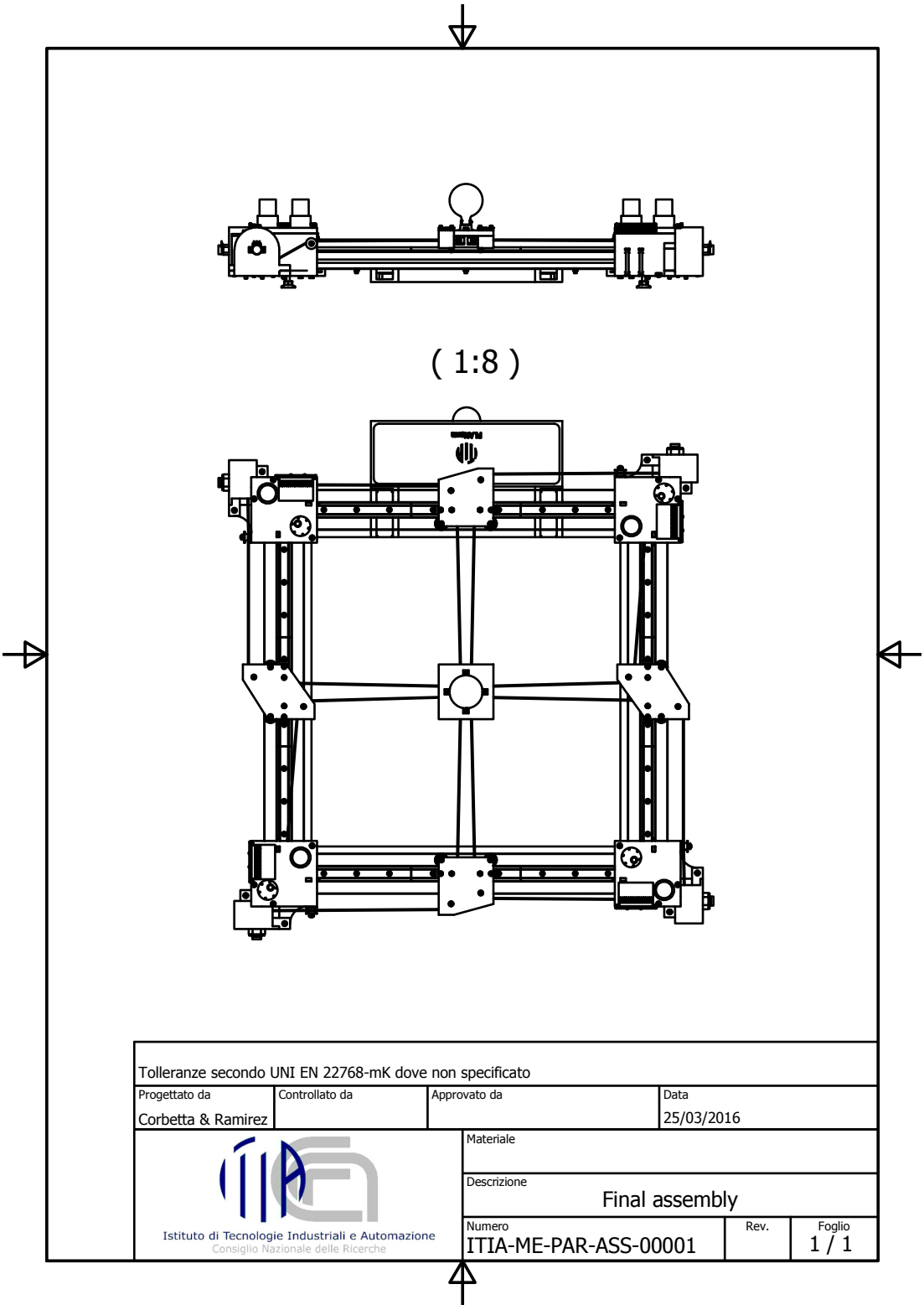
[52] Arduino, "Arduino due 32-bit arm core microcontroller." https://www.arduino.cc/en/Main/ArduinoBoardDue [March 23, 2016].

[53] Pololu, "Dual vnh2sp30 motor driver carrier md03a." https://www.pololu.com/product/708 [March 23, 2016].

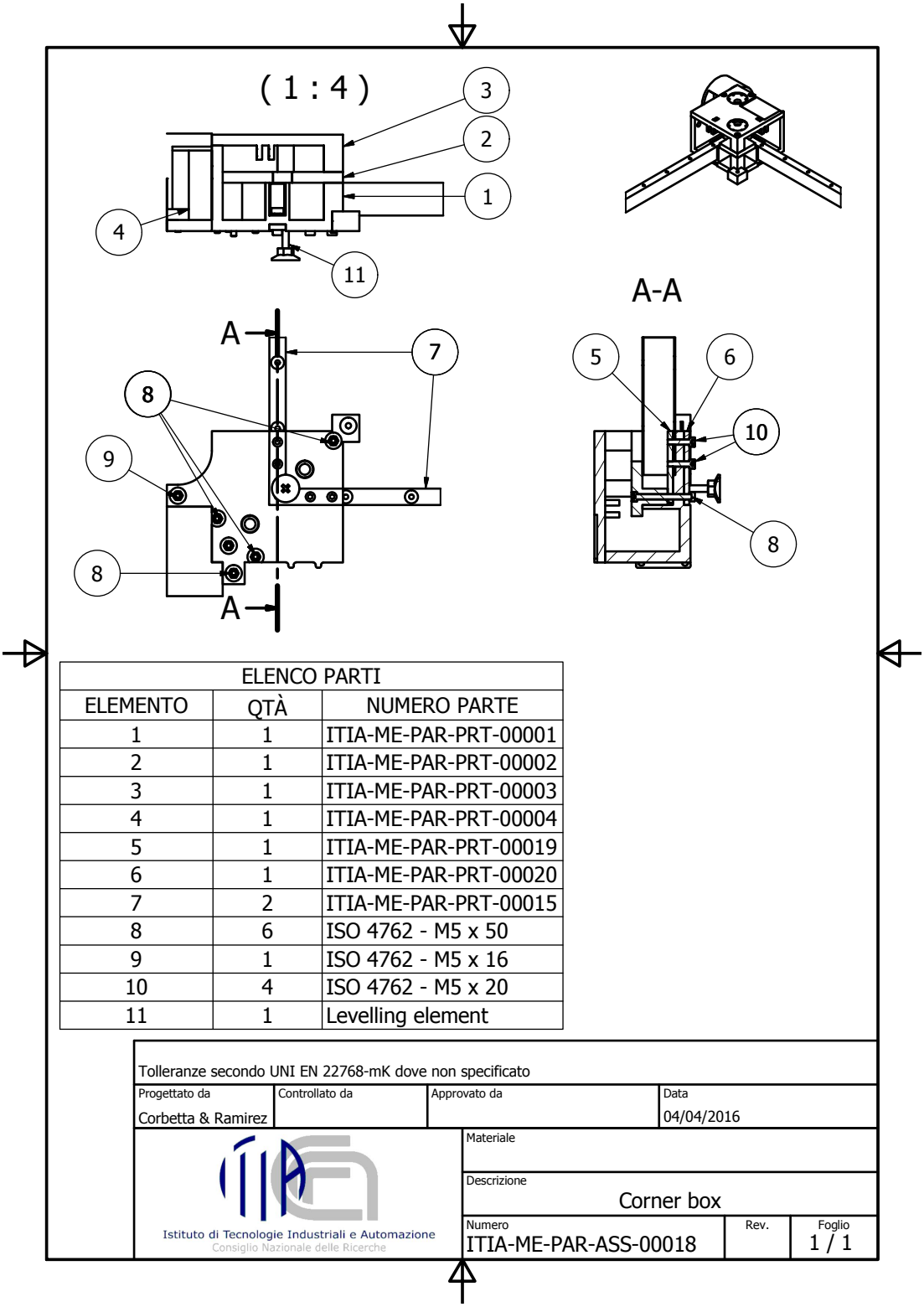
Appendix A

Technical Drawings

The technical drawings used for the manufacturing of the pieces are now presented, including assembly and single piece drawings. The pieces manufactured by mechanized process contain all the necessary dimensions for the manufacturing process. In the other hand, the drawings regarding pieces to be manufactured by FDM are presented as a reference, to give a indication of the overall size, since they pieces are directly manufactured from the digital drawings.



Technical Drawings A.1: Final assembly.



ELENCO PARTI		
ELEMENTO	QTÀ	NUMERO PARTE
1	1	ITIA-ME-PAR-PRT-00001
2	1	ITIA-ME-PAR-PRT-00002
3	1	ITIA-ME-PAR-PRT-00003
4	1	ITIA-ME-PAR-PRT-00004
5	1	ITIA-ME-PAR-PRT-00019
6	1	ITIA-ME-PAR-PRT-00020
7	2	ITIA-ME-PAR-PRT-00015
8	6	ISO 4762 - M5 x 50
9	1	ISO 4762 - M5 x 16
10	4	ISO 4762 - M5 x 20
11	1	Levelling element

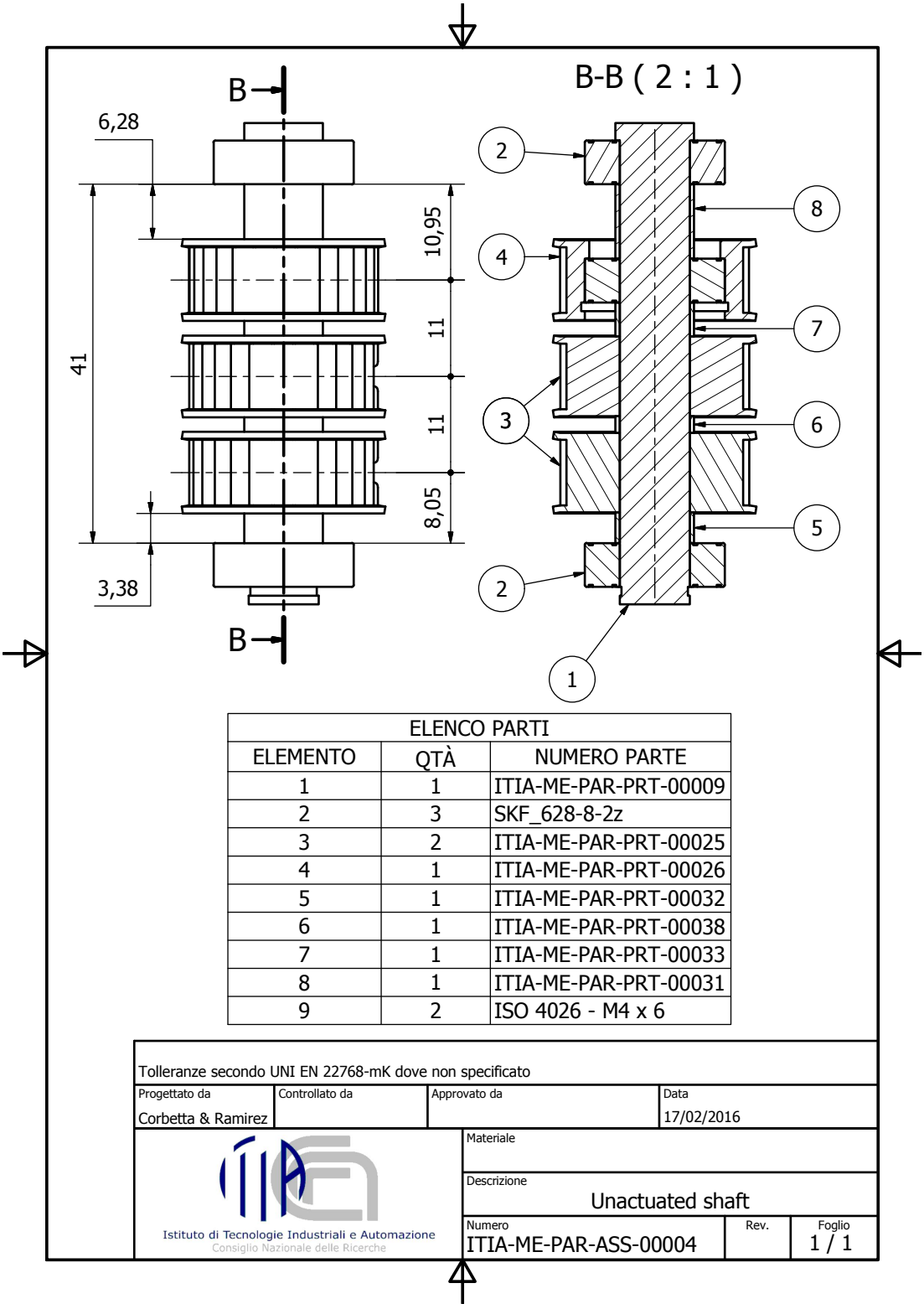
Tolleranze secondo UNI EN 22768-mK dove non specificato

Progettato da	Controllato da	Approvato da	Data
Corbetta & Ramirez			04/04/2016

Istituto di Tecnologie Industriali e Automazione
Consiglio Nazionale delle Ricerche

Materiale		
Descrizione: Corner box		
Numero: ITIA-ME-PAR-ASS-00018	Rev.	Foglio: 1 / 1

Technical Drawings A.2: Assembled corner box.



ELENCO PARTI		
ELEMENTO	QTÀ	NUMERO PARTE
1	1	ITIA-ME-PAR-PRT-00009
2	3	SKF_628-8-2z
3	2	ITIA-ME-PAR-PRT-00025
4	1	ITIA-ME-PAR-PRT-00026
5	1	ITIA-ME-PAR-PRT-00032
6	1	ITIA-ME-PAR-PRT-00038
7	1	ITIA-ME-PAR-PRT-00033
8	1	ITIA-ME-PAR-PRT-00031
9	2	ISO 4026 - M4 x 6

Tolleranze secondo UNI EN 22768-mK dove non specificato

Progettato da	Controllato da	Approvato da	Data
Corbetta & Ramirez			17/02/2016

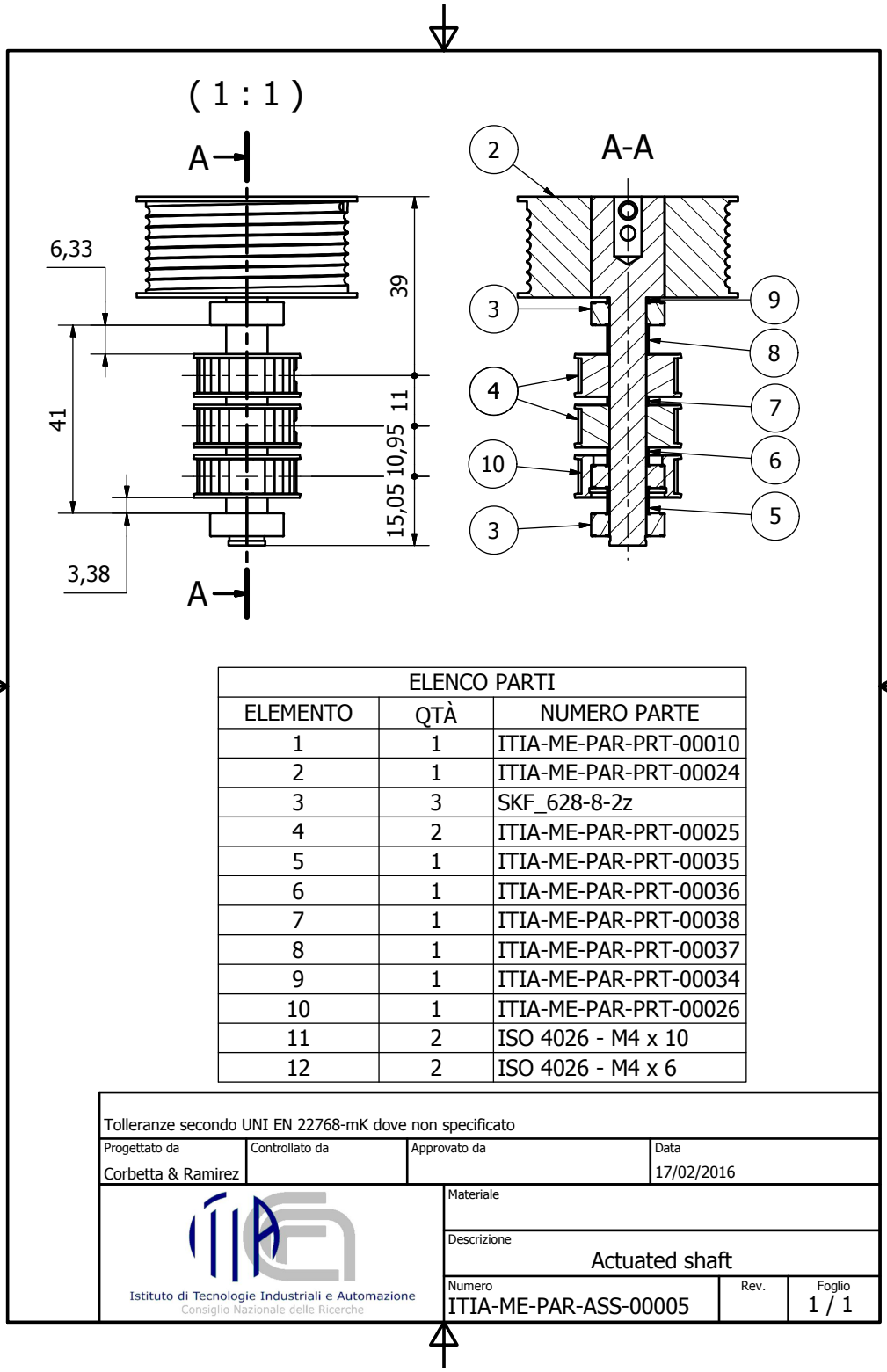
Istituto di Tecnologie Industriali e Automazione
Consiglio Nazionale delle Ricerche

Materiale

Descrizione: Unactuated shaft

Numero	Rev.	Foglio
ITIA-ME-PAR-ASS-00004		1 / 1

Technical Drawings A.3: Assembled unactuated shaft.



ELENCO PARTI		
ELEMENTO	QTÀ	NUMERO PARTE
1	1	ITIA-ME-PAR-PRT-00010
2	1	ITIA-ME-PAR-PRT-00024
3	3	SKF_628-8-2z
4	2	ITIA-ME-PAR-PRT-00025
5	1	ITIA-ME-PAR-PRT-00035
6	1	ITIA-ME-PAR-PRT-00036
7	1	ITIA-ME-PAR-PRT-00038
8	1	ITIA-ME-PAR-PRT-00037
9	1	ITIA-ME-PAR-PRT-00034
10	1	ITIA-ME-PAR-PRT-00026
11	2	ISO 4026 - M4 x 10
12	2	ISO 4026 - M4 x 6

Tolleranze secondo UNI EN 22768-mK dove non specificato

Progettato da	Controllato da	Approvato da	Data
Corbetta & Ramirez			17/02/2016

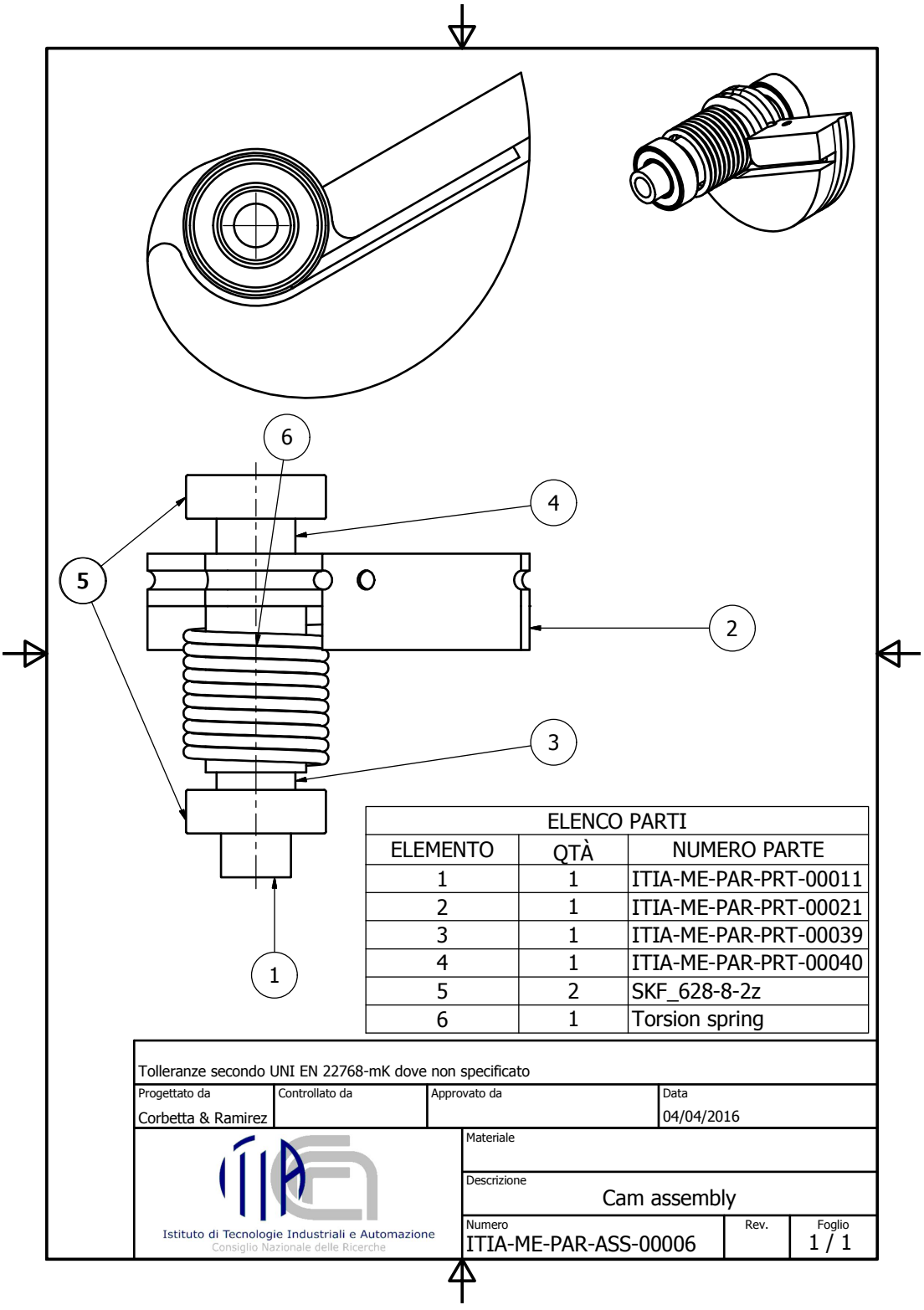
Istituto di Tecnologie Industriali e Automazione
Consiglio Nazionale delle Ricerche

Materiale

Descrizione: Actuated shaft

Numero	Rev.	Foglio
ITIA-ME-PAR-ASS-00005		1 / 1

Technical Drawings A.4: Assembled actuated shaft.



ELENCO PARTI		
ELEMENTO	QTÀ	NUMERO PARTE
1	1	ITIA-ME-PAR-PRT-00011
2	1	ITIA-ME-PAR-PRT-00021
3	1	ITIA-ME-PAR-PRT-00039
4	1	ITIA-ME-PAR-PRT-00040
5	2	SKF_628-8-2z
6	1	Torsion spring

Tolleranze secondo UNI EN 22768-mK dove non specificato

Progettato da	Controllato da	Approvato da	Data
Corbetta & Ramirez			04/04/2016

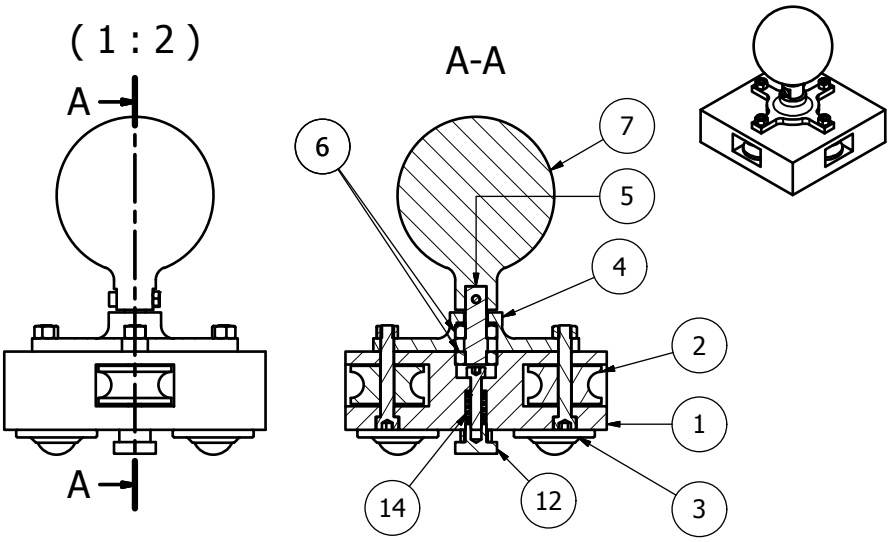
Istituto di Tecnologie Industriali e Automazione
Consiglio Nazionale delle Ricerche

Materiale

Descrizione: Cam assembly

Numero	Rev.	Foglio
ITIA-ME-PAR-ASS-00006		1 / 1

Technical Drawings A.5: Assembled cam.



ELENCO PARTI		
ELEMENTO	QTÀ	NUMERO PARTE
1	1	ITIA-ME-PAR-PRT-00007
2	4	ITIA-ME-PAR-PRT-00022
3	4	ITIA-ME-PAR-PRT-00029
4	1	ITIA-ME-PAR-PRT-00008
5	1	ITIA-ME-PAR-PRT-00012
6	2	SKF_628-8-2z
7	1	ITIA-ME-PAR-PRT-00028
8	4	ISO 4762 - M5 x 35
9	4	ANSI B 18.2.4.1 M - M5 x 0,8
10	1	ISO 4762 - M3 x 16
11	1	ANSI B 18.2.4.1 M - M3 x 0,5
12	1	ITIA-ME-PAR-PRT-00027
13	1	ISO 4762 - M4 x 20
14	1	Compression spring
15	1	ITIA-ME-PAR-PRT-00041

Tolleranze secondo UNI EN 22768-mK dove non specificato

Progettato da	Controllato da	Approvato da	Data
Corbetta & Ramirez			30/03/2016

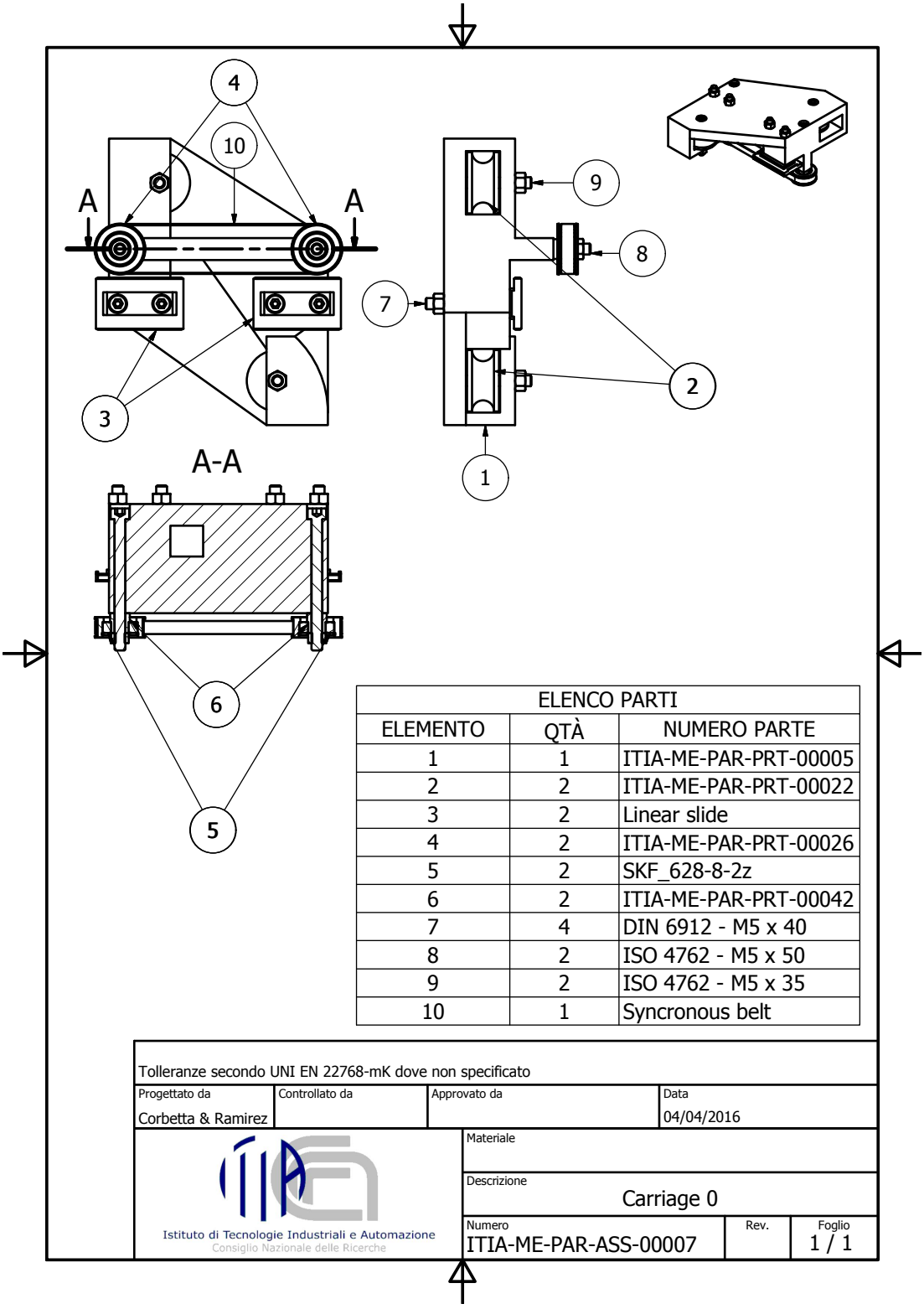
Istituto di Tecnologie Industriali e Automazione
Consiglio Nazionale delle Ricerche

Materiale

Descrizione: End-effector

Numero	Rev.	Foglio
ITIA-ME-PAR-ASS-00003		1 / 1

Technical Drawings A.6: Assembled end-effector.



ELENCO PARTI		
ELEMENTO	QTÀ	NUMERO PARTE
1	1	ITIA-ME-PAR-PRT-00005
2	2	ITIA-ME-PAR-PRT-00022
3	2	Linear slide
4	2	ITIA-ME-PAR-PRT-00026
5	2	SKF_628-8-2z
6	2	ITIA-ME-PAR-PRT-00042
7	4	DIN 6912 - M5 x 40
8	2	ISO 4762 - M5 x 50
9	2	ISO 4762 - M5 x 35
10	1	Syncronous belt

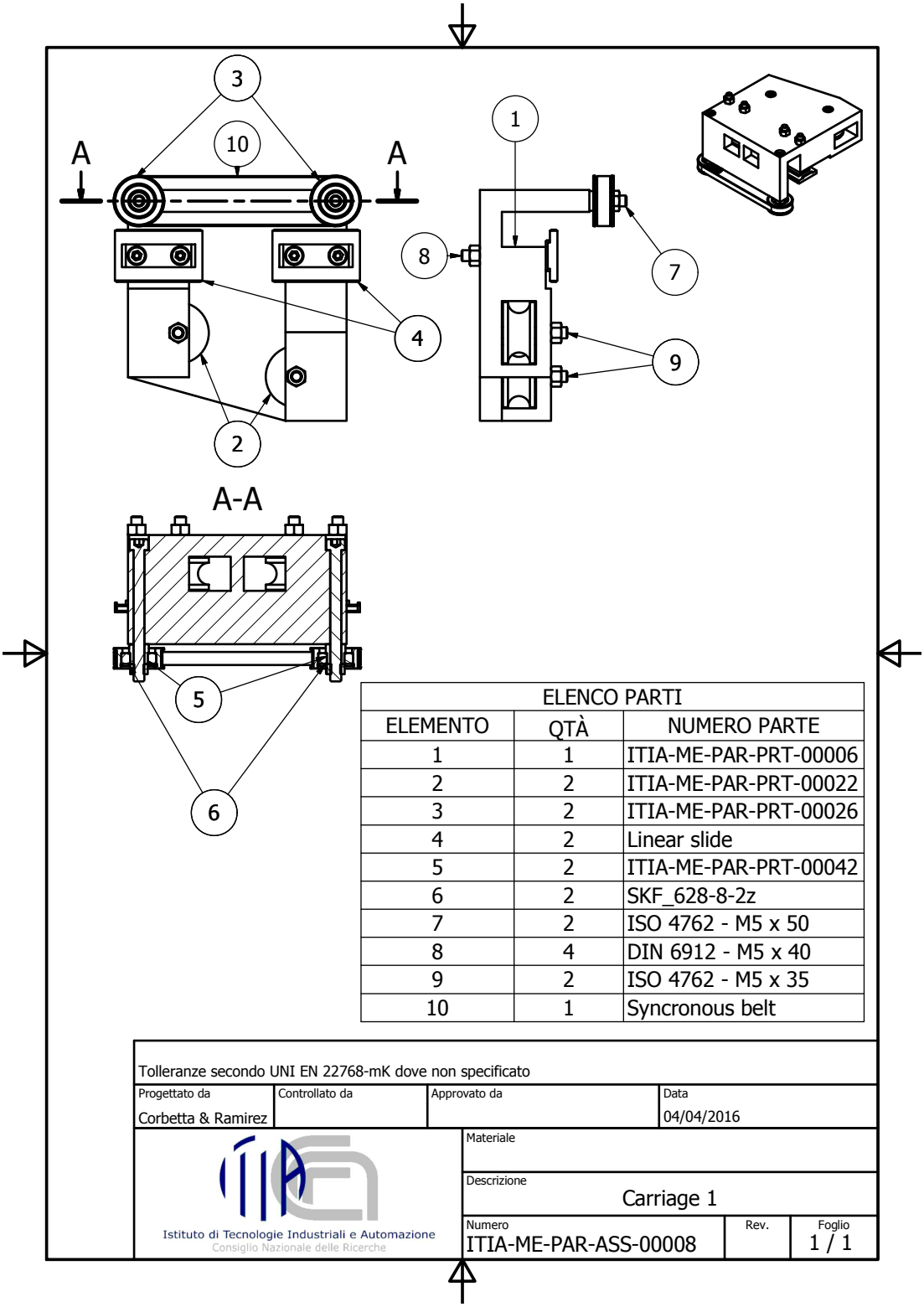
Tolleranze secondo UNI EN 22768-mK dove non specificato

Progettato da	Controllato da	Approvato da	Data
Corbetta & Ramirez			04/04/2016

Istituto di Tecnologie Industriali e Automazione
Consiglio Nazionale delle Ricerche

Materiale		
Descrizione: Carriage 0		
Numero: ITIA-ME-PAR-ASS-00007	Rev.	Foglio: 1 / 1

Technical Drawings A.7: Assembled carriage 0.



ELENCO PARTI		
ELEMENTO	QTÀ	NUMERO PARTE
1	1	ITIA-ME-PAR-PRT-00006
2	2	ITIA-ME-PAR-PRT-00022
3	2	ITIA-ME-PAR-PRT-00026
4	2	Linear slide
5	2	ITIA-ME-PAR-PRT-00042
6	2	SKF_628-8-2z
7	2	ISO 4762 - M5 x 50
8	4	DIN 6912 - M5 x 40
9	2	ISO 4762 - M5 x 35
10	1	Syncronous belt

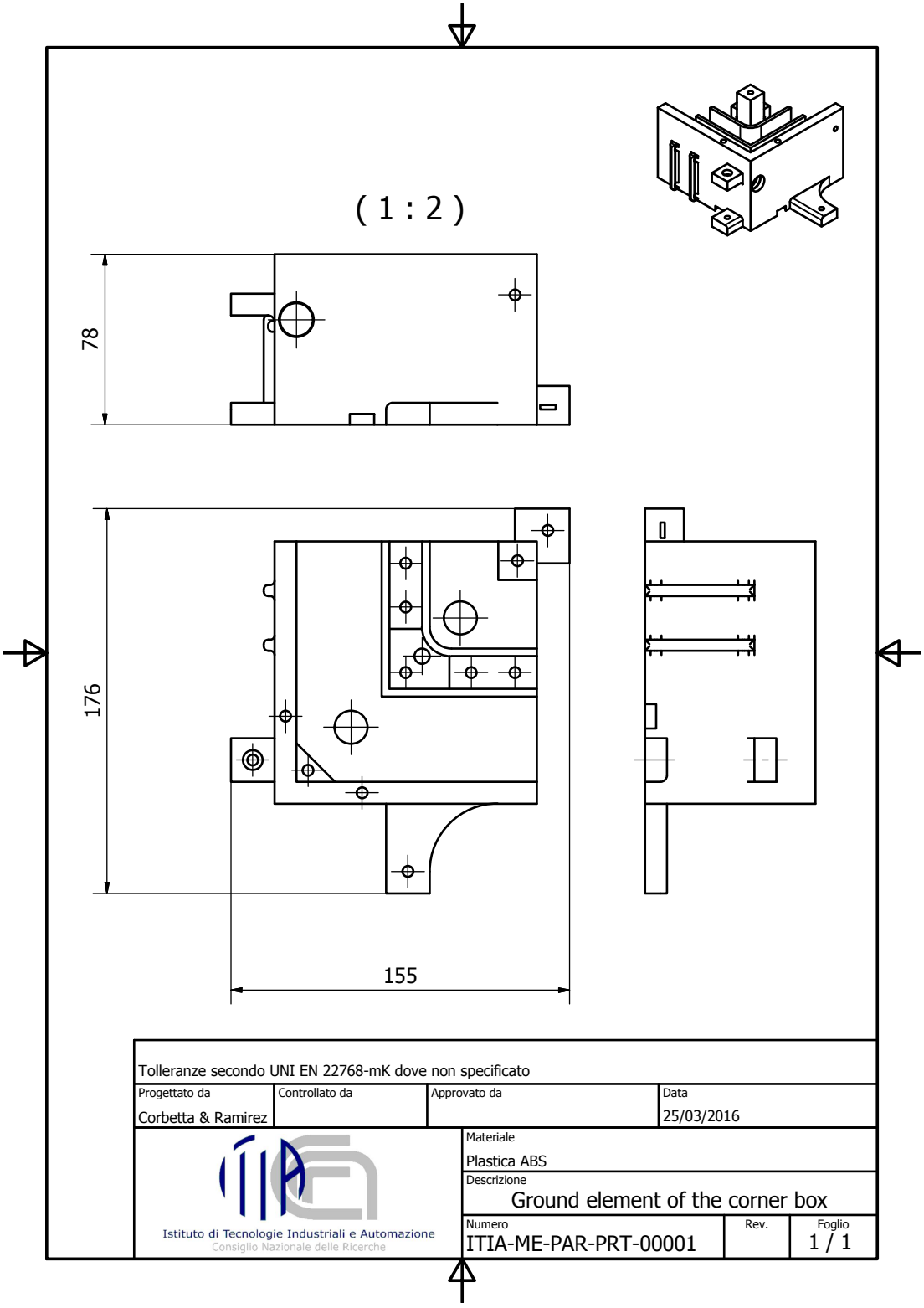
Tolleranze secondo UNI EN 22768-mK dove non specificato

Progettato da	Controllato da	Approvato da	Data
Corbetta & Ramirez			04/04/2016

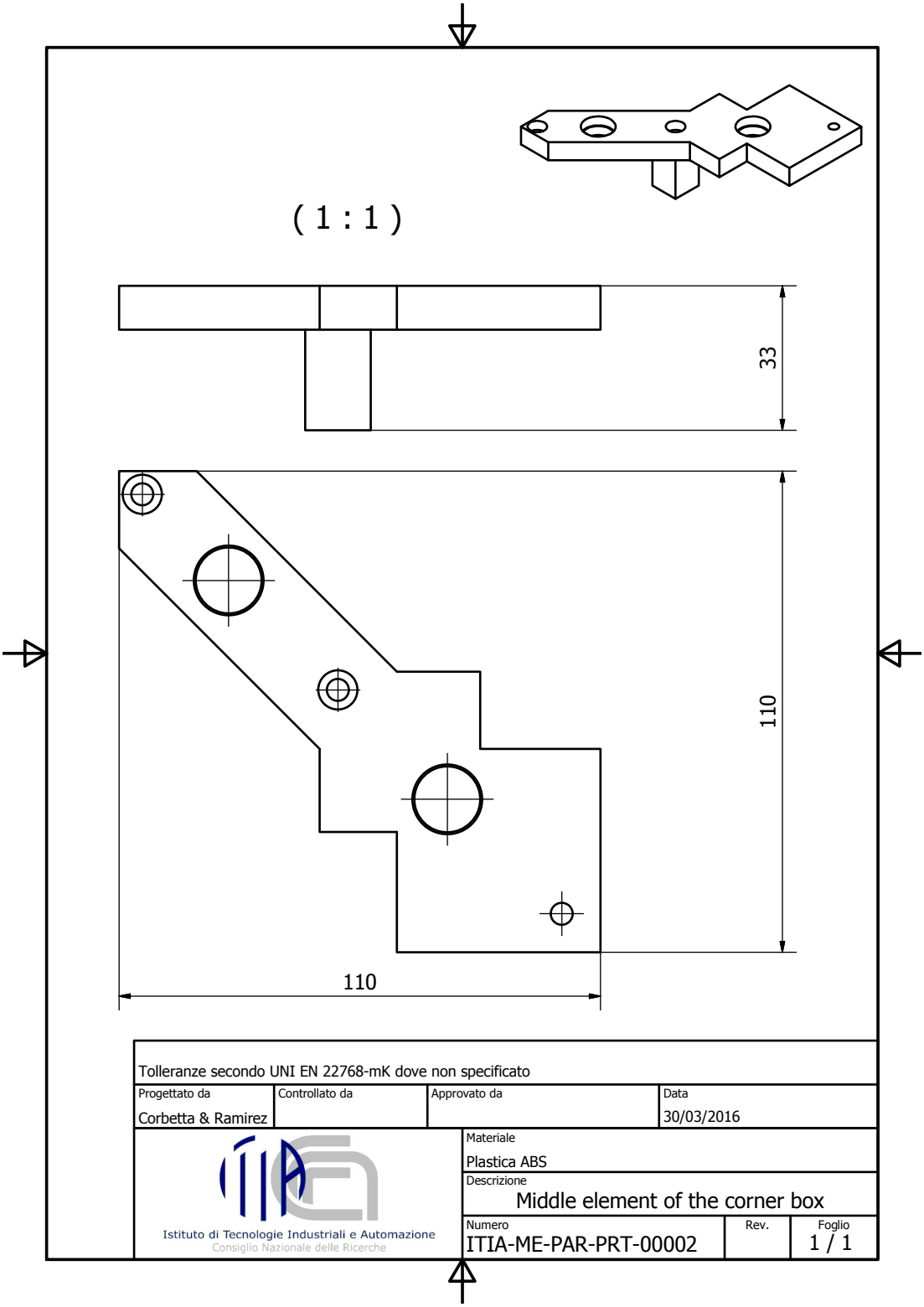
Istituto di Tecnologie Industriali e Automazione
Consiglio Nazionale delle Ricerche

Materiale		
Descrizione: Carriage 1		
Numero: ITIA-ME-PAR-ASS-00008	Rev.	Foglio: 1 / 1

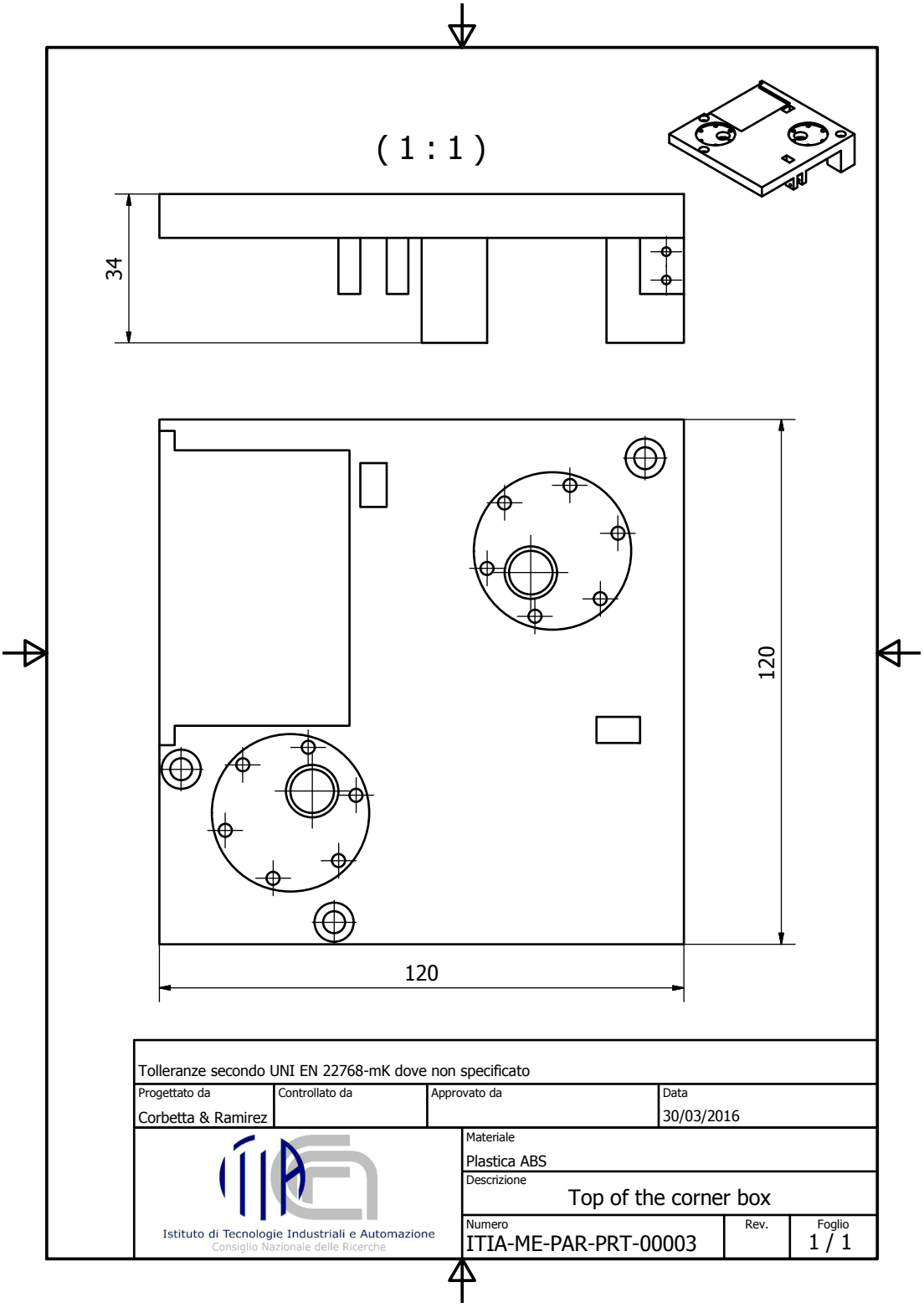
Technical Drawings A.8: Assembled carriage 1.



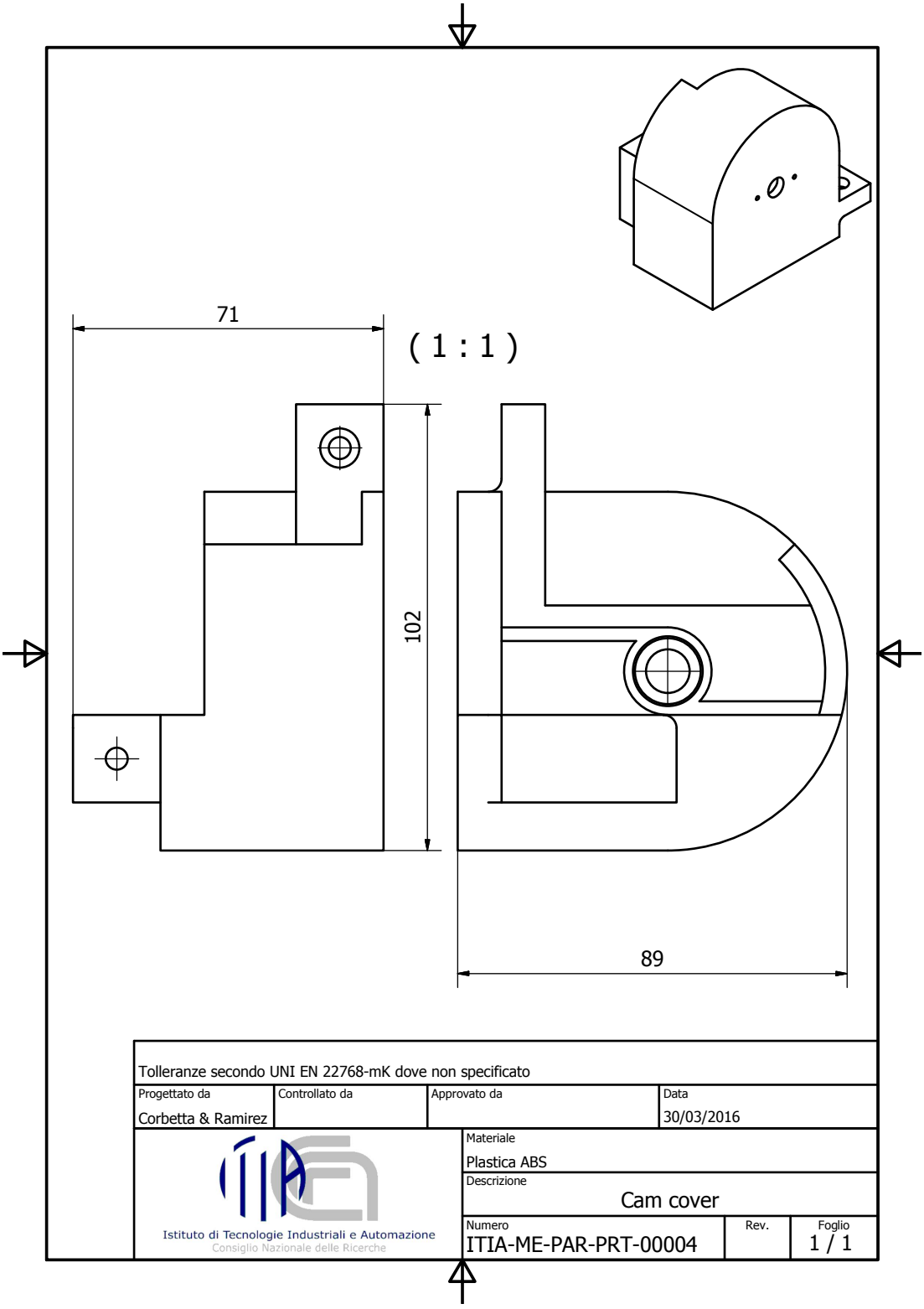
Technical Drawings A.9: Ground element of the corner box.



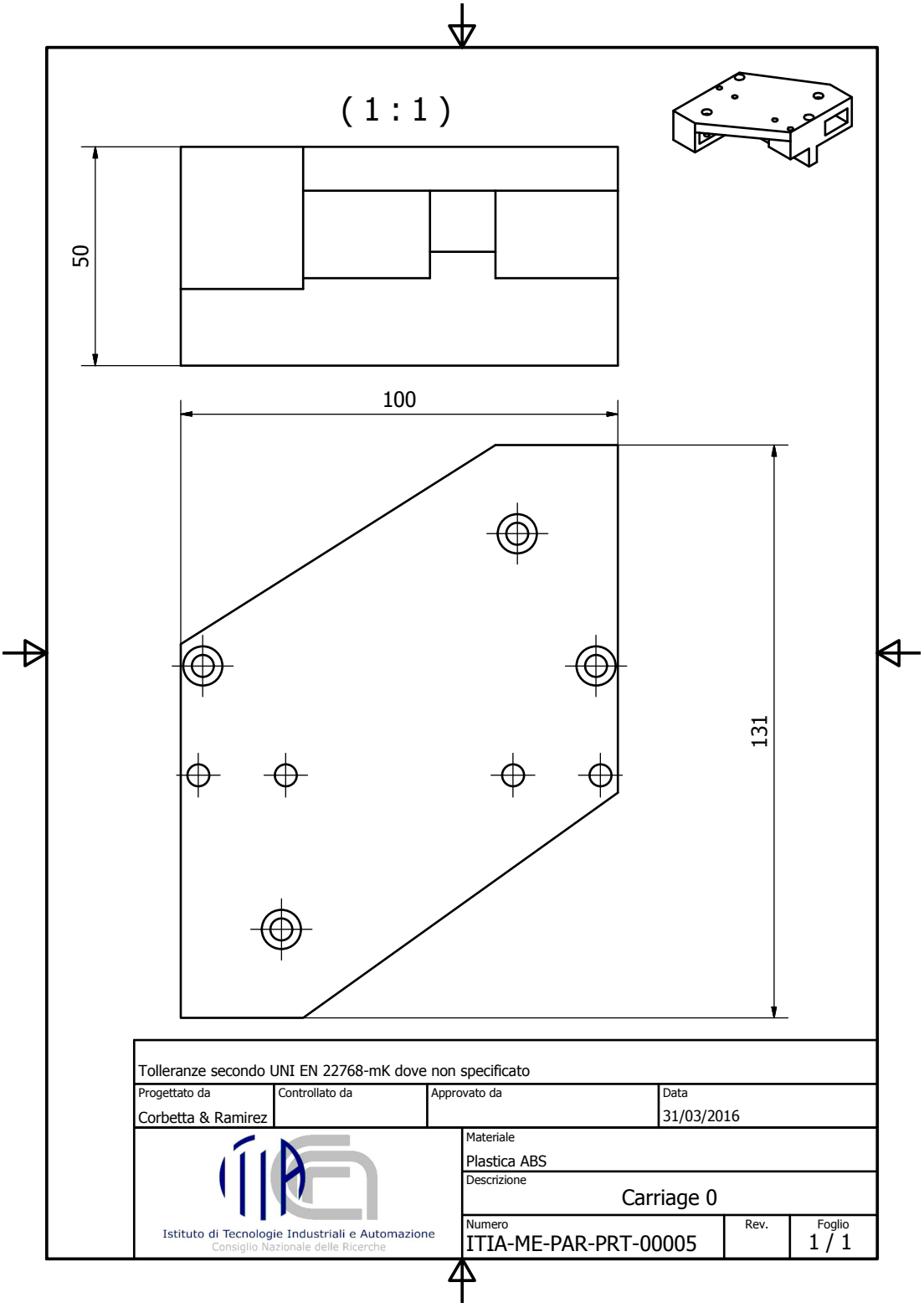
Technical Drawings A.10: Middle element of the corner box.



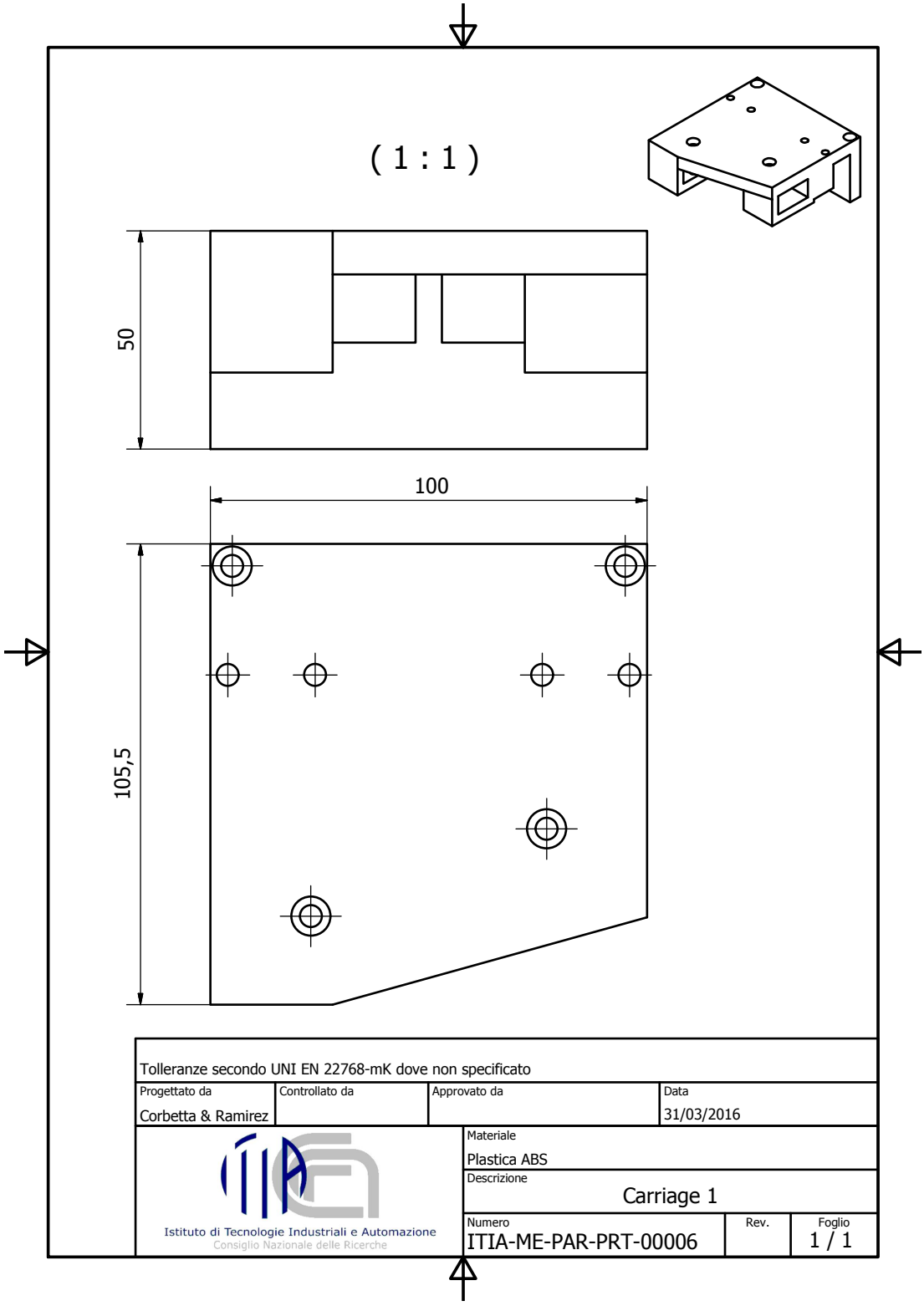
Technical Drawings A.11: Top of the corner box.



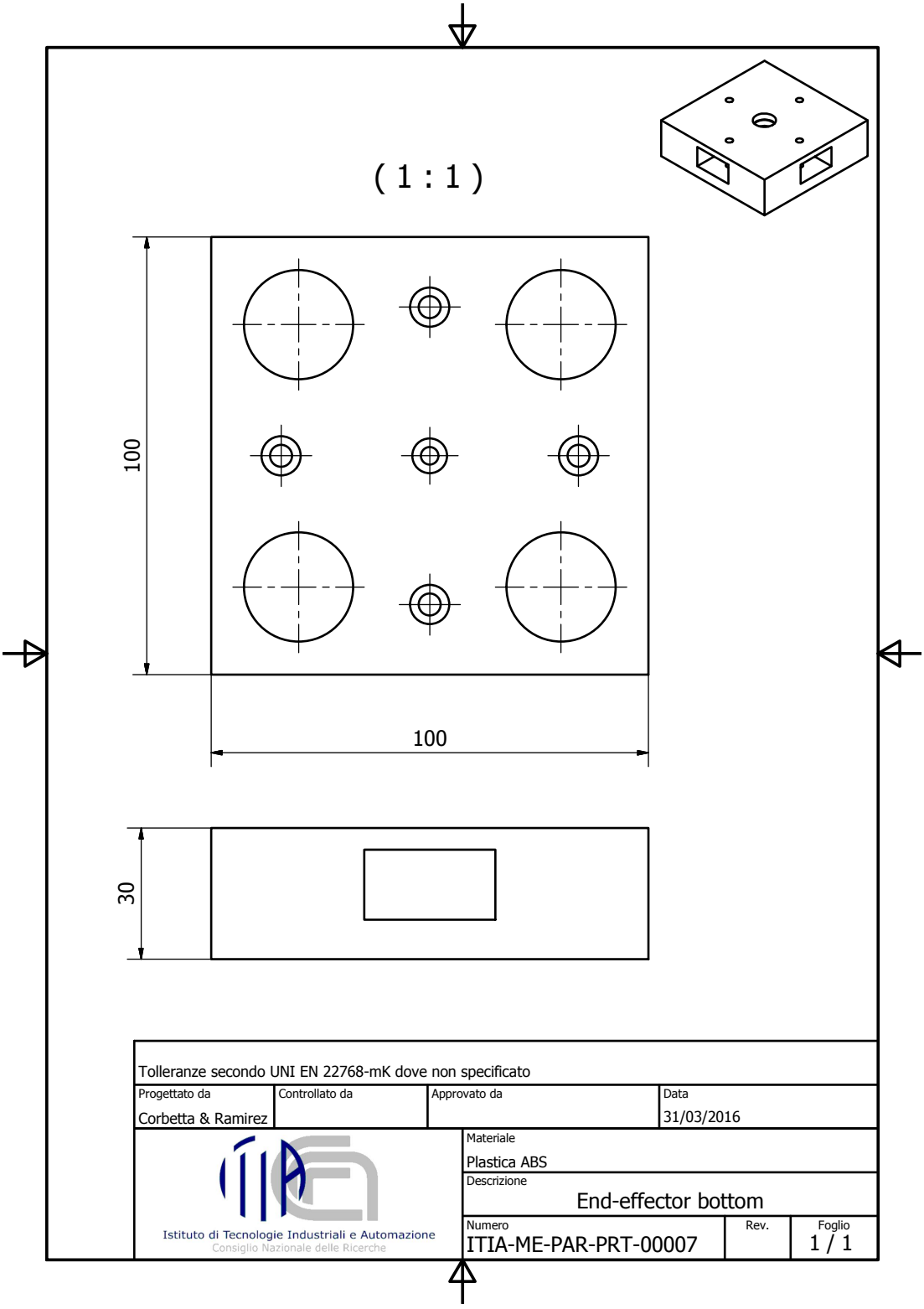
Technical Drawings A.12: Cam cover.



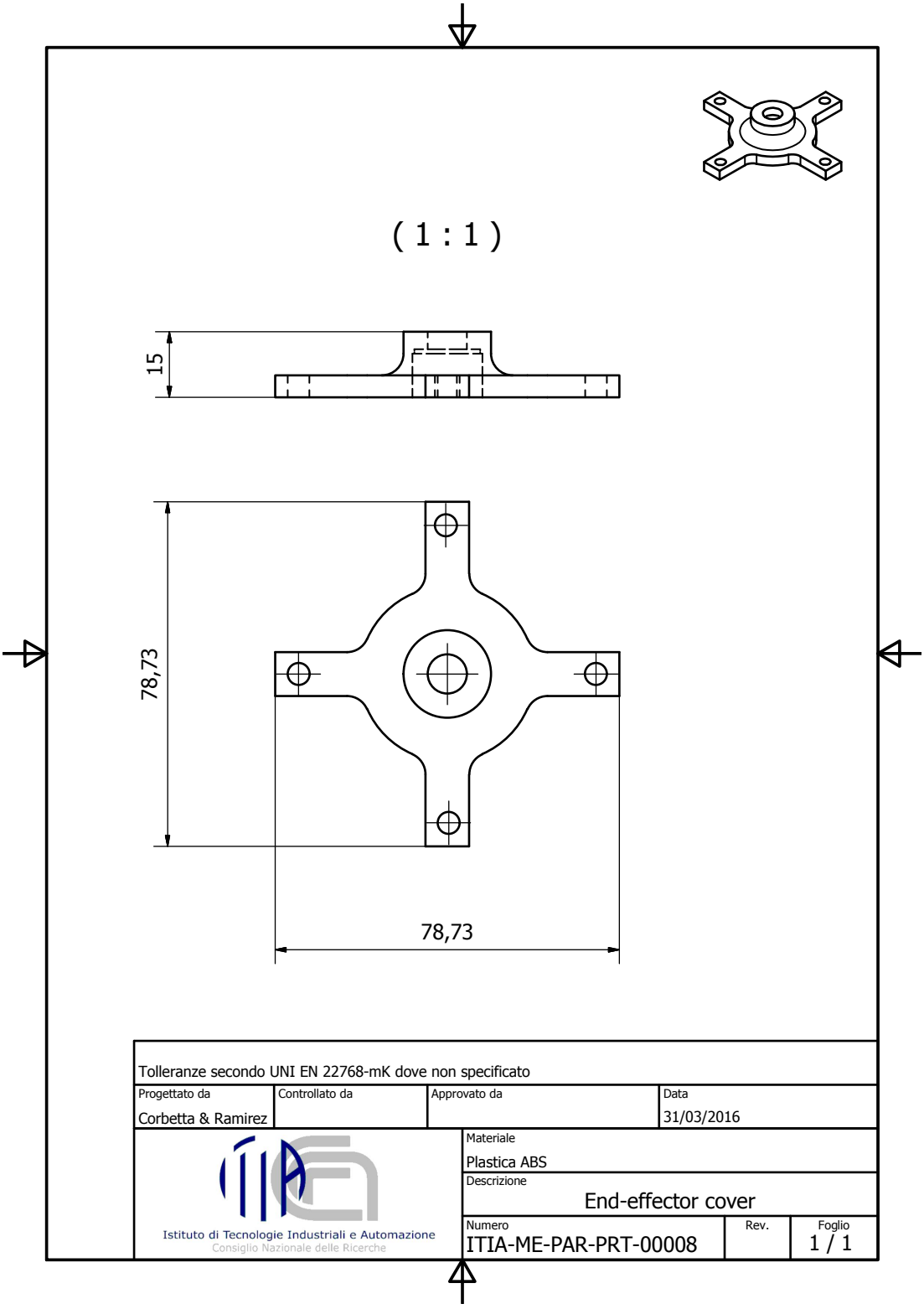
Technical Drawings A.13: Carriage 0.



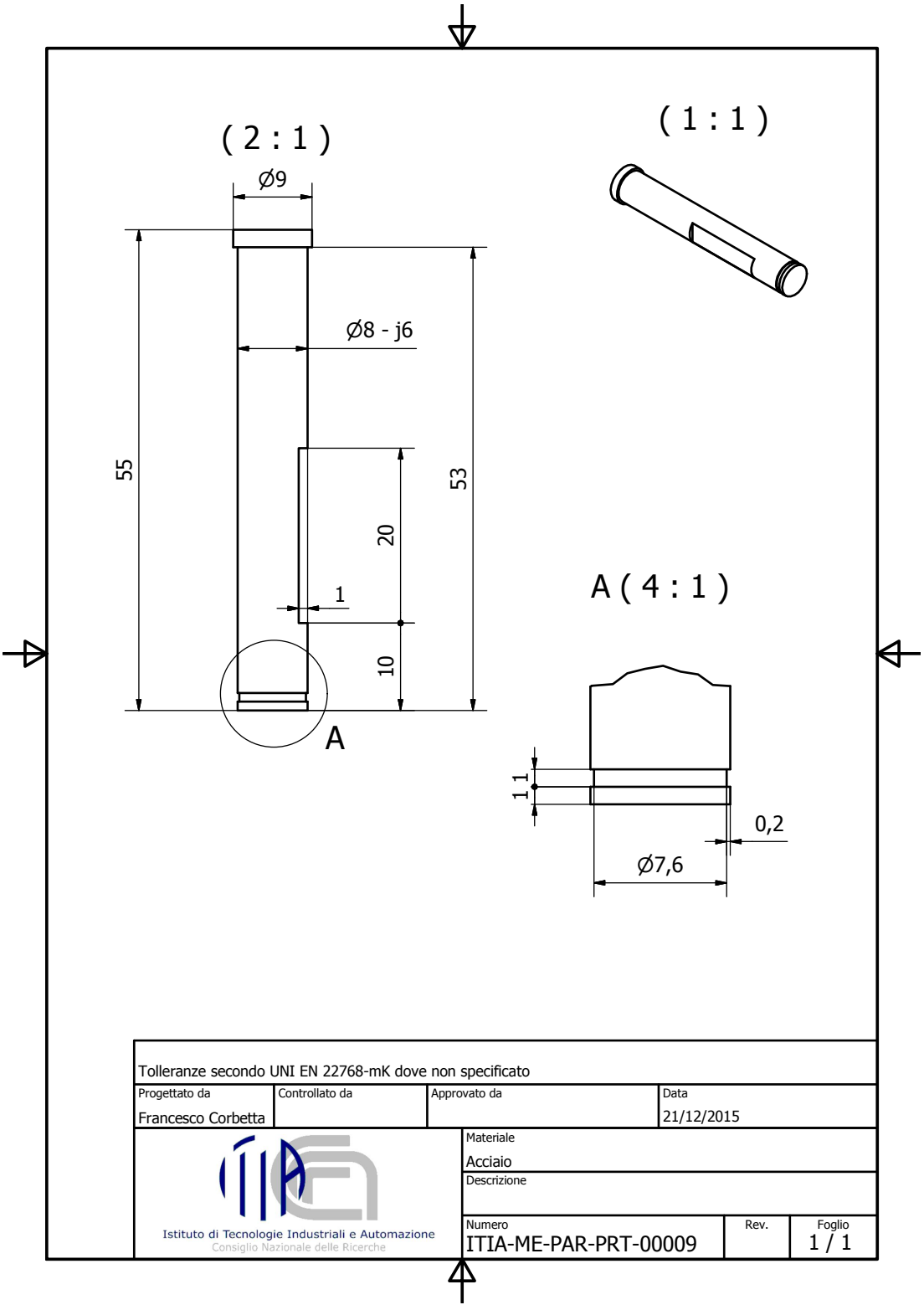
Technical Drawings A.14: Carriage 1.



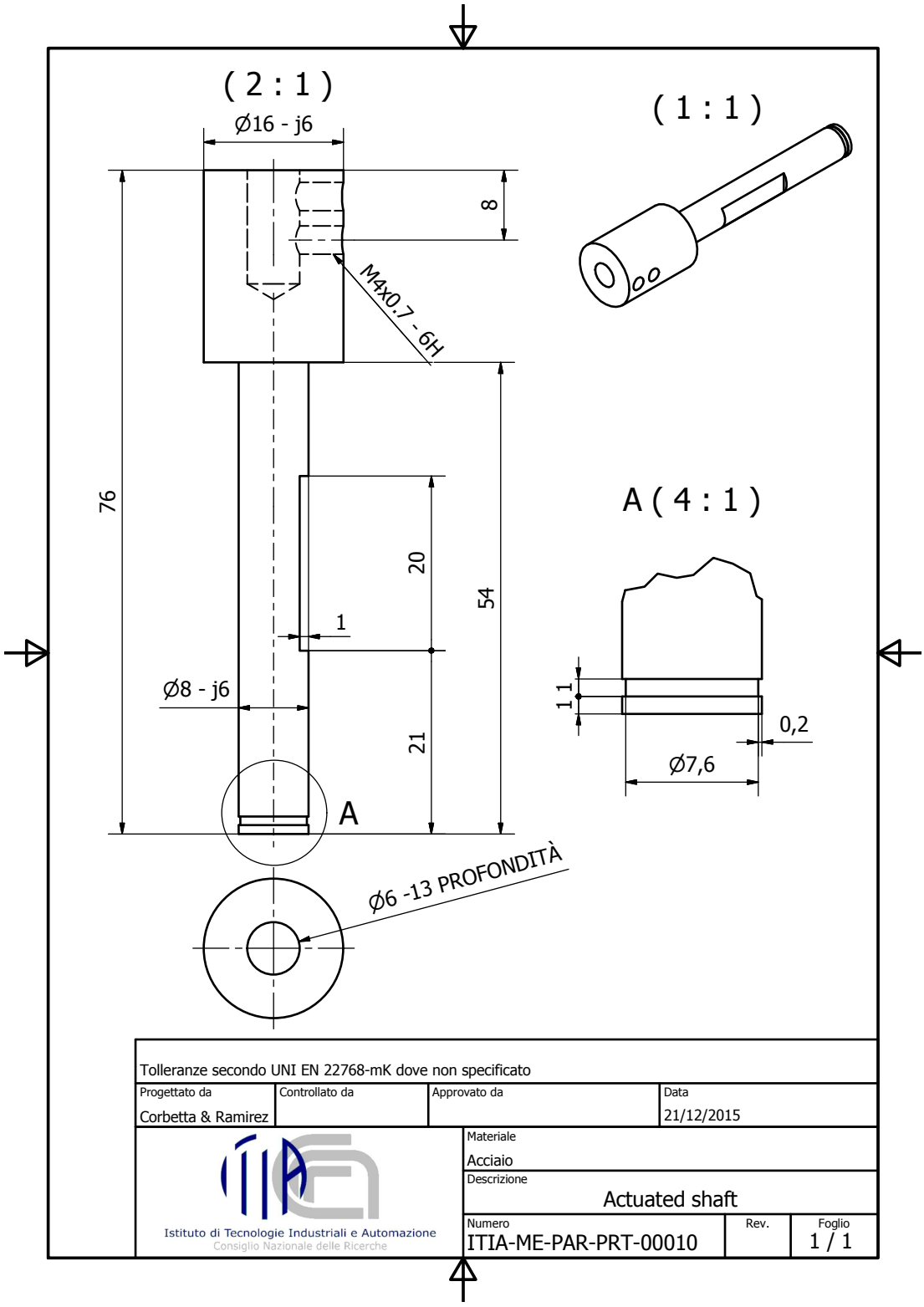
Technical Drawings A.15: End-effector bottom.



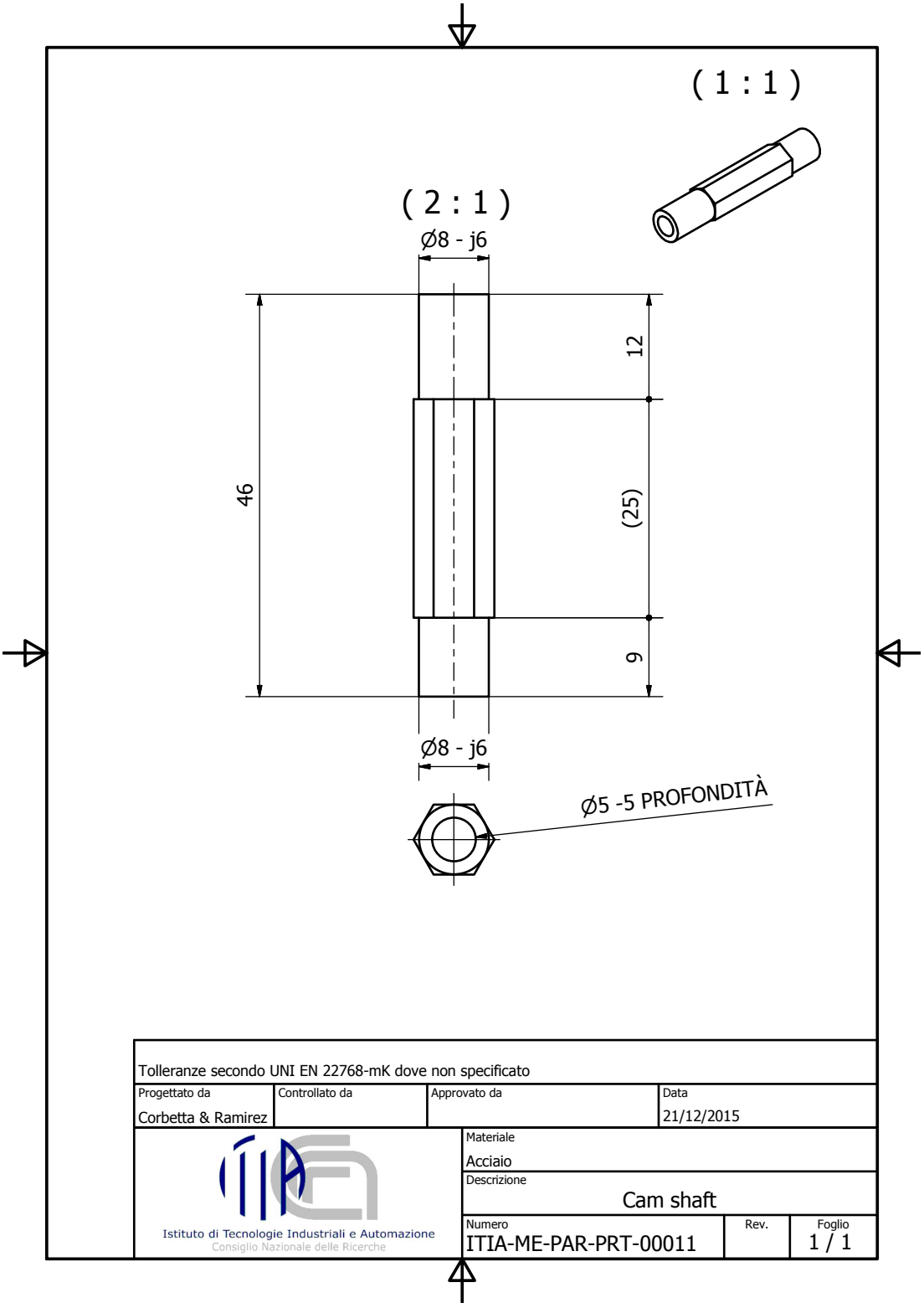
Technical Drawings A.16: End-effector cover.



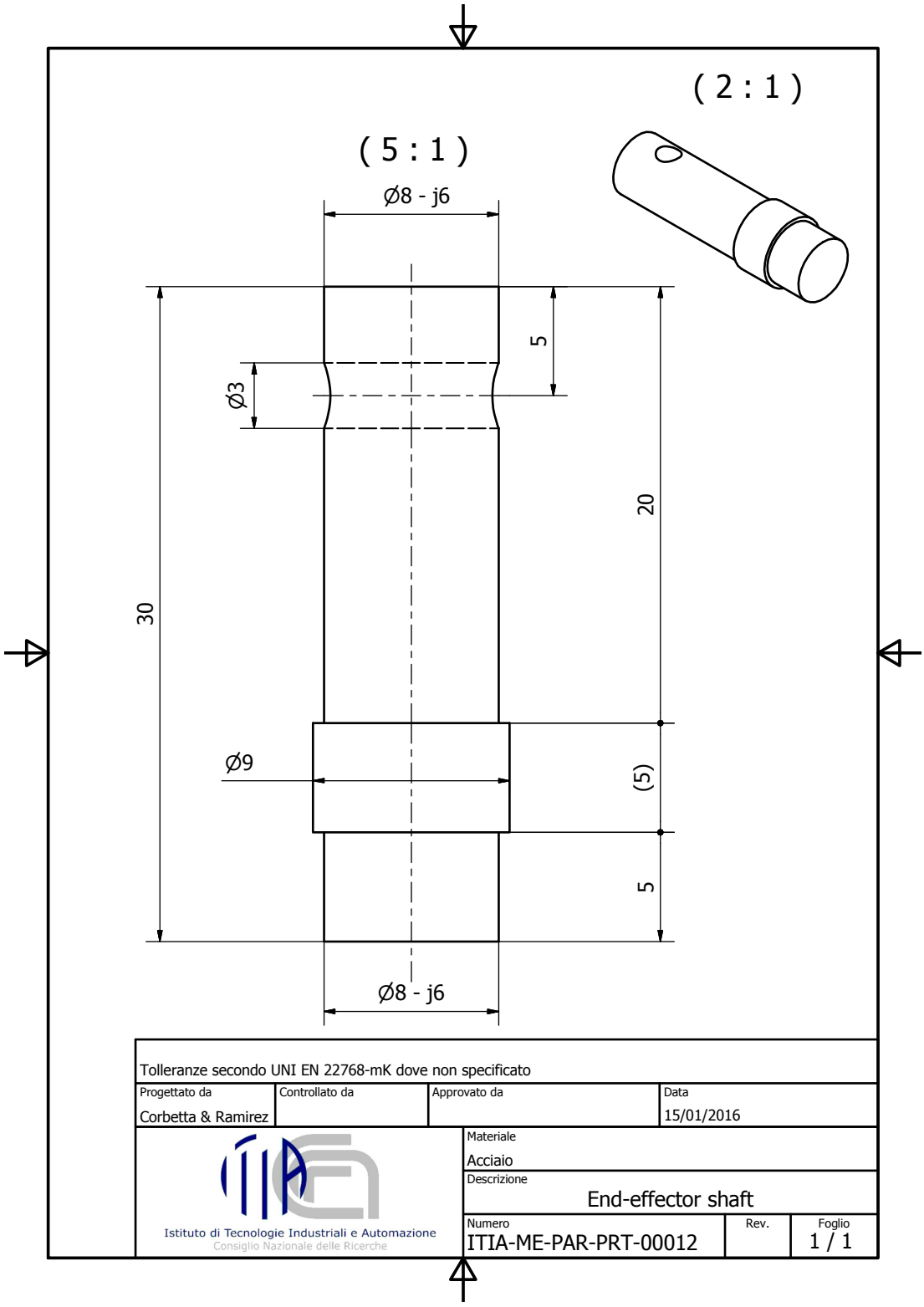
Technical Drawings A.17: Unactuated shaft.



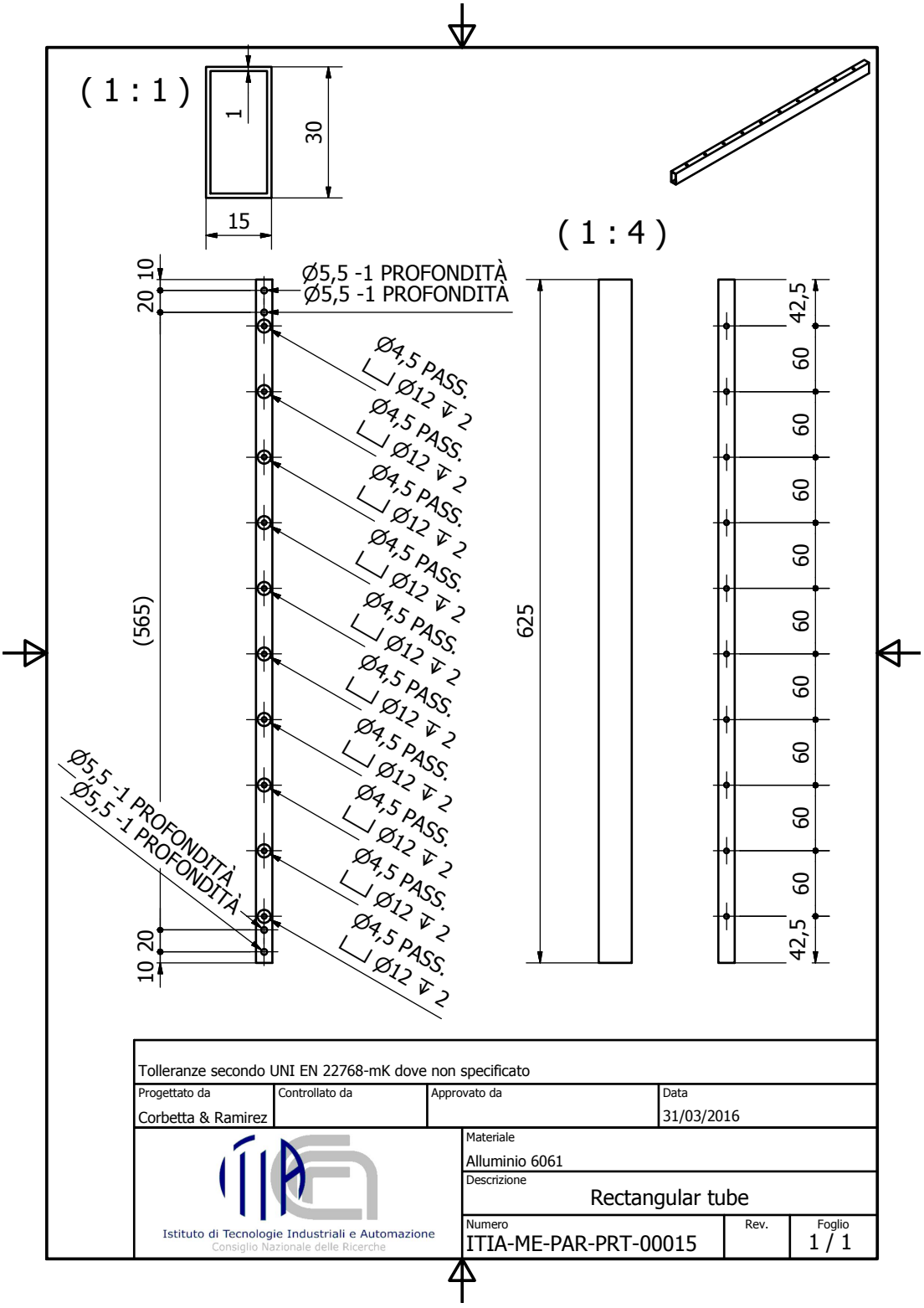
Technical Drawings A.18: Actuated shaft.



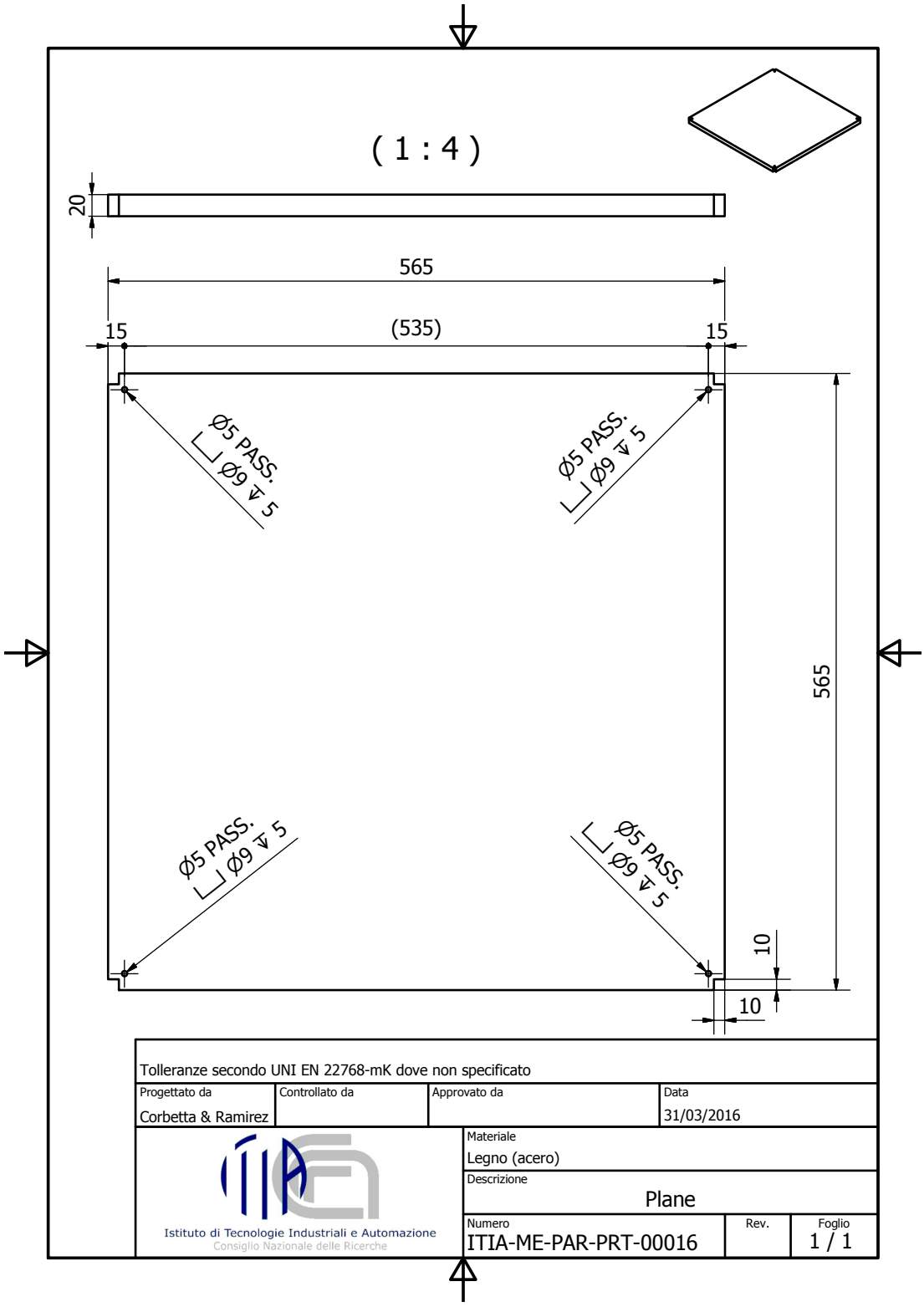
Technical Drawings A.19: Cam shaft.



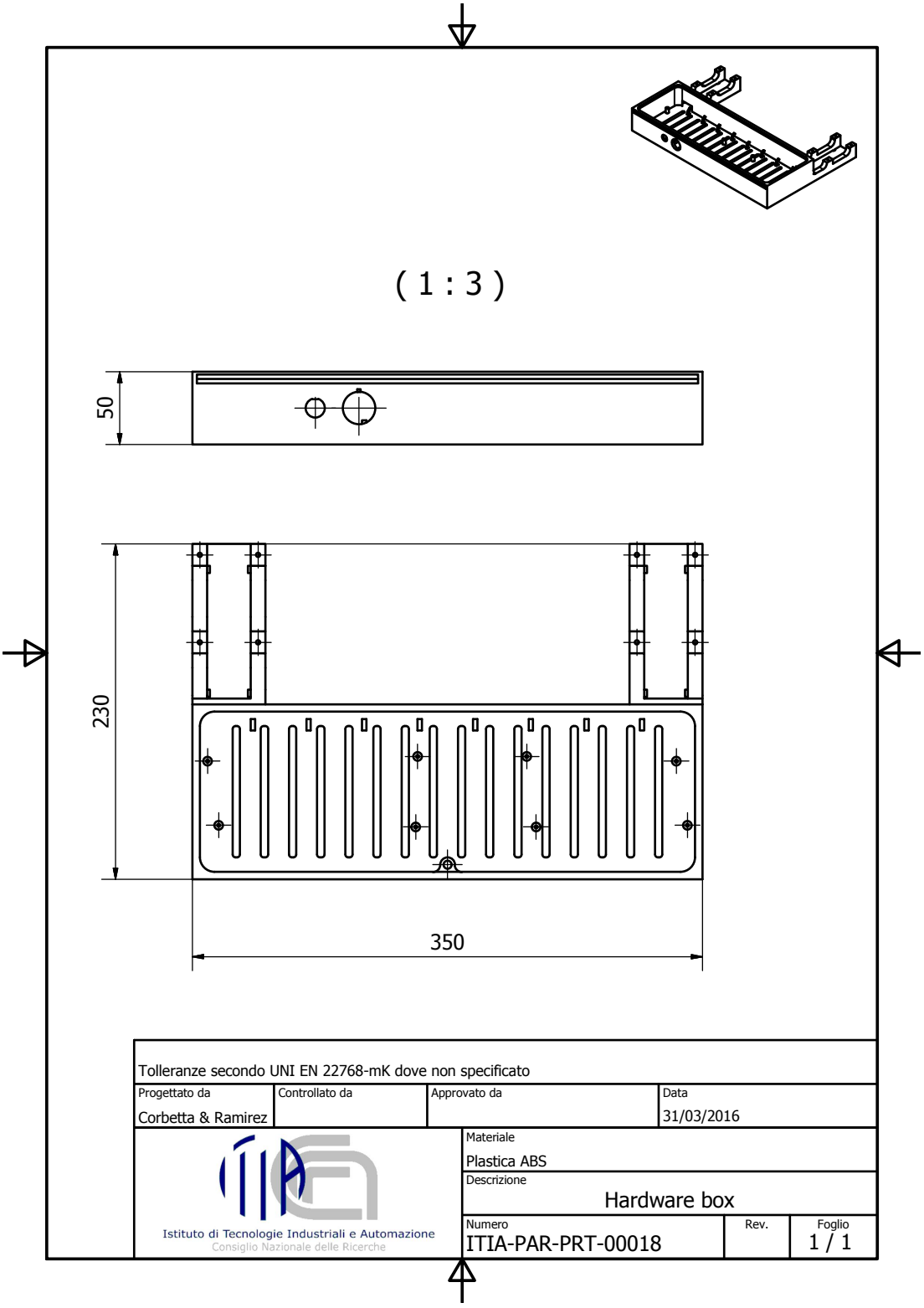
Technical Drawings A.20: End-effector shaft.



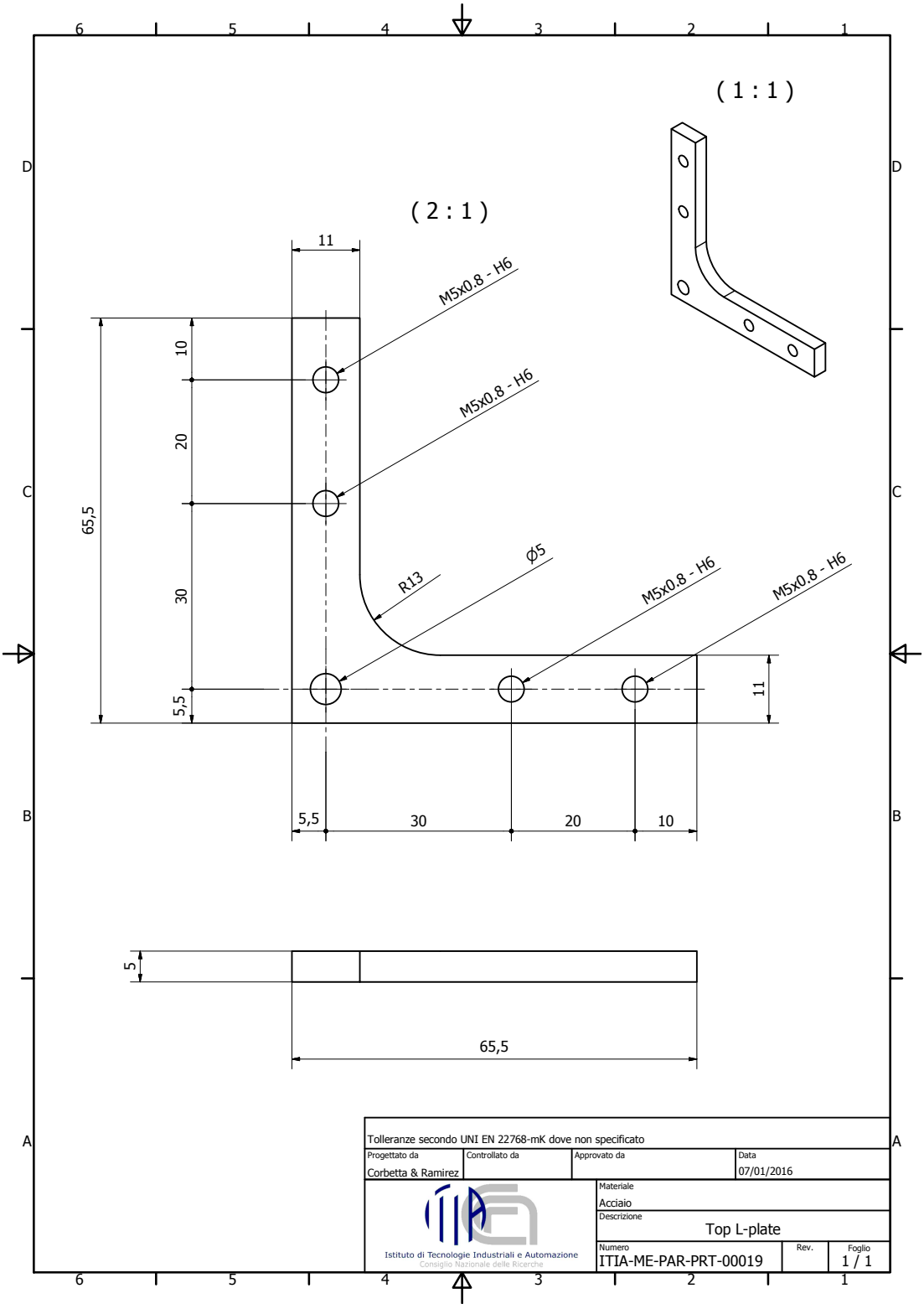
Technical Drawings A.21: Rectangular tube.



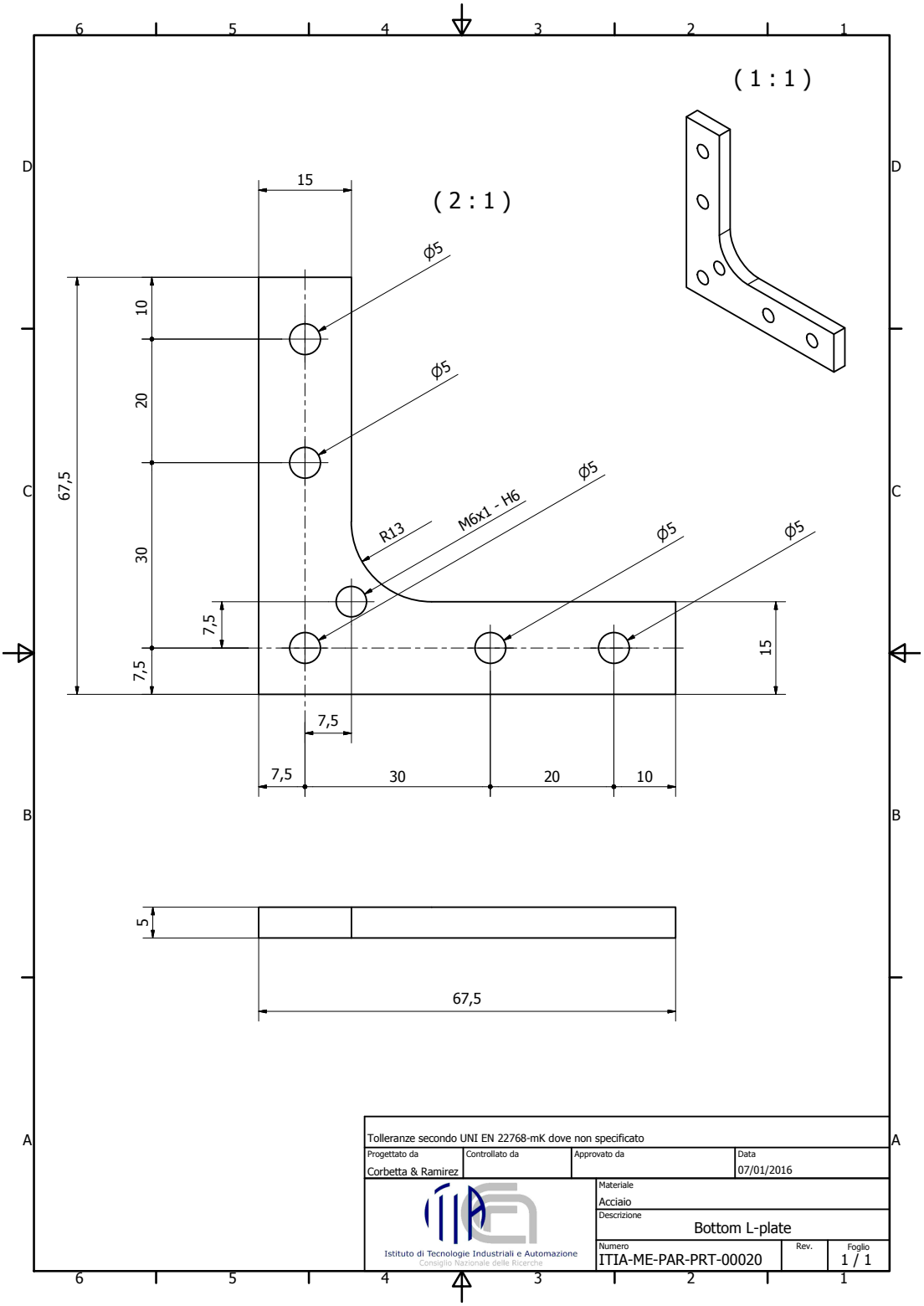
Technical Drawings A.22: Plane.



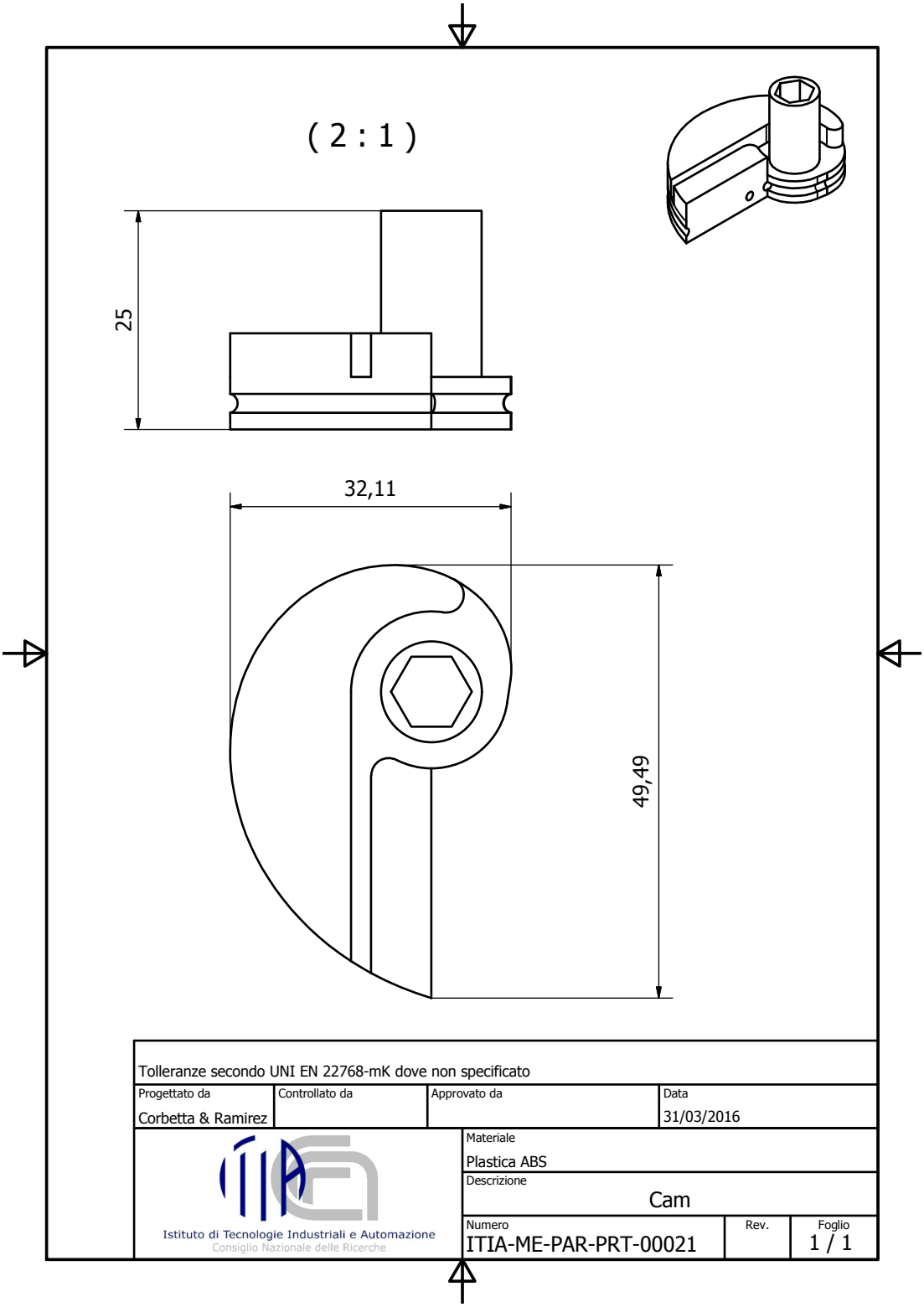
Technical Drawings A.23: Hardware box.



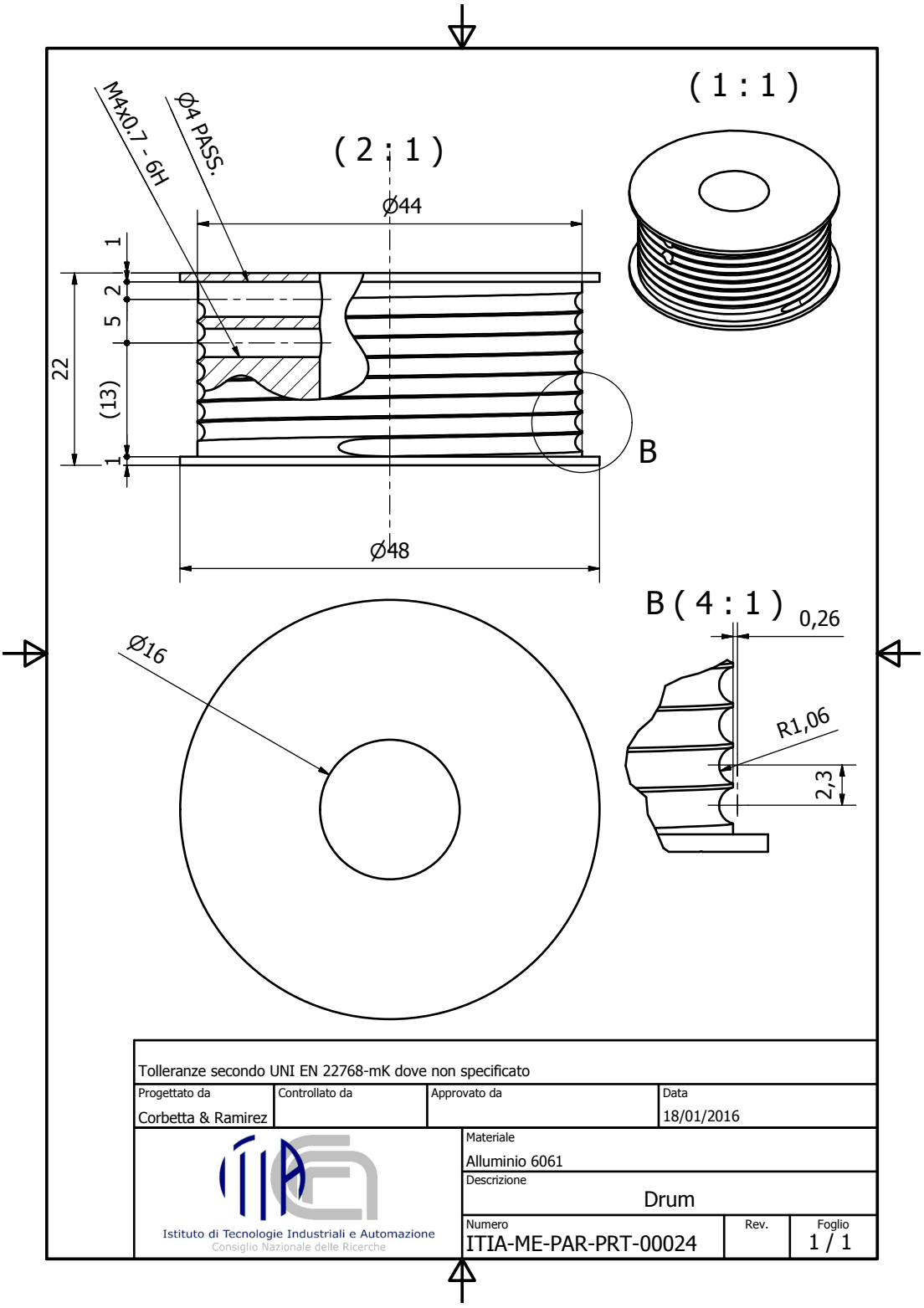
Technical Drawings A.24: Top L-plate.



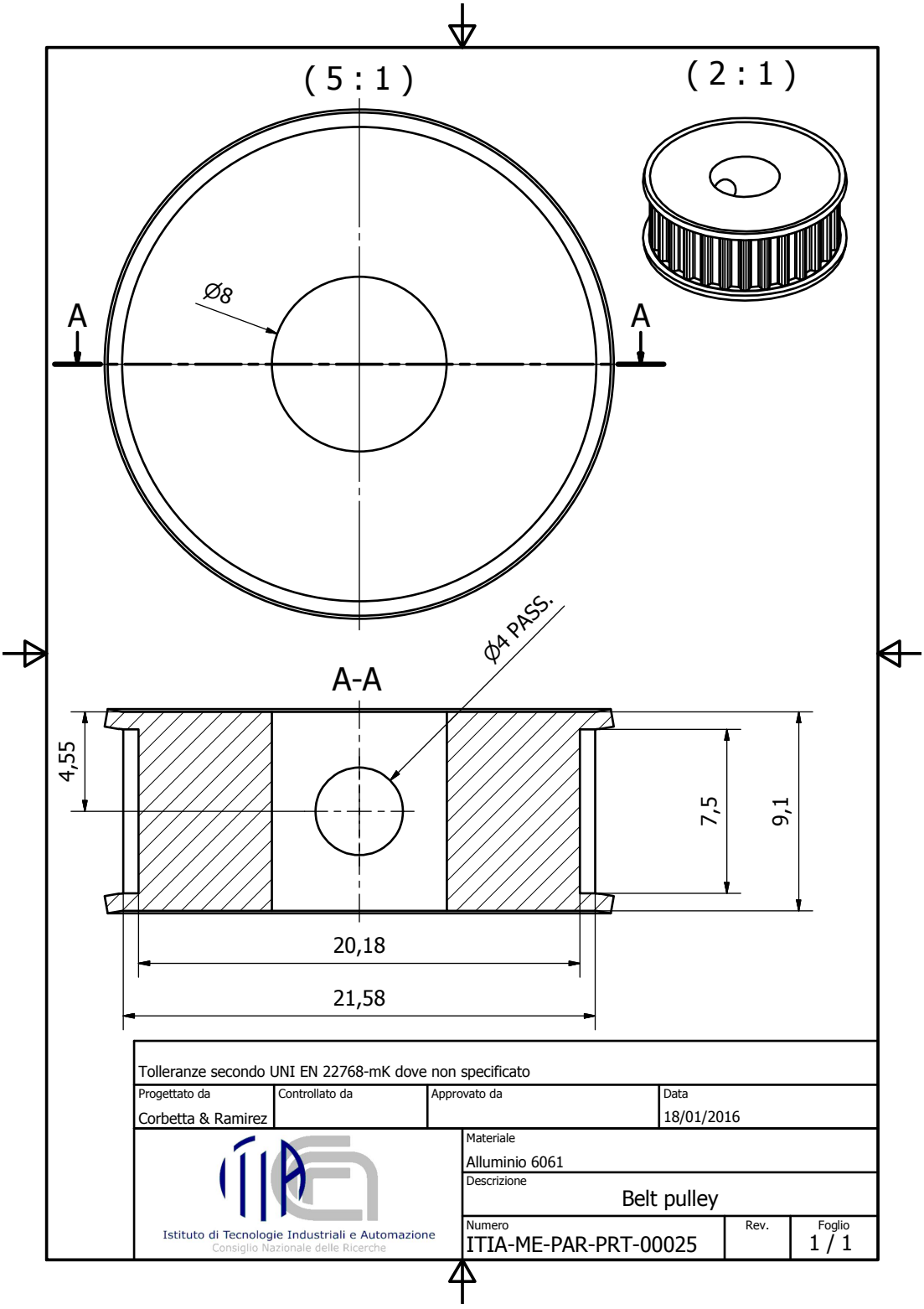
Technical Drawings A.25: Bottom L-plate.



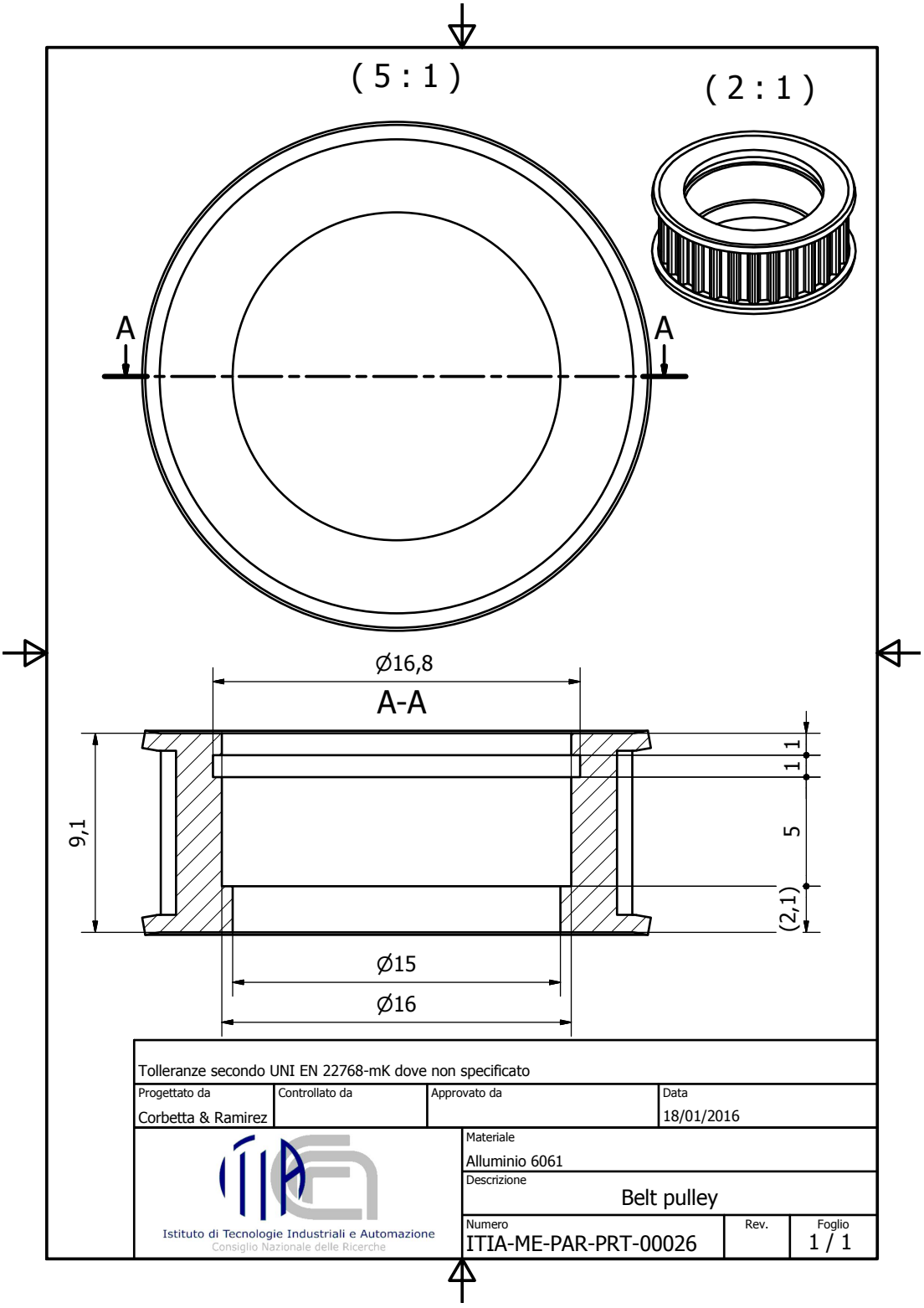
Technical Drawings A.26: Cam.



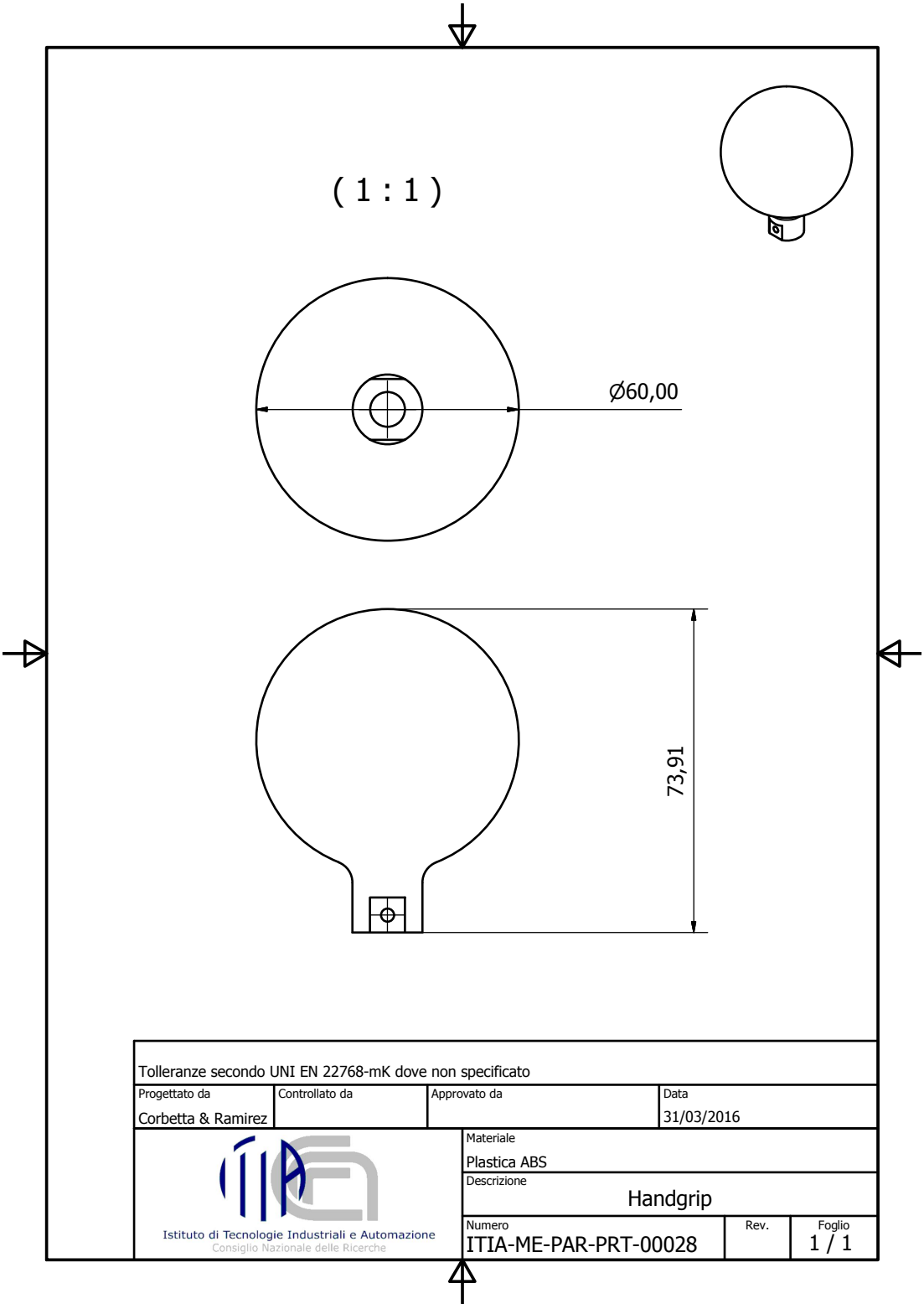
Technical Drawings A.27: Drum.



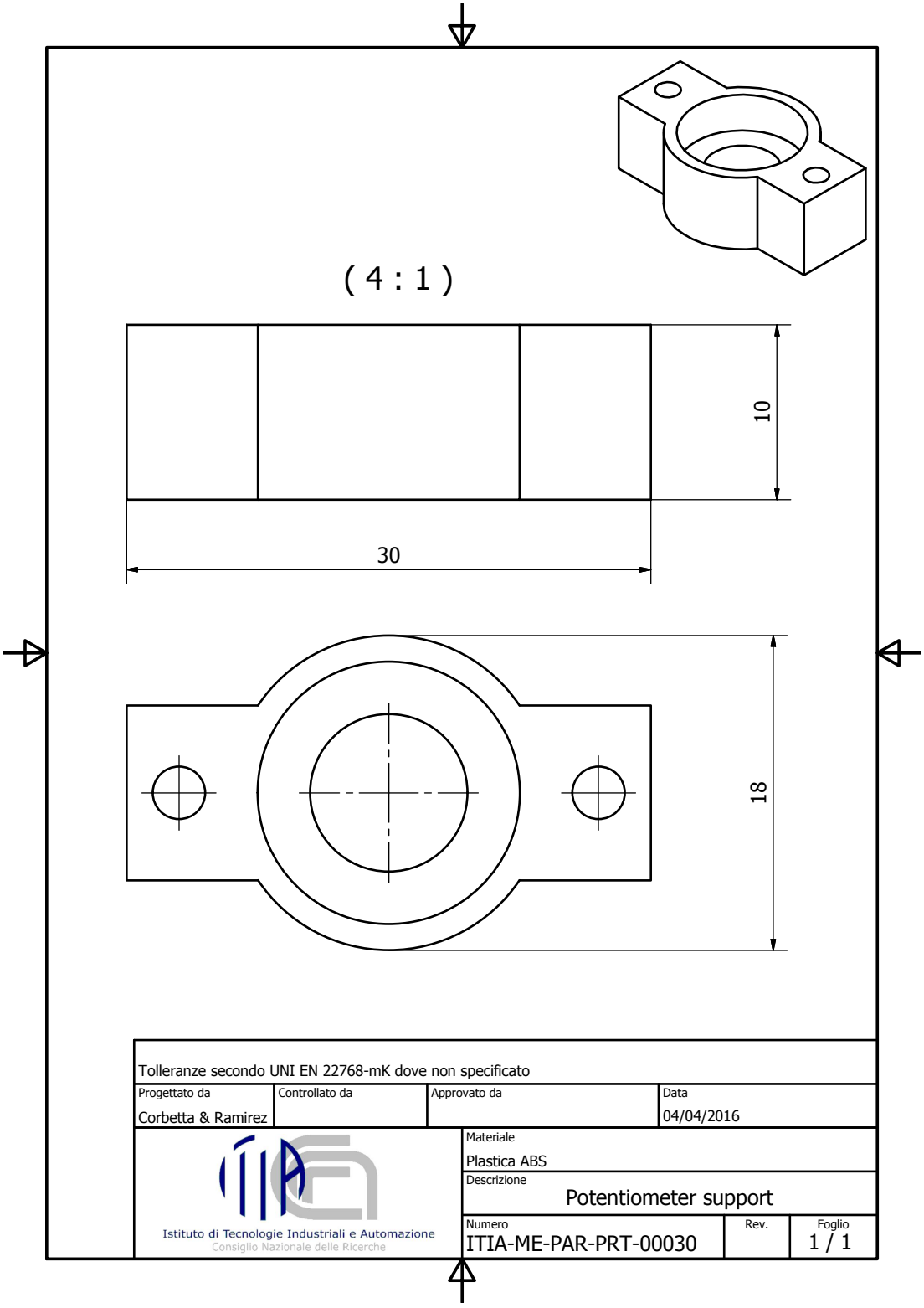
Technical Drawings A.28: Belt pulley A.



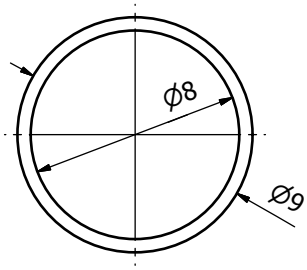
Technical Drawings A.29: Belt pulley B.

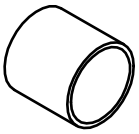


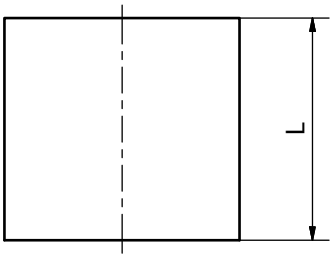
Technical Drawings A.30: Handgrip.



Technical Drawings A.31: Potentiometer support.







(5 : 1)

TABELLA	
Nome parte	L [mm]
ITIA-ME-PAR-PRT-00031	8.5
ITIA-ME-PAR-PRT-00032	3.5
ITIA-ME-PAR-PRT-00033	3.9
ITIA-ME-PAR-PRT-00034	1
ITIA-ME-PAR-PRT-00035	5.5
ITIA-ME-PAR-PRT-00036	3.95
ITIA-ME-PAR-PRT-00037	6.45
ITIA-ME-PAR-PRT-00038	1.9
ITIA-ME-PAR-PRT-00039	2
ITIA-ME-PAR-PRT-00040	4

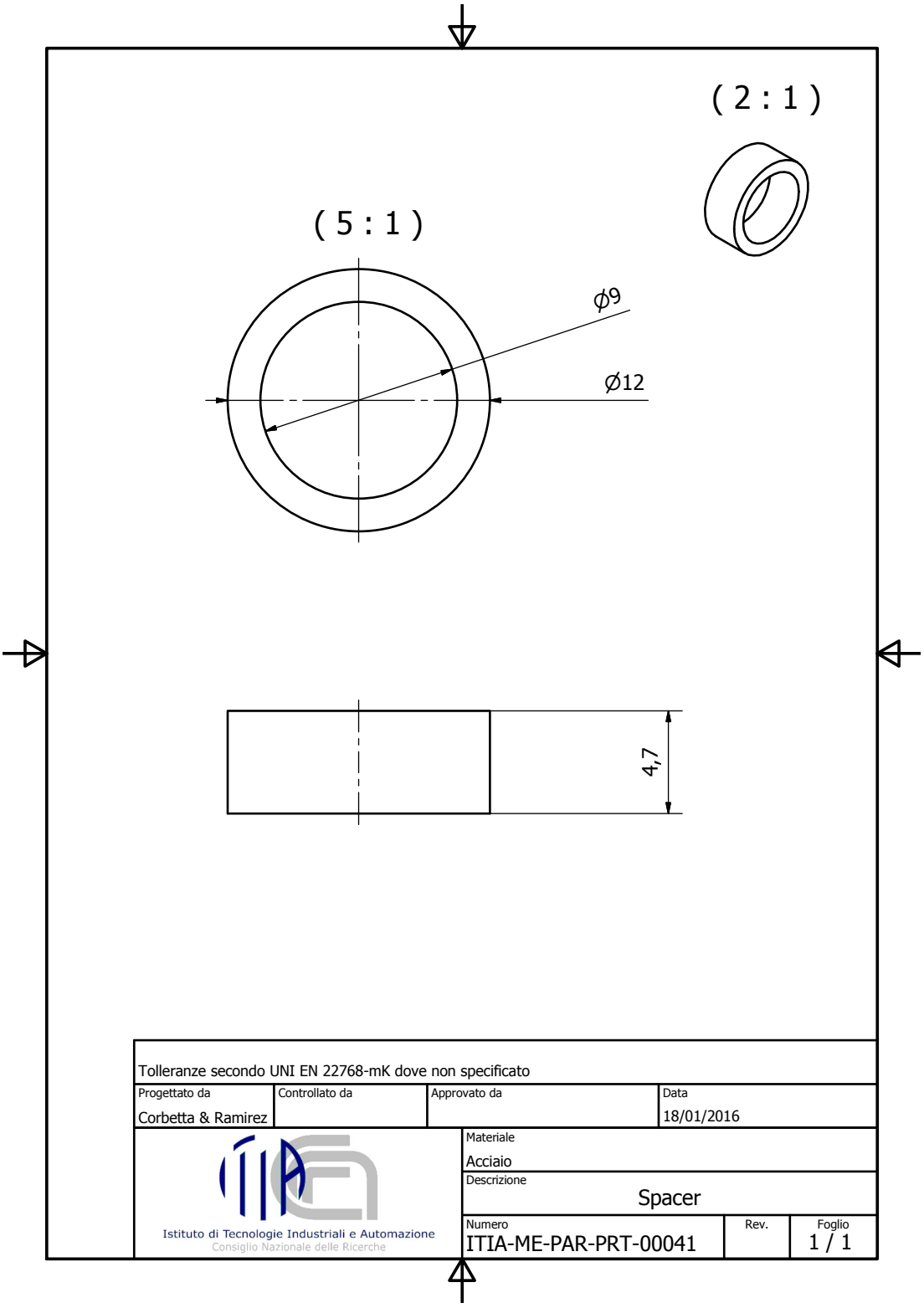
Tolleranze secondo UNI EN 22768-mK dove non specificato

Progettato da	Controllato da	Approvato da	Data
Corbetta & Ramirez			18/01/2016

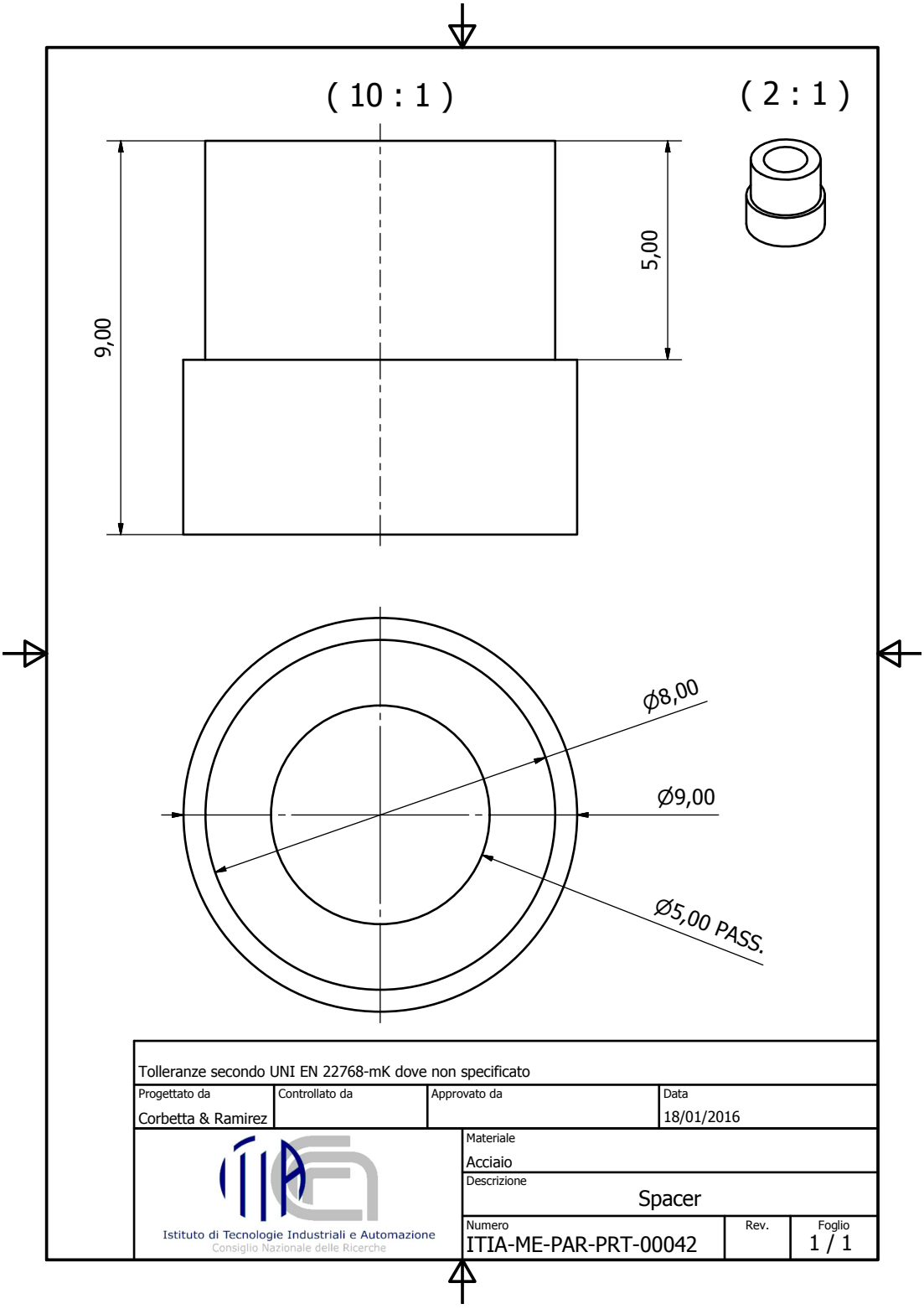
Istituto di Tecnologie Industriali e Automazione
Consiglio Nazionale delle Ricerche

Materiale		
Acciaio		
Descrizione		
Spacer		
Numero	Rev.	Foglio
ITIA-ME-PAR-PRT-00031		1 / 1

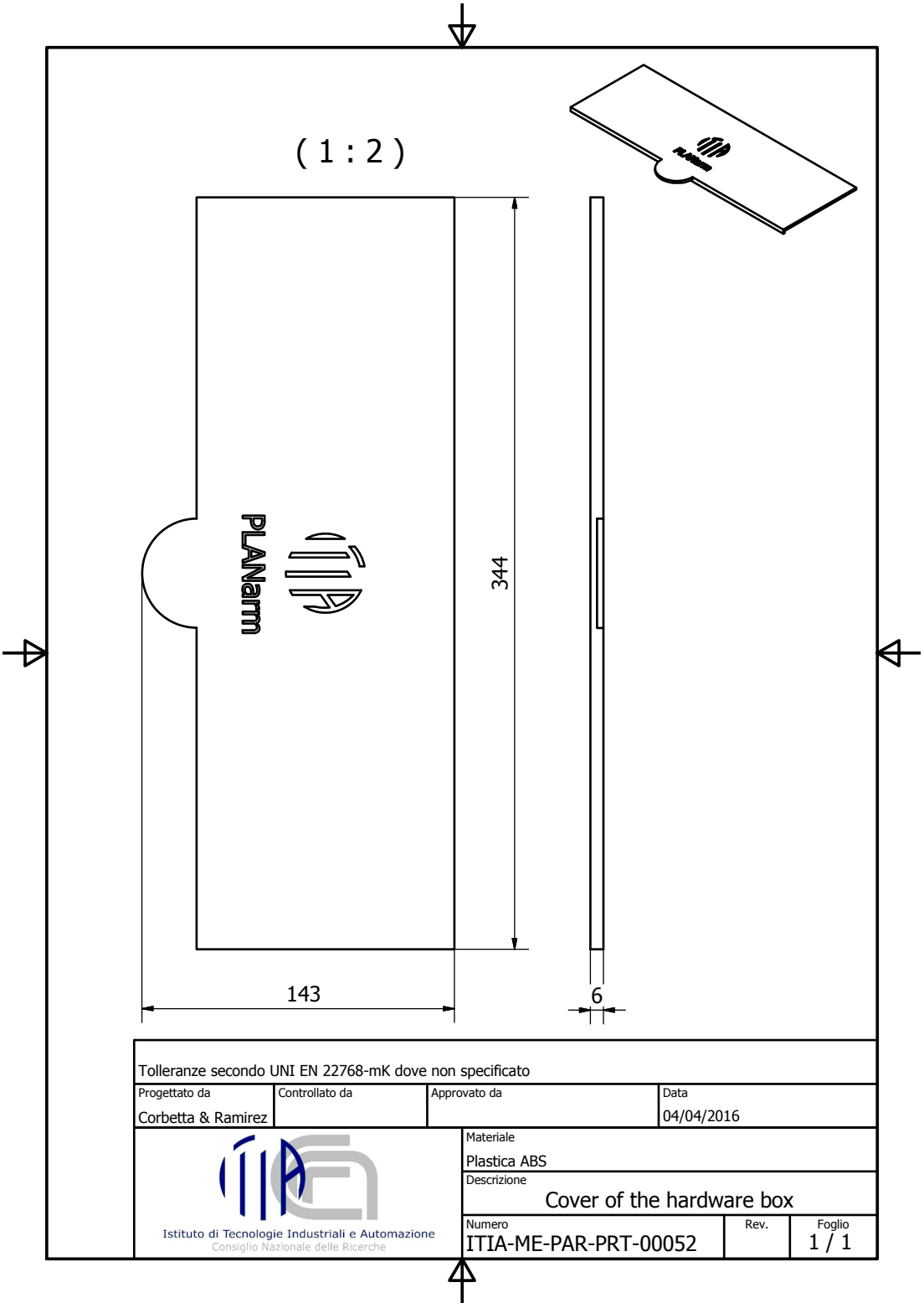
Technical Drawings A.32: Spacers A.



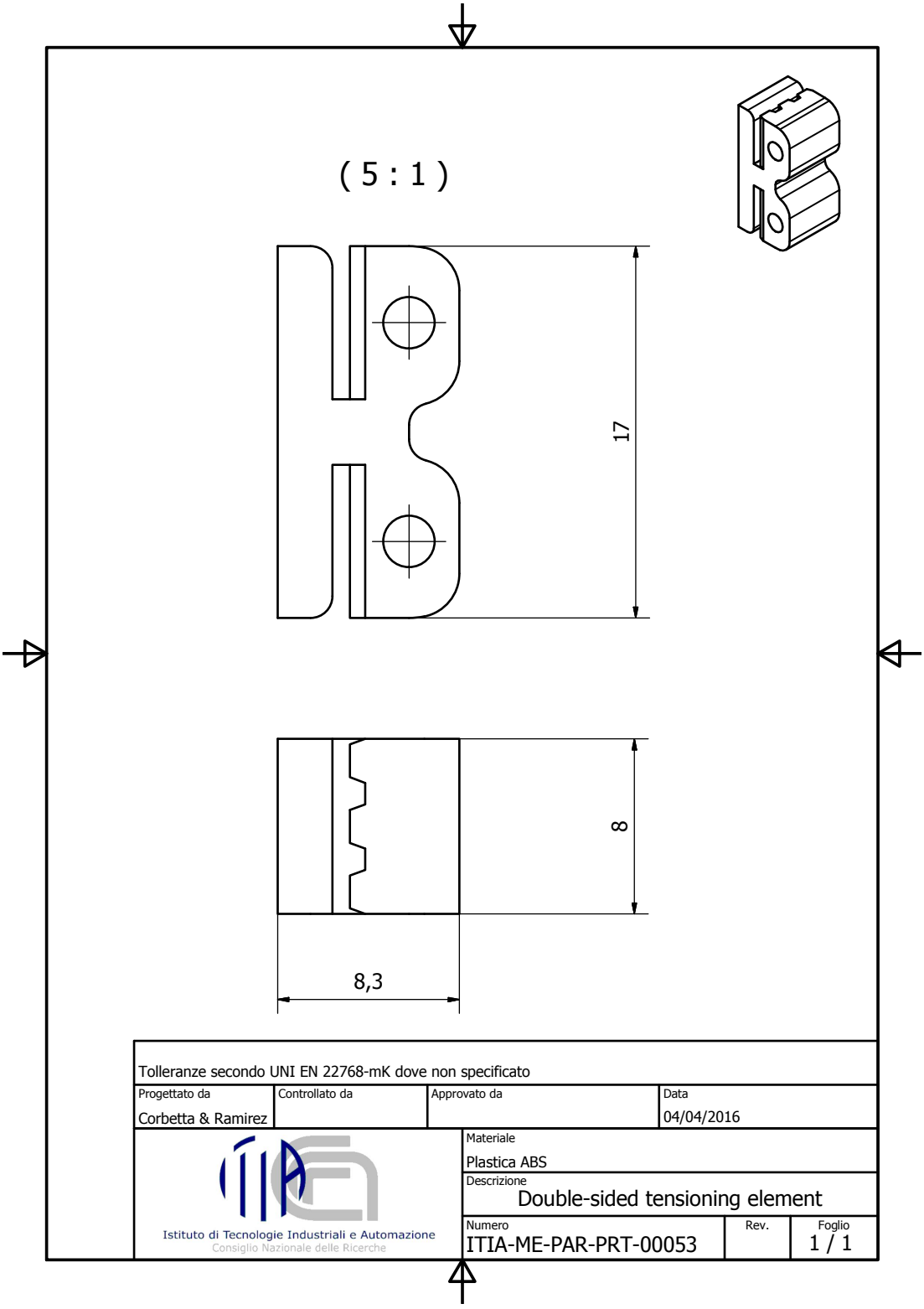
Technical Drawings A.33: Spacer B.



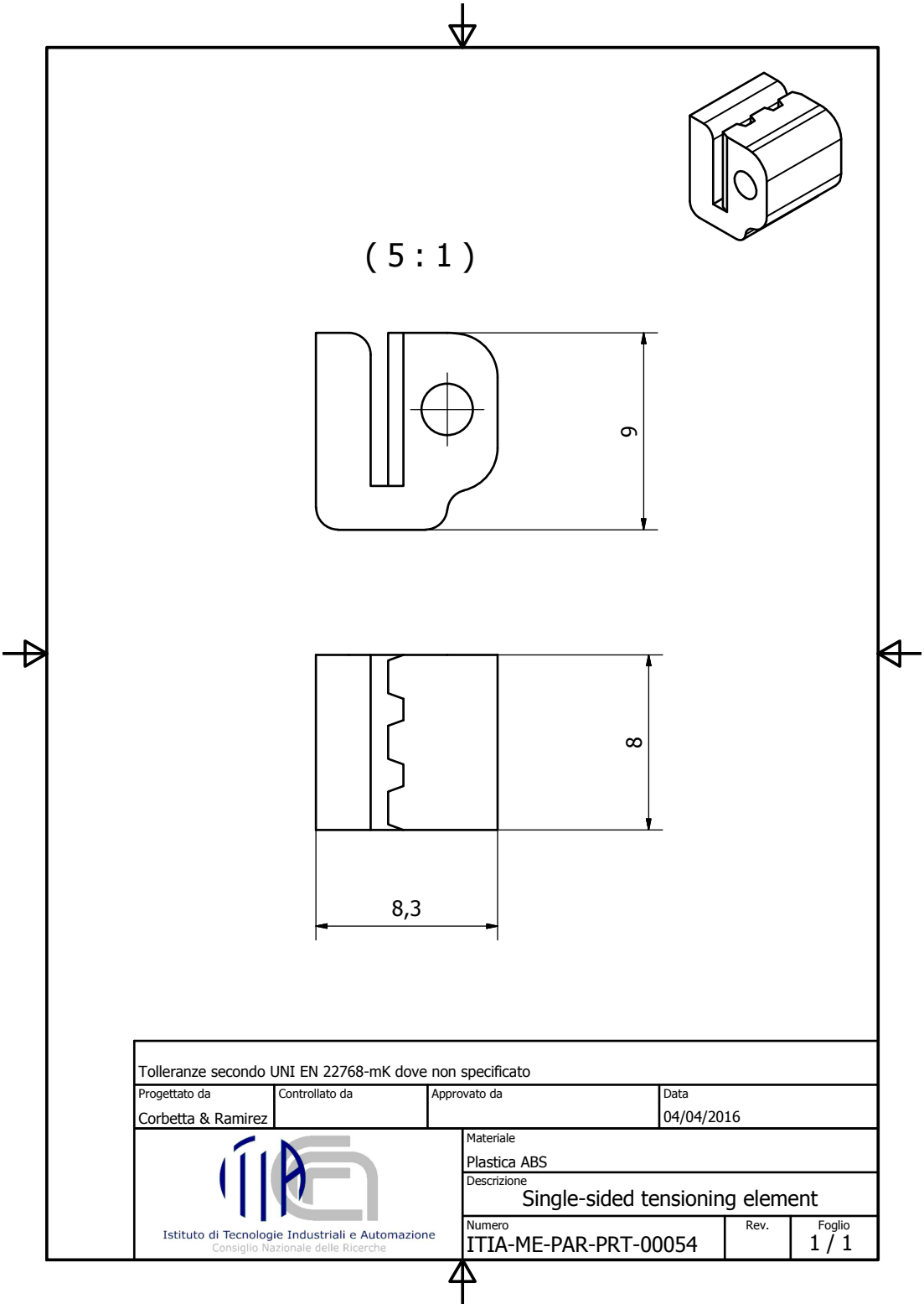
Technical Drawings A.34: Spacer C.



Technical Drawings A.35: Cover of the hardware box.



Technical Drawings A.36: Doubled-sided tensioning element.



Technical Drawings A.37: Single-sided tensioning element.

Appendix B

Resumen en Español

Resumen en lengua madre, según requerido por el artículo 6 del Acuerdo Específico de Doble Título entre el Politecnico di Milano (Milan, Italia) y la Universidad Técnica Federico Santa María (Valparaiso, Chile), firmado en Junio de 2015.

Introducción

El uso de dispositivos robóticos es cada vez más común en distintos campos de aplicación, desde los sistemas productivos automatizados a los dispositivos robóticos de rehabilitación. La introducción de un dispositivo robótico en una actividad tiene algunas ventajas respecto a la misma tarea realizada por un humano: posee un mejor desempeño y una mejor repetibilidad, puede trabajar en ambientes peligrosos y es más eficiente en tareas simples y repetitivas.

En el campo médico, los dispositivos robóticos son ampliamente utilizados en la rehabilitación de pacientes que han sufrido infartos cerebrales. Los infartos cerebrales, una de las principales causas de discapacidad en el mundo, ocurren cuando el flujo de sangre en el cerebro es interrumpido, causando la muerte de las células cerebrales a causa de la privación de oxígeno. Una de las posibles consecuencias del infarto cerebral es la parálisis de los músculos, y su contracción involuntaria. La rehabilitación de estos pacientes tiene como objetivo acelerar y maximizar la recuperación de la funcionalidad perdida. Ejercicios que estimulan movimientos cotidianos (alcanzar, tomar objetos, etc.) efectuados repetitivamente son parte importante de la rehabilitación, con el fin de regenerar los tejidos neuronales asociados a esos movimientos. Los dispositivos robóticos son particularmente adecuados para este tipo de ejercicios. En la rehabilitación del miembro superior, en particular, el uso de dispositivos robóticos se ha revelado eficaz, comparando con la rehabilitación convencional efectuada por un terapeuta.

Las principales ventajas del uso de dispositivos robóticos son múltiples, entre los más significativos se encuentran la posibilidad de practicar ejercicios manteniendo constante el desempeño en el tiempo, la oportunidad de cuantificar objetivamente el progreso del paciente a través de una lectura de fuerza, y la posibilidad de introducir una interfaz interactiva estimulante para el paciente y mejorar la eficacia de las sesiones.

Los dispositivos de rehabilitación para el miembro superior se diferencian entre exoesqueletos y *end-effector*. En esta memoria se ha diseñado un robot del tipo *end-effector*, del cual existe una amplia gamma de dispositivos disponibles para los hospitales. Entre los más relevantes se encuentra el MIT-Manus, los robot Sophia-3 y Sophia-4 ("*String-operated planar haptic interface for arm rehabilitation*"), el CBM-Motus, el NeReBot y

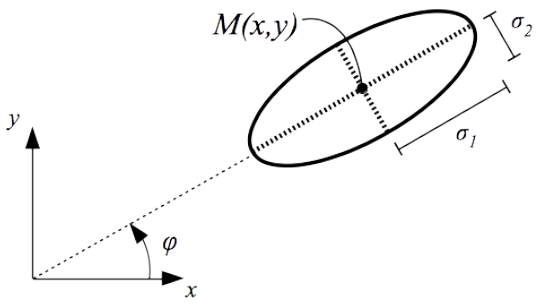


Figura B.1: Elipse de rigidez centrada en $M(x, y)$, orientada con ángulo φ y con valores de rigidez σ_1 y σ_2.

el MACARM.

Estos dispositivos poseen una interfaz robot-paciente flexible y natural a través de un sistema de control de los motores. Una alternativa válida es el uso de actuadores a rigidez variable (VSA, "*Variable Stiffness Actuator*"), donde es posible regular la posición y rigidez aprovechando un elemento elástico responsable de la flexibilidad del contacto paciente-robot. El uso de VSAs como alternativa al control computacional de una estructura rígida tiene como ventajas ser más segura en la interacción hombre-robot, y de poder entregar una lectura de fuerza mediante un sensor de posición, sin la necesidad de sensores de fuerza, comúnmente más costosos.

El dispositivo diseñado en esta memoria tiene como objetivo presentar las siguientes características: permitir un movimiento planar; tener una cinemática paralela accionada mediante cables; utilizar mecanismos VSA; y ser relativamente pequeño y económico, con el objetivo de ser usado directamente en la casa de los pacientes.

Diseño Conceptual

El *PLANarm* consiste en un robot planar, *cable-driven* con arquitectura cinemática paralela de tipo *end-effector*. La cinemática del robot debe ser capaz de entregar un movimiento planar al *manipulandum* y regular la flexibilidad. Con flexibilidad se entiende la resistencia que el robot opone a una fuerza externa. La rigidez en un robot planar se describe a través de la elipse de rigidez.

La elipse de rigidez es una representación gráfica de la flexibilidad del robot en el *manipulandum*. Fundamentalmente, se trata de una elipse centrada en el *manipulandum* en la cual el eje mayor y menor corresponden respectivamente a la rigidez máxima y mínima. La orientación de los ejes identifica la dirección donde se encuentran estos valores de rigidez en el plano, como mostrado en la Fig. B.1.

Con el objetivo de obtener este comportamiento, dos arquitecturas cinemáticas son propuestas. Una primera arquitectura propone el uso de tres SEAs (*Series Elastic Actuators*) dispuestos de manera antagonista entre ellos, como presente en la Fig. B.2. Cada actuador controla una coordenada de posición y rigidez independientemente. Esta arquitectura presenta una limitación: en ciertas direcciones no es capaz de obtener una relación mayor a 3 entre la rigidez mayor y menor de la elipse de rigidez. Como este límite nace de la hipótesis de utilizar solo dispositivos con rigidez positiva, se ha concebido un actuador capaz de entregar rigidez negativa, permitiendo superar esta

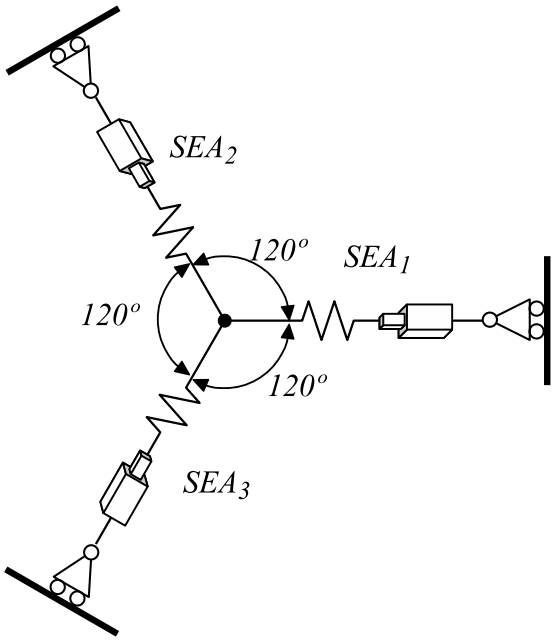


Figura B.2: Arquitectura cinemática con tres SEAs (*Series Elastic Actuators*) antagonistas entre ellos, para controlar posición y rigidez en el plano.

limitación. La introducción del dispositivo en la arquitectura cinemática conlleva la presencia de zonas de inestabilidad donde la rigidez global del dispositivo es negativa. Sistemas inestables no son adecuados para sistemas mecatrónicos debido a que introducen dinámicas indeterminadas, en consecuencia, esta solución cinemática es rechazada.

Se propone una segunda configuración cinemática, que incorpora cuatro SEAs, antagonistas en pares, que componen dos VSAs perpendiculares entre ellos. Esta configuración tiene la desventaja de no lograr controlar arbitrariamente la orientación de la elipse de rigidez. Para obtener este comportamiento es fundamental que los patines donde están fijos los actuadores tengan un movimiento sincronizado con el *end-effector* de tal manera que la configuración ortogonal no se pierda. Esta arquitectura permite controlar independientemente la posición en el plano y la rigidez en las dos direcciones x e y. Sin embargo, se ha encontrado un efecto de acoplamiento entre los dos VSAs, donde la posición y la fuerza que genera un VSA afecta la rigidez del otro VSA. Por lo tanto, la rigidez global en el *manipulandum* para cada dirección resulta (como explicado en la sección 3.2):

$$K_x = 2k_x + f_y \left(\frac{1}{h_{y0}} + \frac{1}{h_{y1}} \right)$$
$$K_y = 2k_y + f_x \left(\frac{1}{h_{x0}} + \frac{1}{h_{x1}} \right)$$

Donde K_x y K_y son valores de rigidez del *manipulandum* en las dos direcciones; k_x y k_y son la rigidez de los resortes, f_x y f_y son las fuerzas generadas por los actuadores y $h_{x0}, h_{x1}, h_{y0}, h_{y1}$ son las distancias descritas en la Fig. B.3. A pesar del efecto encontrado, es posible controlar la rigidez en ambas direcciones teniendo en cuenta el

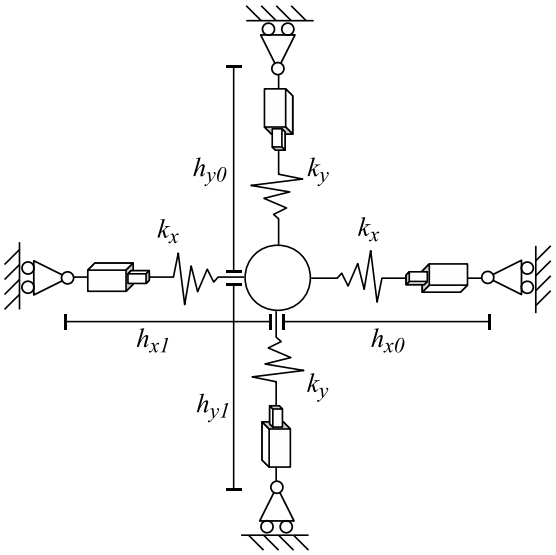


Figura B.3: Arquitectura cinemática con cuatro SEAs (*Series Elastic Actuators*) antagonistas en pares, para controlar posición y rigidez en el plano.

acoplamiento. Por lo tanto, esta última arquitectura es utilizada para el dispositivo.

Análisis Cineto-estático

Viene propuesto el diseño para la transmisión mecánica del dispositivo. Esta tiene como objetivo las siguientes funciones: mantener alineadas las dos parejas de SEAs de modo que se comporten como VSAs, y mantener la ortogonalidad entre ambos VSAs. en la Fig. B.4 es presentado un solo VSA, el cual es responsable de: efectuar la fuerza correspondiente a través de dos cables que traccionan los resortes, y garantizar la ortogonalidad de las fuerzas efectuadas por el otro VSA a través del movimiento de los carros correspondientes a través de una transmisión a correas. El dispositivo está compuesto

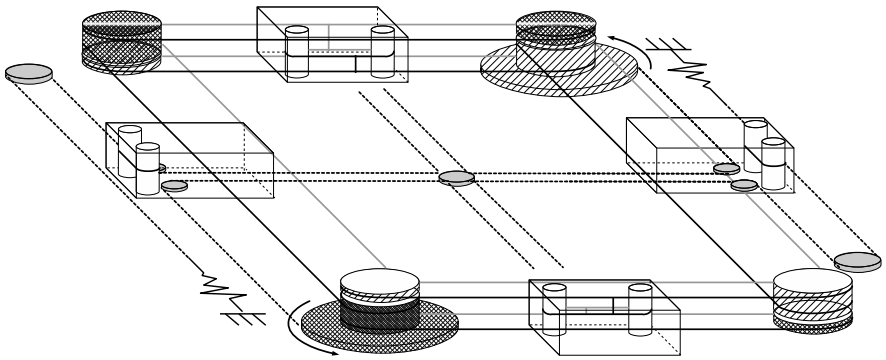


Figura B.4: Mecanismo VSA ideado para implementar la arquitectura cinemática escogida. Representa desplazamiento y control de rigidez para una dirección, mediante dos motores rotativos, dos resortes, y un sistema de transmisión a cables y correas.

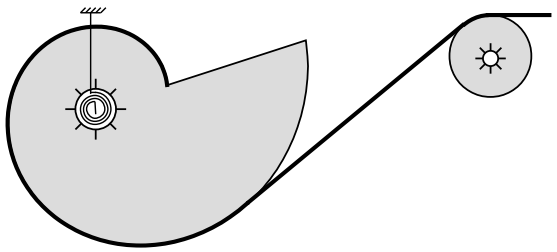


Figura B.5: El LinWWC-SEA (*Linear Wire-Wrapped Cam SEA*), dispositivo que comprende una leva rotativa, un resorte de torsión, un cable y una polea; con el objetivo de generar un efecto de resorte no-lineal en el cable.

de dos VSAs girados en 90°entre ellos, para cubrir las dos direcciones.

El comportamiento de un VSA es el siguiente: los motores rotativos actúan sobre la tensión y la rigidez del cable gracias al alargamiento del resorte no-lineal conectado al otro extremo del cable. A través de la polea en el *end-effector*, la tensión del cable genera una fuerza lineal que produce el movimiento. Dependiendo de la sincronización en la rotación de ambos motores, se pueden conseguir diferentes efectos en el *end-effector*. Cuando un motor enrolla el cable y el otro lo desenrolla en igual cantidad, se genera un movimiento del *end-effector* sin modificar la rigidez. En cambio, cuando los motores enrollan o desenrollan simultáneamente, se genera un alargamiento de ambos resortes no-lineales sin desplazar el *end-effector*, generando en consecuencia un cambio en la rigidez de los cables.

Los motores rotativos están también acoplados a un sistema de correas que mueve los carros del VSA opuesto. La transmisión es capaz de desplazar los carros de manera sincronizada con el movimiento del *end-effector*. Es decir, cuando el *end-effector* es desplazado, los carros lo siguen manteniendo la ortogonalidad de las fuerzas. Cuando los actuadores cambian la rigidez sin mover el *end-effector*, los carros no se mueven.

Un análisis de las fuerzas en el *end-effector*, en combinación con las relaciones cinemáticas de la transmisión, permite obtener la rigidez global en función de la rigidez y la fuerza de tracción en los cables, con las siguientes ecuaciones:

$$k_x = 8k_{w,x} + f_{w,y}\left(\frac{1}{h_{y0}} + \frac{1}{h_{y1}}\right)$$
$$k_y = 8k_{w,y} + f_{w,x}\left(\frac{1}{h_{x0}} + \frac{1}{h_{x1}}\right)$$

donde k_x y k_y son la rigidez total en el *manipulandum* en cada dirección, $k_{w,x}$ y $k_{w,y}$ son la rigidez generada por los resortes, $f_{w,x}$ y $f_{w,y}$ son la tensión en los cables, h_{x0} y h_{x1} son las distancias horizontales de los carros y h_{y0} e h_{y1} son las distancias verticales.

Para la implementación de la rigidez no-lineal en el elemento elástico, se presenta un sistema leva-resorte denominado *Linear Wire-Wrapped Cam SEA* (LinWWC-SEA), mostrado en la Fig. B.5. El SEA es compuesto de un resorte de torsión, una leva, un cable y una polea. El perfil de la leva define la relación entre el desplazamiento lineal del cable y la rotación del resorte de torsión. A través del correcto diseño del perfil de la leva, se puede obtener un comportamiento no lineal, similar a un resorte no

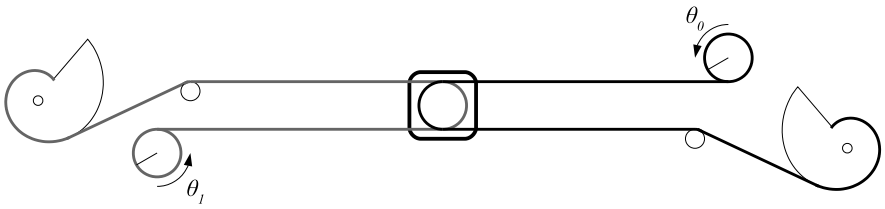


Figura B.6: VSA compuesto de dos LinWWC-SEA antagonistas. Mediante el accionamiento sincronizado de dos motores rotativos, es posible desplazar el *end-effector* y regular la rigidez de los cables.

lineal conectado al cable. El actuador a rigidez variable se obtiene implementando dos sistemas leva-resorte en configuración antagonista, como mostrado en la Fig. B.6.

Diseño Mecánico

El diseño mecánico del *PLANarm* es realizado según las especificaciones definidas para cumplir las características técnicas solicitadas al dispositivo. Considerando las prestaciones necesarias para desarrollar los ejercicios terapéuticos, y tomando como referencia las prestaciones garantizadas de los dispositivos de rehabilitación conocidos, para el *PLANarm* son definidas las siguientes especificaciones:

Área de trabajo Superficie plana de 50x50[cm].

Fuerza objetivo 40 [N] garantizados en todas las direcciones, en cada punto del área de trabajo.

Rango de rigidez Rigidez máxima de $4,2\ [\frac{\mathrm{N}}{\mathrm{mm}}]$, regulable en las dos direcciones principales x e y.

Con base en la configuración cinemática descrita anteriormente, y teniendo en cuenta las especificaciones apena indicadas, se realizan los cálculos para el correcto dimensionamiento del dispositivo. Son evaluadas las fuerzas en juego, la distribución de las cargas y las características dimensionales para el sistema leva-resorte. Los elementos del dispositivo son clasificados en seis grupos principales:

Estructura La estructura es el elemento base que da solidez al dispositivo completo. Está constituida por un chasis compuesto de cuatro tubos rectangulares, donde cuatro compartimientos cúbicos son acoplados en sus cuatro esquinas. En estos esquinas son montados los ejes de la transmisión a correas, los motores, los sistemas leva-resorte y los sensores necesarios para el funcionamiento del dispositivo. En el interior del perímetro compuesto por los tubos se fija un plano de madera cubierto de una lámina de acero, que corresponde al plano de trabajo por donde se desliza el *end-effector*.

End-effector Este es el elemento que entra en contacto con el usuario del dispositivo. Se trata de un "*joystick*" donde son instaladas cuatro poleas responsables de la conexión de los cuatro circuitos de cables. El *end-effector* contiene cuatro ruedas esféricas en su parte inferior para permitir el desplazamiento planar, y posee un

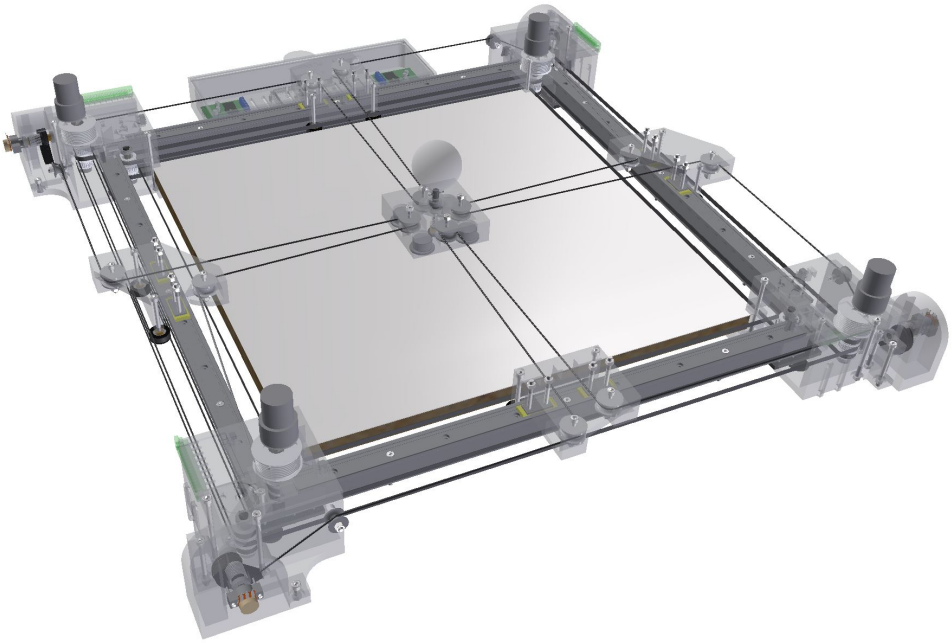


Figura B.7: Diseño CAD del PLANarm

imán para producir una fuerza de atracción entre la lámina de acero y el *end-effector*, evitando la separación entre ellos.

Motores El sistema de accionamiento son cuatro motores rotativos a corriente continua, uno para cada ángulo de la estructura. Estos vienen acoplados a los ejes que accionan las correas y los cables. Junto con los sistemas leva-resorte, son responsables del comportamiento del dispositivo en términos de posición, movimiento y elipse de rigidez.

Elementos elásticos no lineales Corresponden a los sistemas leva-resorte que, junto con los motores, constituyen los VSAs. Estos elementos, fijos en los cuatro esquinas de la estructura, están compuestos de un resorte de torsión instalado dentro una leva, por el cual se enrolla el cable dirigido al *end-effector*. El perfil de la leva y las características del resorte son dimensionadas con el objetivo de cumplir las especificaciones solicitadas al dispositivo.

Sistema de transmisión Se trata de un sistema de correas, poleas, ejes, carros, cables y tambores. Cuatro carros se deslizan sobre los cuatro tubos del perímetro y tienen la función de garantizar la ortogonalidad de los cables. Los carros son desplazados por un sistema a correas, conectadas a las poleas instaladas en los ejes presentes en cada ángulo.

Hardware Para el correcto funcionamiento del dispositivo se introducen los siguientes sensores: los motores presentan *encoders* que leen la posición angular de estos;

y cuatro potenciómetros leen la rotación de las levas. Un sistema de cableado transporta todas las señales a dos tarjetas controladoras basadas en *Arduino Due*.

Desarrollo del Prototipo

El dispositivo diseñado en la sección anterior es realizado en el taller mecánico del *Consiglio Nazionale delle Ricerche Italiane* (*National Research Council of Italy*, CNR). Una parte de los componentes, como los ejes, tambores y otros elementos en acero, son realizados a través de mecanizado convencional. Una gran parte de la piezas, principalmente aquellas con formas y características complejas, son producidas en plástico a través del proceso de impresión 3D (*Fused Deposition Modeling*, FDM). Una vez obtenidos los distintos componentes, son ensamblados la estructura, las correas, los carros, las levas, los cables y el *end-effector*. El prototipo tiene un costo aproximado de €2400, considerando solo el mecanismo y la electrónica.

El sistema de control del dispositivo tiene las siguientes funciones: definir una posición del *end-effector* en el plano, implementar una cierta rigidez y leer la fuerza externa producida sobre el *manipulandum* por el paciente. A través del accionamiento de los motores, posición y rigidez son fácilmente regulables. En términos de lectura de fuerza externa, conociendo el comportamiento cineto-estático de los sistemas leva-resorte, es posible calcular la fuerza midiendo la rotación de las levas por medio de los potenciómetros.

Relativo a este último aspecto, se desarrollan pruebas experimentales con el objetivo de confrontar el comportamiento real del dispositivo con las predicciones del modelo matemático, en relación a las curvas de fuerza vs desplazamiento.